UNIVERSITAT DE BARCELONA

Understanding the physical origin, topology and strength of noncovalent interactions by means of computational tools

Juan Diego Velasquez Benites

Facultat de Química

Departament de Química Inorgànica i Orgànica, Secció de Química Inorgànica

Programa de doctorat de Química Orgànica

Understanding the physical origin, topology and strength of noncovalent interactions by means of computational tools

Juan Diego Velasquez Benites

Grup d'Estructura Electrònica

Director/Tutor: Dr. Santiago Alvarez Reverter (Departament de Química Inorgànica i Orgànica, Secció de Química Inorgànica, Facultat de Química, Universitat de Barcelona)

Director: Dr. Jorge Echeverría López (Departamento de Química Inorgánica, Facultad de Ciencias, Universidad de Zaragoza)

Document signat digitalment per: JUAN DIEGO VELASQUEZ BENITES

SANTIAGO ALVAREZ REVERTER, Catedràtic Emèrit del Departament de Química Inorgànica i Orgànica, Secció de Química Inorgànica de la Universitat de Barcelona.

CERTIFICA: que el treball titulat «**Understanding the physical origin, topology and strength of noncovalent interactions by means of computational tools**» que presenta Juan Diego Velasquez Benites per aspirar al grau de Doctor ha sigut realitzat sota la seva direcció en el Departament de Química Inorgànica i Orgànica, Secció de Química Inorgànica de la Universitat de Barcelona.

Barcelona, juny de 2022

Santiago Alvarez Reverter

JORGE ECHEVERRÍA LÓPEZ, Investigador Ramón y Cajal en el Instituto de Síntesis y Catálisis Homogénea, Universidad de Zaragoza.

CERTIFICA: que el treball titulat «**Understanding the physical origin, topology and strength of noncovalent interactions by means of computational tools**» que presenta Juan Diego Velasquez Benites per aspirar al grau de Doctor ha sigut realitzat sota la seva direcció en el Departament de Química Inorgànica i Orgànica, Secció de Química Inorgànica de la Universitat de Barcelona.

Barcelona, juny de 2022

Jorge Echeverría López

La realització d'aquest Tesis Doctoral ha sigut possible gracies a la concessió d'una beca d'Ajut de Personal Investigador en Formació de la Universitat de Barcelona (APIF 2017-2018)

Agraïments

M'agradaria expressar el meu gran agraïment:

Als doctors Santiago Alvarez Reverter i Jorge Echeverría López per la seva paciència, per les seves conferències apassionades sobre el món de les interaccions no covalents i per ensenyar-me que es poden adquirir grans coneixements amb esforç, però també amb entusiasme.

A Eliseo, Gabriel, Jordi i a la resta de dels membres del grup d'Estructura Electrònica per l'ajuda prestada quan ho he necessitat.

A Adriana, Alejandro, Frank, Laia, Mauricio i Oliver, els meus companys de despatx. Ha sigut un gran plaer treballar amb gent alegre i divertida com vosaltres.

A la doctora Julia Contreras, la meva supervisora durant la meva estància a la Sorbonne Université. Moltes gracies pel dedicar-me temps i paciència per ensenyar-me un nou mètode per visualitzar i quantificar interaccions no covalents. Ha sigut de molta ajuda pel desenvolupament d'aquesta tesi.

A Trinidad, la meva companya de turisme per París. Moltes gracies pel teu suport, tant acadèmic com emocional.

A la meva família, per mostrar el seu suport i ànims en cada moment. Sense vosaltres mai hauria arribat tant lluny.

Als meus gats Cloe y Horus. Moltes gracies per omplir la meva vida de miols i pel vostre amor desinteressat.

A la meva àvia Elena i el meu gat Silvestre, que malauradament no van poder arribar a veure acabat aquest projecte. Em sento molt afortunat per haver compartit la meva vida amb vosaltres. Us trobo molt a faltar.

Als meus amics, que sempre han mostrat interès en aquest projecte.

“Como es arriba, es abajo”

Hermes Trismegisto

Abstract

The structure and stability of molecules, the formation of supramolecular aggregates in the solid state or in solution and, therefore, many chemical and biological processes in which they participate depend heavily on noncovalent interactions (NCIs). To fully exploit these weak interactions in order to reach specific chemical, biological and technological goals, a thorough understanding of their properties at the molecular level is crucial. In this doctoral thesis, different types of NCIs have been studied in detail in the gas phase using a combination of structural and computational methods. On one hand, searches in the Cambridge Structural Database (CSD) have revealed unnoticed intramolecular and intermolecular short contacts that dictate the structure of several families of molecules in their crystalline phases. Moreover, the analysis of the experimental structures has helped to identify the geometrical preferences that maximize the interaction strength. On the other hand, accurate density functional theory (DFT) calculations and other computational techniques have provided reliable information needed to unveil the energetics and physical nature of these interactions. The noncovalent interactions studied in this work are (1) Li···Li and X···X through-ring interactions in Li_2X_2 rings, (2) lone-pair-carbonyl interactions in acyl halides, (3) electrostatically disfavoured Br···C=O contacts, (4) sigma-hole interactions between lead(II) and sulphur or oxygen, (5) $[N{\cdots}I{\cdots}N]^+$ halonium bonding, and (6) azido···azido contacts in metal complexes with different interaction topologies. The results indicate that, although the atoms or moieties involved are different, the origin of all these attractive interactions lies in the subtle interplay of the various contributions (Pauli exchange-repulsion, electrostatics, charge transfer, polarization, and dispersion forces) acting upon the formation of noncovalently-bonded systems, differing only in the relative weights of these forces in the overall interaction strength.

Resum

L'estructura i l'estabilitat de les molècules, la formació d'agregats supramoleculars en estat sòlid i en solucions i, per tant, de molts processos químics i biològics en què participen depenen en gran manera de les interaccions no covalents (NCI). Per aprofitar al màxim aquestes interaccions febles en l'assoliment d'objectius químics, biològics i tecnològics específics, és crucial conèixer a fons les seves propietats a nivell molecular. En aquesta tesi doctoral s'han estudiat amb detall diferents tipus de NCI en fase gasosa mitjançant una combinació de mètodes estructurals i computacionals. D'una banda, les cerques a la Base de Dades Estructurals de Cambridge (CSD) han revelat contactes curts intramoleculars i intermoleculars desapercebuts que dicten l'estructura de diverses famílies de molècules en les seves fases cristal·lines. A més, l'anàlisi de les estructures experimentals ha ajudat a identificar les preferències geomètriques que maximitzen la força d'interacció. D'altra banda, els càlculs precisos basats en la teoria del funcional de la densitat (DFT) i altres tècniques computacionals han proporcionat informació fiable necessària per revelar l'energia i la naturalesa física d'aquestes interaccions. Les interaccions no covalents estudiades en aquest treball són (1) interaccions a través de l'anell Li···Li i X···X en anells de Li_2X_2, (2) interaccions carbonil-parell solitari en halurs d'acil, (3) contactes Br···C=O electroestàticament desafavorits, (4) interaccions "sigma-hole" entre plom(II) i sofre o oxigen, (5) l'enllaç d'haloni $[N\cdots I\cdots N]^+$, i (6) contactes azido···azido en complexos metàl·lics amb diferents topologies d'interacció. Els resultats indiquen que, tot i que els àtoms o fragments implicats són diferents, l'origen de totes aquestes interaccions atractives rau en la interacció subtil de les diverses contribucions (intercanvi-repulsió de Pauli, electroestàtica, transferència de càrrega, polarització i forces de dispersió) que actuen sobre la formació de sistemes enllaçats no covalentment, els quals difereixen només en els pesos relatius d'aquestes forces per a la força global d'interacció.

Index

Introduction

1. Noncovalent interactions

Interactions between and within molecules that do not lead to a chemical reaction, i.e., no bond is formed or broken, are called noncovalent interactions (NCIs). During the last decades, the key role played by these interactions in many chemical and biological processes has been recognized.[1-4] Although such interactions are considerably weaker (by 1 or 2 orders of magnitude) than covalent bonds, they dictate the structure of biomolecules such as DNA[4,5] and proteins,[6,7] molecular crystals,[8,9] and condensed phases. In addition, they play an essential role in molecular recognition.[10-12] NCIs can be classified into two categories: intramolecular and intermolecular. The first group is established within the same molecular entity and modulates the conformational structure of molecules (e.g., the secondary and tertiary structure of proteins). The second group mediates the interaction between molecules (e.g., the quaternary structure of proteins) and determines the physical properties of gases, liquids and crystals.

NCIs can be further classified depending on the element or group that acts as a Lewis base centre (hydrides[13] and halide[14] bonds) or, more usually, as a Lewis acid centre. However, this classification has proved to be challenging and confusing. For example, researchers have coined the terms triel (group 13),[15-17] tetrel (group 14),[8,18,19] pnicogen (group 15),[20-22] chalcogen (group 16),[23,24] and halogen (group 17)[25,26] bonds since they concern elements of the corresponding main group acting as electron acceptors. However, several studies have pointed out that the mechanism that rules these interactions is similar: an interaction between a nucleophile, partially negative, and an electron charge depletion region, partially positive, in the elongation of main group covalent bonds or parallel to them (σ-hole) or perpendicular to planar portion of the molecules (π-hole).[8,15-28] The chaos is aggravated since the triel, tetrel, pnicogen, and chalcogen interactions can be categorized as σ-hole[27] or π-hole[28] bonds depending on the origin of the electron density depletion. Other names related to the elements are hydrogen[29] and lithium bonds.[30] It seems clear that there are no strict criteria for categorizing noncovalent interactions. In a recent report, Grabowsky has shown that different interactions lead to the same structural changes in the units in contact. Therefore, he has proposed a systematic and uniform classification of noncovalent interactions based on the Valence Shell Electron Pair Repulsion (VSEPR) model.[31] Other classifications such as those based on the fundamental forces that contribute to the interaction energy have been proposed.[32] All NCIs are stabilised by the same energy components and counterbalanced by repulsion

between electron clouds. The only difference between noncovalent clusters arises from the relative contribution of these attractive forces to the overall bond strength.

On the basis of the second generation of Energy Decomposition Analysis based on Absolutely-Localized Molecular Orbitals (ALMO-EDA-II; Chapter 1),[33] the energy of a noncovalent interaction can be decomposed into the "frozen density" component (ΔE_{FRZ}) and the orbital-based terms, namely polarization (ΔE_{POL}) and charge-transfer (ΔE_{CT}) terms. The ΔE_{FRZ} term can be further dissected into electrostatic (ΔE_{ELEC}), Pauli exchange-repulsion (ΔE_{PAULI}), and dispersion (ΔE_{DISP}) contributions. The ΔE_{ELEC} term includes the electrostatic interactions between the charge densities of the nucleus and electrons of the interacting fragments.[34] Dispersion, polarization and charge-transfer terms are always attractive, regardless of the orientation, while the electrostatic force can be attractive or repulsive depending on the mutual orientation of molecules. The remaining term, Pauli exchange-repulsion, is always repulsive. Only rarely one of these attractive terms is the main dominant contribution. For example, van der Waals (vdW) interactions between noble gas atoms arise only from dispersion contributions.[35,36] Typically, several attractive terms contribute to the overall stabilization of noncovalent clusters: Classical hydrogen bonds are mostly electrostatic with a non-negligible polarization and charge transfer (covalent) contribution.[33,37] Nonclassical hydrogen bonds typically have a larger dispersion component than classical hydrogen bonds.[38] Thus, a deep knowledge of the origin of a given interaction is crucial to control it and eventually exploit it at the nanoscale, in crystal engineering or materials design with novel physical, optical, electrochemical, photochemical, biological or catalytic properties. Unlike intermolecular NCIs, an EDA partition of intramolecular NCIs is not trivial because the molecule can be partitioned into two fragments in a whole set of ways. To overcome this limitation, several methods have been proposed such as intramolecular analogues of Symmetry-Adapted Perturbation Theory (I-SAPT)[39-41] and EDA,[42] Natural Bond Orbital (NBO),[43] and Interacting Quantum Atoms (IQA).[44]

Understanding the directionality, strength, and nature of NCIs is not a straightforward matter. Although some progress has been made through decades of experimental observations supplemented by theoretical predictions in various model systems, we are still far from obtaining an unambiguous characterization and interpretation of these interactions. First, some NCIs remain hidden within the bonding network due to their tiny interaction energies. Second, the forces that dictate the formation

of the crystal and supramolecular structures very often coexist and cooperate with each other (synergic effect).[45,46] In other cases, they can compete, one predominating over the other when it comes to heteromolecular systems (depending on the partner chosen)[47,48] or leading to polymorphism[49,50] in homomolecular systems. Finally, the environment (condensed phase calculations) strongly affects the properties of noncovalent interactions.[51,52] Thus, it is essential to apply the most accurate and efficient quantum chemical (QC) methods along with experimental studies (e.g., crystal structures) to detect, isolate, and unveil the nature of NCIs from both the structural and energetic points of view.

2. Objectives

The aim of this thesis is, by means of combined structural and computational analyses, the establishment of the geometrical preferences for different noncovalent interactions as well as understanding their nature and the factors that affect their strength. Most systems studied during the PhD intended to analyse different cases of intermolecular or intramolecular contacts in which two or more types of noncovalent interactions may have significant contributions. That would allow me to construct a diagram like the one depicted in Figure 1, where A, B, … would be the systems studied here. On the basis of the results obtained, I should be able to calibrate the position of each case studied and, if possible, in a subsequent analysis unveil which molecular characteristics determine the position of each of them on that map. In that way I explore the diffuse borders between bonding and nonbonding scenarios, hopefully contributing to a better understanding of bond theory in general and of noncovalent interactions in particular. In this thesis, after a brief introduction to the computational methodology, I will introduce the main interactions that I have analysed with this aim.

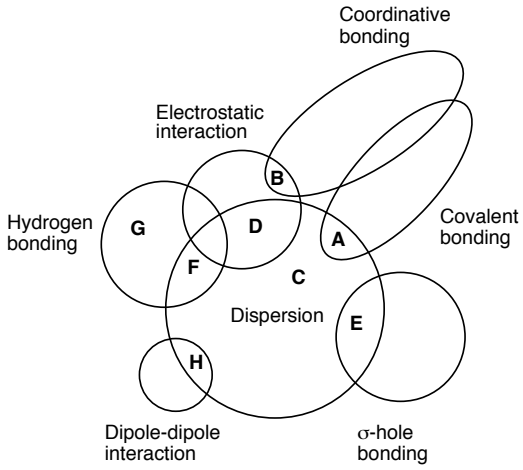

Figure 1. Hypothetical diagram of different noncovalent interactions cooperating or competing with each other in different systems **A** – **G**.

In Chapter 1, I give a brief explanation of the theoretical background of quantum chemical methods (DFT) and the basis sets used for computing noncovalent interactions studied herein. The methods applied for computing the interaction energies (Counterpoise method and EDA), to identify electron-rich and electron-poor regions of the compounds prone to interact between them (MEP), for calculating the atomic charges (NPA) and unveiling the orbitals involved in the charge transfer process (NBO) and for analysing the topology of its electron density (QTAIM and NCI Index) are also explained in that chapter.

In Chapter 2, I have carried out a theoretical study of the bonding within Li_2X_2 frameworks (Scheme 1). In spite of the highly ionic character of most lithium-element bonds, the bonding within Li_2X_2 rings presents similarities with that found in analogous transition metal systems. They obey simple framework electron counting rules that allow us to predict whether they will form a regular ring or a squeezed one with short Li−Li or X−X distances. A combined computational and structural database analysis discloses the orbital conditions that determine the framework electron counting rules. These systems probe the borderline between the covalent and ionic bonding models since, paradoxically, a non-negligible covalent contribution of the two Li atoms (formally Li^+ ions in the ionic model) to the Li−X framework bonding favours them approaching each other within bonding distance.

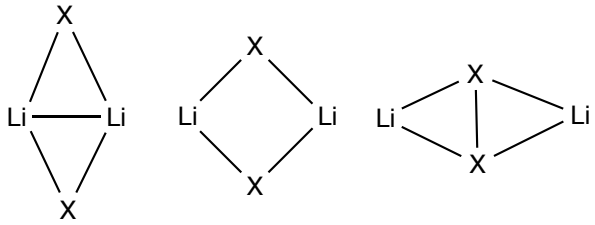

Scheme 1. Three alternative structures for Li_2X_2 rings.

In Chapter 3, I have performed a combined structural and theoretical analysis of intermolecular lone-pair−carbonyl interactions in several families of acyl halides (R-CO-X; Scheme 2). It seems clear nowadays that the physical origin of the interaction involving the lone pair (n) of a nucleophile (Nu) and the electron-deficient region (π-hole) of a carbonyl group (i.e., its C atom) implies different combinations of electrostatic (π-hole bonding) and orbital (n→π* interaction) terms since the π-hole and the π* empty orbital of the carbonyl are located in the same region of the molecule, i.e., the carbonyl carbon atom. CSD searches have allowed me to establish the geometrical preference for such short contacts, which is reminiscent of the Bürgi-Dunitz trajectory[53,54] for a nucleophilic attack. The study of the Molecular Electrostatic Potential (MEP) of several molecules along with an Energy Decomposition Analysis (EDA) has disclosed the nature of the interaction and the factors that affect its strength. Surprisingly, the results indicates that the dispersion term is the main driving force of the interaction. To further understand lone-pair−carbonyl contacts, I have systematically analysed, by means of DFT calculations, the effect of the lone-pair as well as of the halogen atom (X) and the substituent attached to the carbonyl group (R). Interaction energies up to 3 kcal/mol suggest that these interactions can be exploited in crystal design and supramolecular chemistry.

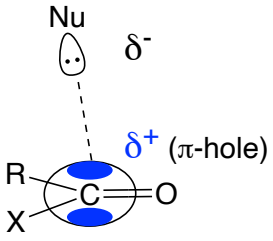

Scheme 2. Schematic depiction of the lone-pair−carbonyl interaction (dashed line) in acyl halides (R-CO-X, where X = F, Cl, Br, and I) studied in Chapter 3. The blue regions represent the π-holes.

In Chapter 4, I have performed a combined structural and computational analysis of short contacts between bromine and the carbon atom of a carbonyl group (Scheme 3). Surprisingly, 9% of such contacts are arranged in such a way that the positively charged regions of the two atoms involved, i.e., Br and C, are in close contact, so the interaction geometry cannot be predicted in terms of molecular electrostatic potential maps. Remarkably, despite this "like-like" electrostatic configuration, the interaction energies associated with these contacts are attractive and relatively large (ca. 1 kcal/mol). Comprehensive EDA and Natural Bond Orbital (NBO) analysis have allowed me to unveil the physical origin of these interactions, which arise from a precise balance between steric factors (Pauli and electrostatics), dispersion, and charge transfer. These results reinforce the idea of noncovalent interactions as a more or less subtle combination of attractive and repulsive forces rather than a "purely electrostatic" or a "purely orbital" process and open the way to explore new types of interactions beyond the electron density holes model.

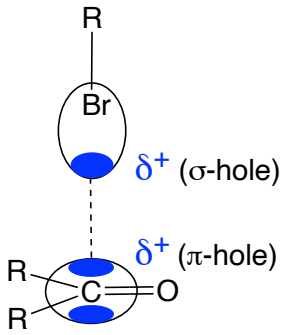

Scheme 3. Schematic depiction of the Br···C=O interaction (dashed line) studied in Chapter 4. The *σ*-hole and the *π*-holes are coloured in blue. Despite the like-like electrostatic configuration, the associated interaction energies are attractive.

In Chapter 5, I have theoretically studied the noncovalent "tetrel" interactions found in the crystal structures of two recently synthetized Pb(II) compounds, in which the lead centre is coordinated by organic ligands via S and O donor atoms (Scheme 4). Remarkably, in both compounds, the Pb coordination is hemidirectional, which facilitates the approach of extra donors to establish interactions at longer distances. Such interactions are of *σ*-hole (electrostatic) nature between the Pb and O/S atoms, acting as Lewis acid and bases, respectively. Interestingly, the Pb···O/S distances are closer to the sum of the covalent radii than to the van der Waals sum, which suggests a considerably strong interaction. I have performed a theoretical analysis based on DFT calculations to gain deeper insight into the origin and features of these *σ*-hole interactions. Moreover, the

nature of the Pb···O/S interactions has been further analysed by means of Quantum Theory of Atoms in Molecules (QTAIM), MEP and NBO calculations. A significant charge transfer from the S lone pairs into an empty antibonding orbital of the metallic centre has been determined, indicating that the so-called "tetrel" bonding is in fact of dual nature. Interaction energies up to 10 and 15 kcal/mol suggest that such NCIs can be exploited for the development of new Pb-containing MOFs in which a supramolecular assembly is dominated by *σ*-hole interactions.

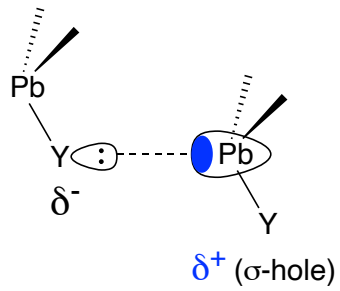

Scheme 4. Schematic depiction of the Y···Pb (Y = O and S) tetrel interaction (dashed line) studied in Chapter 5. The blue region represents the *σ*-hole.

In Chapter 6, I have carried out a combined structural and computational study of the geometrical parameters and the bonding in three-centre-four-electron $[N\cdots I\cdots N]^+$ halonium groups. CSD searches have revealed linear and symmetrical $[N\cdots I\cdots N]^+$ frameworks with neutral donors. By means of DFT, MEP and EDA calculations, I have studied the effect of various halogen atoms (X) on the $[py\cdots X\cdots py]^+$ framework, the effect of different nitrogen-donor groups (D) attached to the iodonium cation and the influence of the electron density alteration on the $[N\cdots I\cdots N]^+$ halonium bond by variation of the R substituents at the N-donor on the symmetry, strength and the nature of the interaction. The physical origin of the interaction arises from a subtle interplay between electrostatic (*σ*-hole bond) and orbital terms. Such a linear, symmetrical and static arrangement results from simultaneous interaction of an electron-deficient halonium ion (X^+) and two Lewis bases by accepting electrons in both lobes of the empty p-orbital of X. On the other hand, due to the anisotropy of the electron density of the central X^+ cation, a *σ*-hole is formed from both lobes of such p-orbital, forming an electrostatic interaction with both donors (Scheme 5). Interaction energies as high as 45 kcal/mol suggest that halonium bonds can be exploited for the development of novel halonium transfer agents, in asymmetric halofunctionalization or as building blocks in supramolecular chemistry.

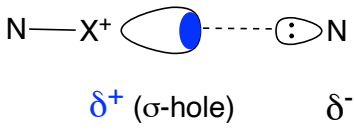

Scheme 5. Schematic depiction of the $[N\text{-}X\text{-}N]^+$ (X = F, Cl, Br and I) halonium bond studied in Chapter 6. The blue region represents the *σ*-hole.

In Chapter 7, I have theoretically investigated the nature and the strength of the different interaction topologies between the azido ligands in transition metal (N_3-M) azide complexes (Scheme 6). A search in the CSD has revealed 9 different bonding patterns with undisclosed intermolecular N···N contacts shorter than twice the nitrogen vdW radius. Eight of these topologies display noncovalent systems that are only bound by unsupported N···N interactions, regardless of whether they are electrostatically favoured (*π*-hole bond) or not. To further understand azido interactions, each topology was studied at dihedral angles ϕ of 90º and 180º, respectively, by means of DFT calculations. The trifluoromethyl-azido-mercury(II) dimer was selected as a model. EDA results reveal that the dispersion force is the dominant factor of the interaction with orbital terms to a lesser extent. Their dispersion-dominated nature was also demonstrated through combined QTAIM and NCI Index analyses. The cooperative effect of the N···Hg interaction, which has been observed in several compounds studied herein, was also analysed. Remarkably, those dimers with this secondary interaction are the most stable ones. Furthermore, it stabilizes electrostatically disfavourable azido···azido contacts. Interaction energies up to -1.10 kcal/mol for unsupported contacts suggest that these NCIs may be useful for dictating the conformation of the molecules and therefore might have various applications in the field of catalysis, reactivity, and crystal engineering, to name just a few examples.

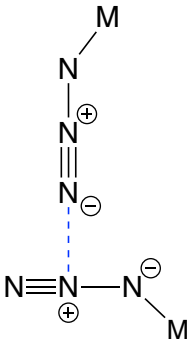

Scheme 6. Schematic description of the azido···azido interaction (dashed line), where M is a transition metal.

3. References

1. Zhao, Y.; Cotelle, Y.; Sakai, N.; Matile, S. Unorthodox Interactions at Work. *J. Am. Chem. Soc.* **2016**, *138*, 4270-4277.
2. Bauzá, A.; Mooibroek, T. J.; Frontera, A. The Bright Future of Unconventional σ/π-Hole Interactions. *ChemPhysChem*. **2015**, *16*, 2496-2517.
3. Govindaraju, T.; Ariga, K. *Molecular Architectonics and Nanoarchitectonics*. Springer: Singapore, 2021.
4. Černý, J.; Hobza, P. Non-covalent interactions in biomacromolecules. *Phys. Chem. Chem. Phys.* **2007**, *9*, 5291-5303.
5. Strekowski, L.; Wilson, B. Noncovalent Interactions with DNA: An Overview. *Mutat. Res.* **2007**, *623*, 3-13.
6. Newberry, R. W.; Bartlett, G. J.; VanVeller, B.; Woolfson, D. N.; Raines, R. T. Signatures of n→π* interactions in proteins. *Protein Sci.* **2014**, *23*, 284-288.
7. Karshikoff, A. *Non-Covalent Interactions In Proteins*, 2nd ed.; World Scientific Publishing: Singapore, 2021.
8. Velasquez, J. D.; Mahmoudi, G.; Zangrando, E.; Gurbanov, A. V.; Zubkov, F. I.; Zorlu, Y.; Masoudiasl, A.; Echeverría, J. Experimental and theoretical study of Pb···S and Pb···O σ-hole interactions in the crystal structures of Pb(II) complexes. *CrystEngComm*. **2019**, *21*, 6018-6025.
9. Velasquez, J. D.; Mahmoudi, G.; Zangrando, E.; Miroslaw, B.; Safin, D. A.; Echeverria, J. Non-covalent interactions induced supramolecular architecture of $Hg(NCS)_2$ with 3-pyridinecarbaldehyde nicotinoylhydrazone. *Inorg. Chim. Acta*. **2020**, *509*, 119700-119706.
10. Rehman, S. U.; Sarwar, T.; Husain, M. A.; Ishqi, H. M.; Tabish, M. Studying Non-Covalent Drug-DNA Interactions. *Arch. Biochem. Biophys.* **2015**, *576*, 49-60.
11. Ceborska, M.; Dąbrowa, K.; Cędrowski, J.; Zimnicka, M. Hydrogen-Bonded Supramolecular Assemblies of Folic Acid with Simple Hexoses. *J. Mol. Struct.* **2022**, *1250*, 131904-131910.
12. Macchiagodena, M.; Pagliai, M.; Procacci, P. Characterization of the Non-Covalent Interaction between the PF-07321332 Inhibitor and the SARS-CoV-2 Main Protease. *J. Mol. Graph. Model.* **2022**, *110*, 108042-108050.

13. Grabowski, S. J. Hydrogen bonds, and σ-hole and π-hole bonds–mechanisms protecting doublet and octet electron structures. *Phys. Chem. Chem. Phys*. **2017**, *19*, 29742-29759.
14. Van der Veken, B. J.; Sluyts, E. J. Reversed Lewis Acidity of Mixed Boron Halides: An Infrared Study of the van der Waals Complexes of BF_xCl_y with CH_3F in Cryosolution. *J. Am. Chem. Soc*. **1997**, *119*, 11516-11522.
15. Yang, Q.; Zhou, B.; Li, Q.; Scheiner, S. Weak σ-Hole Triel Bond between C_5H_5Tr (Tr = B, Al, Ga) and Haloethyne: Substituent and Cooperativity Effects. *Chemphyschem*. **2021**, *22*, 481-487.
16. Karachi, S. S.; Eskandari, K. Boron Triel Bonds: A Quantum Chemical Topology Perspective. *ChemistrySelect*. **2021**, *6*, 12431-12439.
17. Wang, X.; Li, Y.; Wang, H.; Ni, Y.; Wang, H. Which Triel Bond Is Stronger? $TrHX\cdots H_2Y$ versus $TrH_2X\cdots H_2Y$ (Tr = Ga, In; X = F, Cl, Br, I; Y = O, S). *Theor. Chem. Acc.* **2021**, *140*, 80-90.
18. Bauzá, A.; Mooibroek, T. J.; Frontera, A. Tetrel Bonding Interactions. *Chem. Rec.* **2016**, *16*, 473-487.
19. Liu, N.; Liu, J.; Li, Q.; Scheiner, S. Noncovalent Bond between Tetrel π-Hole and Hydride. *Phys. Chem. Chem. Phys.* **2021**, *23*, 10536-10544.
20. Scheiner, S. The Pnicogen Bond: Its Relation to Hydrogen, Halogen, and Other Noncovalent Bonds. *Acc. Chem. Res.* **2013**, *46*, 280-288.
21. Bauzá, A.; Mooibroek, T. J.; Frontera, A. σ-Hole Opposite to a Lone Pair: Unconventional Pnicogen Bonding Interactions between ZF_3 (Z = N, P, As, and Sb) Compounds and Several Donors. *Chemphyschem*. **2016**, *17*, 1608-1614.
22. Bauzá, A.; Quiñonero, D.; Deyà, P. M.; Frontera, A. Pnicogen-π Complexes: Theoretical Study and Biological Implications. *Phys. Chem. Chem. Phys.* **2012**, *14*, 14061-14066.
23. Vogel, L.; Wonner, P.; Huber, S. M. Chalcogen Bonding: An Overview. *Angew. Chem. Int. Ed.* **2019**, *58*, 1880-1891.
24. Esrafili, M. D.; Nurazar, R. Chalcogen Bonds Formed through π-Holes: SO_3 Complexes with Nitrogen and Phosphorus Bases. *Mol. Phys.* **2016**, *114*, 276-282.
25. Clark, T. Halogen Bonds and σ-Holes. *Faraday Discuss.* **2017**, *203*, 9-27.
26. Zhang, Y.; Ma, N.; Wang, W. A New Class of Halogen Bonds That Avoids the σ-Hole. *Chem. Phys. Lett.* **2012**, *532*, 27-30.

27. Politzer, P.; Murray, J. S.; Clark, T.; Resnati, G. The σ-Hole Revisited. *Phys. Chem. Chem. Phys.* **2017**, *19*, 32166-32178.
28. Politzer, P.; Murray, J. S.; Clark, T. The π-Hole Revisited. *Phys. Chem. Chem. Phys.* **2021**, *23*, 16458-16468.
29. Huttermann, A. *The Hydrogen Bond: A Bond for Life*, 1st ed.; De Gruyter: Berlin, Germany, 2019.
30. Velasquez, J. D.; Echeverría, J.; Alvarez, S. Delocalized Bonding in Li_2X_2 Rings: Probing the Limits of the Covalent and Ionic Bonding Models. *Inorg. Chem.* **2021**, *60*, 345-356.
31. Grabowski, S. J. Classification of So-Called Non-Covalent Interactions Based on VSEPR Model. *Molecules*. **2021**, *26*, 4939-4961.
32. Hobza, P.; Zahradník, R.; Müller-Dethlefs, K. The world of non-covalent interactions: 2006. *Collect. Czech. Chem. Commun*. **2006**, *71*, 443-531.
33. Horn, P. R.; Mao, Y.; Head-Gordon, M. Probing non-covalent interactions with a second generation energy decomposition analysis using absolutely localized molecular orbitals. *Phys. Chem. Chem. Phys*. **2016**, *18*, 23067-23079.
34. Mao, Y.; Loipersberger, M.; Horn, P. R.; Das, A.; Demerdash, O.; Levine, D. S.; Prasad Veccham, S.; Head-Gordon, T.; Head-Gordon, M. From Intermolecular Interaction Energies and Observable Shifts to Component Contributions and Back Again: A Tale of Variational Energy Decomposition Analysis. *Annu. Rev. Phys. Chem.* **2021**, *72*, 641-666.
35. Eisenschitz, R.; London, F. Über das Verhältnis der van der Waalsschen Kräfte zu den homöopolaren Bindungskräften. *Zeitschrift für Physik*. **1930**, *60*, 491-527.
36. Su, P.; Li, H. Energy Decomposition Analysis of Covalent Bonds and Intermolecular Interactions. *J. Chem. Phys.* **2009**, *131*, 014102-014116.
37. Khaliullin, R. Z.; Bell, A. T.; Head-Gordon, M. Electron Donation in the Water-Water Hydrogen Bond. *Chem. Eur. J*. **2009**, *15*, 851-855.
38. Sánchez-de-Armas, R.; Ahlquist, M. S. G. On the Nature of Hydrogen Bonds to Platinum(II) - Which Interaction Can Predict Their Strength? *Phys. Chem. Chem. Phys.* **2015**, *17*, 812-816.
39. Gonthier, J. F.; Corminboeuf, C. Exploration of Zeroth-Order Wavefunctions and Energies as a First Step toward Intramolecular Symmetry-Adapted Perturbation Theory. *J. Chem. Phys.* **2014**, *140*, 154107-154116.

40. Pastorczak, E.; Prlj, A.; Gonthier, J. F.; Corminboeuf, C. Intramolecular Symmetry-Adapted Perturbation Theory with a Single-Determinant Wavefunction. *J. Chem. Phys.* **2015**, *143*, 224107-224117.
41. Parrish, R. M.; Gonthier, J. F.; Corminbœuf, C.; Sherrill, C. D. Communication: Practical Intramolecular Symmetry Adapted Perturbation Theory via Hartree-Fock Embedding. *J. Chem. Phys.* **2015**, *143*, 051103-051107.
42. Su, P.; Chen, Z.; Wu, W. An Energy Decomposition Analysis Study for Intramolecular Non-Covalent Interaction. *Chem. Phys. Lett.* **2015**, *635*, 250-256.
43. Reed, A. E.; Curtiss, L. A.; Weinhold, F. Intermolecular Interactions from a Natural Bond Orbital, Donor-Acceptor Viewpoint. *Chem. Rev.* **1988**, *88*, 899-926.
44. Pendás, Á. M; Blanco, M. A.; Francisco, E. Chemical Fragments in Real Space: Definitions, Properties, and Energetic Decompositions. *J. Comput. Chem.* **2007**, *28*, 161-184.
45. Corradi, E.; Meille, S. V.; Messina, M. T.; Metrangolo, P.; Resnati, G. Halogen Bonding versus Hydrogen Bonding in Driving Self-Assembly Processes. *Angew. Chem. Int. Ed*. **2000**, *39*, 1782-1786.
46. Li, X.-N.; Yang, M.; Chen, X.-L.; Jia, J.-H.; Zhao, W.-W.; Wu, X.-Y.; Wang, S.-S.; Meng, L.; Lu, C.-Z. Synergistic Intra- and Intermolecular Noncovalent Interactions for Ultralong Organic Phosphorescence. *Small* **2019**, *15*, e1903270-e1903274.
47. Aakeröy, C. B.; Desper, J.; Helfrich, B. A.; Metrangolo, P.; Pilati, T.; Resnati, G.; Stevenazzi, A. Combining halogen bonds and hydrogen bonds in the modular assembly of heteromeric infinite 1-D chains. *Chem. Commun*. **2007**, 4236-4238.
48. Saha, B. K.; Nangia, A.; Jaskólski, M. Crystal engineering with hydrogen bonds and halogen bonds**.** *CrystEngComm.* **2005**, *7*, 355-358.
49. Sharber, S. A.; Mann, A.; Shih, K.-C.; Mullin, W. J.; Nieh, M.-P.; Thomas III, S. W. Directed Polymorphism and Mechanofluorochromism of Conjugated Materials through Weak Non-Covalent Control. *J. Mater. Chem. C Mater. Opt. Electron. Devices*. **2019**, *7*, 8316-8324.
50. Roy, S.; Hazra, A.; Bandyopadhyay, A.; Raut, D.; Madhuri, P. L.; Rao, D. S. S.; Ramamurty, U.; Pati, S. K.; Krishna Prasad, S.; Maji, T. K. Reversible Polymorphism, Liquid Crystallinity, and Stimuli-Responsive Luminescence in a Bola-Amphiphilic π-System: Structure-Property Correlations through Nanoindentation and DFT Calculations. *J. Phys. Chem. Lett.* **2016**, *7*, 4086-4092.

51. Obenchain, D. A.; Spada, L.; Alessandrini, S.; Rampino, S.; Herbers, S.; Tasinato, N.; Mendolicchio, M.; Kraus, P.; Gauss, J.; Puzzarini, C.; Grabow, J.-U.; Barone, V. Unveiling the Sulfur-Sulfur Bridge: Accurate Structural and Energetic Characterization of a Homochalcogen Intermolecular Bond. *Angew. Chem. Int. Ed.* **2018**, *57*, 15822-15826.

52. Lee, J.-U.; Lee, S.-S.; Lee, S.; Oh, H. B. Noncovalent Complexes of Cyclodextrin with Small Organic Molecules: Applications and Insights into Host-Guest Interactions in the Gas Phase and Condensed Phase. *Molecules* **2020**, *25*, 4048-4075.

53. Burgi, H. B.; Dunitz, J. D.; Shefter, E. Geometrical reaction coordinates. II. Nucleophilic addition to a carbonyl group. *J. Am. Chem. Soc.* **1973**, *95*, 5065-5067.

54. Burgi, H. B.; Dunitz, J. D.; Lehn, J. M.; Wipff, G. Stereochemistry of reaction paths at carbonyl centres. *Tetrahedron* **1974**, *30*, 1563-1572.

Chapter 1

Methodology

1.1 Introduction

Since its modest beginning in the 1950's, computational chemistry has been widely used to investigate the behaviour and properties of molecules, groups of molecules and solids through the use of computer modelling and simulation.[1] Computational techniques have allowed us to understand the reactivity, the dynamics and the functions of chemical, biological, and physical systems and build predictive models in order to design new drugs or materials. While the results obtained normally complement the experimentally-derived data, it has also provided invaluable insight which is difficult to obtain otherwise, such as vibrational frequencies, reactivity and energies. There are two main branches of computational chemistry: one is based on classical mechanics and the other is based on quantum mechanics (QM). The former approach, called Molecular mechanics or force fields methods,[2] is useful in conformational studies of proteins and protein-ligand binding thermodynamics. The latter approach, the quantum mechanical model,[3] is useful for describing the quantum behaviour of atoms and molecules. The QM model can usually be classified either as *ab initio* (without empirical parameters) or *semi-empirical* approach.

1.2 Electronic Structure Methods

1.2.1 Density Functional Theory

One of the postulates of QM is that the wavefunction contains all information that is known or can be known about a molecule.[4] Hence, finding solutions to the time-independent, non-relativistic Schrödinger equation[5] (Eq. 1.1) is the main goal of quantum chemistry:

$$\hat{H}\Psi = E\Psi \qquad \text{(Eq. 1.1)}$$

where $\hat{H}$ is the Hamiltonian operator for the system, Ψ is the wavefunction to be determined, and E is the energy of the system.

Analytical solutions of the Schrödinger equation are only available for very small systems ($N_{particles} \leq 2$) due to the electron-electron repulsion term. For more than two particles, the Schrödinger equation is simplified using the Born-Oppenheimer[6] approximation. Within this method, the electronic Schrödinger equation that describes the system is (Eq. 1.2):

$$\hat{H}\Psi = \left[\hat{T} + \hat{V}_{ee} + \hat{V}_{Ne}\right]\Psi = E\Psi \qquad \text{(Eq. 1.2)}$$

where $\hat{T}$ is the electron kinetic energy, $\hat{V}_{ee}$ is the repulsive potential due to electron-electron interaction, and $\hat{V}_{Ne}$ is the attractive external potential exerted on the electrons due to the nuclei. The operators $\hat{T}$ and $\hat{V}_{ee}$ are called universal operators, as they are unique for any N-electron system, while $\hat{V}_{Ne}$ is system-dependent, uniquely determined by the nuclear charge (Z_A) and its position (R_A).

Approximate solutions of Eq. 1.2 are obtained using *ab initio* wavefunction theory methods such as Hartree-Fock (HF) theory,[7] in which each electron feels only the average Coulombic repulsion of all other electrons. It can be enhanced, with the price of added computational cost, by adding the electron correlation via "post-HF" methods, such as the Møller-Plesset (MP)[8] perturbation theory or the coupled cluster (CC) approach.[9] Another approximation, based on the functionals of electron density (ρ) rather than the wavefunction, is the Density Functional Theory (DFT).[1,10-14] The computational cost is relatively low compared to wavefunction methods (HF and post-HF methods) since ρ is much easier to calculate than the total wavefunction used in the orbital approximation. Although this method has its roots in the Thomas-Fermi model,[11,12] modern DFT calculations were established on the basis of Hohenberg-Kohn theorems[13] and Kohn-Sham equations.[14]

1.2.1.1 Hohenberg-Kohn theorems

According to the first Hohenberg-Kohn theorem, the external potential ($\hat{V}_{Ne}$), and hence the Hamiltonian operator and all the ground state properties of the system, are determined by the ground state electron density (ρ_0). In other words, the ground state wavefunction (Ψ_0) is a unique functional of ρ_0 (Eq. 1.3):

$$\Psi_0 = \Psi_0[\rho_0] \qquad \text{(Eq. 1.3)}$$

so the ground state energy (E_0) is also a functional of ρ_0 (Eq. 1.4):

$$E_0 = E_0[\rho_0] = T[\rho_0] + E_{ee}[\rho_0] + E_{Ne}[\rho_0] \qquad \text{(Eq. 1.4)}$$

where $T[\rho_0]$ is the kinetic energy, $E_{ee}[\rho_0]$ is the repulsive energy due to electron-electron interaction, and $E_{Ne}[\rho_0]$ is attractive energy due to the nuclei-electron interaction at the ground state electron density.

In the sense of their dependence on the system under study (N, Z_A and R_A), the energy components can be separated into universal functionals ($T[\rho_0]$ and $E_{ee}[\rho_0]$) and non-universal functional ($E_{Ne}[\rho_0]$; Eq. 1.5). Collecting the former group into the Hohenberg-Kohn functional ($F_{HK}[\rho_0]$), we arrive at (Eq. 1.6).

$$E_{Ne}[\rho_0] = \int \rho_0(\vec{r})\, V_{Ne}\, d\vec{r} \qquad \text{(Eq. 1.5)}$$

$$E_0[\rho_0] = F_{HK}[\rho_0] + \int \rho_0(\vec{r})\, V_{Ne}\, d\vec{r} \qquad \text{(Eq. 1.6)}$$

For an arbitrary density ($\rho(\vec{r})$), the Hohenberg-Kohn functional can be written as the sum of the kinetic energy and the electron-electron repulsion operator with the ground state wavefunction (Ψ) that yields $\rho(\vec{r})$ and delivers the lowest energy (Eq. 1.7):

$$F_{HK}[\rho] = T[\rho] + E_{ee}[\rho] = \langle \Psi[\rho] | \hat{T} + \hat{V}_{ee} | \Psi[\rho] \rangle \qquad \text{(Eq. 1.7)}$$

The explicit form of the functional $F_{HK}[\rho]$ is unknown. If it were known we would have solved the Schrödinger equation exactly even for gigantic systems such as DNA, given the universality of the operators it contains.

The second theorem establishes a variational principle: the functional (Eq. 1.6) that delivers the ground state energy of the system attains its exact value if and only if the input density is the true ground state density. Otherwise, for all other allowed $\tilde{\rho}(\vec{r})$ such that $\tilde{\rho}(\vec{r}) \geq 0$ and $\int \tilde{\rho}(\vec{r})\, d\vec{r} = N$ associated with some external potential, the energy obtained ($E[\tilde{\rho}]$) represents an upper bound to the true ground state energy (E_0; Eq. 1.8):

$$E_0 \leq E[\tilde{\rho}] = T[\tilde{\rho}] + E_{ee}[\tilde{\rho}] + E_{Ne}[\tilde{\rho}] \qquad \text{(Eq. 1.8)}$$

1.2.1.2 Kohn-Sham equations

Kohn and Sham proposed a method for approximating the unknown universal $F_{HK}[\rho]$ functional, concretely the kinetic contribution. They introduce a fictitious system of N non-interacting electrons moving under an effective potential (V_S), such that the density ($\rho_S(\vec{r})$) of this non-interacting system exactly equals the ground state density ($\rho_0(\vec{r})$) of our real target system of interacting particles (Eq. 1.9):

$$\rho_S(\vec{r}) = \rho_0(\vec{r}) = \sum_i^N \sum_s |\varphi_i(\vec{r}, s)|^2 \qquad \text{(Eq. 1.9)}$$

where φ_i is the Kohn–Sham (KS) orbital, which depends on the 3N spatial coordinates ($\vec{r}$) and the N spin coordinates (s). The energy functional (Eq. 1.6) can be arranged as shown in Eq. 1.10:

$$E[\rho(\vec{r})] = F[\rho] + E_{Ne}[\rho] \qquad \text{(Eq. 1.10)}$$

where $F[\rho]$ is the KS functional. This term (Eq. 1.11) is the sum of the kinetic energy of the non-interacting system ($T_S[\rho]$), the classical Coulombic interaction ($J[\rho]$), and the exchange-correlation energy ($E_{XC}[\rho]$):

$$F[\rho(\vec{r})] = T_S[\rho] + J[\rho] + E_{XC}[\rho] \qquad \text{(Eq. 1.11)}$$

The exchange-correlation functional ($E_{XC}[\rho]$) encapsulates all the quantum chemical effects not contained in the other functionals, i.e., the missing energy contributions (Eq. 1.12):

$$E_{XC}[\rho] = (T[\rho] - T_S[\rho]) + (E_{ee}[\rho] - J[\rho]) = T_C[\rho] + E_{ncl}[\rho] \qquad \text{(Eq. 1.12)}$$

where $T_C[\rho]$ is the residual part of the true kinetic energy ($T[\rho]$) which is not covered by $T_S[\rho]$ and $E_{ncl}[\rho]$ is the non-classical contribution to the electron-electron interaction ($E_{ee}[\rho]$) containing all the effects of self-interaction correction, exchange, and Coulomb correlation.

Applying the variational theorem to the energy functional given in Eq. 1.10 with respect to variation in the electron density leads to the one-electron KS equation (Eq. 1.13):

$$\hat{H}_{KS}\varphi_i = \left[-\frac{1}{2}\nabla^2 + V_S(\vec{r})\right]\varphi_i = \varepsilon_i\varphi_i \qquad \text{(Eq. 1.13)}$$

where $\hat{H}_{KS}$ is the KS Hamiltonian of the system, ∇^2 is the Laplacian operator, $V_S(\vec{r})$ is the effective potential in which the particles are moving, and ε_i is the orbital energy of the corresponding $\varphi_i(\vec{r})$. The $V_S(\vec{r})$ can be split into three potential terms (Eq. 1.14):

$$V_S(\vec{r}) = V_H(\vec{r}) + V_{XC}(\vec{r}) + V_{ext}(\vec{r}) \qquad \text{(Eq. 1.14)}$$

where $V_H(\vec{r})$ is the Hartree-Fock potential, $V_{XC}(\vec{r})$ is the exchange-correlation potential, and $V_{ext}(\vec{r})$ is the external potential due to the fixed nuclei.

Overall, the Kohn-Sham equations have reduced the main drawback of DFT methods from the search of an unknown universal functional to a search of an unknown universal exchange-correlation term (E_{XC} and V_{XC}). Except for a free electron gas, the explicit form of both contributions remains in the dark. Several DFT functionals have been developed to describe approximately these two quantities which offer good accuracy for many types of chemical problems at a moderate computational cost.[15]

1.2.1.3 Minnesota functionals

Conventional DFT functionals generally produce poor results for noncovalent interactions such as those dominated by electrostatic and dispersion contributions. Minnesota functionals have been developed in order to model diverse types of problems, including barrier heights (chemical kinetics), metal-ligand and metal-metal bond dissociation, main group thermochemistry, and noncovalent interactions.[16] Among them, M06-2X (widely used in this thesis) is a global hybrid meta-Generalized Gradient Approximation (GGA) functional that provides reasonable results for noncovalent complexes at a moderate computational cost compared to many other DFT functionals, even in its own family.[17,18] The MN12-SX method, a range-separated hybrid meta-Nonseparable Gradient Approximation (NGA) functional,[19] gives near close geometry configuration with the Multi-Configuration Self-Consistent Field (MCSCF) multireference theory which has allowed the computation of the phenothiazine (PTZ) deactivation pathway channel over the potential energy hyper-surface.[20] Furthermore, it can be successfully used to describe the keto-enol tautomeric equilibrium in tautomeric azodyes and Schiff bases in cyclohexane, carbon tetrachloride, and acetonitrile[21] and the geometric parameters and nature of the halonium $[N\cdots I\cdots N]^+$ bond (Chapter 6).

In this work, all DFT calculations were done with Gaussian 09[22] (Chapters 2 and 5) and Gaussian 16[23] packages using the aforementioned functionals and the basis sets described in the next section for all atoms.

1.2.2 Basis sets

A basis set is a set of functions combined linearly to model one-electron atomic orbitals (AOs), which in turn can be combined linearly to model molecular orbitals (MOs). They were introduced in QM calculations because the equations defining the MOs are otherwise difficult to solve. Basis sets can be constructed from AOs centred at atoms

(e.g., Slater, Gaussian or numerical atomic orbitals),[24] plane waves or delta functions. Among them, those most widely used are contracted Gaussian-type orbitals, due to their chemical accuracy and computational efficiency.[25] The size of the basis set is as important as the choice of the method for the quality of the results obtained. The larger the basis set (the more orbitals it contains), the better is the description of the molecular wavefunction for a given correlation method and the higher its computational cost is. In the limit of an infinite basis set (the Hartree-Fock limit) and exact treatment of electron correlation, the electronic Schrödinger equation would be solved exactly. Nevertheless, this is feasible for small systems only. The researcher must find a balance between accuracy and computational cost and choose the corresponding level of theory (functional and basis set) to obtain reliable results in a reasonable amount of time. The addition of polarization and diffuse functions can often improve the accuracy of the calculations.[26]

1.2.2.1 Effective Core Potentials

For heavy atoms, the use of Effective Core Potentials (ECPs) or pseudopotentials[27,28] simplify the electronic structure calculations by 'freezing' the core electrons and treating only the chemically active valence orbitals. This reduces the number of atomic and fitting basis functions significantly, includes relativistic and other effects for heavy atoms, and diminishes the basis set superposition error.[29]

The def2-bases provide consistent accuracy for all elements up to radon (Z = 86).[30] The def2-TZVP, a valence triple-ζ basis set with polarization functions, is widely used in this thesis due to its good performance in describing several noncovalent interactions with dispersive nature.[31,32] TZVP[33] has been used to describe the Li_2X_2 frameworks (Chapter 2)[34] due to the large size of various of the systems studied herein.

1.3 Computing intermolecular interactions

The calculation of the interaction energy between two fragments is a very useful way to calibrate the strength of a given interaction. Although absolute values may not be reliable sometimes due to a low level of theory, comparison of the interaction energies for series of systems helps us to determine, for instance, the importance of substitution effects.

1.3.1 The Counterpoise method

In the supermolecular approach (Eq. 1.15), the interaction energy (ΔE_{INT}) of a supramolecular system A-B is calculated as the energy difference between the adduct (E_{AB}^{AB}) and the energies of the two isolated fragments (E_A^A and E_B^B):

$$\Delta E_{INT} = E_{AB}^{AB} - \left(E_A^A + E_B^B\right) \qquad \text{(Eq. 1.15)}$$

where the superscript indicates the basis set used and the subscript the geometries that the independent fragments A and B adopt in the optimized supermolecule A-B.

The major shortcoming of this method is that the energy of the complex A-B is usually overestimated at short intermolecular distances, since each fragment "borrows" basis set functions of the other fragment to describe its electron distribution, effectively improving its basis set and therefore its energy. The resulting artificial extra-stabilization of the adduct with respect to the energy of the isolated monomers is called the basis set superposition error (BSSE).[35,36] The smaller the basis set, the higher is the BSSE due to the poor description of dispersion interaction. Consequently, the calculated binding energy of the adduct is usually higher than it should be. The counterpoise (CP) method, introduced by Boys and Bernardi,[37] was developed for correcting the BSSE. The CP method consists in counter the artificial stabilization by letting the separate fragments improve their basis set by borrowing functions of an empty basis set associated with the dimer, i.e., each component is calculated with the full AB basis set. Hence, assuming that the geometry of the monomers does not significantly change as they approach each other and form the dimer, the CP corrected interaction energy (ΔE_{INT}^{CP}) is (Eq. 1.16):

$$\Delta E_{INT}^{CP} = E_{AB}^{AB} - (E_A^{AB} + E_B^{AB}) \qquad \text{(Eq. 1.16)}$$

where the superscript AB means that the whole basis set is used. This is accomplished by introducing "ghost" atoms, which have empty basis set functions centred on them but no associated nuclear charges or electrons.

1.3.2 Energy Decomposition Analysis

The second generation of Energy Decomposition Analysis based on Absolutely-Localized Molecular Orbitals (ALMO-EDA-II)[38-40] is a powerful method for unveiling the nature of intermolecular interactions and quantifying these attractive or repulsive contributions to the overall interacting network in both chemical and biological systems.

The total interaction energy (ΔE_{INT}) between two fragments A and B in a molecule A-B at a particular geometry is decomposed into the frozen density (ΔE_{FRZ}) term and the orbital-based terms, namely polarization (ΔE_{POL}) and charge transfer (ΔE_{CT}) contributions (Eq. 1.17):

$$\Delta E_{INT} = \Delta E_{FRZ} + \Delta E_{POL} + \Delta E_{CT} \quad \text{(Eq. 1.17)}$$

The "frozen density" term is defined as the energy change involved in bringing infinitely separated fragments to close proximity without allowing for orbital relaxation. This energy can be further dissected into the electrostatic (ΔE_{ELEC}), the Pauli exchange-repulsion (ΔE_{PAULI}) and the dispersion (ΔE_{DISP}) term using the orthogonal fragment decomposition of the frozen wavefunction of the system (Eq. 1.18).[41] The ΔE_{ELEC} term describes the quasi-classical Coulombic interaction between the fragments with their charge distributions unperturbed and may be either attractive or repulsive, the ΔE_{PAULI} term is always repulsive due to the Pauli's exclusion principle between electrons of the same spin and the ΔE_{DISP} term arises from the attractive forces between the induced dipoles of the interacting species.

$$\Delta E_{FRZ} = \Delta E_{ELEC} + \Delta E_{PAULI} + \Delta E_{DISP} \quad \text{(Eq. 1.18)}$$

The ΔE_{CT} term, on the other hand, can be pictured as the electron transfer from the occupied MOs of one fragment into the unoccupied MOs of the other fragment. It includes the CP correction of the BSSE. Finally, the ΔE_{POL} term arises from the induced electrostatic interaction resulting from the deformation (or polarization) of the electron clouds of one fragment in the presence of all other fragments in the system. This includes mixing of occupied and empty MOs within one fragment (i.e., rehybridization).[39,40] Both ΔE_{CT} and ΔE_{POL} terms are always attractive (i.e., negative). The charge transfer component is often viewed as an indicator of the covalency of a chemical bond.[42]

When pseudopotentials are used, the orthogonal decomposition method is not available. Consequently, the classical decomposition[43] of the interaction strength can be used instead. The "frozen density" is dissected into the classical electrostatic (ΔE_{ELEC}^{cls}) term, which only depends on monomer properties and the distances between fragments, and the classical Pauli exchange-repulsion (ΔE_{Pauli}^{cls}) term (Eq. 1.19):

$$\Delta E_{FRZ} = \Delta E_{ELEC}^{cls} + \Delta E_{Pauli}^{cls} \quad \text{(Eq. 1.19)}$$

When the dispersion is calculated, its contribution is subtracted from the classical Pauli exchange-repulsion term. The remaining part constitutes the modified Pauli exchange-repulsion (ΔE_{Pauli}^{mod}) term (Eq. 1.20). Therefore, the overall decomposition of the frozen density is (Eq. 1.21):

$$\Delta E_{Pauli}^{mod} = \Delta E_{PAULI}^{cls} - \Delta E_{DISP} \qquad \text{(Eq. 1.20)}$$

$$\Delta E_{FRZ} = \Delta E_{ELEC}^{cls} + \Delta E_{Pauli}^{mod} + \Delta E_{DISP} \qquad \text{(Eq. 1.21)}$$

Overall, a deep knowledge of the interplay between the different modes of interaction that governs the intermolecular binding in both chemical and biological systems is crucial to modulate the strength of noncovalent interactions (NCIs) into a desirable range by making appropriate chemical modifications, and thus, it could aid in the design of new chemical species and materials.

In this work, EDA analyses were carried out with Q-Chem 5.0 (Chapter 3), 5.2 (Chapter 4) and 5.3 (Chapter 6 and 7) software[44] by means of the ALMO-EDA-II method.

1.4 Molecular Electrostatic Potential as a predictor

The Molecular Electrostatic Potential (MEP or $V(r)$) is defined as the force acting on a positive test charge located at the point r(x,y,z) around the molecular charge distribution generated by the electrons and nuclei of the compound. The MEP equation[45,46] is based on Coulomb's law (Eq. 1.22):

$$V(r) = \sum_{A} \frac{Z_A}{|R_A - r|} - \int \frac{\rho(r')}{|r' - r|} dr' \qquad \text{(Eq. 1.22)}$$

where Z_A is the charge of nucleus A located at R_A and $\rho(r')$ is the electron density of the compound at the point r'. In any given region, $V(r)$ will be positive or negative depending upon whether the positive contribution of the nuclei or the negative one of the electrons is dominant there.[47]

The MEP can be visualized, by mapping its value onto the electron density surfaces, as a three-dimensional rainbow-like outer surface surrounding the molecule, where the electron-poor sites ($V(r) > 0$) are conventionally depicted in blue and the electron-rich ones ($V(r) < 0$) in red. Since the red regions of a molecule (nucleophile) tend to interact with the blue regions of another one (electrophile), this approach has been

used as a tool for the qualitative interpretation and prediction of intermolecular noncovalent interactions, e.g., hydrogen bond,[48,49] σ-hole,[50,51] and π-hole[52,53] interactions. Furthermore, it has been applied to the prediction of molecular reactivity patterns,[54,55] description of the crystalline state,[50,56] catalysis,[57-59] and molecular recognition (e.g., enzyme-substrate and drug-DNA binding),[60-65] where a long-range interaction (electrostatic term) is dominant.

Despite the success of the MEP for the description of chemical reactivity, this method has some limitations: (1) The dependence of the MEP values on the basis set and electron correlation prevents us from a quantitative description of NCIs.[66] (2) Apart from the electrostatic contribution, other energy terms (e.g., polarization) are not included in the definition of MEP. Consequently, this tool fails for the prediction of attractive interactions between atoms with "like-like" electrostatic configuration. In these systems, charge transfer or dispersion can overcome the repulsive electrostatic term, leading to an attractive overall interaction (Chapter 4).[67]

In this thesis, MEP maps were built on the 0.001 Å (0.002 Å in Chapter 3) isosurface with GaussView 5.0[68] on the molecular geometries of the interacting systems at the selected M06-2X/def2-TZVP and MN12-SX/def2-TZVP (Chapter 6) level. These maps have been used to identify the electron-poor and electron-rich areas of a compound that are thus prone to attractively interact with each other. The MEP values (in kcal/mol) are visualized by a colour spectrum ranging from red (negative MEP value) to blue (positive MEP value).

1.5 Natural Bond Orbitals

The Natural Bond Orbital (NBO)[69-74] analysis is a powerful tool for interpreting electronic structure calculations in terms of chemical bonding concepts. This method transforms the fully delocalized molecular wavefunctions in optimized electron pairs (or individual electrons in the open-shell case) with maximum electron density localized on one (lone-pairs) or two atomic centres (bonds). Thus, NBOs provide a valence bond-type description of the wavefunction corresponding to the widely used Lewis structures. These "Lewis-type" (bonding) NBOs (with occupation number close to 2) are complemented by formally empty "non-Lewis-type" (antibonding or Rydberg) NBOs (occupation number close to 0). Weak occupancies of these valence antibonds indicate "delocalization effects"[75] (e.g., charge transfer) between the filled orbitals of one subsystem (donors) and

unfilled orbitals of another subsystem (acceptors). The strength ($E^{(2)}$) of each donor (i) → acceptor (j) interaction is calculated by second-order perturbation theory (Eq. 1.23):[76]

$$E^{(2)} = \Delta E_{ij} = q_i \frac{F^2(i,j)}{\varepsilon_j - \varepsilon_i} \qquad \text{(Eq. 1.23)}$$

where q_i is the donor orbital occupancy; ε_j and ε_i are NBO orbital energies and F is the Fock operator.

The NBO method provides useful insight for studying intra[77] and intermolecular[67] interactions between atoms or bonds and also provides a convenient basis for investigating charge transfer,[67] hybridization,[78] reactivity,[79,80] and the delocalization of the electron density within the molecule.[81]

1.5.1 Natural Population Analysis

Partial atomic charges describe the electron density distribution in a molecule, thus providing insights into the chemical behaviour of the compounds. In computational chemistry, these charges can be used, for example, for calculating electrostatic interactions, describing the reactivity of the molecule, and interpreting experimental data.[82] Atomic charges cannot be determined experimentally and their calculation from QM is not straightforward. There are myriad ways of partitioning the molecule's electrons between its atomic constituents.[83-92] A popular approach, based on occupancies of the orthonormal Natural Atomic Orbitals (NAOs) of each atom, is the Natural Population Analysis (NPA).[90] This tool has been developed to calculate the atomic charges ($q^{(A)}$) and orbital populations ($q_i^{(A)}$) of molecular wavefunctions on general atomic basis sets and describes the electron distribution in various sub-shells (Core, Valence, Rydberg) of their atomic orbitals. NPA rigorously satisfies the Pauli exclusion principle ($0 \leq q_i^{(A)} \leq 2$) and charge additivity. Unlike Mulliken population analysis (MPA),[83-86] natural populations are intrinsically nonnegative quantities, independently of the choice of the basis set and wavefunction form, and useful to describe the electron distribution in compounds with highly ionic character, such as those containing metal atoms (Chapter 2).[34]

In this thesis, Natural Population Analyses (NPA) were carried out with the NBO3.1[89] software as implemented in Gaussian 09[22] (Chapter 2)[34] to calculate the atomic charges. Natural Bond Orbital (NBO) analyses were done within the same software as

implemented in Gaussian 09[22] (Chapter 5)[50] and Gaussian 16[23] (Chapter 4)[67] to unveil the charge transfer processes and the orbitals involved in each of them.

1.6 Analysis of the topology of the electron density

1.6.1 Quantum Theory of Atoms in Molecules

The Quantum Theory of Atoms in Molecules (QTAIM)[93-97] has become a popular option for defining atomic properties in molecular systems. Molecular structures and the nature of chemical bonds and interactions can be retrieved from the study of the topology of the electron density (ρ) and its Laplacian, obtained from both experimental and theoretical methods.[98] Therefore, the QTAIM framework acts as a bridge between the quantum chemical and experimental methods, providing chemists with a choice of how to interpret, understand, and predict the observations of experimental chemistry. This method is based on the partitioning of the molecular space into mononuclear "atomic basins" delimited by zero-flux surfaces in the gradient vector field of the electron density ($\nabla\rho(r)$). There are 4 kinds of points where the field of $\nabla\rho(r)$ vanishes namely "critical points" (CP). They are classified as a local maximum, a local minimum, or a saddle point, according to the rank (ω) and the signature (σ) of the Hessian matrix of the electron density. The rank is the number of non-zero eigenvalues of ρ at the critical point and the signature is the sum of the signs of the eigenvalues (λ_1, λ_2, λ_3).[99,100]

(3,-3): Nuclear critical points (NCP). All three eigenvalues of the Hessian matrix are negative ($\lambda_1, \lambda_2, \lambda_3 < 0$). They are generally found at the positions of the nuclei, where ρ is a local maximum in all directions.

(3.-1): Bond critical point (BCP). Two eigenvalues of the Hessian matrix are negative, namely second-order saddle point ($\lambda_1, \lambda_2 < 0, \lambda_3 > 0$). They are generally found between two attractive atoms pair, where ρ is maximum in the plane defined by the corresponding eigenvectors but is minimum along the interaction path between these atoms, which is perpendicular to that plane.

(3,+1): Ring critical point (RCP). Only one eigenvalue of the Hessian matrix is negative, namely first-order saddle point ($\lambda_1 < 0, \lambda_2, \lambda_3 > 0$). They are generally found at the centre of the ring of chemically bonded atoms, where ρ is a minimum in the ring plane

defined by the corresponding eigenvectors and a maximum along the direction orthogonal to the molecular plane.

(3,+3): Cage critical point (CCP). All three eigenvalues of the Hessian matrix are positive ($\lambda_1, \lambda_2, \lambda_3 > 0$). They are generally found at the centre of a cage system, enclosed by at least two ring surfaces,[101] where ρ is a local minimum in all directions.

The number and type of critical points that can coexist in a molecule follow the Poincaré-Hopf relationship (Eq. 1.24),[100] which is useful to verify if all CPs may have been identified:

$$n_{(3,-3)} - n_{(3,-1)} + n_{(3,+1)} - n_{(3,+3)} = 1 \qquad \text{(Eq. 1.24)}$$

The QTAIM theory predicts that the values of some local indicators (e.g. electron density, delocalization index) calculated at the BCP are closely related to the nature of interactions between atoms.[98,102] In the equilibrium geometry, the existence of a BCP between two bonded atoms in a molecule is always accompanied by a single line of locally maximum electron density, namely bond path (BP), linking the two nuclei (NCP) through the associated BCP.[103] BPs are a universal indicator for all kinds of chemical bonding: weak, strong, closed-shell and open-shell interactions.[104] BP can be a straight line or a curve, the latter being indicative of significant ring strain. The set of bond paths and their associated BCPs are defined as a "molecular graph", which provides an unambiguous definition of the structure and bonding within a molecule or crystal, and can thus be used to locate changes in structure along a reaction path.[100]

1.6.1.1 Non-nuclear Attractors

Occasionally, non-nuclear attractors (NNAs)[105-107] appear if the molecular electron density is also maximum at other positions not associated with an atomic nucleus. These pseudoatoms are topologically indistinguishable from the nuclear maxima and can be linked to other nuclei or pseudoatoms in the compound through a BP and BCP. NNAs can be caused by the poor quality of the wavefunction[108] or the existence of metallic bonding.[109-112] It has also been detected in semiconductors, electrodes,[113] solvated or dipole-bound electrons,[114,115] and in crystal defects and colour F-centers.[116] Hence, NNAs are of substantial theoretical interest.

1.6.1.2 The Laplacian of the electron density

The topological analysis of the Laplacian of the electron density ($\nabla^2\rho(r)$) reveals the regions of charge depletion ($\nabla^2\rho(r) > 0$, Lewis acid) and charge concentration ($\nabla^2\rho(r) < 0$, Lewis base) in a molecule relative to its average distribution.[100] Furthermore, it provides insights into the electronic and conformational properties of compounds (i.e., the position of electron pairs).[117,118] This is the basis for its use to predict molecular geometries[119,120] and to rationalize the chemical reactivity and formation of the complexes (the "lock and key" mechanism).[121] The nature of the interactions depends on the sign of $\nabla^2\rho(r)$ at the internuclear region of two interacting atom pairs (BCP). Positive and negative values of $\nabla^2\rho_{BCP}$ are associated with closed (ionic and NCIs) and shared-shell (covalent) interactions, respectively.[122]

1.6.1.3 Energy Densities

In the framework of the local virial theorem,[93,123,124] the Laplacian is related to the local kinetic energy density ($G(r)$) and the local potential energy density ($V(r)$) by means of Eq. 1.25:

$$\frac{1}{4}\nabla^2\rho(r) = 2G(r) + V(r) \qquad \text{(Eq. 1.25)}$$

The former parameter represents the tendency of the system to dilute electrons at point r, whereas the latter represents the capacity of the system to concentrate electrons at the same point. Because $G(r) > 0$ and $V(r) < 0$, if at BCP the electron density is locally concentrated ($\nabla^2\rho_{BCP} < 0$), the interaction is dominated by local reduction of potential energy. Conversely, if at BCP the electron density is locally depleted ($\nabla^2\rho_{BCP} > 0$), the interaction is dominated by local excess in kinetic energy.[99,100]

The total energy density ($H(r)$)[125] is defined as the sum of these two energy densities (Eq. 1.26):

$$H(r) = G(r) + V(r) \qquad \text{(Eq. 1.26)}$$

The sign of the H_{BCP} is often viewed as a useful index for discriminating between covalent ($H_{BCP} < 0$) and noncovalent bonds ($H_{BCP} > 0$),[125-128] whereas its magnitude reflects the "covalence" of the bond.[125]

Another useful descriptor of the nature of the interaction is the $|V_{BCP}|/G_{BCP}$ ratio. Closed-shell interaction, intermediate (mixed) interactions and covalent interactions are associated to $|V_{BCP}|/G_{BCP} < 1$, $1 < |V_{BCP}|/G_{BCP} > 2$ and $|V_{BCP}|/G_{BCP} > 2$, respectively.[129]

1.6.1.4 Electron Delocalization index

The electron delocalization index[130] ($\delta(A,B)$ or DI) quantitatively measures the electron-pair sharing between two atoms or basins A and B, whether bonded or not. For open-shell systems, DI is calculated for each electron spin separately[131] (Eq. 1.27):

$$\delta(A,B) = \delta^{\alpha}(A,B) + \delta^{\beta}(A,B) = 2|F^{\alpha}(A,B)| + 2\left|F^{\beta}(A,B)\right| \quad \text{(Eq. 1.27)}$$

where the factor 2 accounts for the two possible ways of putting two electrons in two atoms: $\delta^{\alpha(\beta)}(A{\rightarrow}B)$ and $\delta^{\alpha(\beta)}(B{\rightarrow}A)$, F^{α} and F^{β} represent the Fermi correlation[1,100] and the superscript indicates the spin (α and β). Since in closed-shell systems $\delta^{\alpha}(A,B) = \delta^{\beta}(A,B)$, the DI equation can be rewritten as (Eq. 1.28):

$$\delta(A,B) = 2\delta^{\alpha}(A,B) = 4|F^{\alpha}(A,B)| \quad \text{(Eq. 1.28)}$$

These indices can be calculated exactly at any level of theory (i.e., HF and CI levels) if and only if the first- and second-order electron densities are available. DFT is an exception since the electron-pair density is not defined within the method. Approximate values can be calculated by deriving a HF-like electron-pair density from the KS orbitals.[132] However, it has to be taken into account that this method does not fully consider the Coulomb electron correlation, and thus tends to overestimate DI between covalently bonded atoms. Nevertheless, DFT delocalization indices are easy to calculate and have proved to be useful in the analysis of molecular electron-pair structure.[132-136]

In this work, the QTAIM analyses of the topology of the electron density were carried out with the AIMAII program[137] (Chapter 2 and 5) and Multiwfn 3.7 software[138] (Chapter 7) at the selected M06-2X/TZVP (Chapter 2) and M06-2X/def2-TZVP level.

1.6.2 Noncovalent Interactions Index

The Noncovalent Interactions (NCI) Index is an electron density-based topology approach that allows simultaneous analysis and visualization of a wide range of noncovalent interaction types as real space surfaces.[139] Densities can be calculated with

the self-consistent field (SCF) method or the promolecular approach.[140] The "promolecular density" (ρ^{pro}), obtained as the sum of atomic densities (ρ_i^{at}), is (Eq. 1.29):

$$\rho^{\mathrm{pro}} = \sum_i \rho_i^{at} \qquad \text{(Eq. 1.29)}$$

The latter approach reduces the computational cost and enables the application of the method in large biomolecular systems (e.g., proteins and DNA) while keeping a reasonable accuracy.[141] An NCI Index can be traced to the normalized and dimensionless reduced density gradient (RDG or $s(r)$),[142] a simple function of the electron density ($\rho(r)$) and its gradient (Eq. 1.30):

$$s(r) = \left(\frac{1}{2(3\pi^2)^{1/3}}\right)\frac{\|\nabla\rho(r)\|}{\rho(r)^{4/3}} \qquad \text{(Eq. 1.30)}$$

When the reduced density ($s(r)$) is plotted as a function of the molecular electron density ($\rho(r)$), noncovalent interactions appear as troughs associated with regions of small $s(r)$ at low $\rho(r)$ in the plot when $\nabla\rho(r) \to 0$. In a molecular system there are two situations in which $\nabla s(r)$, the gradient of RDG, is zero.[143,144] The first one corresponds to density critical points (CP), in which $\nabla s(r) = 0$ due to the annihilation of the density gradient ($\nabla\rho(r) = 0$). Such CPs have been thoroughly studied within QTAIM theory and therefore they have been termed "AIM-CP". The second situation is that in which $\nabla s(r) = 0$ but $\nabla\rho(r) \neq 0$. These points are characterized by fulfilling the following equality (Eq. 1.31):

$$\frac{\nabla^2\rho(r)}{\rho(r)} = \frac{4}{3}\frac{(\nabla\rho(r))^2}{\rho^2(r)} \qquad \text{(Eq. 1.31)}$$

By analogy, these points are called "non-AIM-CPs" and are associated with closed-shell interactions since it can be inferred from Eq. 1.31 that the Laplacian must be positive. Such interactions are not associated with CPs in the electron density and thus remain undetected by QTAIM topology. To sum up, NCI Index analysis not only recovers QTAIM results but goes beyond it due to its ability to reveal interactions that can only be found if we consider the entire NCI region rather than just the CPs.[145]

Not only noncovalent interactions can be revealed with this method, but also covalent bonding.[146] An easy way to distinguish between covalent and noncovalent

interactions is to look at the $\rho(r)$ values within the troughs, which can be related to the interaction strength. As we have seen, $\rho(r)$ has much higher values in the critical points associated with covalent bonding. The classification of weak interactions, however, is not trivial. Although hydrogen bonds (H) and van der Waals (vdW) interactions can be distinguished following the same criteria described above ($\rho_H(r) >> \rho_{vdW}(r)$), steric clashes and hydrogen bonds appear in the same region of density and overlap in plots of $s(\rho)$. The Laplacian of $\rho(r)$ is also useless because it is dominated by the principal axis of variation and is positive for all closed-shell interactions.[122] Instead, NCI Index uses the sign of the second eigenvalue of the electron density Hessian matrix (λ_2), which measures the charge accumulation ($\lambda_2 < 0$) or depletion ($\lambda_2 > 0$) in the plane perpendicular to the interaction. Plotting $s(r)$ as a function of $\text{sign}(\lambda_2)\rho$, the electron density with the sign of λ_2, the peaks belonging to steric clashes ($\lambda_2 > 0$, conventionally depicted in red), van der Waals interactions ($\lambda_2 \approx 0$, green) and strongly attractive (e.g., hydrogen bonds, covalent bonds, $\lambda_2 < 0$, blue) can be easily identified. Along with the nature of the interaction, the position of the NCIs can be visualized by plotting these peaks in real space as isosurfaces of $s(r)$, typically $s(r) < 0.3$ for promolecular approach and $s(r) < 0.5$ for SCF densities, along with a small cutoff of $\rho(r)$ which properly accommodates the density of all NCI peaks.[139,146] The colour of the NCI isosurfaces corresponds with the colour-coding used in the 2D plots.

In this work, NCI Index analyses were carried out with NCIPLOT software[147,148] (Chapter 5) and Multiwfn 3.7 program[131] (Chapter 7) based on promolecular densities. The NCI isosurfaces were generated for s = 0.3 a.u. (s = 0.4 a.u. in Chapter 7), coloured according to a BGR scheme and visualized by VMD 1.9.3 program.[149] These isosurfaces have been used to identify regions of different interactions by simply examining their colours.

1.7 References

1. Jensen, F. *Introduction to Computational Chemistry*, 2nd ed.; John Wiley & Sons, Ltd: Hoboken, 2007.
2. Vanommeslaeghe, K.; Guvench, O.; Mackerell Jr., A. D. Molecular Mechanics. *Curr Pharm Des*. **2014**, *20*, 3281-3292.

3. Fedotov, A.; Vakhrushev, A.; Severyukhina, O.; Sidorenko, A.; Savva, Y.; Klenov, N.; Soloviev, I. Theoretical Basis of Quantum-Mechanical Modeling of Functional Nanostructures. *Symmetry*. **2021**, *13*, 883-902.
4. McQuarrie, D. A. *Quantum Chemistry*. 2nd ed.; University Science Books: Mill Valley, 2008.
5. Schrödinger, E. An Undulatory Theory of the Mechanics of Atoms and Molecules. *Phys. Rev*. **1926**, *28*, 1049-1070.
6. Born, M.; Oppenheimer, R. Zur Quantentheorie der Molekeln. *Ann. Phys.* **1927**, *389*, 457-484.
7. Blinder, S. M. Introduction to the Hartree-Fock method. In *Mathematical Physics in Theoretical Chemistry*; Blinder, S. M.; House, J. E., Eds.; Elsevier: Cambridge, 2019; pp 1-30.
8. Møller, C.; Plesset, M. S. Note on an Approximation Treatment for Many-Electron Systems. *Phys. Rev*. **1934**, *46*, 618-622.
9. Bartlett, R. J.; Musial, M. Coupled-cluster theory in quantum chemistry. *Rev. Mod. Phys*. **2007**, *79*, 291-352.
10. Koch, W.; Holthausen, M. C. *A Chemist's Guide to Density Functional Theory*, 2nd ed.; Wiley-VCH Verlag: Weinheim, 2001.
11. Thomas, L. H. The Calculation of Atomic Fields. *Math. Proc. Camb. Philos. Soc.* **1927**, *23*, 542-548.
12. Fermi, E. Statistical method to determine some properties of atoms. *Rend. Accad. Naz. Lincei*. **1927**, *6*, 602-607.
13. Hohenberg, P.; Kohn, W. Inhomogeneous Electron Gas. *Phys. Rev. B*. **1964**, *136*, 864-871.
14. Kohn, W.; Sham, L. J. Self-Consistent Equations Including Exchange and Correlation Effects. *Phys. Rev. A*. **1965**, *140*, 1133-1138.
15. Mardirossian, N.; Head-Gordon, M. How Accurate Are the Minnesota Density Functionals for Noncovalent Interactions, Isomerization Energies, Thermochemistry, and Barrier Heights Involving Molecules Composed of Main-Group Elements. *J. Chem. Theory Comput.* **2016**, *12*, 4303-4325.
16. DiLabio, G. A.; Otero-de-la-Roza, A. Noncovalent interactions in density-functional theory. In *Reviews in Computational Chemistry*; Parrill, A. L., Lipkowitz, K. B., Eds.; John Wiley & Sons, Inc.: Hoboken, 2016; Vol. 29, pp. 1-97.

17. Zhao, Y.; Truhlar, D. G. The M06 suite of density functionals for main group thermochemistry, thermochemical kinetics, noncovalent interactions, excited states, and transition elements: two new functionals and systematic testing of four M06-class functionals and 12 other functionals. *Theor. Chem. Acc*. **2008**, *120*, 215-241.
18. Walker, M.; Harvey, A. J. A.; Sen, A.; Dessent, C. E. H. Performance of M06, M06-2X, and M06-HF Density Functionals for Conformationally Flexible Anionic Clusters: M06 Functionals Perform Better than B3LYP for a Model System with Dispersion and Ionic Hydrogen-Bonding Interactions. *J. Phys. Chem. A*. **2013**, *117*, 12590-12600.
19. Peverati, R.; Truhlar, D. G. Screened-exchange density functionals with broad accuracy for chemistry and solid-state physics. *Phys. Chem. Chem. Phys*. **2012**, *14*, 16187-16191.
20. Bende, A. Low-lying Excited States and Their Relaxation Pathways of Phenothiazine. *AIP Conf. Proc*. **2017**, *1917*, 020002-020006.
21. Antonov, L. Tautomerism in Azo and Azomethyne Dyes: When and If Theory Meets Experiment. *Molecules*. **2019**, *24*, 2252-2265.
22. Frisch, M. J.; Trucks, G. W.; Schlegel, H. B.; Scuseria, G. E.; Robb, M. A.; Cheeseman, J. R.; Scalmani, G.; Barone, V.; Mennucci, B.; Petersson, G. A.; Nakatsuji, H.; Caricato, M.; Li, X.; Hratchian, H. P.; Izmaylov, A. F.; Bloino, J.; Zheng, G.; Sonnenberg, J. L.; Hada, M.; Ehara, M.; Toyota, K.; Fukuda, R.; Hasegawa, J.; Ishida, M.; Nakajima, T.; Honda, Y.; Kitao, O.; Nakai, H.; Vreven, T.; Montgomery Jr., J. A.; Peralta, J. E.; Ogliaro, F.; Bearpark, M.; Heyd, J. J.; Brothers, E.; Kudin, K. N.; Staroverov, V. N.; Kobayashi, R.; Normand, J.; Raghavachari, K.; Rendell, A.; Burant, J. C.; Iyengar, S. S.; Tomasi, J.; Cossi, M.; Rega, N.; Millam, J. M.; Klene, M.; Knox, J. E.; Kross, J. B.; Bakken, V.; Adamo, C.; Jaramillo, J.; Gomperts, R.; Stratmann, R. E.; Yazyev, O.; Austin, A. J.; Cammi, R.; Pomelli, C.; Ochterski, J. W.; Martin, R. L.; Morokuma, K.; Zakrzewski, V. G.; Voth, G. A.; Salvador, P.; Dannenberg, J. J.; Dapprich, S.; Daniels, A. D.; Farkas, O.; Foresman, J. B.; Ortiz, J. V.; Cioslowski, J.; Fox, D. J. Gaussian 09, revision D.01; Gaussian, Inc.: Wallingford, CT, 2009.
23. Frisch, M. J.; Trucks, G. W.; Schlegel, H. B.; Scuseria, G. E.; Robb, M. A.; Cheeseman, J. R.; Scalmani, G.; Barone, V.; Petersson, G. A.; Nakatsuji, H.; Li, X.; Caricato, M.; Marenich, A. V.; Bloino, J.; Janesko, B. G.; Gomperts, R.;

Mennucci, B.; Hratchian, H. P.; Ortiz, J. V.; Izmaylov, A. F.; Sonnenberg, J. L.; Williams-Young, D.; Ding, F.; Lipparini, F.; Egidi, F.; Goings, J.; Peng, B.; Petrone, A.; Henderson, T.; Ranasinghe, D.; Zakrzewski, V. G.; Gao, J.; Rega, N.; Zheng, G.; Liang, W.; Hada, M.; Ehara, M.; Toyota, K.; Fukuda, R.; Hasegawa, J.; Ishida, M.; Nakajima, T.; Honda, Y.; Kitao, O.; Nakai, H.; Vreven, T.; Throssell, K.; Montgomery Jr., J. A.; Peralta, J. E.; Ogliaro, F.; Bearpark, M. J.; Heyd, J. J.; Brothers, E. N.; Kudin, K. N.; Staroverov, V. N.; Keith, T. A.; Kobayashi, R.; Normand, J.; Raghavachari, K.; Rendell, A. P.; Burant, J. C.; Iyengar, S. S.; Tomasi, J.; Cossi, M.; Millam, J. M.; Klene, M.; Adamo, C.; Cammi, R.; Ochterski, J. W.; Martin, R. L.; Morokuma, K.; Farkas, O.; Foresman, J. B.; Fox, D. J. Gaussian 16, rev. B.01; Gaussian, Inc.: Wallingford, CT, 2016.

24. Lehtola, S. A review on non-relativistic, fully numerical electronic structure calculations on atoms and diatomic molecules. *Int. J. Quantum Chem*. **2019**, *119*, e25968-e25998.
25. Jensen, F. Atomic orbital basis set. *WIREs Comput. Mol. Sci*. **2013**, *3*, 273-295.
26. Check, C. E.; Faust, T. O.; Bailey, J. M.; Wright, B. J.; Gilbert, T. M.; Sunderlin, L. S. Addition of Polarization and Diffuse Functions to the LANL2DZ Basis Set for P-Block Elements. *J. Phys. Chem. A.* **2001**, *105*, 8111-8116.
27. Kahn, L. R.; Goddard III, W. A. *Ab Initio* Effective Potentials for Use in Molecular Calculations. *J. Chem. Phys*. **1972**, *56*, 2685-2701.
28. van Lenthe, E.; Baerends, E. J.; Snijders, J. G. Relativistic Total Energy Using Regular Approximations. *J. Chem. Phys.* **1994**, *101*, 9783-9792.
29. Xu, X.; Truhlar, D. G. Accuracy of Effective Core Potentials and Basis Sets for Density Functional Calculations, Including Relativistic Effects, As Illustrated by Calculations on Arsenic Compounds. *J. Chem. Theory Comput*. **2011**, *7*, 2766-2779.
30. Weigend, F.; Ahlrichs, R. Balanced basis sets of split valence, triple zeta valence and quadruple zeta valence quality for H to Rn: Design and assessment of accuracy. *Phys. Chem. Chem. Phys*. **2005**, *7*, 3297-3305.
31. Echeverria, J. Intermolecular Carbonyl···Carbonyl Interactions in Transition-Metal Complexes. *Inorg. Chem.* **2018**, *57*, 5429-5437.
32. Díaz-Torres, R.; Echeverría, J.; Loveday, O.; Harding, P.; Harding, D. J. Interplay of halogen and hydrogen bonding in a series of heteroleptic iron(III) complexes. *CrystEngComm.* **2021***, 23*, 4069-4076.

33. Schäfer, A.; Huber, C.; Ahlrichs, R. Fully optimized contracted Gaussian basis sets of triple zeta valence quality for atoms Li to Kr. *J. Chem. Phys.* **1994**, *100*, 5829-5835.

34. Velasquez, J. D.; Echeverria, J.; Alvarez, S. Delocalized Bonding in Li_2X_2 Rings: Probing the Limits of the Covalent and Ionic Bonding Models. *Inorg. Chem.* **2021**, *60*, 345-356.

35. Jansen, H. B.; Ros, P. Non-empirical molecular orbital calculations on the protonation of carbon monoxide. *Chem. Phys. Lett*. **1969**, *3*, 140-143.

36. Liu, B.; McLean, A. D. Accurate calculation of the attractive interaction of two ground state helium atoms. *J. Chem. Phys*. **1973**, *59*, 4557-4558.

37. Boys, S. F.; Bernardi, F. The calculation of small molecular interactions by the differences of separate total energies. Some procedures with reduced errors. *Mol. Phys*. **1970**, *19*, 553-566.

38. Horn, P. R.; Mao, Y.; Head-Gordon, M. Probing non-covalent interactions with a second generation energy decomposition analysis using absolutely localized molecular orbitals. *Phys. Chem. Chem. Phys*. **2016**, *18*, 23067-23079.

39. Mao, Y.; Levine, D. S.; Loipersberger, M.; Horn, P. R.; Head-Gordon, M. Probing Radical-Molecule Interactions with a Second Generation Energy Decomposition Analysis of DFT Calculations Using Absolutely Localized Molecular Orbitals. *Phys. Chem. Chem. Phys.* **2020**, *22*, 12867-12885.

40. Mao, Y.; Loipersberger, M.; Horn, P. R.; Das, A.; Demerdash, O.; Levine, D. S.; Prasad Veccham, S.; Head-Gordon, T.; Head-Gordon, M. From Intermolecular Interaction Energies and Observable Shifts to Component Contributions and Back Again: A Tale of Variational Energy Decomposition Analysis. *Annu. Rev. Phys. Chem.* **2021**, *72*, 641-666.

41. Horn, P. R.; Mao, Y.; Head-Gordon, M. Defining the contributions of permanent electrostatics, Pauli repulsion, and dispersion in density functional theory calculations of intermolecular interaction energies. *J. Chem. Phys*. **2016**, *144*, 114107-114119.

42. Khaliullin, R. Z.; Cobar, E. A.; Lochan, R. C.; Bell, A. T.; Head-Gordon, M. Unravelling the Origin of Intermolecular Interactions Using Absolutely Localized Molecular Orbitals. *J. Phys. Chem. A*. **2007**, *111*, 8753-8765.

43. See the online Q-Chem 5.3 Program Manual, Sec. 12.7.3. https://manual.q-chem.com/5.3/qchem_manual_5.3.pdf.

44. Shao, Y.; Gan, Z.; Epifanovsky, E.; Gilbert, A. T. B.; Wormit, M.; Kussmann, J.; Lange, A. W.; Behn, A.; Deng, J.; Feng, X.; Ghosh, D.; Goldey, M.; Horn, P. R.; Jacobson, L. D.; Kaliman, I.; Khaliullin, R. Z.; Kuś, T.; Landau, A.; Liu, J.; Proynov, E. I.; Rhee, Y. M.; Richard, R. M.; Rohrdanz, M. A.; Steele, R. P.; Sundstrom, E. J.; Woodcock, H. L.; Zimmerman, P. M.; Zuev, D.; Albrecht, B.; Alguire, E.; Austin, B.; Beran, G. J. O.; Bernard, Y. A.; Berquist, E.; Brandhorst, K.; Bravaya, K. B.; Brown, S. T.; Casanova, D.; Chang, C.-M.; Chen, Y.; Chien, S. H.; Closser, K. D.; Crittenden, D. L.; Diedenhofen, M.; DiStasio, R. A.; Do, H.; Dutoi, A. D.; Edgar, R. G.; Fatehi, S.; Fusti-Molnar, L.; Ghysels, A.; Golubeva-Zadorozhnaya, A.; Gomes, J.; Hanson-Heine, M. W. D.; Harbach, P. H. P.; Hauser, A. W.; Hohenstein, E. G.; Holden, Z. C.; Jagau, T.-C.; Ji, H.; Kaduk, B.; Khistyaev, K.; Kim, J.; Kim, J.; King, R. A.; Klunzinger, P.; Kosenkov, D.; Kowalczyk, T.; Krauter, C. M.; Lao, K. U.; Laurent, A. D.; Lawler, K. V.; Levchenko, S. V.; Lin, C. Y.; Liu, F.; Livshits, E.; Lochan, R. C.; Luenser, A.; Manohar, P.; Manzer, S. F.; Mao, S.-P.; Mardirossian, N.; Marenich, A. V.; Maurer, S. A.; Mayhall, N. J.; Neuscamman, E.; Oana, C. M.; Olivares-Amaya, R.; O'Neill, D. P.; Parkhill, J. A.; Perrine, T. M.; Peverati, R.; Prociuk, A.; Rehn, D. R.; Rosta, E.; Russ, N. J.; Sharada, S. M.; Sharma, S.; Small, D. W.; Sodt, A.; Stein, T.; Stück, D.; Su, Y.-C.; Thom, A. J. W.; Tsuchimochi, T.; Vanovschi, V.; Vogt, L.; Vydrov, O.; Wang, T.; Watson, M. A.; Wenzel, J.; White, A.; Williams, C. F.; Yang, J.; Yeganeh, S.; Yost, S. R.; You, Z.-Q.; Zhang, I. Y.; Zhang, X.; Zhao, Y.; Brooks, B. R.; Chan, G. K. L.; Chipman, D. M.; Cramer, C. J.; Goddard, W. A.; Gordon, M. S.; Hehre, W. J.; Klamt, A.; Schaefer, H. F.; Schmidt, M. W.; Sherrill, C. D.; Truhlar, D. G.; Warshel, A.; Xu, X.; Aspuru-Guzik, A.; Baer, R.; Bell, A. T.; Besley, N. A.; Chai, J.-D.; Dreuw, A.; Dunietz, B. D.; Furlani, T. R.; Gwaltney, S. R.; Hsu, C.-P.; Jung, Y.; Kong, J.; Lambrecht, D. S.; Liang, W.; Ochsenfeld, C.; Rassolov, V. A.; Slipchenko, L. V.; Subotnik, J. E.; Van Voorhis, T.; Herbert, J. M.; Krylov, A. I.; Gill, P. M. W.; Head-Gordon, M. Advances in molecular quantum chemistry contained in the Q-Chem 4 program package. *Mol. Phys*. **2015**, *113*, 184-215.

45. Scrocco, E.; Tomasi, J. The Electrostatic Molecular Potential as a Tool for the Interpretation of Molecular Properties. In: N*ew Concepts II. Topics in Current Chemistry Fortschritte der Chemischen Forschung*; Davison, A.; Dewar, M. J. S., Eds.; Springer Berlin Heidelberg: Berlin, Heidelberg, 1973; Vol. 42, pp. 95-170.

46. Scrocco, E.; Tomasi, J. Electronic Molecular Structure, Reactivity and Intermolecular Forces: An Euristic Interpretation by Means of Electrostatic Molecular Potentials. In *Advances in Quantum Chemistry*; Löwdin, P.-O., Eds.; Elsevier/Academic Press, Inc.: New York, San Francisco, London, 1978; Vol. 11, pp. 115-193.
47. Murray, J. S.; Politzer, P. Molecular electrostatic potentials and noncovalent interactions. *WIREs Comput. Mol. Sci.* **2017**, *7*, e1326-e1335.
48. Sandhu, B.; McLean, A.; Sinha, A. S.; Desper, J.; Sarjeant, A. A.; Vyas, S.; Reutzel-Edens, S. M.; Aakeröy, C. B. Evaluating Competing Intermolecular Interactions through Molecular Electrostatic Potentials and Hydrogen-Bond Propensities. *Cryst. Growth Des*. **2018**, *18*, 466-478.
49. Oliveira, B. G. State of the art in hydrogen bond. *Quim. Nova*. **2015**, *38*, 1313-1322.
50. Velasquez, J. D.; Mahmoudi, G.; Zangrando, E.; Gurbanov, A. V.; Zubkov, F. I.; Zorlu, Y.; Masoudiasl, A.; Echeverría, J. Experimental and theoretical study of Pb···S and Pb···O σ-hole interactions in the crystal structures of Pb(II) complexes. *CrystEngComm*. **2019**, *21*, 6018-6025.
51. Ibrahim, M. A. A.; Telb, E. M. Z. σ-Hole and Lone-Pair Hole Interactions in Chalcogen-Containing Complexes: A Comparative Study. *ACS Omega*. **2020**, *5*, 21631-21640.
52. Velasquez, J. D.; Echeverria**,** J.; Alvarez, S. Effect of the Substituents on the Nature and Strength of Lone-Pair–Carbonyl Interactions in Acyl Halides. *Cryst. Growth Des.* **2019**, *19*, 6511-6518.
53. Echeverría, J. Alkyl groups as electron density donors in π-hole bonding**.** *CrystEngComm*. **2017**, *19*, 6289-6296.
54. Gadre, S. R.; Suresh, C. H.; Mohan, N. Electrostatic Potential Topology for Probing Molecular Structure, Bonding and Reactivity. *Molecules*. **2021**, *26*, 3289-3313.
55. Liu, L.; Miao, L.; Li, L.; Li, F.; Lu, Y.; Shang, Z.; Chen, J. Molecular Electrostatic Potential: A New Tool to Predict the Lithiation Process of Organic Battery Materials. *J. Phys. Chem. Lett*. **2018**, *9*, 3573-3579.
56. Velasquez, J. D.; Mahmoudi, G.; Zangrando, E.; Miroslaw, B.; Safin, D. A.; Echeverria, J. Non-covalent interactions induced supramolecular architecture

of $Hg(NCS)_2$ with 3-pyridinecarbaldehyde nicotinoylhydrazone. *Inorg. Chim. Acta*. **2020**, *509*, 119700-119706.

57. Sandhya, K. S.; Remya, G. S.; Suresh, C. H. Pincer Ligand Modifications To Tune the Activation Barrier for H_2 Elimination in Water Splitting Milstein Catalyst. *Inorg. Chem.* **2015**, *54*, 11150-11156.
58. Mathew, J.; Suresh, C. H. Assessment of Stereoelectronic Effects in Grubbs First-Generation Olefin Metathesis Catalysis Using Molecular Electrostatic Potential. *Organometallics*. **2011**, *30*, 1438-1444.
59. Sandhya, K. S.; Suresh, C. H. Designing metal hydride complexes for water splitting reactions: a molecular electrostatic potential approach. *Dalton Trans.* **2014**, *43*, 12279-12287.
60. Roy, D. K.; Balanarayan, P.; Gadre, S. R. Signatures of molecular recognition from the topography of electrostatic potential. *J. Chem. Sci*. **2009**, *121*, 815-821.
61. Hadži, D.; Hodošček, M.; Kocjan, D.; Šolmajer**,** T.; Avbelj, F. The Molecular Electrostatic Potential as a Determinant of Receptor-Drug Recognition. *Croat. Chem. Acta*. **1984**, *57*, 1065-1074.
62. Anigboro, A. A.; Avwioroko, O. J.; Akeghware, O.; Tonukari, N. J. Anti-obesity, antioxidant and in silico evaluation of Justicia carnea bioactive compounds as potential inhibitors of an enzyme linked with obesity: Insights from kinetics, semi-empirical quantum mechanics and molecular docking analysis. *Bioph. Chem*. **2021**, *274*, 106607-106620.
63. Qamar, S.; Perveen, F.; Akhter, Z.; Yousuf, S.; Sultan, M.; Ela, S. E.; Ullah, N.; Fatima, K.; Kanwal, S. 4,4-Nitrophenoxyaniline derived Azo ester: Structural elucidation, DFT simulation, and DNA interactional studies via wet and in silico methods. *J. Mol. Struct*. **2022**, *1250*, 131695-131703.
64. Oliveira, L. F. S. de; Cordeiro, H. C.; Brito, H. G. de; Pinheiro, A. C. B.; Santos, M. A. B. dos; Bitencourt, H. R.; Figueiredo, A. F. de; Araújo, J. de J. O.; Gil, F. dos S.; Farias, M. de S.; Barbosa, J. P.; Pinheiro, J. C. Molecular electrostatic potential and pattern recognition models to design potentially active pentamidine derivatives against *Trypanosoma brucei rhodesiense*. *RSD*. **2021**, *10*, e261101220207-e261101220225.
65. Kovacic, P.; Wakelin, L. P. G. DNA molecular electrostatic potential: novel perspectives for the mechanism of action of anticancer drugs involving electron transfer and oxidative stress. *Anti-Cancer Drug Des.* **2001**, *16*, 175-184.

66. Köster, A. M.; Leboeuf, M.; Salahub, D. R. Molecular Electrostatic Potentials from Density Functional Theory. *Theor. Comput. Chem*. **1996**, *3*, 105-142.
67. Echeverría, J.; Velasquez, J. D.; Alvarez, S. Understanding the Interplay of Dispersion, Charge Transfer, and Electrostatics in Noncovalent Interactions: The Case of Bromine–Carbonyl Short Contacts. *Cryst. Growth Des.* **2020**, *20*, 7180-7187.
68. Dennington, R.; Keith, T.; Millam, J. GaussView, ver. 5; Semichem Inc.: Shawnee Mission, KS, 2009.
69. Foster, J. P.; Weinhold, F. Natural Hybrid Orbitals. *J. Am. Chem. Soc.* **1980**, *102*, 7211-7218.
70. Glendening, E. D.; Landis, C. R.; Weinhold, F. Natural bond orbital methods. *WIREs Comput Mol Sci*. **2012**, *2*, 1-42.
71. Weinhold, F.; Landis, C. R.; Glendening, E. D. What is NBO analysis and how is it useful? *Int. Rev. Phys. Chem.* **2016**, *35*, 399-440.
72. Weinhold, F. Natural Bond Orbital Analysis: A Critical Overview of Relationships to Alternative Bonding Perspectives. *J. Comput. Chem.* **2012**, *33*, 2363-2379.
73. Reed, A. E.; Curtiss, L. A.; Weinhold, F. Intermolecular Interactions from a Natural Bond Orbital, Donor-Acceptor Viewpoint. *Chem. Rev.* **1988**, *88*, 899-926.
74. Weinhold, F.; Landis, C. R. *Valency and Bonding: A Natural Bond Orbital Donor-Acceptor Perspective*. Cambridge University Press: Cambridge, 2005.
75. Weinhold, F.; Landis, C. R. Natural Bond Orbitals and Extensions of Localized Bonding Concepts. *Chem. Educ. Res. Pract.* **2001**, *2*, 91-104.
76. See the online NBO 7.0 Program Manual, Sec. A.3.5. https://nbo6.chem.wisc.edu/nboman.pdf.
77. Javan, M. J. Effect of multiple & cooperative intramolecular hydrogen bonding on polyhydroxylated thiopyrans acidities: Detailed view from AIM & NBO analyses. *Comput. Theor. Chem*. **2021**, *1205*, 113440-113449.
78. Glendening, E. D.; Weinhold, F. Pauling's Conceptions of Hybridization and Resonance in Modern Quantum Chemistry. *Molecules*. **2021**, *26*, 4110-4124.
79. Dunnington, B. D.; Schmidt, J. R. Generalization of Natural Bond Orbital Analysis to Periodic Systems: Applications to Solids and Surfaces via Plane-Wave Density Functional Theory. *J. Chem. Theory Comput.* **2012**, *8*, 1902-1911.

80. Abuelela, A. M.; Soliman, U. A.; El-hagali, G. A. M.; Zoghaib, W. M.; Mohamed, T. A. Synthetic routes and vibrational analysis of 5-(4-Chlorophenyl)-3H-pyrazol-3-one molecule: Raman, Infrared and DFT calculations. *J. Mol. Struct.* **2021**, *1245*, 131036-131048.

81. Charanya, C.; Sampathkrishnan, S.; Balamurugan, N. Natural Bond Orbital (NBO), Natural Population Analysis and Mulliken Analysis of Atomic Charges of 4-Amino-3-Phenylbutanoic Acid. *Spectr. Spec. Anal*. **2019**, *39*, 977-981.

82. Mao, J. X. Atomic Charges in Molecules: A Classical Concept in Modern Computational Chemistry. *PostDoc Journal: Reviews*. **2014**, *2*, 15-18.

83. Mulliken, R. S. Electronic Population Analysis on LCAO-MO Molecular Wave Functions. I. *J. Chem. Phys.* **1955**, *23*, 1833-1840.

84. Mulliken, R. S. Electronic Population Analysis on LCAO-MO Molecular Wave Functions. II. Overlap Populations, Bond Orders, and Covalent Bond Energies. *J. Chem. Phys.* **1955**, *23*, 1841-1846.

85. Mulliken, R. S. Electronic Population Analysis on LCAO-MO Molecular Wave Functions. III. Effects of Hybridization on Overlap and Gross AO Populations. *J. Chem. Phys.* **1955**, *23*, 2338-2342.

86. Mulliken, R. S. Electronic Population Analysis on LCAO-MO Molecular Wave Functions. IV. Bonding and Antibonding in LCAO and Valence-Bond Theories. *J. Chem. Phys.* **1955**, *23*, 2343-2346.

87. Löwdin, P.-O. On the Non-Orthogonality Problem Connected with the Use of Atomic Wave Functions in the Theory of Molecules and Crystals. *J. Chem. Phys.* **1950**, *18*, 365-375.

88. Geidl, S.; Bouchal, T.; Raček, T.; Vařeková, R. S.; Hejret, V.; Křenek, A.; Abagyan, R.; Koča, J. High-quality and universal empirical atomic charges for chemoinformatics applications. *J. Cheminform.* **2015***, 7***,** 59-68.

89. Montgomery, J. A.; Frisch, M. J.; Ochterski, J. W.; Petersson, G. A. A complete basis set model chemistry. VII. Use of the minimum population localization method. *J. Chem. Phys.* **2000**, *112*, 6532-6542.

90. Reed, A. E.; Weinstock, R. B.; Weinhold, F. Natural population analysis. *J. Chem. Phys.* **1985**, *83*, 735-746.

91. Besler, B. H.; Merz, K. M.; Kollman, P. A. Atomic Charges Derived from Semiempirical Methods. *J. Comput. Chem*. **1990**, *11*, 431-439.

92. Trabada, D. G.; Soler-Polo, D.; Mendieta-Moreno, J. I.; Ortega, J. Mulliken-Dipole Population Analysis. *ChemRxiv*. **2020**, 1-22.

93. Bader, R. F. W. *Atoms in Molecules: A Quantum Theory*. Clarendon Press: Oxford, 1994.

94. Popelier, P. L. A. *Atoms in Molecules. An Introduction.* Longman: London, 1999.

95. Bader, R. F. W. A Quantum Theory of Molecular Structure and Its Applications. *Chem. Rev*. **1991**, *91*, 893-928.

96. Bader, R. F. W. From Schrodinger to atoms in molecules. *Pure & Appl. Chem*. **1988**, *60*, 145-155.

97. Bader, R. F. W. The Quantum Mechanical Basis of Conceptual Chemistry. *Monatshefte für Chemie – Chemical Monthly*. **2005**, *136*, 819-854.

98. Farrugia, L. J.; Evans, C.; Lentz, D.; Roemer, M. The QTAIM Approach to Chemical Bonding Between Transition Metals and Carbocyclic Rings: A Combined Experimental and Theoretical Study of $(\eta^5\text{-}C_5H_5)Mn(CO)_3$, $(\eta^6\text{-}C_6H_6)Cr(CO)_3$, and (E)-$\{(\eta^5\text{-}C_5H_4)CF{=}CF(\eta^5\text{-}C_5H_4)\}(\eta^5\text{-}C_5H_5)_2Fe_2$. *J. Am. Chem. Soc.* **2009**, *131,* 1251-1268.

99. Popelier, P. L. A. The QTAIM Perspective of Chemical Bonding. In *The Chemical Bond: Fundamental Aspects of Chemical Bonding*; Frenking, G., Shaik, S., Eds.; Wiley-VCH Verlag: Weinheim, 2014; pp. 271-308.

100. Matta, C. F.; Boyd, R. J. An Introduction to the Quantum Theory of Atoms in Molecules. In *The Quantum Theory of Atoms in Molecules: From Solid State to DNA and Drug Design*; Matta, C. F., Boyd, R. J., Eds.; Wiley-VCH Verlag: Weinheim, 2007, pp. 1-34.

101. Castillo, N.; Matta, C. F.; Boyd, R. J. The first example of a cage critical point in a single ring: A novel twisted *α*-helical ring topology. *Chem. Phys. Lett*. **2005**, *409*, 265-269.

102. Pilmé, J.; Renault, E.; Bassal, F.; Amaouch, M.; Montavon, G.; Galland, N. QTAIM Analysis in the Context of Quasirelativistic Quantum Calculations. *J. Chem. Theory Comput.* **2014**, *10*, 4830-4841.

103. Runtz, G. R.; Bader, R. F. W.; Messer, R. R. Definition of bond paths and bond directions in terms of the molecular charge distribution. *Can. J. Chem.* **1977**, *55*, 3040-3045.

104. Bader, R. F. W. A Bond Path: A Universal Indicator of Bonded Interactions. *J. Phys. Chem. A*. **1998**, *102*, 7314-7323.

105. Gatti, C.; Fantucci, P.; Pacchioni, G. Charge density topological study of bonding in lithium clusters. *Theor Chim Acta*. **1987**, *72*, 433-458.

106. Glaser, R.; Waldron, R. F.; Wiberg, K. B. Origin and Consequences of the Nonnuclear Attractor in the ab Initio Electron Density Functions of Dilithium. *J. Phys. Chem.* **1990**, *94*, 7357-7362.

107. Platts, J. A.; Overgaard, J.; Jones, C.; Iversen, B. B.; Stasch, A. First Experimental Characterization of a Non-nuclear Attractor in a Dimeric Magnesium(I) Compound. *J. Phys. Chem. A.* **2011**, *115*, 194-200.

108. See the online Multiwfn 3.8 Program Manual, Sec. 4.17.1. http://sobereva.com/multiwfn/misc/Multiwfn_3.8_dev.pdf.

109. Marqués, M.; Ackland, G. J.; Lundegaard, L. F.; Stinton, G.; Nelmes, R. J.; McMahon, M. I.; Contreras-García, J. Potassium under Pressure: A Pseudobinary Ionic Compound. *Phys. Rev. Lett*. **2009**, *103*, 115501-115504.

110. Marqués, M.; McMahon, M. I.; Gregoryanz, E.; Hanfland, M.; Guillaume, C. L.; Pickard, C. J.; Ackland, G. J.; Nelmes, R. J. Crystal Structures of Dense Lithium: A Metal-Semiconductor-Metal Transition. *Phys. Rev. Lett*. **2011**, *106*, 095502-095505.

111. Gatti, M.; Tokatly, I. V.; Rubio, A. Sodium: A Charge-Transfer Insulator at High Pressures. *Phys. Rev. Lett*. **2010**, *104*, 216404-216407.

112. Li, P.; Gao, G.; Wang, Y.; Ma, Y. Crystal Structures and Exotic Behaviour of Magnesium under Pressure. *J. Phys. Chem. C*. **2010**, *114*, 21745-21749.

113. Sitkiewicz, S. P.; Ramos-Cordoba, E.; Luis, J. M.; Matito, E. How Many Electrons Does a Molecular Electride Hold? *J. Phys. Chem. A*. **2021**, *125*, 4819-4835.

114. Timerghazin Q. K.; Rizvi I.; Peslherbe. G. H. Can a Dipole-Bound Electron Form a Pseudo-Atom? An Atoms-In-Molecules Study of the Hydrated Electron. *J. Phys. Chem. A*. **2011**, *115*, 13201-13209.

115. Timerghazin Q. K.; Peslherbe. G. H. Non-nuclear attractor of electron density as a manifestation of the solvated electron. *J. Chem. Phys*. **2007**, *127*, 064108-06411.

116. Bader, R. F. W.; Platts, J. A. Characterization of an *F*-center in an alkali halide cluster. *J. Chem. Phys.* **1997**, *107*, 8545-8553.

117. Bader, R. F. W.; MacDougall, P. J.; Lau, C. D. H. Bonded and Non-bonded Charge Concentrations and Their Relation to Molecular Geometry and Reactivity, *J. Am. Chem. Soc*. **1984**, *106*, 1594-1605.

118. Bader, R. F. W.; Gillespie, R. J.; MacDougall, P. J. A Physical Basis for the VSEPR Model of Molecular Geometry. *J. Am. Chem. Soc*. **1988**, *110*, 7329-7336

119. Bytheway, I.; Gillespie, R. J.; Tang, T.-H.; Bader, R. F. W. Core Distortions and Geometries of the Difluorides and Dihydrides of Ca, Sr, and Ba. *Inorg. Chem*. **1995**, *34*, 2407-2414.

120. Gillespie, R. J.; Bytheway, I.; Tang, T.-H.; Bader, R. F. W. Geometry of the Fluorides, Oxofluorides, Hydrides, and Methanides of Vanadium(V), Chromium(VI), and Molybdenum(VI): Understanding the Geometry of Non-VSEPR Molecules in Terms of Core Distortion. *Inorg. Chem*. **1996**, *35*, 3954-3963.

121. Cortés-Guzmán, F.; Bader, R. F. W. Complementarity of QTAIM and MO theory in the study of bonding in donor-acceptor complexes. *Coord. Chem. Rev*. **2005**, *249*, 633-662.

122. Bader, R. F. W.; Essén, H. The characterization of atomic interactions. *J. Chem. Phys*. **1984**, *80*, 1943-1960.

123. Bader, R. F. W. Principle of Stationary Action and the Definition of a Proper Open System. *Phys. Rev. B Condens. Matter* **1994**, *49*, 13348-13356.

124. Bader, R. F. W.; Nguyen-Dang, T. T. Quantum Theory of Atoms in Molecules-Dalton Revisited. In *Advances in Quantum Chemistry*; Löwdin, P.-O., Eds.; Elsevier/ Academic Press, Inc.: Hamilton, Ontario, 1981; Vol. 14, pp. 63-124.

125. Cremer, D.; Kraka, E. Chemical Bonds without Bonding Electron Density? Does the Difference Electron-Density Analysis Suffice for a Description of the Chemical Bond? *Angew. Chem. Int. Ed.* **1984**, *23*, 627-628.

126. Cukrowski, I.; de Lange, J. H.; Mitoraj, M. Physical Nature of Interactions in Zn(II) Complexes with 2,2'-Bipyridyl: Quantum Theory of Atoms in Molecules (QTAIM), Interacting Quantum Atoms (IQA), Noncovalent Interactions (NCI), and Extended Transition State Coupled with Natural Orbitals for Chemical Valence (ETS-NOCV) Comparative Studies. *J. Phys. Chem. A.* **2014**, *118*, 623-637.

127. Venkataramanan, N. S.; Suvitha, A.; Kawazoe, Y. Intermolecular Interaction in Nucleobases and Dimethyl Sulfoxide/Water Molecules: A DFT, NBO, AIM and NCI Analysis. *J. Mol. Graph. Model.* **2017**, *78*, 48-60.

128. Mahmoudi, G.; Lawrence, S. E.; Cisterna, J.; Cárdenas, A.; Brito, I.; Frontera, A.; Safin, D. A. A New Spodium Bond Driven Coordination Polymer Constructed

from Mercury(II) Azide and 1,2-Bis(Pyridin-2-Ylmethylene)Hydrazine. *New J Chem*. **2020**, *44*, 21100-21107.

129. Espinosa, E.; Alkorta, I.; Elguero, J.; Molins, E. From Weak to Strong Interactions: A Comprehensive Analysis of the Topological and Energetic Properties of the Electron Density Distribution Involving X–H···F–Y Systems. *J. Chem. Phys.* **2002**, *117*, 5529-5542.
130. Fradera, X.; Austen, M. A.; Bader, R. F. W. The Lewis Model and Beyond. *J. Phys. Chem. A*. **1999**, *103*, 304-314.
131. See the online Multiwfn 3.8 Program Manual, Sec. 3.18.5. http://sobereva.com/multiwfn/misc/Multiwfn_3.8_dev.pdf.
132. Kar, T.; Ángyán, J. G.; Sannigrahi, A. B. Comparison of Ab Initio Hartree-Fock and Kohn-Sham Orbitals in the Calculation of Atomic Charge, Bond Index, and Valence. *J. Phys. Chem. A*. **2000**, *104*, 9953-9963.
133. Poater, J.; Solà, M.; Duran, M.; Fradera, X. The calculation of electron localization and delocalization indices at the Hartree–Fock, density functional and post-Hartree-Fock levels of theory. *Theor. Chem. Acc.* **2002**, *107*, 362-371.
134. Foroutan-Nejad, C. A double bond with weak σ- and strong π-interactions is still a double bond. *Nat. Commun.* **2021**, *12*, 4037-4040.
135. Bartashevich, E. V.; Mukhitdinova, S. E.; Tsirelson, V. G. Bond orders and electron delocalization indices for S-N, S-C and S-S bonds in 1,2,3-dithiazole systems. *Mendeleev Commun.* **2021**, *31*, 680-683.
136. Foroutan-Nejad, C. Bonding and Aromaticity in Electron-Rich Boron and Aluminum Clusters. *J. Phys. Chem. A*. **2021**, *125*, 1367-1373.
137. Keith, T. A. AIMAll; TK Gristmill Software: Overland Park, KS, 2013.
138. Lu, T.; Chen, F. Multiwfn: A Multifunctional Wavefunction Analyzer. *J. Comput. Chem*. **2012**, *33*, 580-592.
139. Laplaza, R.; Peccati, F.; Arias-Olivares, D.; Contreras-García, J. Visualizing non-covalent interactions with NCIPLOT. In *Complementary Bonding Analysis*; Grabowsky, S., Eds.; De Gruyter: Berlin, Boston, 2021; pp. 353-378.
140. Spackman, M. A.; Maslen, E. N. Chemical Properties from the Promolecule. *J. Phys. Chem.* **1986**, *90*, 2020-2027.
141. Contreras-García, J.; Boto, R. A.; Izquierdo-Ruiz, F.; Reva, I.; Woller, T.; Alonso, M. A benchmark for the non-covalent interaction (NCI) index or... is it really all in the geometry? *Theor. Chem. Acc*. **2016**, *135*, 242-255.

142. Perdew, J. P.; Burke, K.; Ernzerhof, M. Generalized Gradient Approximation Made Simple. *Phys. Rev. Lett*. **1996**, *77*, 3865-3868.

143. Boto, R. A.; Contreras-García, J.; Tierny, J.; Piquemal, J.-P. Interpretation of the reduced density gradient. *Mol. Phys*. **2016**, *114*, 1406-1414.

144. Boto, R. A.; Piquemal, J.-P.; Contreras-García, J. Revealing strong interactions with the reduced density gradient: a benchmark for covalent, ionic and charge-shift bonds. *Theor. Chem. Acc.* **2017**, *136*, 139-147.

145. Lane, J. R.; Contreras-García, J.; Piquemal, J.-P.; Miller, B. J.; Kjaergaard, H. G. Are Bond Critical Points Really Critical for Hydrogen Bonding? *J. Chem. Theory Comput*. **2013**, *9*, 3263-3266.

146. Laplaza, R.; Peccati, F.; Boto, R. Á.; Quan, C.; Carbone, A.; Piquemal, J.-P.; Maday, Y.; Contreras-García, J. NCIPLOT and the analysis of noncovalent interactions using the reduced density gradient. *WIREs Comput. Mol Sci*. **2021**, *11*, e1497-e1514.

147. Johnson, E. R.; Keinan, S.; Mori-Sánchez, P.; Contreras-García, J.; Cohen, A. J.; Yang, W. Revealing Noncovalent Interactions. *J. Am. Chem. Soc*. **2010**, *132*, 6498-6506.

148. Contreras-García, J.; Johnson, E. R.; Keinan, S.; Chaudret, R.; Piquemal, J.-P.; Beratan, D. N.; Yang, W. NCIPLOT: A Program for Plotting Noncovalent Interaction Regions. *J. Chem. Theory Comput*. **2011**, *7*, 625-632.

149. Humphrey, W.; Dalke, A.; Schulten, K. VMD: Visual Molecular Dynamics. *J. Mol. Graph*. **1996**, *14*, 33-38.

Chapter 2

Delocalized bonding in Li_2X_2 rings. Probing the limits of the covalent and ionic bonding

2.1 Introduction

Lithium is a remarkable element in several respects.[1-2] It has important applications such as its incorporation in aluminium alloys for the aircraft industry, the use of lithium carbonate for the treatment of the bipolar disorder, its wide application in the synthesis of organometallic compounds, and its extended use in rechargeable batteries. It is the most electropositive of the alkali metals due to its high hydration enthalpy, and yet in the highly ionic solid LiF, some amount of electron density is shared between the two elements.[3] In spite of the highly ionic character of lithium bonds to electronegative atoms such as O or N, it is common to represent it forming bonds in Lewis structures of lithium-containing compounds rather than as independent cations. Moreover, it is commonly accepted that lithium can exhibit a high degree of covalency in its bonding due to the high polarizing power of its cation associated with a high charge/radius ratio.[2]

In this context, the Li−Li bond in Li_2, expected to be purely covalent as confirmed by Generalized Valence Bond (GVB) calculations,[4] deserves special attention. Such a diatomic molecule has been characterized in the gas phase with a Li−Li bond distance of 2.673 Å,[5] and a dissociation energy of 105 kJ/mol.[6] However, in all molecules characterized in the solid state found in the Cambridge Structural Database (CSD)[7] that have a Li−Li bond, it is always supported by bridging ligands. The distribution of the Li−Li bond distances (Figure 2.1a) shows a maximum at relatively short distances (~ 2.6 Å), compared to twice the covalent[8] (2.56 Å) and van der Waals[9] (4.24 Å) radii.

A search for Li···Li "contacts" in the CSD shows also a distribution with a peak at short distances (Figure 2.1a) that might correspond to undisclosed Li−Li bonds, with many cases of bond distances smaller than in the covalent Li_2 molecule[5] and shorter also than twice the Li covalent radius.[8] The large number of contacts at longer distances can be attributed to randomly distributed, essentially non-interacting atom pairs. Notice, however, that there is no gap between bonds and no-bonds, suggesting that the existence of Li−Li bonding at distances of 3.0 Å or longer cannot be established based purely on a bond length criterion. A look at the structures that present such Li−Li short distances reveals a strong tendency of lithium atoms to cluster together forming Li_2X_2 rings, Li_4R_4 clusters in which the organic groups are linked in a μ_3 fashion to the faces of a Li_4 tetrahedron (R = e.g., Me,[10] ^{t}Bu,[11] or $CH_2CH_2{}^t$Bu[12]), six-member rings in a chair conformation,[13-16] a Li_8 cube,[17] a Li_8 gyrobifastigium,[18] larger clusters up to Li_{37},[19]

reminiscent of a chunk of the bcc structure of metallic lithium but with shorter Li−Li distances (2.74 − 2.93 Å) than in the metal,[20] and in a square network in lithium cyanamide, $Li_2(NCN)$.[21] The most common motifs with Li−Li bonds or short contacts found in the CSD are Li_2X_2 rings, where the bridging atom X is most frequently C, N or O but can also be almost any element of groups 14 − 17, from carbon to iodine. Combining all those rhombuses, regardless of whether they indicate the presence of a through-ring Li−Li bond, I found the distribution seen in Figure 2.1b, covering from rather short, probably bonding, distances (Scheme 2.1a) to very long distances and correspondingly short bonding through-ring X−X distances (Scheme 2.1c), with an intermediate region in which the distances do not support the existence of through-ring bonding (Scheme 2.1b), showcasing again a continuous distribution between bonding and nonbonding.

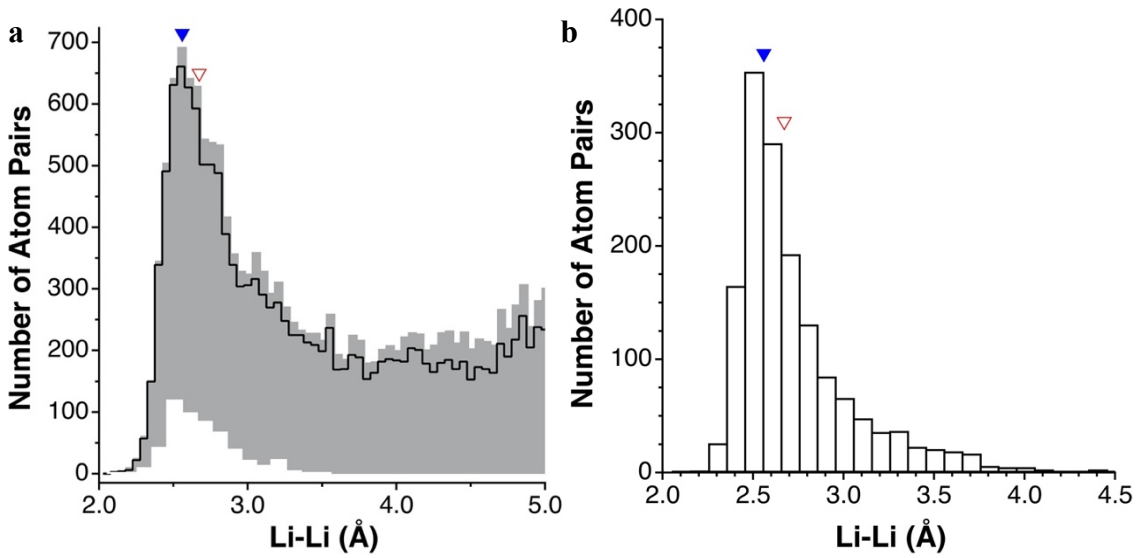

Figure 2.1. (**a**) Distribution of Li−Li bond (white bars) and Li···Li contact distances (grey bars for all contacts, solid line for intramolecular contacts) in the CSD. (**b**) Distribution of Li···Li distances in Li_2X_2 rings. The filled triangle indicates twice the lithium covalent radius[8] and the empty triangle the experimental Li-Li bond distance in Li_2 in the gas phase.[5]

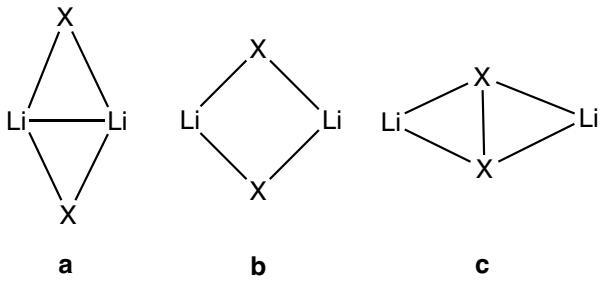

Scheme 2.1. Three alternative structures for Li_2X_2 rings.

2.2 Framework Electron Counting Scheme

In the past, Alvarez and co-workers have analysed the bonding in the M_2X_2 skeletons of doubly-bridged transition metal dinuclear complexes with several coordination environments and established a rationale for the existence or not of through ring M−M (or sometimes X−X) bonds,[22-33] and a similar treatment has been presented for M_3X_2 scaffolds.[34-35] Such an approach can be applied for similar cores in which M is a main group metal, such as Li, two of whose valence orbitals are able to participate in framework bonding, a radial sp hybrid and a tangential p orbital (Scheme 2.2a and 2.2b, respectively), both unoccupied if the lithium atoms are considered as Li^+ cations. Alternatively, these orbitals can be represented as two sp^2 or sp^3 hybrid orbitals (Scheme 2.2c). The bridging fragments can be of different types, classified according to the valence orbitals and electrons they contribute to framework bonding with the lithium atoms (Scheme 2.3).

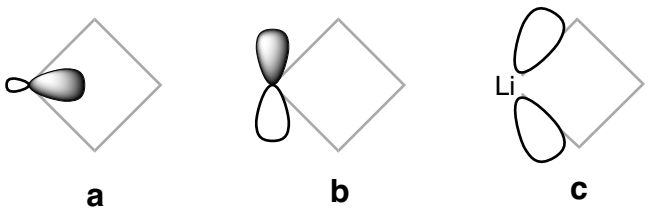

Scheme 2.2. Lithium valence orbitals that participate in the framework bonding (**a** and **b**), alternatively represented as two sp^2 or sp^3 hybrid orbitals in **c**.

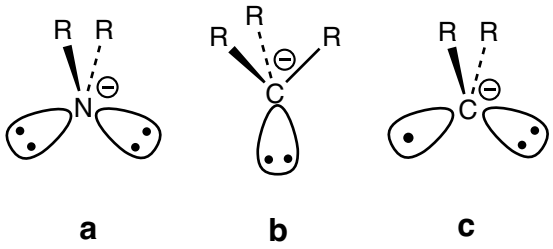

Scheme 2.3. Bridging atoms valence orbitals (and electrons) that participate in the framework bonding.

2.2.1 FEC = 8

I started by analysing the case of ligands such as amides or phosphides, represented here by two hybrid orbitals carrying two electrons each (Scheme 2.3a). The interaction of the four orbitals (Scheme 2.2c) of the two lithium atoms with the four

orbitals (Scheme 2.3a) of the X bridging atoms results in the molecular orbitals (MOs) shown schematically in Figure 2.2a that provide a semiquantitative representation of those obtained from DFT calculations for the Li_2X_2 ring in $[\{(en)Li\}_2(\mu{-}NH_2)_2]$ (compound **Y**).

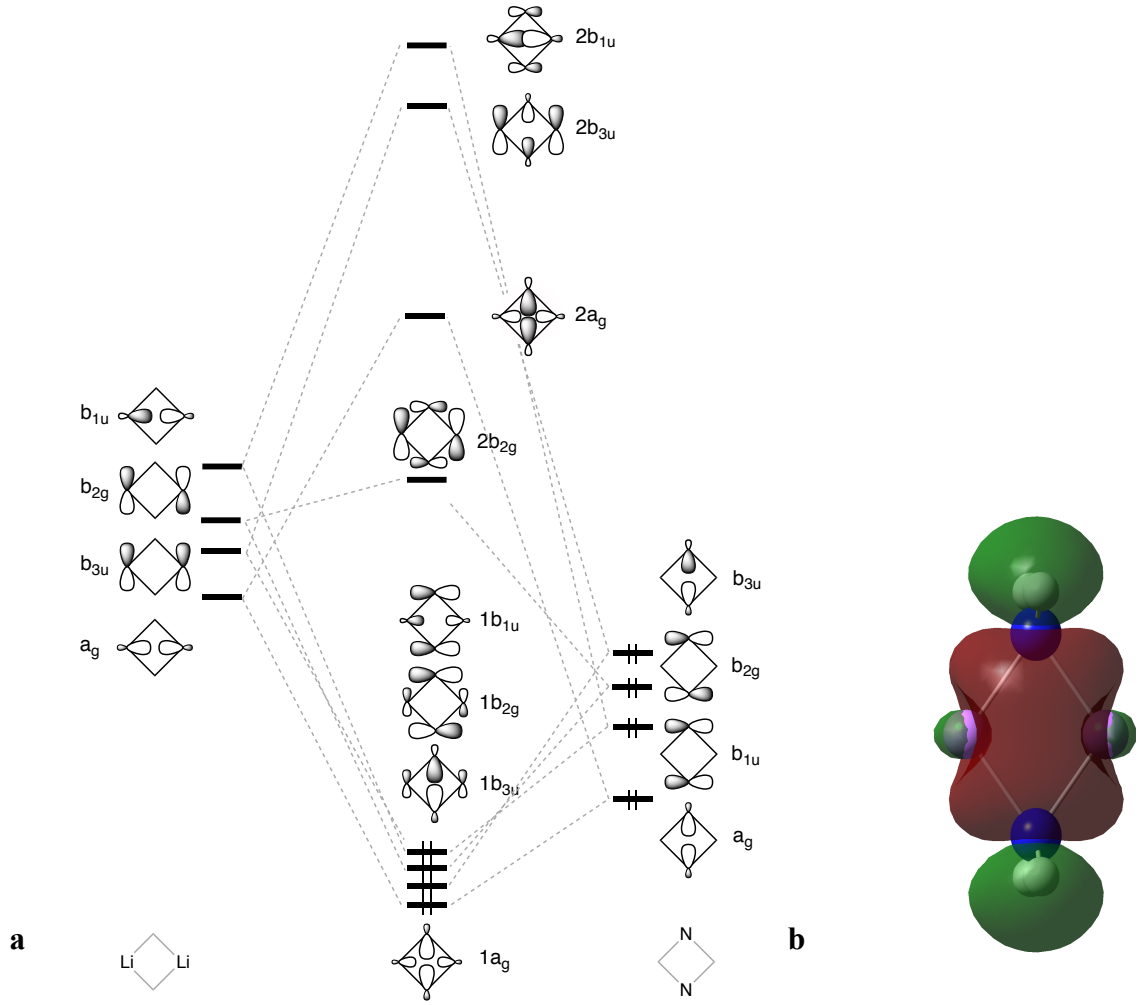

Figure 2.2. (**a**) Framework orbital interaction diagram for $[\{(en)Li\}_2(\mu{-}NH_2)_2]$ (compound **Y**) with 8 framework electrons (FEC = 8). (**b**) Isodensity plot (0.02 e^-) of the $1a_g$ MO of $[Li_2(\mu{-}NH_2)_2]$ (compound **T**).

In brief, the electronic structure of this rhombic framework consists of eight delocalized MOs in the Li_2X_2 plane. The lowest four MOs have framework (Li–X) bonding character, while the upper four are Li–X antibonding. It is important to notice that one of the framework-bonding MOs, $1b_{3u}$, has through-ring X···X σ antibonding character, while $1b_{1u}$ is Li···Li σ antibonding, a fact that will have important structural effects when the occupation of those orbitals is varied, or when the bridging group X does not have a π-type orbital available for framework bonding, e.g., when X = CH_3 or Ph (see

below). On the contrary, the $1a_g$ MO is bonding with respect to both the X···X and Li···Li couples (Figure 2.2b), and changes in the X−Li−X bond angles may enhance either the Li···Li (large angles) or the X···X (small angles) through-ring interactions.

When the four framework bonding MOs are filled with a total of eight electrons, as in $[\{(en)Li\}_2(\mu{-}NH_2)_2]$ (compound **Y**, Figure 2.2a), the framework electron count is 8 (abbreviated FEC = 8), and the orbital occupation accounts for four M−X single bonds (Scheme 2.1b). Note that the bonding MOs have much less contribution from the Li atoms than from the N ones, due to the much higher electronegativity of the latter. This fact is reflected in a calculated natural charge for the Li atoms of +0.60, compatible with a formal oxidation state of +1, despite their participation in four occupied MOs. Even if the calculated charge may somewhat vary depending on the method of population analysis applied, the qualitative message is clear: Li−N bonding has a non-negligible degree of covalency. For this reason, the two Li "ions" can be in closer contact than in the Li_2 molecule, in spite of the Coulombic repulsion.

2.2.2 FEC = 4

If one considers now systems with bridging ligands such as alkyl, phenyl, silyl, amines, or phosphines, they contribute each with only one sp^3 orbital and two valence electrons to the framework bonding (Scheme 2.3b), and a simpler MO diagram results, as can be seen for the case of $[\{(en)Li\}_2(\mu{-}CH_3)_2]$ (compound **A**) in Figure 2.3. The main consequence is that the σ^*(Li···Li) $1b_{1u}$ and π^*(Li···Li) $1b_{2g}$ MOs (Figure 2.2a) are no longer stabilized by the π-type orbitals of the bridges, and their high energy favours a compression of the Li_2C_2 diamond as in Scheme 2.1a, with a framework electron count of 4 (abbreviated FEC = 4). Given the proximity of the two lithium atoms in Scheme 2.1a and the Li···Li bonding nature of the only low-lying MOs, $1a_g$ and $1b_{3u}$, they describe a four centre-four electron (4c−4e) system with delocalized Li−C and Li−Li bonding character.

A similar situation appears if the Li atoms are replaced by BH_2 groups and the bridging groups by H atoms, thus forming diborane, $(H_2B)_2(\mu{-}H)_2$. The μ−H atoms only contribute one valence orbital each to framework bonding, and the MO diagram is qualitatively similar to Figure 2.3 (where the terminal B−H bonding orbitals are omitted for simplicity).[36] The $B_2(\mu{-}H)_2$ core has a FEC = 4 and is therefore expected to present delocalized 4c−4e B−H and B−B bonding, consistent with a B−B distance of 1.75 Å in

the solid state, to be compared to twice the atomic radius (1.68 Å). The main difference between the FEC = 4 Li_2X_2 rings studied here and B_2H_6 is that the latter has a higher degree of covalency due to the smaller electronegativity difference between B and H than between Li and X.

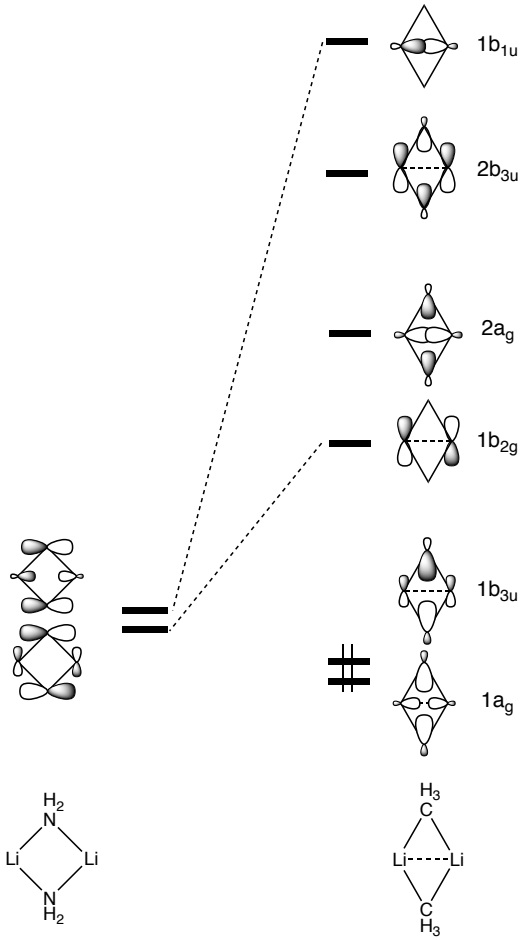

Figure 2.3. Framework MO diagram for [{(en)Li}$_2$(μ−CH_3)$_2$] (compound **A**) with four framework electrons (FEC = 4, right) and comparison with the energies and topologies of the $1b_{2g}$ and $1b_{1u}$ orbitals in the FEC = 8 compound [{(en)Li}$_2$(μ−NH_2)$_2$] (left, compound **Y**, Figure 2.2a).

2.2.3 FEC = 6

A third case corresponds to the rings with bridges of the type shown in Scheme 2.3c, analogous to 2.3a but with one less electron per lithium, which leads to a FEC of 6. In this situation, one of the four framework bonding MOs in Figure 2.2a is perforce unoccupied, and the best choice is to empty the $1b_{3u}$ MO with strongly antibonding σ*(X···X) character. As a result, the approach of the two X atoms is favoured, strongly stabilizing the occupied $1a_g$ and destabilizing the empty $1b_{3u}$ MO. The resulting orbital diagram is shown in Figure 2.4 for the case of [{(THF)Li}$_2$(μ−CH_2)$_2$] (compound **L**).

There, it can be seen that the σ(C···C) $1a_g$ MO describes a carbon-carbon bond since its antibonding counterpart (distributed among $1b_{3u}$ and $2b_{3u}$) is empty. Formally, there is no π bonding between the C atoms, since both the π and π^* orbitals ($1b_{1u}$ and $1b_{2g}$) are occupied. In summary, by simply counting the electrons available for framework bonding, one can foretell in which cases to expect a regular ring (FEC = 8), and in which ones a squeezed ring with either X···X (FEC = 6) or M···M (FEC = 4) short distances may appear.

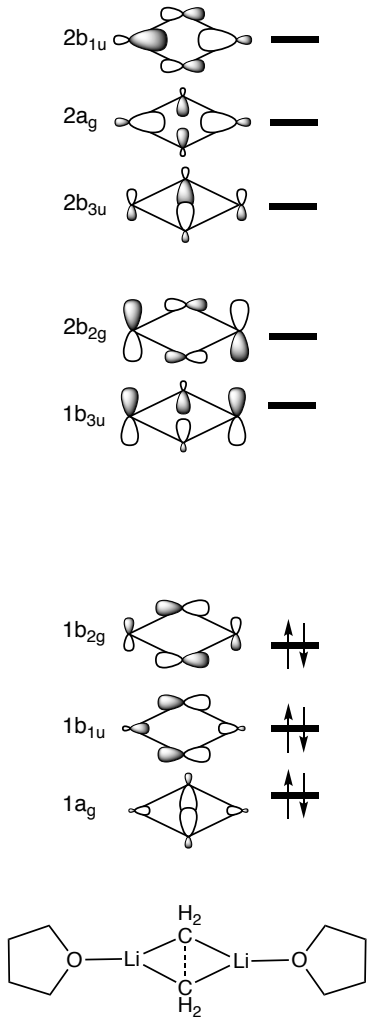

Figure 2.4. Framework MO diagram of [{(THF)Li}$_2$(μ–CH_2)$_2$] (compound **L,** FEC = 6).

2.3 Geometry Optimizations

To analyse the applicability of the framework electron counting rules to the lithium diamonds, I have optimized a number of model complexes, based on experimentally known structures with varying degrees of simplification of the ligands, in order to test steric and inductive effects. The results are summarized in Table 2.1.

Table 2.1. Optimized Structures and related experimental data[a] for $[\{(L_2)Li\}_2(\mu{-}X)_2]$ rings.[b]

				Calculated				Experimental			
FEC	Cpd.[c]	X	L_2	Li-Li	X-Li-X	ρ(X-X)[d]	Li^{charge}	refcode[e]	Li-Li	X-Li-X	Ref.
4	**A**	CH_3	en	2.274	117.4	0.013	+0.52				
	B	SiH_3	en	2.763	118.0	0.009	+0.42				
	C (2+)	NH_3	en	2.597	106.0	0.008	+0.64				
	D	CH_3	tmen	2.255	117.7	0.014	+0.53	xijlim	2.412	113.4	37
	E	CH_3	OMe_2	2.178	118.4	[0.015] [f]	+0.64				
	F	CH_3	OEt_2	2.223	116.2	0.015	+0.54				
	G	CMe_3	OEt_2	2.246	112.7	0.016	+0.54	suhbom	2.303	110.7	11
	H	$C(SiH_3)_3$	OEt_2	2.444	112.6	0.012	+0.59				
	I	Ph	en	2.440	113.2	0.012	+0.54				
	J	Ph	tmen	2.403	108.3	0.014	+0.55	phenli	2.491	105.6	38
	K	Ph	$Cy(NH_2)_2$	2.423	111.6	0.013	+0.52	kobcel	2.541	105.3	39
6	**L**	CH_2	thf	3.679	44.8	-	+0.66				
				C-C 1.551		0.220					
	M	CMe_2	thf	3.831	44.0	-	+0.54				
				C-C 1.552		0.226					
	N	$C(SiMe_3)_2$	thf	3.758	45.3	-	+0.65	jamsev01	3.827	45.1	40
				C-C 1.579		0.198			1.589		
	O	PH	en	4.358	55.9	-	+0.49				
				P-P 2.315		0.092					
	P	PPh	tmen	4.294	55.8	-	+0.49	reqcog	4.430	53.7	41
				P-P 2.275		0.101			2.244		
	Q	AsH	$(OEt_2)_2$	4.460	59.4	-	+0.47				
				As-As 2.542		0.071					
	S	SiR_2 S=1[g]	thf	2.667	118.8	0.011	+0.53	yodrep	3.021	112.3	42
8	**T**	NH_2	-	2.314	106.1	0.016	+0.80				
	U	$N\{SiH_3\}\{Si(SiH_3)_3\}$	-	2.395	104.8	0.017	+0.79				
	V	$N\{tms\}\{Si(tms)_3\}$	-	2.321	108.4	0.015	+0.70	pektuu	2.287	111.0	43
	W	$N(tms)_2$	-					gas phase	2.558	100.0	44
	Y	NH_2	en	2.397	106.6	0.014	+0.60				
	Z	NPh_2	tmen	2.730	99.6	0.013	+0.67	ohezor	2.810	98.4	45
	AA (2+)	H_2O	$(H_2O)_2$	2.905	90.6	0.012	+0.78	6 structs.	2.84 (3)	91 (1)	46-51
	AB	PH_2	en	3.062	106.2	0.009	+0.48				
	AC	PPh_2	en	2.826	113.3	0.011	+0.45				
	AD	PH_2	tmen	3.162	102.0	0.010	+0.45				
	AE	PPh_2	tmen	3.604	90.0	0.012	+0.50	gedduo	3.611	92.9	52
	AF	AsH_2	$(OEt_2)_2$	3.605	94.6	0.010	+0.48				
	AG	$AsPh_2$	$(OEt_2)_2$	3.724	91.8	0.010	+0.50	duwzaw	3.889	88.3	53

[a] Bond distances in Å, bond angles in degrees. [b] Abbreviations: tms = $SiMe_3$; en = ethylenediamine; tmen = tetramethyl-ethylenediamine. [c] All compounds are neutral except when otherwise specified. [d] ρ(X-X) is the electron density at the X-X bond critical point (BCP), except for compound **E**, for which it corresponds to a Li_2C_2 RCP. [e] CSD reference codes for the experimental structures. [f] The density in this case corresponds to an RCP. [g] The ground state for this molecule is a triplet, both computationally and experimentally; R = Si^tBu_2Me.

The analysis of the molecular orbitals of the calculated compounds shows that all those with FEC = 8 present a set of four occupied framework orbitals similar to those presented in Figure 2.2a for [{(en)Li}$_2$(μ−NH$_2$)$_2$] (compound **Y**), and those with FEC = 4 have framework orbitals much like those shown in Figure 2.3 for [{(en)Li}$_2$(μ−CH$_3$)$_2$] (compound **A**).

Comparison of the computational results with those of related experimental geometries (last three columns of Table 2.1) shows a fair agreement, both in the solid state and in the gas phase. In Figure 2.5, I represent the ranges of Li···Li distances grouped by FEC number. There, it can be seen that the compounds with bridging atoms X of the third period and beyond occupy three different zones, according to the expectations deduced from the discussion of Figures 2.2 − 2.4: short Li···Li distances for FEC = 4, very long distances (i.e., short X···X distances) for FEC = 6, and intermediate values for FEC = 8. However, for molecules with bridging atoms of the second period (C, N, O), the FEC = 8 and FEC = 4 sets overlap, in apparent contradiction with the expectations. I think that the small bridging atoms enforce short distances between lithium atoms even when no through-ring bonding is expected (FEC = 8). Therefore, I examined additionally another geometric parameter, the X−Li−X bond angle, since large values of that angle could indicate a tendency of the two lithium atoms to approach each other (deviation from a regular square) due to an attractive Li···Li interaction.

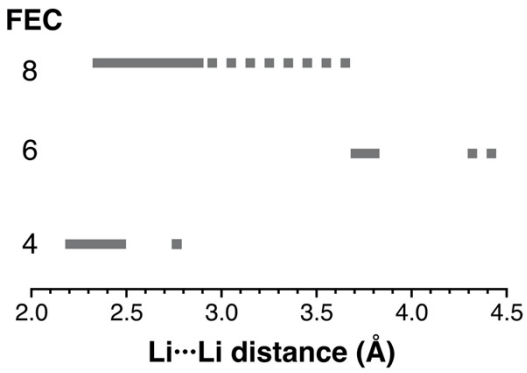

Figure 2.5. Distribution of the calculated Li···Li distances for three different framework electron counts (FEC). The continuous lines correspond to compounds with bridging atoms of the second period, the discontinuous lines to those with heavier bridging atoms.

To consider the two geometric indications of Li···Li attraction, I present in Figure 2.6 a geometry map in which the Li···Li distances are plotted as a function of the X−Li−X bond angle, separately showing the compounds with small and large bridging atoms. It

can be seen that all compounds with FEC = 4, for which some bonding Li···Li interaction is expected, occupy the region of large bond angles of the plot (106 − 118º), while the Li···Li distances are shortest for compounds with small bridging atoms (2.22 − 2.60 Å) and slightly longer for the compound with a silane bridge (2.76 Å), in fair agreement with twice the covalent radius of Li (2.56 Å).[8]

The next group of structures in Figure 2.6, with FEC = 8, occupy two regions at intermediate X−Li−X bond angles (91 − 113º) and longer Li···Li distances (2.31 − 3.72 Å) than those with FEC = 4, which is consistent with a lesser tendency of the two Li atoms to approach each other for the FEC = 8 systems. While the different behaviour of the two sets of complexes roughly follows the theoretical expectations, the regions with those two electron counts slightly overlap, but much less so if only systems with heavier bridging atoms are considered.

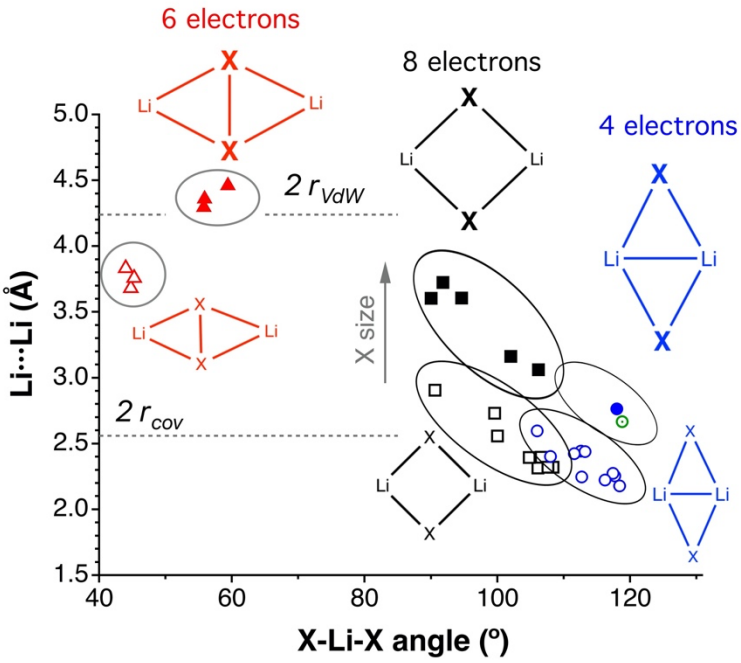

Figure 2.6. Scatterplot of Li···Li distances and X−Li−X bond angles in optimized structures of [{$(L_2)Li\}_2(\mu$−$X)_2$] rings (Table 2.1). The data are grouped according to their framework electron counts (FEC) and the size of the bridging atom X (empty symbols for elements of the second period, filled symbols for heavier elements), and the rightmost green dotted circle corresponds to the triplet compound [{$(THF)Li\}_2\{\mu$−$Si(Si^tBu_2Me)_2\}_2$] (compound **S**) with FEC = 6 in its triplet ground state. The straight dotted lines represent twice the covalent and van der Waals radius of lithium, respectively.

Finally, the compounds with FEC = 6 present a clear-cut behaviour, all having very acute X−Li−X bond angles (44 − 60º), consistent with the existence of short through-ring X···X distances (1.55 − 2.54 Å, with X = C, P, or As) and correspondingly large Li···Li distances (3.68 − 4.46 Å). Note that in the compounds with XR bridges (X = P, As; R = H, Ph), the X−R bond is practically perpendicular to the Li_2X_2 ring. This geometry allows me to consider those groups as three electron donors, assuming them as monoanionic, since a lone pair is oriented away from the ring and therefore does not contribute to the framework bonding (Scheme 2.4). The same behaviour is found in the experimental structures of two compounds with XR bridges.[54-55]

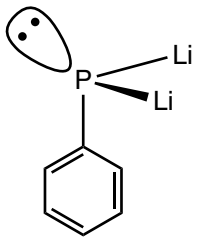

Scheme 2.4. Distribution of the P lone pair and P−Ph bond with respect to the Li−P−Li plane.

Still focusing on electronic effects, the calculations using XR and XR_2 bridges (X = P, As; R = H, Ph) allow me to compare the geometries of similar molecules which differ only in the presence or absence of a second substituent at the bridging atom. Since I am considering the rings as formed by Li^+ ions, and monoanionic XR and XR_2 groups have the valence orbitals and electrons shown in Scheme 2.5, combined with two lithium cations they give place to framework electron counts of 6 and 8, respectively. For instance, ongoing from PH to PH_2, a lone pair that does not participate in framework bonding is replaced by an R group. Thus, the contribution of the P atom to framework bonding increases from three (Scheme 2.5a) to four electrons (Scheme 2.5b). By comparing those pairs of similar compounds, it can be observed that substituting the XR bridges for the XR_2 ones, with the corresponding change in the FEC, going from molecules with bonding through-ring X···X distances to regular rings without through-ring bonding.

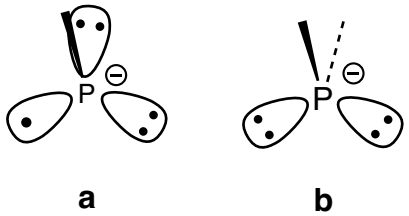

Scheme 2.5. Distribution of P valence orbitals (and electrons) in (**a**) PR and (**b**) PR_2.

Also interesting is the comparison of the alkyl and carbene bridges: while the neutral CR_3 bridging groups contribute only one orbital and one electron to framework bonding (or two electrons if they are considered as anionic, Scheme 2.3b), the CR_2 ones provide two orbitals and two electrons (three electrons in the ionic model, Scheme 2.3c). As a consequence, the molecules with alkyl bridges have a FEC of 4, whereas those with carbene bridges have six framework electrons and give Li−Li and C−C through-ring bonds, respectively.

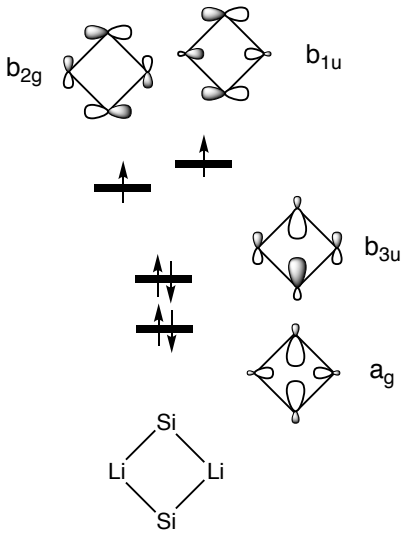

Figure 2.7. Occupation of the framework bonding MOs of [{(THF)Li}$_2${μ−Si(Si^{t}Bu$_2$Me)$_2$}$_2$] (compound **S**) in its triplet ground state.

A special case is that of compound **S**[42] in which the Li atoms are bridged by the Si(Si^{t}Bu$_2$Me)$_2$ group. This compound has been characterized in solution by Electron Paramagnetic Resonance (EPR) and found to be a radical that dimerizes in the solid state. I therefore suspected that the dimer may be a diradical, with a triplet ground state rather than the singlet found for other six-electron systems. Indeed, the computational results shown in Table 2.1 correspond to the triplet state, whereas attempts to optimize a singlet state resulted in dissociation of the ring. In such a triplet state, the orbital occupation (Figure 2.7) favours the mechanism for through-ring bond formation, and its geometry is similar to those of the FEC = 4 systems: the σ*(Li···Li) MO $2b_{1u}$ is left unoccupied (Figure 2.2a), the two framework bonding orbitals with Li···Li antibonding character ($1b_{2g}$ and $1b_{1u}$, Figure 2.2a) are half-occupied, and the other two framework bonding MOs ($1a_g$ and $1b_{3u}$, Figure 2.2a) are fully occupied. That there is some bonding interaction between the Li atoms in this compound is clearly shown by its Li···Li distance (Li···Li =

2.667 Å), shorter than in the FEC = 8 compounds with heavy bridging atoms (2.83 − 3.72 Å), and its X−Li−X bond angle (118.8º) being wider than in the FEC = 8 molecules (90−113º). The behaviour of this triplet FEC = 6 compound is therefore similar to those of the rings with FEC = 4 (Figure 2.3). The fact that the two unpaired electrons occupy MOs localized mostly at the more electronegative atoms of the ring, the silicon bridges, accounts for the calculated spin densities for Si (0.91) and Li (0.07).

2.4 Analysis of Experimental Structures

With the perspective obtained from the analysis of calculated compounds with different electron counts, one can now analyse in a similar way the experimental data for a wealth of Li_2X_2 rings (391 structural datasets) in a geometry map (Figure 2.8). The compounds analysed comprise a variety of bridging atoms: C, Si, Ge, and Sn for FEC = 4; C, Si, N, and P for FEC = 6, and N, P, As, O, S, Se, Te, Cl, Br, and I for FEC = 8. The map shows those compounds distributed in similar regions than found for the computational results (Figure 2.6), showing also an area where the structures with 4 and 8 framework electrons somewhat overlap. The compounds with FEC = 6,[40,54-58] in the zone of very small angles and very long Li···Li and short X−X distances, are not shown for clarity (see Appendix; Figure A2.1).

A very special case of Li_2X_2 ring appears in a dinitrogen bridged dilithium dicationic compound $[\{(THF)_3Li\}_2(\mu{-}N)_2]^{2+}$.[56] In this compound each Li atom, coordinated by three tetrahydrofuran molecules, has only one orbital and no electrons available for framework bonding (Scheme 2.6). We are therefore in a situation similar to that of the Li_2Me_2 rings (Figure 2.3) which can only accommodate four framework bonding electrons. Nevertheless, the roles of the Li and bridging atoms are interchanged and a FEC = 4 system with short N−N distance must result. That number of framework bonding electrons is achieved if the two in-plane orbitals of each N atom (Scheme 2.7b and 2.7c) are occupied with one electron, two electrons occupy an outward pointing lone pair orbital (Scheme 2.7a), and one electron occupies the out of plane p orbital (Scheme 2.7d). Since the four framework electrons imply a short N−N distance, the two out of plane p orbitals significantly overlap and form a π bond that complements the orbital and electron-deficient framework bonding. Consistently, the experimental N−N distance is as short as 1.058 Å, and the Li−N−Li bond angles are 152.8º. Notice that a compound containing a $Li_2B_2^{2+}$ ring with a short B−B distance of 1.452 Å has a similar electronic

structure, with the lone pairs of Scheme 2.7a replaced by NHC carbenes coordinated to the boron atoms, and has been described in an alternative way as two lithium cations bound to the triple bond of a neutral diboryne molecule.[59]

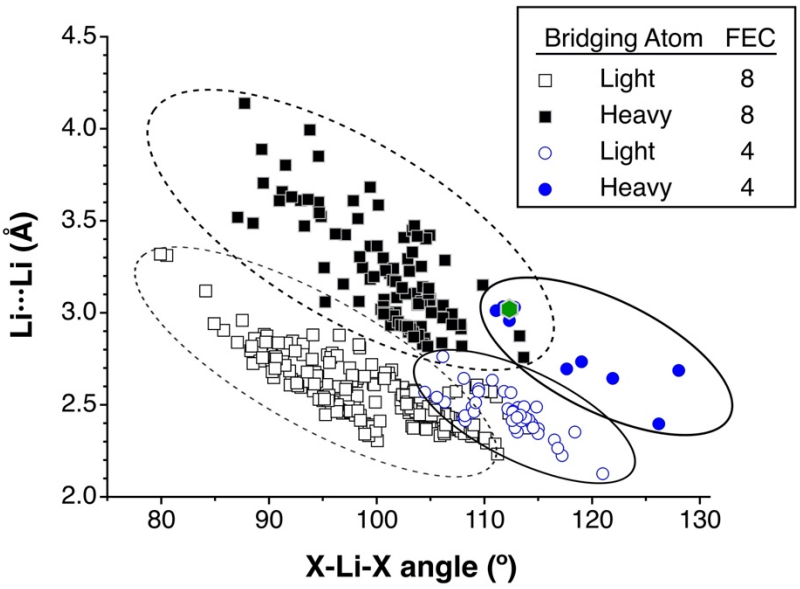

Figure 2.8. Scatterplot of Li···Li distances and X−Li−X bond angles in experimental structures of [{(L$_2$)Li}$_2$(μ−X)$_2$] rings (see Appendix; Tables A2.1 − A2.5). The data are grouped according to the framework electron count (FEC) and the size of the bridging atom X (empty symbols for elements of the second period, filled symbols for heavier elements); the green circle corresponds to the FEC = 6 triplet compound **S** (X = Si). Other compounds with FEC = 6, not shown, appear in a region of longer Li···Li distances and smaller X−Li−X bond angles (see Appendix; Figure A2.1).

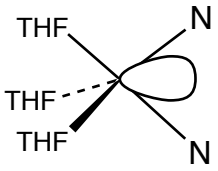

Scheme 2.6. Li valence orbital that participates in the framework bonding.

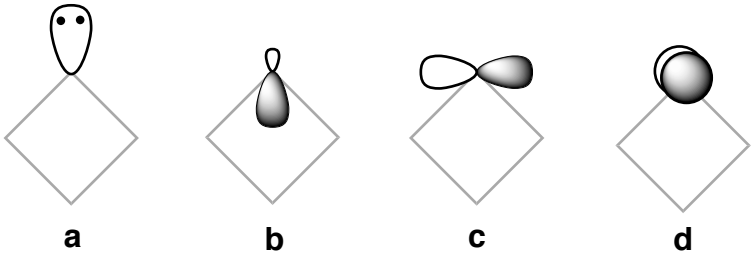

Scheme 2.7. Distribution of the N atom valence orbitals.

2.5 Effect of intramolecular steric and secondary noncovalent interactions

That some compounds with eight framework electrons have shorter Li···Li distances than others with four electrons, as observed for both calculated and experimental structures, is a result that apparently contradicts the expectations from the delocalized MO picture. Are there other factors, besides through-ring bonding, that may also affect the geometry of the Li_2X_2 rings? Let us look at the two analogous molecules with eight framework electrons: [{(en)Li}$_2$(μ−NH_2)$_2$] and [{(tmen)Li}$_2$(μ−NPh_2)$_2$] (compounds **Y** and **Z**, Table 2.1). While the latter presents a geometry characteristic of a regular ring, with a non-bonding Li···Li distance of 2.73 Å, the analogous with unsubstituted amido bridges presents a much shorter distance and a wider X−Li−X bond angle (2.397 Å and 106.6º, respectively). In the model with NH_2 bridges, the ethylenediamine ligands attached to the Li atoms are significantly bent toward the bridges, resulting in H···H contacts at about 2.4 – 2.6 Å, typical distances at which H···H interactions are attractive.[60] In the NPh_2 bridged complex, besides the short contacts between hydrogen atoms of tmen and Ph groups (2.3 – 2.6 Å), there are also pretty short Ph···Ph contacts (2.12 Å). A similar situation is found if [{(en)Li}$_2$(μ−PH_2)$_2$] (compound **AB**) is compared with [{(tmen)Li}$_2$(μ−PPh_2)$_2$] (compound **AE**), with Li···Li distances of 3.06 and 3.60 Å, respectively, and X−Li−X angles of 106 and 90°. I therefore propose as a working hypothesis that the van der Waals interactions between the substituents may have a non-negligible effect in fine-tuning the geometry of the Li_2X_2 rings.

It therefore seems that the Li_2X_2 rings have a high plasticity, and their geometries can be modulated, aside from the electron count, by the size of the bridging atoms and by intramolecular noncovalent interactions. To verify the plasticity of the Li_2X_2 rhombuses, I have carried out partial optimizations of three model compounds, one with a FEC of 4 and two with a FEC of 8: [{(en)Li}$_2$(μ−CH_3)$_2$] (compound **A**), [{(en)Li}$_2$(μ−NH_2)$_2$] (compound **Y**), and [{(tmen)Li}$_2$(μ−NPh_2)$_2$] (compound **Z**). In each of these calculations, the ring was frozen at a given X−Li−X angle, and the rest of the structure was reoptimized. The resulting dependence of the energy on that bond angle for one of the cases is shown in Figure 2.9 (for numerical data and the graphical representation of all compounds see Table A2.6 and Figure A2.2 of Appendix, respectively). It can be seen that distortions of the ring of up to ±10º, that imply variations in the Li···Li distance of up to 0.6 Å, require less than 8 kcal/mol (< 5 kcal/mol in compounds **Y** and **Z**), while the overlap between the FEC = 4 and FEC = 8 regions in Figure 2.6 is of only 2º and 0.28 Å.

The large Li···Li distance variability observed within a family of compounds with the same electron count indicates that changes in intramolecular van der Waals interactions (including steric effects) or in intermolecular noncovalent interactions modulate the geometry of the rings. Notice, though, that in several cases larger variations in the Li···Li distances are associated with the presence of bulkier bridging atoms and correspondingly longer Li−X distances. It is worth noting also that most of the calculated Li−Li distances in the Li_2X_2 rings are shorter than the covalent bond of the Li_2 molecule (2.698 Å) at the same computational level.

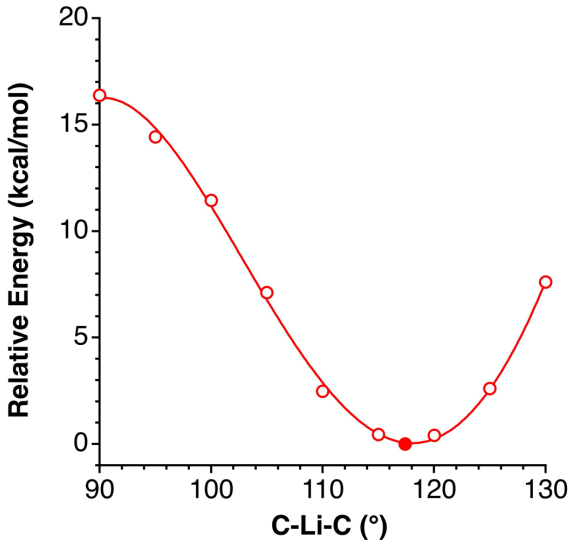

Figure 2.9. Scan of the energy dependence of [{(en)Li}$_2$(μ−CH_3)$_2$] (compound **A**) on the C−Li−C bond angle. The energy minimum corresponds to the filled circle.

2.6 Analysis of the ionic and covalent character of Lithium bonding

Since alkaline atoms are often considered to be present in the crystal state as cations, that interact with anions via purely Coulombic forces, I have evaluated the ionic character of Li in the structures studied here by looking at its calculated atomic charges. Even if the numerical values of the calculated charges may vary depending on the population analysis scheme applied, I looked for trends rather than numerical values, and this discussion considers the values obtained from a Natural Population Analysis (NPA).

I have noted that the atomic charges at the Li atoms (Table 2.1) are in all cases between +0.48 and +0.70, except for compounds **T**, **U**, and **AA**. Since the electron density at the Li atoms comes from both the framework bonding MOs and donation from its terminal ligands L, it is not a surprise to find that the calculated lithium charges depend

mostly on the electronegativity of the bridging atoms (χ^X) and the number of terminal ligands at each Li atom (n_L). A multilinear regression (Eq. 2.1, $R^2 = 0.87$, standard error of the estimate: ± 0.038), roughly quantifies those dependences and shows that the most important effect comes from χ^X. In addition, inclusion of the electronegativity of the terminal donor atoms (χ^L) does not significantly improve the regression coefficient. For the compounds with $n_L = 2$, the dependence of the calculated charge on the electronegativity of the bridging atoms X (χ^X) can be fitted to a second order expression (Figure 2.10 and Eq. 2.2, $R^2 = 0.95$).

$$\text{Li charge} = 0.166 + 0.196 \cdot \chi^X - 0.057 \cdot n_L \qquad \text{[Eq. 2.1]}$$

$$\text{Li charge} = 0.556 - 0.205 \cdot \chi^X + 0.077 \cdot (\chi^X)^2 \qquad \text{[Eq. 2.2]}$$

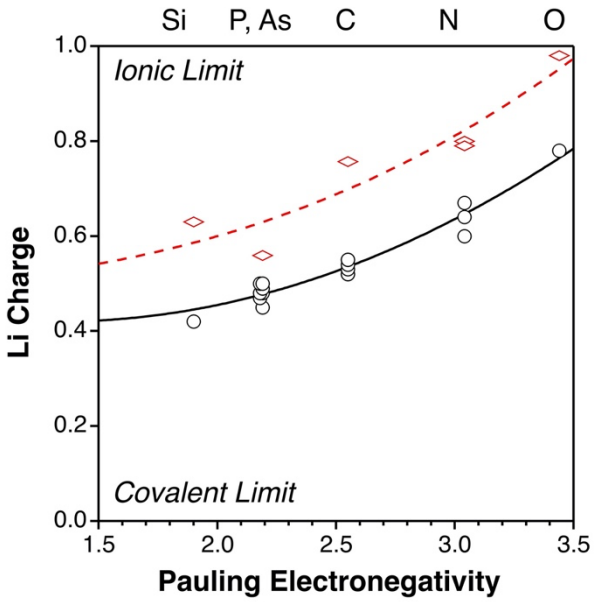

Figure 2.10. Atomic charge calculated at the Li atoms in Li_2X_2 compounds with two (circles) and no terminal ligands (rhombuses), represented as a function of the electronegativity of the bridging atoms X.

If we wish to disregard the effect of the ligands on the net Li charge and evaluate the degree of covalency of the Li−X bonding, we can focus on compounds **T – V**, with no terminal ligands. In those cases, each Li atom holds 20 to 30% of its valence electron, thus indicating a lower limit for the degree of covalency in Li-X bonding. To obtain a rough estimate of the population of the Li valence shell in Li_2X_2 rings with no ligands attached to Li, I have reoptimized structures of compounds **B**, **E**, **AA,** and **AE** removing

such ligands, and the resulting atomic charges, represented in Figure 2.10, indicate that the covalency with less electronegative bridges may be as high as 40%.

2.7 Analysis of the topology of the electron density

To discuss the results of the topological analysis of the electron density within the Quantum Theory of Atoms in Molecules (QTAIM) framework,[61] let us start with the simple Li_2 molecule, for which a covalent bond can be assigned without problem, which I have optimized at the same computational level used throughout this chapter. The optimized Li−Li distance is 2.698 Å, very close to the experimental value in the gas phase (2.673 Å) and larger than in all the Li_2X_2 rings with bridging atoms of the second period (Table 2.1). A map of the calculated electron density and the critical points found (Figure 2.11) is shown for the case of $[\{(en)Li\}_2(\mu{-}NH_3)_2]^{2+}$ (compound **C**), as well as for the Li_2 molecule for comparison.

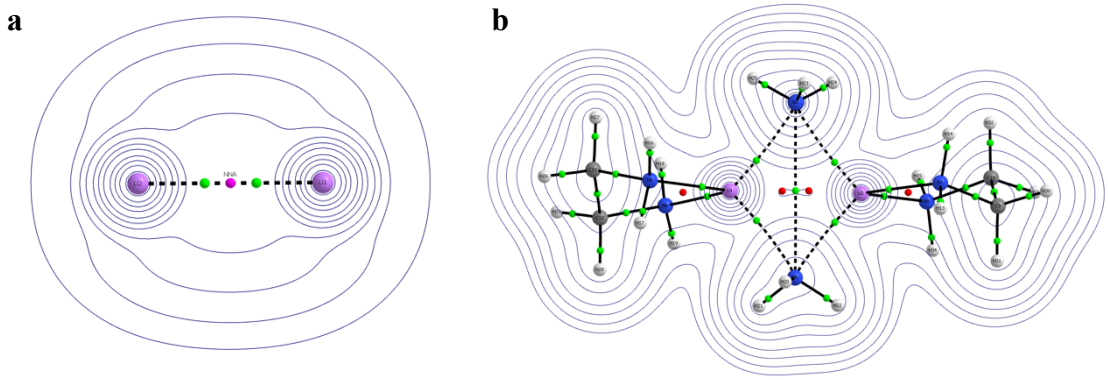

Figure 2.11. Electron density map for (**a**) the Li_2 molecule and (**b**) for $[\{(en)Li\}_2(\mu{-}NH_3)_2]^{2+}$ (compound **C**). The green spheres represent bond critical points (BCPs); the red ones, the ring critical points (RCPs); and the magenta sphere at the centre of the Li_2 molecule, a non-nuclear attractor (NNA).

A first remarkable feature of the electron density topology in Li_2 (Figure 2.11a) is that at the centre of the Li−Li bond there is no a bond critical point (BCP) but a nonnuclear attractor (NNA), i.e., a point in which the electron density is a maximum in the three directions of space. This NNA is surrounded by two BCPs that mark corresponding minima in the electron density along the Li−Li direction. This situation has been attributed[62] to the nodal surface in the Li 2s orbital, which should be responsible for the two minima in the electron density (formally BCPs). A similar NNA has also been reported in the topological analysis of the experimental electron density of an unsupported Mg−Mg bond.[63] It must be noted, however, that the electron densities in Li_2 are very

small in that region, and the differences between the BCPs and the NNA are almost negligible (0.0128 and 0.0134, respectively). The small electron density found in the interatomic region in Li_2 can be explained by the highly electropositive character of the Li atoms that hold most of the electron density in the vicinity of their nuclei.

For the FEC = 4 complex **C**, as well as for practically all other compounds with the same electron count, I found a N−N bond path (Figure 2.11b) with similar electron densities at the BCP (between 0.008 and 0.016, Table 2.1) that can be explained also by the much larger contribution of the N atoms to the framework bonding orbitals (Figure 2.3) and the consequent accumulation of electron density at the bridging atoms, due to their higher electronegativity relative to lithium. The only exception is compound **E**, for which there is a ring critical point (RCP) at the centre of the Li_2C_2 unit rather than a BCP, although its electron density at the centre of the ring is identical to that at the BCP of analogous compounds. Although one might speculate that the absence of a BCP(C···C) in this case could be due to the short Li−Li distance, the shortest one in this family of compounds, the lack of correlation between ρ(BCP) and the Li···Li distance or X−Li−X bond angle, together with the rather small values of the former parameter, prevents us from discussing further along this line. What is clear, however, is that the electron density at the BCP(X···X) and at the two RCPs(Li−X−X) differ in practically all cases by less than 0.001 units (see Appendix; Figure A2.3).

I have also looked at the electron density distribution of only the two bridges in compounds **C** (X = NH_3, FEC = 4) and **Y** (X = NH_2^-, FEC = 8) with the same geometry of the full molecules and found in both cases a BCP between the two nitrogen atoms, with electron densities of 0.006 and 0.010, respectively, slightly smaller than those found in the full molecules (Table 2.1). The difference between the two bridges considered is undoubtedly due to the longer N···N distance in the former (3.517 vs 3.216 Å). Since the interaction between the two bridges is repulsive in the absence of the lithium ions (4.4 kcal/mol for the NH_3 dimer in compound **C**), the BCP along the N···N path for the isolated ligands cannot be interpreted as indicative of some degree of N−N bonding. A look at the MO picture of compound **Y** (Figure 2.2a), where the four framework bonding orbitals have much larger contributions from the N than from the Li atoms, indicates that the N···N bond path and the BCP are due to the high electronegativity difference between N and Li that results in a concentration of electron density closer to the N atoms. Since all compounds with FEC = 8 (compounds **T** – **AG** in Table 2.1) have similarly small

electron densities at the BCP, between 0.008 and 0.017, the considerations made here for compound **Y** can be extended to all the FEC = 8 compounds. For both families of compounds, the electron densities at the BCP(X···X) and at the RCP(Li−X−X) are very small (the average for 22 compounds is 0.0005(6)), indicating that the electron density at the centre of the rings along the Li···Li line is practically flat.

If we turn our eyes to the compounds with six framework electrons (compounds **L**−**Q**), we see that the short X−X distances found go along with much higher electron densities at the BCP(X−X), 0.071 − 0.226, now compatible with the existence of a covalent through-ring X−X bond. It is not therefore strange that these compounds are in some cases described as having an X=X double bond, side-on coordinated to two Li ions. However, if we compare the electron density at the BCP between two CH_2 units in compound **L** (0.220 at a C−C distance of 1.551 Å) with that found for the ethylene molecule C_2H_4 (0.363 at a C=C distance of 1.317 Å),[61] we see that the C−C link in compound **L** is closer to that in ethane (0.252 at 1.527 Å),[61] thus stressing the high delocalization of the framework electrons in that system.

I have noted above that van der Waals interactions between the substituents may have a non-negligible influence on the geometry of the Li_2X_2 rings. This circumstance is reflected in the topological analysis of the electron density, in which many bond critical points are observed between hydrogen atoms of the organic groups present in the molecules, at distances of 2.5 Å or less, typical of homopolar noncovalent C−H···H−C interactions.[60]

An analysis of the Laplacian of the electron density of all optimized structures has been carried out, and the corresponding maps for some of them in the Li_2X_2 plane are given as Appendix (Figures A2.4 – A2.6). For the FEC = 4 compounds, those maps indicate a charge accumulation inside the ring, centred at the nitrogen atoms, a situation analogous to that found for diborane (Figure A2.4). The main difference is that in the latter case the charge concentration reaches the B–B interatomic region due to the much smaller electronegativity difference between B and H than between Li and C in compounds **A** and **E**. In the FEC = 8 systems (Figure A2.5), the charge density is more contracted in the X···X direction and extends also along the X–Li directions, consistent with a higher localization to form four X–Li bonds, and for compound **AG** becomes a nice depiction of four X–centred lone pairs directed toward the Li ions. Finally, a FEC =

6 compound (**N**, Figure A2.6) shows a clear accumulation of the electron density along the X–X direction, eloquently pointing to a covalent bond that is consistent with the high values of the electron density found in the centre of the ring (Table 2.1).

2.8 Summary

A structural analysis of the X-ray and calculated structures of molecules with Li_2X_2 rings shows that they can be found in different regions of a geometry map (a scatterplot of Li···Li distance and X–Li–X bond angle), depending on their electron count (FEC) and the size of the bridging atom. The dependence on the electron count can be accounted for by the different characteristics and occupation of delocalized framework bonding molecular orbitals, similar to what has been reported earlier for dinuclear transition metal rings with the same topology. The qualitative predictions have been computationally verified for a number of molecules. In particular, the calculated Li–Li distances in Li_2X_2 rings with a FEC of 4 and bridging atoms of the second period are shorter than the covalent bond of the Li_2 molecule, 2.698 Å, at the same computational level.

The existence of some overlap between the regions of the map corresponding to FEC = 4 and FEC = 8 systems has been shown to be the result of potential energy curves with rather flat minima. Such flat potential minima are due to the combined ionic and covalent contributions to the framework bonding orbitals that are concentrated at the more electronegative bridging atoms.

The nature of the framework bonding correlates with the electronegativity of X and is predominantly ionic only for F and O, and to a lesser extent for N and other less electronegative bridges. The topology of the electron density at the ring centre of compounds with those two electron counts is consistently flat and small, resulting in artefactual X···X bond paths.

Changes in intramolecular steric repulsions or van der Waals interactions and in intermolecular weak interactions may be responsible for the variability observed within a family of compounds with the same electron count. Notice, though, that in the latter case larger variations in the Li···Li distances are associated with the presence of bulkier bridging atoms and correspondingly longer Li–X distances. All in all, and at difference with the behaviour of a variety of analogous transition metal rings, the geometry of the

Li_2X_2 frameworks depends on several factors: the FEC, the electronegativity of the bridging ligands, the size of the X atoms, and intramolecular (and possibly intermolecular) noncovalent interactions. This peculiar bonding situation may be the basis of the high tendency of lithium atoms to cluster together in molecular systems.

In summary, a delocalized MO description of the Li_2X_2 rings captures the geometrical effects of the framework electron count, as well as the importance of both covalent and ionic contributions to chemical bonding therein. Since we are still in need of structural formulas for communication purposes, we must be aware that alternative Lewis-type covalent and ionic structures in Scheme 2.8 (solid lines represent Lewis electron pairs; the dashed lines, four delocalized electrons; the dotted lines, ionic bonding; and the arrows, dative bonds) each partially describe the electronic structure in the diffuse border between the covalent and ionic bonding regions.

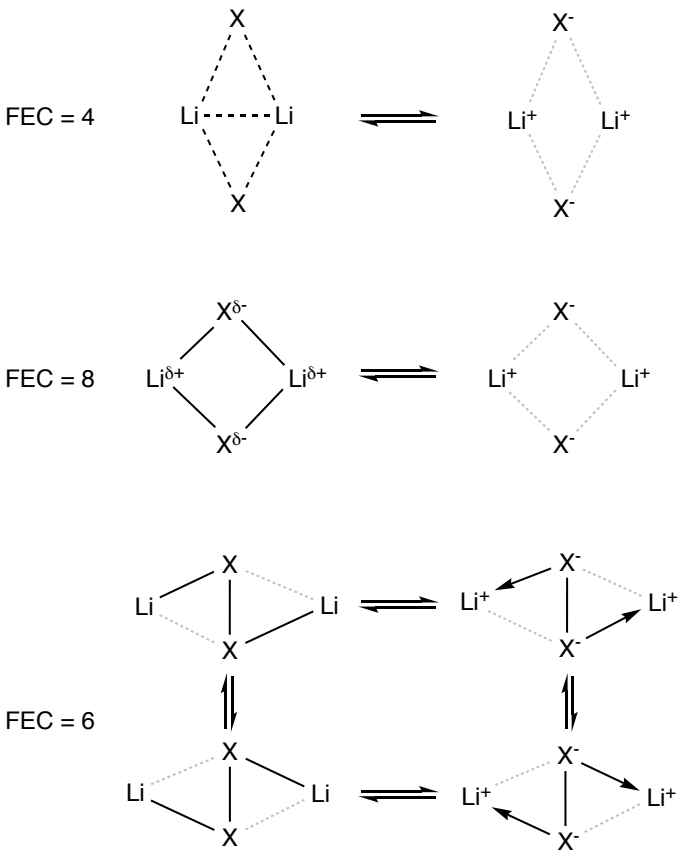

Scheme 2.8. Lewis structure of the three framework electron counts (FEC).

2.9 Appendix

Annex 2.1. Experimental through-ring Li-Li distance and X-Li-X bond angle for molecular structures of type $[\{(L_2)Li\}_2(\mu{-}X)_2]$ found in the CSD, represented in Figure 2.8.

Table A2.1. Systems with FEC = 8 and 2nd period bridging atoms.

refcode	Li-Li (Å)	X-Li-X (º)	X	refcode	Li-Li (Å)	X-Li-X (º)	X
GEQSEA	2.233	111.2	N1	FIWBAO	2.406	107.9	N1
PEKTUU	2.287	111.0	N1	JOKSIM	2.409	104.9	N1
KIKVUY	2.293	110.2	N1	HOLSUW	2.410	105.3	N2
KEQBIR	2.306	100.1	OR	XASZOG	2.412	100.3	O1
KIKVUY	2.319	110.0	N3	XASZUM	2.417	98.5	O1
HAXWEJ	2.329	108.9	N1	JECQIU	2.423	106.6	N1
GEQSAW	2.331	108.8	N4	FIJSEW	2.426	107.0	N1
NENVIM	2.333	105.9	N1	NEDWEB	2.428	106.8	N3
GEQSAW	2.334	108.9	N1	NUWBOW	2.433	106.7	N3
UJAPAY	2.334	99.3	O1	ITAZEJ	2.434	106.0	N1
CASZAX	2.342	98.9	O1	NUWBIQ	2.437	106.3	N1
SOLXUM	2.343	106.3	N2	LIBLUE	2.437	105.7	N1
MAZZIW	2.345	108.1	N1	LUXXEJ	2.438	105.3	N1
HAXWAF	2.345	108.6	N1	PUDFUQ	2.439	104.4	N1
GEQSAW	2.346	108.7	N3	YUDDEG	2.443	98.5	O1
SOLXUM	2.354	106.2	N1	NUWBOW	2.443	106.2	N1
SUSDEP	2.354	108.9	N1	BUXNOX03	2.444	106.1	N1
WEDVUX	2.358	99.9	O1	ROLRIU	2.444	98.0	O1
EABNEA	2.359	107.8	N1	GENGUC	2.445	105.5	N3
CAPSUI	2.365	107.5	N1	FUYWIF	2.445	105.1	N1
DAPGAC	2.368	104.6	N1	JECQAM	2.445	106.0	N1
DAPGAC10	2.368	104.6	N1	ZEGNOO10	2.445	104.0	N1
EABNEA	2.371	107.6	N3	XASZAS	2.447	95.2	O1
SOXYEL01	2.373	103.4	N1	ZEGNOO	2.447	104.0	N1
WIBKEX	2.375	113.7	C14	QOLFOM	2.449	106.3	N1
CUGJAP01	2.381	99.5	O1	MUJMAG	2.450	104.3	N3
GEQRUP	2.383	106.8	N1	FABDER01	2.452	105.5	N1
UQUGUK	2.384	99.6	O1	BUXNOX04	2.453	106.1	N1
CAZLIB	2.384	107.6	N1	QOLFOM	2.453	106.4	N5
SOXYEL	2.385	103.3	N3	BUXNOX02	2.454	105.9	N1
XENYAQ	2.391	109.0	N1	FIBYOE	2.456	96.8	O1
CUGJAP	2.392	99.3	O1	COSPOS	2.456	112.3	C14
WOBZAP	2.392	106.4	N1	NELCUC	2.458	103.0	N2
CUGJAP01	2.398	98.9	O2	FABDER02	2.458	105.6	N1
POPYOI	2.403	106.2	N1	AZEVAC	2.461	97.6	O2

Table A2.1. Systems with FEC = 8 and 2nd period bridging atoms. (continuation)

refcode	Li-Li (Å)	X-Li-X (°)	X	refcode	Li-Li (Å)	X-Li-X (°)	X
GIZBEY	2.461	104.4	N1	VITCUY	2.526	104.3	N1
DUKRIK	2.462	105.5	N1	XASXUK	2.527	97.1	O1
VISTUO	2.464	103.7	N1	CEDLAY	2.528	102.2	N1
XEKTOX	2.464	96.3	O1	NUWBEM	2.529	104.2	N1
ROTWOP	2.466	97.5	O1	ZEWMOG	2.530	94.6	O1
IJAXAT	2.467	104.1	N1	ZEWMOG	2.532	95.1	O3
XASZIA	2.468	98.2	O1	REMHOG	2.540	104.1	C9
WAVHEG	2.468	105.1	N2	VITDIN	2.542	104.0	N1B
NOFCIW	2.470	96.6	O1	JECQEQ	2.543	104.2	N1
XENYEU	2.472	105.4	N1	XEKTUD	2.543	95.0	O1
DUKRIK	2.474	105.1	N4	RURLAR	2.545	111.1	C1
QOKCIC	2.475	106.0	N1	XASYOF	2.547	95.5	O1
IJAXAT01	2.475	103.9	N1	GOHHAO	2.548	98.2	O1
RUMRAT	2.475	103.0	N1	VUVQAF	2.549	102.7	N3
RAJREA	2.476	96.5	O1	VUVQAF	2.549	102.8	N1
FERVON	2.477	95.8	O1	VUVQAF	2.551	102.7	N5
COLFEP	2.477	104.3	N1	XASYUL	2.553	95.6	O1
APOQON	2.478	105.3	N1A	KOCFEN	2.553	102.7	N5
VISTUO	2.483	103.2	N3	VUVQAF	2.555	102.4	N7
REFQUP	2.484	102.3	N1	VITDOT	2.555	102.6	N1
XEWFUA	2.484	105.5	N1	VITDEJ	2.555	103.3	N2
TOKMIP	2.484	104.1	N1	VITDEJ	2.557	102.4	N1
OTOKAL	2.485	95.8	O1	CIGXUL	2.565	106.7	C1
JOVTUJ	2.489	97.9	O1	VITDAF	2.569	103.4	N1
DETRAV	2.490	97.3	O1	HAJHEF	2.571	110.6	C18
VOTYEI	2.491	104.8	N1	ZIYZOW	2.573	103.6	N1
BUXNOX	2.492	105.6	N1	QUPJUI	2.574	107.4	C13
NITLEH	2.494	104.6	N1	GAYYIO	2.576	94.1	O1
GIDQAL	2.494	103.4	N4	MIZTEU	2.577	109.8	C16
TOPQUK	2.502	104.6	N1	JUJXER	2.581	103.5	C1
RAJRIE	2.502	96.3	O1	QUFXEU	2.585	97.1	O2
BUXNOX01	2.504	104.9	N1	KAMXUS	2.592	96.4	O1
ZEGNUU	2.505	102.8	N4	HAJHEF	2.595	109.2	C1
ZEGNUU10	2.505	102.8	N4	VAFHIT	2.596	102.4	N1
LUXXIN	2.515	104.6	N1	JAJMAI	2.596	93.0	O1
SILYUH	2.515	99.9	O1	PIDHUF	2.600	97.2	O1
FOXZAV	2.516	95.9	O2	GOHHAO	2.600	96.5	O3
KOCCEK	2.517	102.9	N1	VISTAU	2.602	101.6	N1
XEKVEP	2.524	95.5	O1	LACREO	2.604	92.7	O1
DETPUN	2.524	95.0	O1	JIXXET	2.608	101.7	N1

Table A2.1. Systems with FEC = 8 and 2nd period bridging atoms. (continuation)

refcode	Li-Li (Å)	X-Li-X (°)	X	refcode	Li-Li (Å)	X-Li-X (°)	X
ZUHVIJ	2.608	109.3	C14	EFIMOX	2.736	91.3	O5B
ROLSOC	2.609	92.0	O1	KUFSAF	2.739	89.1	O1
SIMZIX	2.610	99.8	N3	ZEHMEE	2.749	94.0	O1
QUFXEU	2.611	95.4	O1	UNODAD	2.750	90.7	O1
KIMHOF	2.614	94.2	O1	ZZZKDE01	2.757	89.4	O2
SIMZIX	2.616	99.7	N1	IHEYAV	2.758	95.7	N3
KEGHUZ	2.616	94.1	O1	QEXNEM	2.763	90.6	O1
XASYEV	2.620	92.6	O1	IHEYAV	2.768	96.3	N1
GAQPOE	2.628	93.2	O9	SUQCAI	2.772	95.4	N1
FAHBEV01	2.628	98.1	N1	KUPFUW	2.773	93.1	O2
RACGUX	2.628	94.4	O1	COBHAC	2.774	90.2	O2
CIPJOA	2.630	97.7	O1	OBILOC	2.782	88.7	O1
BUKYAJ	2.639	92.1	O1	IHEYEZ	2.782	95.9	N1
QIPWOD	2.642	93.8	O2	KUFSEJ	2.785	89.3	O1
XIXMOG	2.643	100.7	N2	AKACAQ	2.793	92.4	O1
VITDUZ	2.644	100.7	N1	TUVSEI	2.795	88.3	O1
GAHFUR	2.644	101.2	N1	JOGWUZ	2.798	91.3	O1
FAHBEV	2.644	98.2	N1	OHEZOR	2.810	98.4	N1
HALCII	2.646	100.8	N1	FUHCIW	2.820	88.4	O1
ALUGAQ	2.647	94.5	O2	JORRUD	2.822	90.1	O1
FIGHEI	2.649	90.4	O1	SEWMAI	2.828	98.4	N1
FOGTAW	2.654	100.8	N1	NIKVUA	2.831	93.2	O4
YEDDOB	2.655	98.9	N1	SIYXAZ	2.832	89.4	O1
UQUGEU	2.658	94.5	O1	CELGUV	2.836	91.6	O1
YATYAU	2.659	94.4	O1	GEFDEA	2.838	90.9	O1
FOGTAW	2.660	101.2	N2	KETMOL	2.840	87.1	O1
SUQCOW	2.661	97.7	N1	CUSWES01	2.842	89.7	O7
AYUGUW	2.674	101.1	N1	HOCGIQ	2.847	92.2	O4
VITFAH	2.675	100.8	N1	REHBUC	2.861	88.7	O3
JAKNAK	2.678	94.3	O1	JESRIJ	2.875	89.8	O7
ALUGEU	2.679	93.5	O1	ZITBIN	2.879	96.5	N1
CECZOA	2.680	90.3	O2	QOPJEK	2.880	94.1	N1
GAQPOE	2.685	91.9	O4	HOXZIF	2.884	89.6	O8
FATPEV	2.690	101.4	C1B	REHBUC	2.906	85.8	O5
BUKXUC	2.698	90.6	O1	JAPKIX	2.941	84.9	O5
HIMHAM	2.702	97.5	N1	FUQLIO	2.960	87.5	O7
TOQFIP	2.715	91.5	O5	AJUKOG	3.119	84.1	O1
XIXMOG	2.720	99.5	N1	TASGIG	3.313	80.5	O1
XUNSUW	2.725	88.5	O1	TASGIG01	3.319	79.9	O1
PEJVOP	2.730	95.6	N1				

Table A2.2. Systems with FEC = 8 and 3rd or higher period bridging atoms.

refcode	Li-Li (Å)	X-Li-X (°)	refcode	Li-Li (Å)	X-Li-X (°)	refcode	Li-Li (Å)	X-Li-X (°)
CESFIP	2.759	113.6	IXEPUW01	3.042	106.2	MUDFEY	3.330	103.3
WAXZEA	2.818	104.7	CINLET	3.045	103.8	BEMDON	3.363	99.4
SETNAG	2.820	107.9	TAMQUU	3.050	103.9	FOFGAI	3.364	100.0
PITCAW	2.831	104.3	XOLGAH	3.060	95.2	VETJUC	3.403	104.6
NOZBEJ	2.837	106.0	YULHUJ	3.062	98.3	DIZSUB	3.410	102.5
PAKDIO	2.862	104.4	JEPSAY	3.062	104.1	WECNOI	3.417	103.8
YOXPEH	2.870	103.4	HIPSAD	3.069	104.9	JOXKAI	3.422	104.9
MEWQEK	2.875	113.3	ITATIG	3.073	100.7	LAFPEN	3.425	97.1
UFEGIX	2.879	103.9	HEQYEK	3.075	105.0	UGABOU	3.429	96.2
WAWDIJ	2.893	103.4	GIPZAI	3.083	101.9	MORGIL	3.448	103.3
VIJMAC	2.896	102.9	CILYED	3.103	102.8	ZIWCEP	3.472	93.3
IBOROJ	2.904	103.8	LAYDUN	3.104	102.7	RUYZAM	3.474	103.5
WAXFUZ	2.914	103.1	VUFBAZ	3.105	104.8	ANUGAT	3.487	88.5
COMSOM	2.914	107.8	FORBOD	3.107	103.6	NETVEN	3.512	98.2
SILVOZ	2.925	103.1	YILZUO	3.134	104.8	ANUGAT	3.519	87.1
MOZZAE	2.927	104.1	SAWSUE01	3.138	102.4	MAVTIN	3.523	94.8
WAXFUZ	2.927	102.9	SEHHOC	3.142	104.3	XORSAY	3.545	94.7
VIJMAC01	2.930	102.6	PERXUF	3.152	109.8	VAFWEE	3.550	94.6
QINTIQ	2.933	102.2	TUQQUS	3.157	96.9	GAJZAS	3.586	100.1
HAQXOM	2.934	101.3	SAWSUE	3.171	101.8	VAGNEY	3.602	94.6
TIZCEK	2.936	107.0	REMHEW	3.178	101.5	GEDDUO	3.610	91.0
DIGZIF	2.937	107.8	KIMHUL	3.183	99.4	CECYAL	3.610	97.8
MILCOC	2.952	102.0	TEZZAZ	3.197	99.7	GEDDUO	3.611	92.9
SAJVEE01	2.973	106.1	DECXEO01	3.215	101.2	YIJLUY	3.617	93.6
LUPBEF	2.985	101.5	HEBVAL	3.227	103.0	VAFWEE	3.630	92.1
QIWFUA	2.994	107.0	HEQYAG	3.231	100.8	GEDDUO	3.658	91.2
VEVQIX	2.995	100.7	GAJYUL	3.242	101.6	SATMAD	3.683	99.4
LUPBAB	2.996	101.0	FORBOD	3.246	98.7	GEDDUO	3.705	89.5
QIMCIA	3.002	100.6	ZOKVIG	3.246	95.1	CEMYAU	3.803	91.5
TAPKEB	3.002	105.1	HINLEW	3.253	104.1	JEPSEC	3.852	94.6
GAJYOF	3.004	101.8	SAJVAA	3.286	106.3	DUWZAW	3.889	89.3
DEMPAN	3.019	100.4	HINLEW	3.294	102.9	KADJAA	3.995	93.8
YODREP	3.021	112.3	DUHCAK	3.299	100.6	CEMYAU	4.139	87.7
LUPBAB	3.035	100.6	RABSAP	3.305	98.4			

Table A2.3. Systems with FEC = 4 and 2nd period bridging atoms.

refcode	Li-Li (Å)	X-Li-X (°)	X	refcode	Li-Li (Å)	X-Li-X (°)	X
VAJZAJ	2.127	121.0	C8	PEXZUQ	2.441	108.2	C1
MOBREA	2.225	117.2	C1	EDOWEA	2.444	113.3	C13
LEFSIY	2.265	116.8	C1	CUSMOT	2.461	112.6	C17
LEFSIY	2.310	116.5	C25	DAHTUC	2.463	113.3	C1
KOPCOH	2.345	115.0	C38	CEPLEO	2.463	109.0	C2
KIRPEG	2.353	118.4	C1	ENAWIZ01	2.466	112.7	C1
LOJGUP	2.353	113.0	C1A	QIBQUP	2.479	112.2	C1
QIMRAH	2.371	115.0	C11	ENAWIZ	2.486	113.1	C16
EMUWIS	2.377	112.8	C1	ULOWEY	2.489	114.8	C8
KOPCOH	2.377	114.5	C20	XIJLOS	2.489	108.9	C11
NOXLIV	2.390	112.9	C1	GAFCAR	2.490	113.7	C1B
CUSMOT	2.399	114.4	C1	XIJLOS	2.513	109.2	C37
XIJLIM	2.412	113.4	C1	COHPIZ	2.515	106.3	C1
EMUWIS	2.415	112.6	C26	KOBCEL	2.541	105.6	C5
IFOGIU	2.415	108.2	C1	KAGSES	2.567	112.4	C1
GABHIA	2.421	114.1	C1	NAGDUV	2.570	104.5	C2
KOPCOH	2.422	112.8	C56	HIGQUJ	2.572	109.4	C1B
JIDQOF	2.427	113.7	C7	KAGSES	2.573	111.8	C45
QIBRAW	2.427	108.1	C1	XOXFAT	2.575	109.4	C3
CEMDEG	2.429	113.7	C1	JIDQIZ	2.588	109.5	C1
ESOXIU	2.429	113.8	C4B	KAGSUI	2.635	110.7	C8
KOPCOH	2.432	113.0	C2	SINFOM	2.644	108.1	C1
XOLYON	2.436	113.6	C7	KECTIW	2.763	106.1	C1
GUPLIO	2.440	112.9	C1				

Table A2.4. Systems with FEC = 4 and 3rd or higher period bridging atoms.

refcode	Li-Li (Å)	X-Li-X (°)	refcode	Li-Li (Å)	X-Li-X (°)
NICWOL	2.397	126.2	LUGFIC	2.959	112.3
REPKUS	2.644	121.9	LUGFOI	3.013	111.1
IYALID	2.688	128.0	CAPGEG	3.030	112.8
DACXIP	2.696	117.6	REPLAZ	3.034	111.8
DACXEL	2.735	119.0			

Table A2.5. Systems with FEC = 6 and 2nd or higher period bridging atoms.

refcode	Li-Li (Å)	X-Li-X (°)	X-X	X	refcode	Li-Li (Å)	X-Li-X (°)	X-X	X
JAMSEV	3.900	44.5	1.597	C	SULKIT	4.372	27.2	1.058	N
JAMSEV01	3.827	45.1	1.589	C	YARDUT	4.347	55.2	2.272	P
NIHDOX	3.940	44.1	1.597	C	ULETIO	5.217	50.5	2.457	Ge

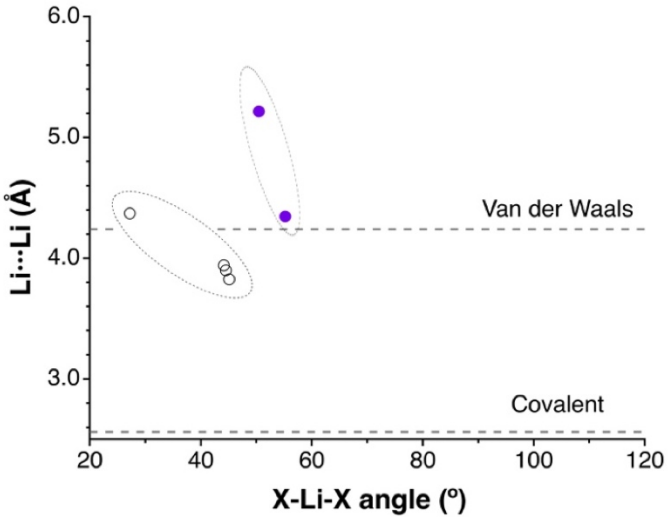

Figure A2.1. Scatterplot of Li···Li distances and X−Li−X bond angles in experimental structures of [{(L_2)Li}$_2$(μ−X)$_2$] rings with FEC = 6, to complement Figure 2.8. The data are grouped according to the size of the bridging atom X (empty symbols for elements of the second period, filled symbols for heavier elements).

Annex 2.2. Effect of intramolecular steric and secondary noncovalent interactions.

Table A2.6. Calculated values for the relative energy (kcal/mol) and through-ring Li···Li distance at fixed X−Li−X bond angles (X = C or N) in [{(en)Li}$_2$(μ−CH_3)$_2$] (compound **A**; represented in Figure 2.9), [{(en)Li}$_2$(μ−NH_2)$_2$] (compound **Y**), and [{(tmen)Li}$_2$(μ−NPh_2)$_2$] (compound **Z**).

Compound **A**			Compound **Y**			Compound **Z**		
$\alpha_{C\text{-}Li\text{-}C}$ (°)	**Energy**	**Li-Li (Å)**	$\alpha_{N\text{-}Li\text{-}N}$ (°)	**Energy**	**Li-Li (Å)**	$\alpha_{N\text{-}Li\text{-}N}$ (°)	**Energy**	**Li-Li (Å)**
80.0			80.0	17.24	3.381	80.0	10.86	3.148
85.0			85.0	13.06	3.206	85.0	5.99	2.991
90.0	16.38	3.225	90.0	7.00	3.038	90.0	2.64	2.853
95.0	14.43	3.005	95.0	3.68	2.876	95.0	0.60	2.718
100.0	11.44	2.794	100.0	1.24	2.730	99.6	0.00	2.579
105.0	7.11	2.628	105.0	0.08	2.717	100.0	0.03	2.441
110.0	2.48	2.496	106.6	0.00	2.559	105.0	0.91	2.397
115.0	0.45	2.348	110.0	0.35	2.404	110.0	3.34	2.305
117.4	0.00	2.274	115.0	2.23	2.253	115.0	7.54	2.169
120.0	0.41	2.201	120.0	5.96	2.104	120.0	13.82	2.034
125.0	2.61	2.060	125.0	11.84	1.956	125.0	22.62	1.900
130.0	7.61	1.921	130.0	20.23	1.808	130.0	34.39	1.770

Figure A2.2. Scan of the energy dependence of (**a**) [{(en)Li}$_2$(μ−NH$_2$)$_2$] (compound **Y**) and (**b**) [{(tmen)Li}$_2$(μ−NPh$_2$)$_2$] (compound **Z**) on the N−Li−N bond angle. The energy minima correspond to the filled circle.

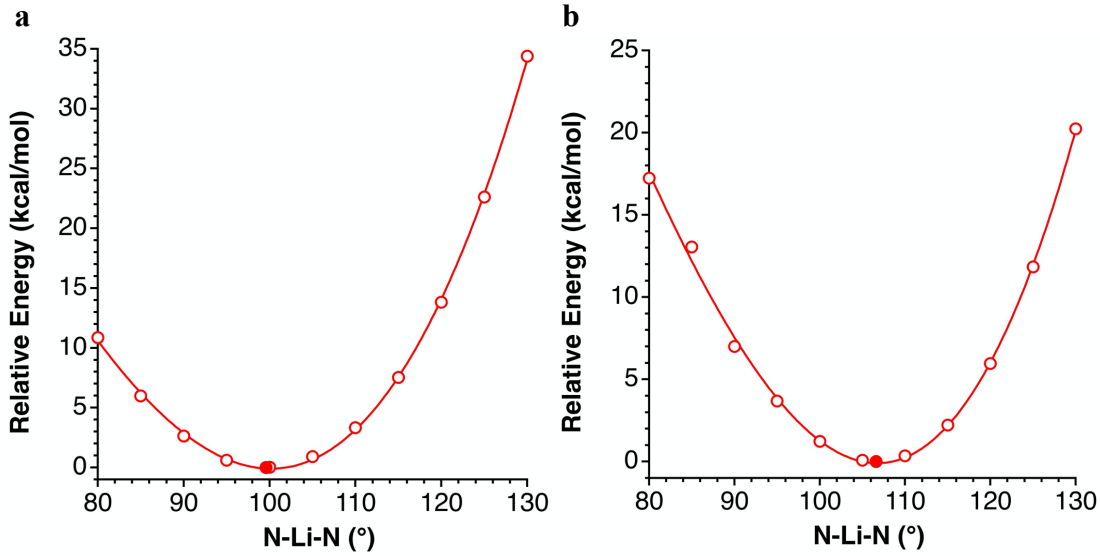

Annex 2.3. Analysis of the electron density.

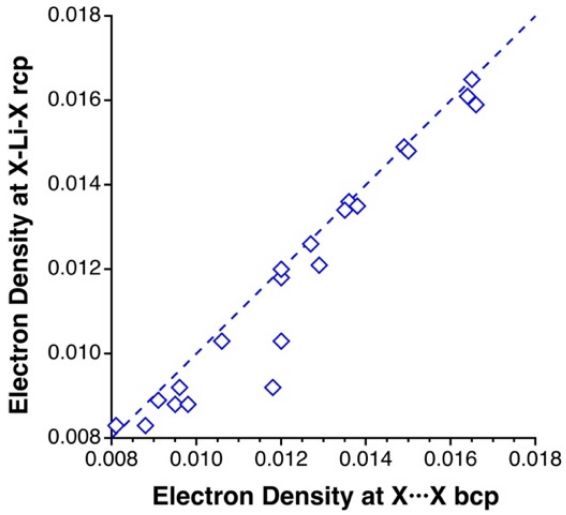

Figure A2.3. Comparison of the electron density at the X···X bond critical point (bcp) and at the X−Li−X ring critical point (rcp) for compounds with FEC = 4 or 8 (Table 2.1). The dashed line corresponds to the ideal case in which ρ(rcp) = ρ(bcp). The outliers are compounds **AA** and **AE**.

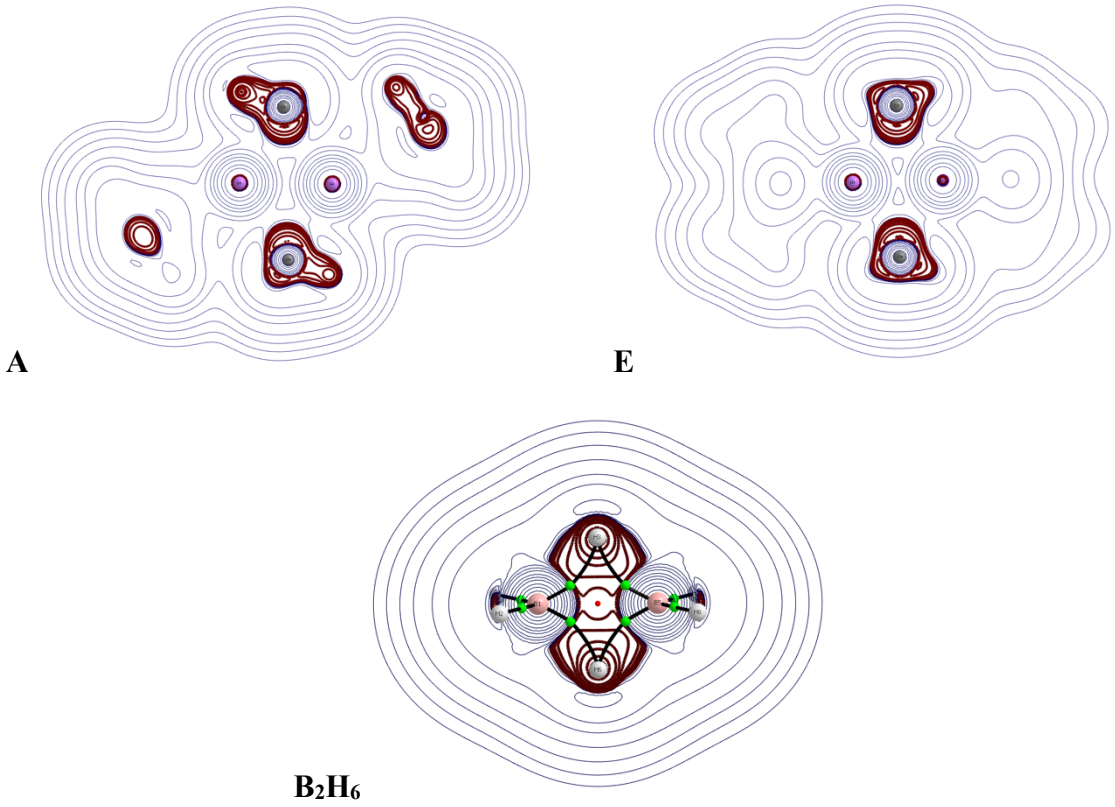

Figure A2.4. Laplacian of the electron density of [{(en)Li}$_2$(μ–CH_3)$_2$] (compound **A**), [{(Me_2O)Li}$_2$(μ–CH_3)$_2$] (compound **E**), and B_2H_6, with FEC = 4. Only the atoms of the Li_2X_2 skeleton of **A** and **E** are shown for clarity. The blue lines indicate charge depletion (positive values) and the red lines charge concentration (negative values).

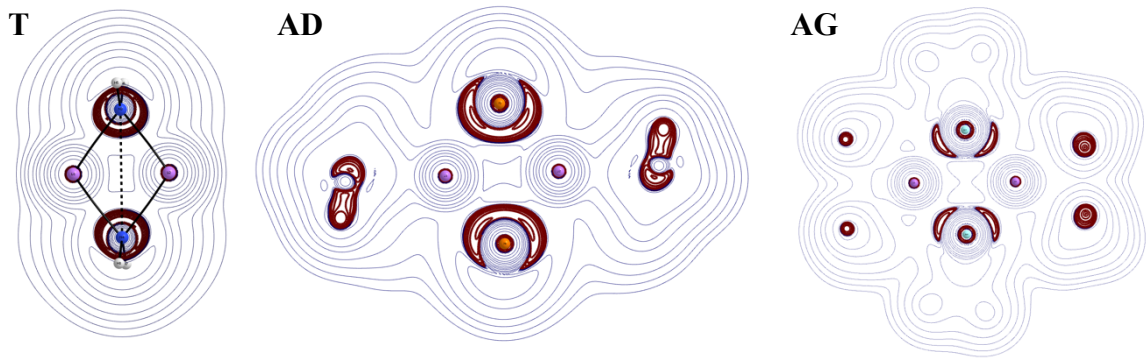

Figure A2.5. Laplacian of the electron density of [Li_2(μ–NH_2)$_2$] (compound **T**), [{(tmen)Li}$_2$(μ–PH_2)$_2$] (compound **AD**), and [{(Et_2O)$_2$Li}$_2$(μ–$AsPh_2$)$_2$] (compound **AG**), with FEC = 8. Only the atoms of the Li_2X_2 skeletons are shown for clarity. The blue lines indicate charge depletion (positive values) and the red lines charge concentration (negative values).

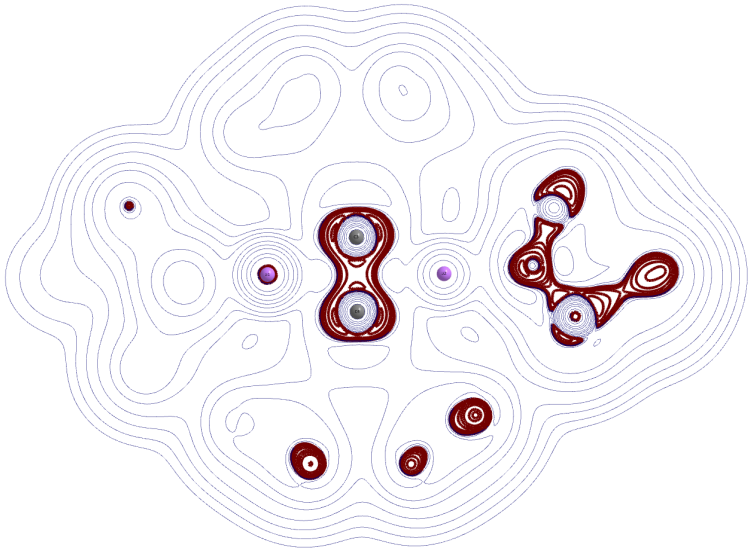

Figure A2.6. Laplacian of the electron density of [{(thf)Li}$_2$(μ–C(SiMe$_3$)$_2$)$_2$] (compound **N**), with FEC = 6. Only the atoms of the Li_2C_2 skeleton are shown for clarity. The blue lines indicate charge depletion (positive values) and the red lines charge concentration (negative values).

2.10 References

1. Greenwood, N. N. *Chemistry of the Elements*. Pergamon Press: Oxford, 1986.
2. Weller, M.; Overton, T.; Rourke, J.; Armstrong, F. *Inorganic Chemistry*. Oxford University Press: Oxford, 2014.
3. Israel, S.; Saravanan, R.; Srinivasan, N.; Rajaram, R. K. High resolution electron density mapping for LiF and NaF by maximum entropy method (MEM). *J. Phys. Chem. Solids* **2003**, *64*, 43-49.
4. Shaik, S.; Danovich, D.; Wu, W.; Hiberty, P. C. Charge-shift bonding and its manifestations in chemistry. *Nature Chem.* **2009**, *1*, 443-449.
5. Huber, K. P.; Herzberg, G. *Molecular Spectra and Molecular Structure. IV. Constants of Diatomic Molecules*. Van Nostrand Reinhold: New York, 1979.
6. Luo, Y. R. *Comprehensive Handbook of Chemical Bond Energies*. CRC Press: Boca Raton, FL, 2007.
7. Groom, C. R.; Bruno, I. J.; Lightfoot, M. P.; Ward, S. C. The Cambridge Structural Database. *Acta Cryst.* **2016**, *B72*, 171-179.
8. Cordero, B.; Gómez, V.; Platero-Prats, A. E.; Revés, M.; Echeverría, J.; Cremades, E.; Barragán, F.; Alvarez, S. Covalent radii revisited. *Dalton Trans.* **2008**, 2832-2838.

9. Alvarez, S. A Cartography of the Van der Waals Territory. *Dalton Trans.* **2013**, *42*, 8617-8636.

10. Ogle, S. A.; Huckabee, B. K.; Johnson, H. C.; Sims, P. F.; Winslow, S. D.; Pinkerton, A. A. Isolation, characterization, and crystal structure of $[MeLi{\cdot}THF]_4$. *Organometallics* **1993**, *12*, 1960-1963.

11. Kottke, T.; Stalke, D. Structures of Classical Reagents in Chemical Synthesis: $(nBuLi)_6$, $(tBuLi)_4$, and the Metastable $(tBuLi \cdot Et_2O)$. *Angew. Chem. Int. Ed.* **1993**, *32*, 580-582.

12. Kottke, T.; Lagow, R. J.; Hoffmann, D.; Thomas, R. D. Isolation and Structure Analysis of Neohexyllithium Generated by Ether Cleavage: Primary and Secondary Coordination in Alkyllithium Aggregates. *Organometallics* **1997**, *16*, 789-792.

13. Clegg, W.; Snaith, R.; Shearer, H. M. M.; Wade, K.; Whitehead, G. Azomethine derivatives. Part 20. Crystal and molecular structures of the lithioketimine $[\{Li(N{=}CBu^t_2)\}_6]$ and lithioguanidine $[\{Li[N{=}C(NMe_2)_2]\}_6]$; electron-deficient bridging of Li_3 triangles by methyleneamino-nitrogen atoms. *J. Chem. Soc., Dalton Trans.* **1983**, 1309-1317.

14. Maercker, A.; Bsata, M.; Buchmeier, W.; Engelen, B. Darstellung und Kristallstruktur von 3-(Lithiomethyl)-1,1,2,2-tetramethylcyclopropan, einer stabilen Cyclopropylmethyllithium-Verbindung. *Chem. Ber.* **1984**, *117*, 2547-2554.

15. Barr, D.; Clegg, W.; Mulvey, R. E.; Snaith, R.; Wade, K. Bonding implications of interatomic distances and ligand orientations in the iminolithium hexamers $[LiN[{=}C(Ph)But]_6$ and $[LiN[{=}C(Ph)NMe_2]_6$: a stacked-ring approach to these and related oligomeric organolithium systems. *J. Chem. Soc., Chem. Comm.* **1986**, 295-297.

16. Siemeling, U.; Redecker, T.; Neumann, B.; Stammler, H.-G. Crystal Structure of Isopropyllithium. *J. Am. Chem. Soc.* **1994**, *116*, 5507-5508.

17. Otero, A.; Fernández-Baeza, J.; Antiñolo, A.; Tejada, J.; Lara-Sánchez, A.; Sánchez-Barba, L. F.; López-Solera, I.; Rodríguez, A. M. Lithium, Titanium, and Zirconium Complexes with Novel Amidinate Scorpionate Ligands. *Inorg. Chem.* **2007**, *46*, 1760-1770.

18. Koch, T.; Blaurock, S.; Somoza-Jr, F.; Hey-Hawkins, E. P−H-Functionalized Phosphanyl Alcohols: $RHPCH_2CHMeOH$ and 2-PHR-1-OH-cyclo-C_6H_{10} (R = Ph,

2,4,6-$Me_3C_6H_2$, 2,4,6-i $Pr_3C_6H_2$) and Molecular Structures of (CR ,CR ,PR /CS ,CS ,PS)-2-PH(2,4,6-i $Pr_3C_6H_2$)-1-OH-cyclo-C_6H_{10} and its Dilithio Salt [Li_2(THF)0.5{(CR ,CR /CS ,CS)-2-P(2,4,6-i $Pr_3C_6H_2$)-1-O-cyclo-C_6H_{10}}]$_4$. *Eur. J. Inorg. Chem.* **2000**, 2167-2172.

19. Stasch, A. Well-Defined, Nanometer-Sized LiH Cluster Compounds Stabilized by Pyrazolate Ligands. *Angew. Chem. Int. Ed.* **2014**, *53*, 1338-1341.
20. Covington, E. J.; Montgomery, D. J. Lattice constants of separated lithium isotopes. *J. Chem. Phys.* **1957**, *27*, 1030-1032.
21. Down, M. G.; Haley, M. J.; Hubberstey, P.; Pulham, R. J.; Thunder, A. E. Solutions of lithium salts in liquid lithium: preparation and X-ray crystal structure of the dilithium salt of carbodi-imide (cyanamide). *J. Chem. Soc., Dalton Trans.* **1978**, 1407-1411.
22. Alvarez, S.; Alemany, P.; Aullón, G.; Palacios, A. A.; Novoa, J. J. Heterodox Bonding Effects Between Transition Metal Atoms. In *The Synergy Between Dynamics and Reactivity at Clusters and Surfaces*, Farrugia, L. J., Ed. Kluer Academic: Dordrecht, 1995; pp 241-255.
23. Alvarez, S.; Aullón, G. Ligand Orientation Effects on Metal-Metal Bonds. In *Metal Clusters in Chemistry*, Braunstein, P.; Oro, L. A.; Raithby, P., Eds. Wiley-VCH: New York, 1999; Vol. 1, pp 308-322.
24. Alvarez, S.; Palacios, A. A.; Aullón, G. Ligand Orientation Effects on Metal-Metal, Metal-Ligand and Ligand-Ligand Interactions. *Coord. Chem. Rev.* **1999**, *185/186*, 431-450.
25. Aullón, G.; Alemany, P.; Alvarez, S. Through-ring Bonding in Edge-Sharing Dimers of Square Planar Complexes. *J. Organomet. Chem.* **1994**, *478*, 75-82.
26. Aullón, G.; Alvarez, S. Molecular Structures of Edge-sharing Square-planar Dinuclear Complexes with Unsaturated Bridges. *Inorg. Chem.* **2001**, *40*, 4937-4946.
27. Aullón, G.; Alvarez, S. Molecular Structure and Isomerization in Square-planar Edge-Sharing Dinuclear Complexes with Alkynyl Bridges. *Organometallics* **2002**, *21*, 2627-2634.
28. Aullón, G.; Alvarez, S. Formation of Sulfur-Sulfur Bonds in Copper Complexes. *Eur. J. Inorg. Chem.* **2004**, 4430-4489.

29. Aullón, G.; Hamidi, M.; Lledós, A.; Alvarez, S. Chalcogen-chalcogen Bonds in Edge-sharing Square-planar d^8 Complexes. Are They Possible? *Inorg. Chem.* **2004**, *43*, 3702-3714.

30. Aullón, G.; Ujaque, G.; Lledós, A.; Alvarez, S. Edge-sharing Binuclear d^8 Complexes with XR Bridges: Theoretical and Structural Database Study of their Molecular Conformation. *Chem. Eur. J.* **1999**, *5*, 1391-1410.

31. Aullón, G.; Ujaque, G.; Lledós, A.; Alvarez, S. Structural Correlations and Conformational Preference in Edge-sharing Binuclear d^8 Complexes with XR_2 Bridges. *Inorg. Chem.* **2000**, *39*, 906-916.

32. Palacios, A. A.; Aullón, G.; Alemany, P.; Alvarez, S. Through-ring Bonding in Edge-Sharing Dimers of Octahedral Complexes. *Inorg. Chem.* **2000**, *39*, 3166-3175.

33. Simmons, R. S.; Galat, K. J.; Bradshaw, J. D.; Youngs, W. J.; Tessier, C.; Aullón, G.; Alvarez, S. Reaction Chemistry, NMR Spectroscopy, and X-ray Crystallography of $[Fe_2(\mu\text{-}SiMe_2)_2(CO)_8]$ and $[Fe_2(\mu\text{-}SiMeCl)_2(CO)_8]$. Electronic Structure and Bonding in Fe_2E_2 Rings of $[Fe_2(\mu\text{-}ER_2)_2(CO)_8]$ Binuclear Complexes (E = C, Si, Ge, Sn, Pb). *J. Organomet. Chem.* **2001**, *628*, 241-254.

34. Brown, E. C.; Aboelella, N. W.; Reynolds, A. M.; Aullón, G.; Alvarez, S.; Tolman, W. B. A New Class of (μ-η^2:η^2-Disulfido)dicopper Complexes: Synthesis, Characterization, and Disulfide Exchange. *Inorg. Chem.* **2004**, *43*, 3335-3337.

35. Carrasco, R.; Aullón, G.; Alvarez, S. X-X Through-Cage Bonding in Cu, Ni and Cr Complexes with M_3X_2 Cores (X = S, As). *Chem. Eur. J.* **2009**, *15*, 536-546.

36. Albright, T. A.; Burdett, J. K.; Whanbo, M. H. *Orbital Interactions in Chemistry*. John Wiley & Sons: Hoboken, NJ, 2013.

37. Strohmann, C.; Gessner, V. H. Crystal Structures of the Chiral Diamine (R,R)-TMCDA with the Commonly Used Alkyllithium Bases Methyllithium, iso-Propyllithium, and sec-Butyllithium. *J. Am. Chem. Soc.* **2007**, *129*, 8952-8953.

38. Eckert, P. K.; Schnura, B.; Strohman, C. Unexepcted structural motifs in diamine coordination compounds with allyllithium. *Chem. Commun.* **2014**, *50*, 2532-2534.

39. Thoennes, D.; Weiss, E. Über Metallalkyl- und -aryl-Verbindungen, XX: Darstrellung und Kristallstruktur des dimeren Phenyllithium · N, N, N', N'-Tetramethylethylendiamins, Bis[μ-phenyl-(N, N, N', N'-tetramethylethylendiamin)lithium]. *Chem. Ber.* **1978**, *111*, 3157-3161.

40. Marsh, R. E.; Clemente, D. A. A survey of crystal structures published in the Journal of the American Chemical Society. *Inorg. Chim. Acta*. **2007**, *360*, 4017-4024.

41. Stein, D.; Dransfeld, A.; Flock, M.; Ruegger, H.; Grutzmacher, H. Lithium Oligophosphanediides in the Li/$PhPCl_2$ System. *Eur. J. Inorg. Chem.* **2006**, 4157-4167.

42. Inoue, S.; Ichinohe, M.; Sekiguchi, A. Isolable Alkali-Metal_Substituted Silyl Radicals ($(^tBu_2MeSi)_2SiM$ (M = Li, Na, K): Electronically and Sterically Accessible Planar Silyl Radicals. *Organometallics* **2008**, *27*, 1358-1360.

43. Westerhausen, M.; Schwarz, W. Tris(trimethylsilyl)silylamin und seine lithiierten und silylierten Derivate — Kristallstruktur des dimeren Lithium-trimethylsilyl-[tris(trimethylsilyl)silyl]amids. *Z. Anorg. Allgem. Chem.* **1993**, *619*, 1053-1063.

44. Fjeldberg, T.; Lappert, M. F.; Thorne, A. J. The molecular structure of dimeric bis(trimethylsilyl)amidolithium, $[LiN(Si(CH_3)_3)_2]_2$, as determined by gas-phase electron diffraction. *J. Mol. Struct.* **1984**, *125*, 265-275.

45. Kennedy, A. R.; Klett, J.; O'Hara, C. T.; Mulvey, R. E.; Robertson, G. M. Structural Elucidation of tmeda-Solvated Alkali Metal Diphenylamide Complexes. *Eur. J. Inorg. Chem.* **2009**, 5029-5035.

46. Ymen, I. Structure of lithium diethyldithiocarbamate trihydrate, $Li[C_5H_{10}NS_2]\cdot 3H_2O$. *Acta Crystallogr., Sect. C. Cryst. Struct. Commun.* **1984**, *40*, 241-243.

47. Srinivasan, B. R.; Shetgaonkar, S. Y.; Dhavskar, K. T.; Sundar, J. K.; Natarajan, S. Synthesis and structural characterization of bis(mu-2-aqua)tetrakis(aqua(dilithium(I) bis(4-nitrobenzoate). *Indian J. Chem., Sect. A* **2012**, *51*, 564-570.

48. Raston, C. L.; Whitaker, C. R.; White, A. H. Lewis-Base Adducts of Main Group 1 Metal Compounds. VI. Novel Hydrogen Bonding and a Novel Binuclear Aquated Lithium Cation in $[(H_2O)_2Li(OH_2)_2Li(OH_2)_2]^{2+}.2Cl^-.6L$ (L = 2,6-Dimethylpyridine). *Austr. J. Chem.* **1988**, *41*, 413-416.

49. Drukenmuller, I. E.; Klapotke, T. M.; Morgenstern, Y.; Rusan, M.; Stiestorfer, J. Metal Salts of Dinitro-, Trinitropyrazole, and Trinitroimidazole. *Z. Anorg. Allgem. Chem.* **2014**, *640*, 2139-2148.

50. Kloskowska, M.; Chojnacki, J.; Wojnowski, W.; Becker, B. The first compound with an unusual type of anion, $[Li(SR)_2]^-$: bis-[μ_2-aqua-d_2)tetra-kis(aqua-

d_2)dilithium(I) bis-[bis-(tri-tert-butoxy-silanethiol-ato-κ^2O,S)lithate(I)] dihydrate-d_2. *Acta Crystallogr., Sect. C. Cryst. Struct. Commun.* **2006**, *62*, m541-m544.

51. Maigrot, N.; Ricard, L.; Charrier, C.; Mathey, F. Tetraphosphafulvalene Dianions: Isoelectronic Species of Tetrathiafulvalene Dications. *Angew. Chem. Int. Ed.* **1992**, *31*, 1031-1032.
52. Mulvey, R. E.; Wade, K.; Armstrong, D. R.; Walker, G. T.; Snaith, R.; Clegg, W.; Reed, D. X-ray crystallographic and solution studies of the pentamethyldiethylenetriamine and tetramethylethylenediamine adducts of lithium diphenylphosphide. *Polyhedron* **1987**, *6*, 987-993.
53. Bartlett, R. A.; Dias, H. V. R.; Hope, H.; Murray, B. D.; Olmstead, M. M.; Power, P. P. Isolation and structural characterization of the solvated lithium salts of the Group VA (15) anions $[EPh_2]^-$ (E = nitrogen, phosphorus, arsenic or antimony) and $[Sb_3Ph_4]^-$. *J. Am. Chem. Soc.* **1986**, *108*, 6921-6926.
54. Asami, S.; Suzuki, K.; Yamashita, M. Two-electron Reduction of Diboryldiphosphene: Formation of Intramolecular Charge-transfer Complex of Dianionic B^-=P-P=B^- Species. *Chem. Lett.* **2017**, *46*, 686-689.
55. Lihung, P.; Phillips, A. D.; Richards, A. F.; Stender, M.; Simons, R. S.; Olmstead, M. M.; Power, P. P. Germanium and Tin Analogues of Alkynes and Their Reaction Products. *J. Am. Chem. Soc.* **2003**, *125*, 11626-11636.
56. Janwei, H.; Drake, R. J.; Stephan, D. W. $[Cp_2Zr(\mu\text{-PPh})]_2[((THF)_3Li)_2(\mu\text{-}N_2)]$: a remarkable salt of a zirconocene phosphinidene dianion and lithium dication containing side-bound dinitrogen. *J. Am. Chem. Soc.* **1993**, *115*, 3792-3793.
57. Sekiguchi, A.; Ichinohe, M.; Takahashi, M.; Kabuto, C.; Sakurai, H. 1,1,2,2-Tetrakis(dimethylsilyl)-1,2-ethanediylithium-bis(diethyl ether): Observation of a SiH–Li Agostic Interaction. *Angew. Chem. Int. Ed.* **1997**, *36*, 1533-1534.
58. Sekiguchi, A.; Ichinohe, M.; Yamaguchi, S. An unexpected reaction of silacyclopropene to form an organidilithiosilane: Isolation and characterization of a 1,1-dilithiosilane derivative. *J. Am. Chem. Soc.* **1999**, *121*, 10231-10232.
59. Bertermann, R.; Braunschweig, H.; Constantinidis, P.; Dellermann, T.; Dewhurst, R. D.; Ewing, W. C.; Fischer, I.; Kramer, T.; Mies, J.; Phukan, A. K.; Vargas, A. Exclusive p Encapsulation of Light Alkali Metal Cations by a Neutral Molecule. *Angew. Chem. Int. Ed.* **2015**, *54*, 13090-13094.

60. Echeverría, J.; Aullón, G.; Danovich, D.; Shaik, S.; Alvarez, S. Dihydrogen Contacts in Alkanes and Polyhedranes are Subtle but not Faint. *Nature Chem.* **2011**, *3*, 323-330.

61. Bader, R. F. W. *Atoms in Molecules. A Quantum Theory*. Clarendon Press: Oxford, 1990.

62. Glaser, R.; Waldron, R. F.; Wiberg, K. B. Origin and Consequences of the Nonnuclear Attractor in the ab Initio Electron Density Functions of Dilithium. *J. Phys. Chem.* **1990**, *92*, 7357-7362.

63. Platts, J. A.; Overgaard, J.; Jones, C.; Iversen, B. B.; Stasch, A. First Experimental Characterization of a Non-nuclear Attractor in a Dimeric Magnesium(I) Compound. *J. Phys. Chem. A* **2011**, *115*, 194-200.

Chapter 3

Effect of the substituents on the nature and strength of lone-pair–carbonyl interactions in acyl halides

3.1 Introduction

Among the abundance of noncovalent interactions, those involving carbonyl groups have attracted increasing interest in recent years. Short contacts between an electron density donor and the electron-deficient region of a carbonyl group (*i.e.* the C atom) have been found and investigated in many families of compounds.[1-12] The nature of such interactions has been the subject of discussion for a long time.[13,14] It seems clear nowadays that lone-pair−carbonyl interactions imply a combination of orbital and electrostatic contributions. The orbital interaction is associated with electron density delocalization from the lone pair into the π^* empty orbital of the carbonyl to establish the so-called n→π^* interaction.[15] On the other hand, the electrostatic interaction is the result of the attraction between a region of the electron-rich species (the lone pair) and another of the electron-deficient species (the carbonyl carbon atom), negatively and positively charged, respectively.[16,17] This electrostatic interaction has been rationalized in terms of π-hole bonding by Politzer and co-workers.[18]

From a topological point of view, it is difficult to assess the contribution of each component, orbital and electrostatic, to the total interaction energy since both the π-hole and the empty π^* orbital are located in the same molecular region: *i.e.*, the carbon atom of the carbonyl group. The intermolecular distance gives an indication to determine the strength of the n→π^* interaction, which depends on the n/π^* orbital overlap. On the other hand, the π-hole bonding is associated with a marked directionality to precisely connect the positive and negative regions.

Here, I present a combined structural and computational study of lone-pair-carbonyl interactions in acyl halides. I wish to investigate how the presence of the halogen atom affects the reactivity of the carbonyl groups towards nucleophiles. Furthermore, different substituents on the CO-X groups have been studied as well as oxygen- and nitrogen-containing lone pairs. Special attention has been paid to possible correlations between geometrical descriptors and molecular properties, such as the value of the electrostatic potential. To further investigate the nature of the interaction, an Energy Decomposition Analysis (EDA)[19] has been performed on dimers at several interaction distances. Moreover, I have tried to link our theoretical results with experimental structures when possible. I have focused on EDA analysis because, to the best of our knowledge, it has been rarely applied to study noncovalent interactions involving

carbonyl compounds. I have performed neither a Natural Bond Orbital (NBO) analysis nor Quantum Theory of Atoms in Molecules (QTAIM) analysis because EDA provides enough information about the nature of the interaction.

3.2 Structural Analysis

I have searched the Cambridge Structural Database (CSD)[20] for short intermolecular contacts between carbonyl groups of acyl halides and lone-pair-containing donor atoms (Scheme 3.1). In my searches, the donor (Y) was set to be any element of groups 15 − 17 whereas X could be any halogen. Only contacts shorter than the sum of the van der Waals radii plus 0.1 Å ($d_{Y\cdots C} < (\sum r_{vdW} + 0.1)$) were taken into account. A total of 111 short Y···C=O contacts were found in 78 different crystal structures for Y = N (7 hits), O (47 hits), F (7 hits), and Cl (17 hits). As for the nature of the halogen atom X, I found 23 contacts for F, 54 for Cl, only one for Br and none for I.

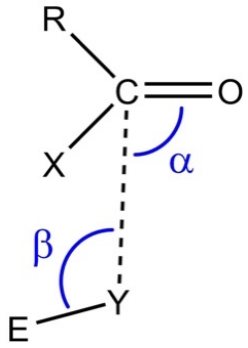

Scheme 3.1. Angles involved in the interaction between a lone-pair-containing group and an acyl halide.

I have then analysed the Y···C=O attack angle (α) associated with the short Y···C contacts. Remarkably, as the angle α approaches 100°, the shortest Y···C distance decreases, as shown in Figure 3.1. This tendency has been seen before in other lone-pair−carbonyl interactions[1-3,15] and is associated with the Bürgi−Dunitz trajectory for a nucleophilic attack.[21,22] It can also be seen in the plot of Figure 3.1 that the shortest contacts are found for Y = O, with no contacts below the vdW corrected distance of -0.2 Å for Y = N, F, and Cl (the vdW corrected distance is defined as the difference between the measured experimental distance and the sum of the van der Waals radii of the atoms involved). The outlier point showing a Cl···C contact at -0.3 Å is actually a Cl···O=C halogen bond with a Cl···O distance shorter than the Cl···C distance (3.009 and 3.281 Å, respectively).

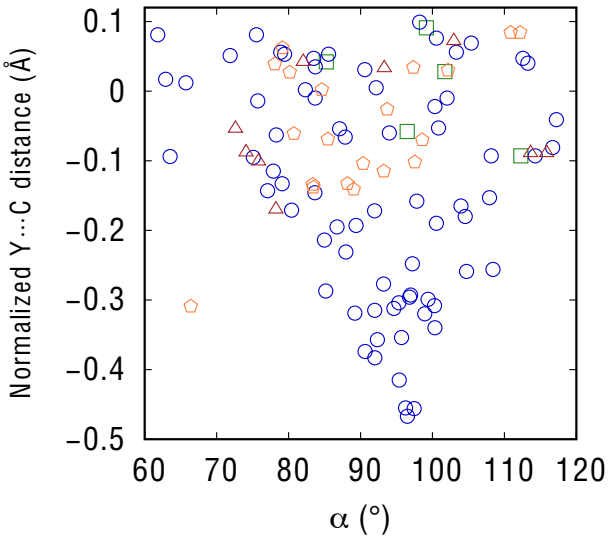

Figure 3.1. Normalized Y···C distance (normalized distance = $d_{Y\cdots C}$ - $\sum r_{vdW}$) as a function of the Y···C=O angle (see Appendix, Tables A3.1 − A3.4). Different donor atoms are represented with different colours: Y = N (green squares), O (blue circles), F (red triangles), and Cl (orange pentagons).

The other angle involved in the interaction moiety (β, Scheme 3.1) also shows some particularities. When the donor atom is a halogen (Y = F and Cl), 78% of the E−Y···C angles are located in the range 90 − 120° (58% in 90 − 100°), presumably to facilitate a hypothetical electrostatic interaction dictated by the electron density distribution of covalently-bonded halogen atoms, in which there are clearly differentiated regions of charge accumulation and depletion. On the other hand, when the donor is an O atom in the form of a carbonyl group, the approach angle C=O···C is more variable with a random distribution of values between 80 and 180°, in good agreement with previous reports on carbonyl−carbonyl interactions.[13]

I show in Figure 3.2 an example of crystal structure in which the molecules of fluoroformic acid anhydride (DALJAC)[23] are held together by carbonyl···carbonyl contacts as the only intermolecular interaction. In such a crystal structure, there are O···C contacts as short as 2.81 Å: i.e., 0.4 Å shorter than the sum of the van der Waals radii. However, the shortest C=O···C=O contact is found at 2.803 Å (α = 96.5°) in the crystal structure of pentafluoropropanoyl fluoride (HALWUP),[24] in which there is also a F···C=O contact at 3.129 Å: i.e., 0.1 Å shorter than the sum of the corresponding van der Waals radii. In the crystal structure of 1,4-dioxane oxalyl fluoride (FAYNOI),[25] in which the donor oxygen is an ether, the O···C contact is found at a very short distance of 2.590 Å (Figure 3.2).

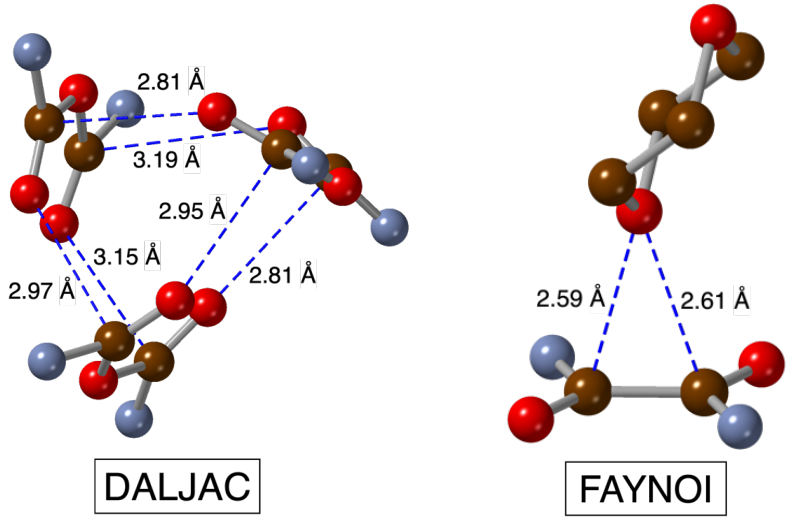

Figure 3.2. Short carbonyl···carbonyl contacts in the crystal structure of fluoroformic acid anhydride (DALJAC)[23] and 1,4-dioxane oxalyl fluoride (FAYNOI).[25] Colour code: grey, C; red, O; purple, F.

3.3 Analysis of the Molecular Electrostatic Potential

The Molecular Electrostatic Potential (MEP) approach was used to analyse a possible electrostatic interaction between acyl halides and lone pairs.[18,26-28] Acyl halides of formula CF_3-COX (X = F, Cl, Br, and I) have been first selected to evaluate the effect of the different halogens on the magnitude of the π-hole associated with the carbonyl carbon atom. The corresponding MEP maps are plotted in Figure 3.3. As can be seen there, the π-hole is more pronounced for X = F, although it is present in all four cases. Values of MEP between 46 and 56 kcal/mol are high enough to expect a marked affinity for electron density donors.

Next, I have modified the group attached to the fluoroformate moiety (I kept F as the reference X because it showed the most marked π-hole) to study their effect on the electron density distribution over the molecules. Several substituents have been studied (R = CH_3, OCH_3, OCF_3, SCN, NH_2, C_6H_5, C_6H_4F, $C_6H_2F_3$, and C_6F_5), all of them realistic since they were found in our structural analysis. The results are presented in Figure 3.4. Two main groups can be distinguished: those in which the region of maximum MEP value ($V_{s,max}$) is located on the carbonyl carbon atom and those in which $V_{s,max}$ is located in a different region of the molecule. In the first group R = OCH_3, OCF_3, SCN, and C_6F_5 are found and in the second R = CH_3, NH_2, C_6H_5, C_6H_4F, and $C_6H_2F_3$. Of course, R = CF_3, as previously seen (Figure 3.3), is the paradigmatic case of the first group.

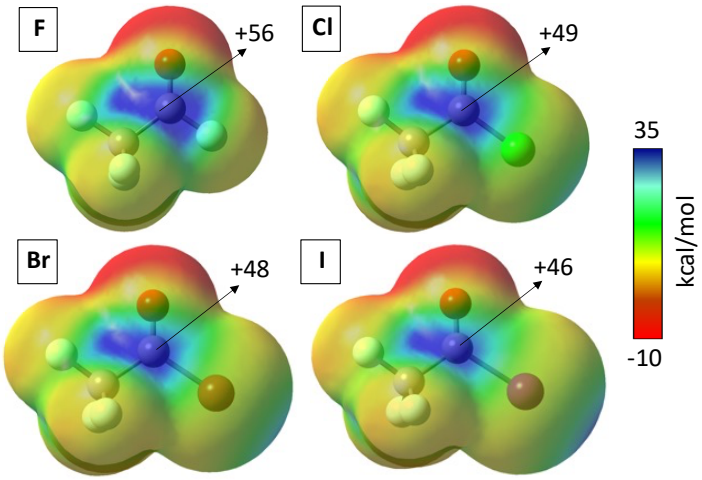

Figure 3.3. MEP maps for trifluoromethyl haloformate derivatives CF_3-COX (X = F, Cl, Br, and I) calculated at the M06-2X/def2-TZVP level and plotted on the electron density isosurface (s = 0.002 Å). Energies are given in kcal/mol. Red and blue colours indicate a more negative and a more positive MEP value, respectively.

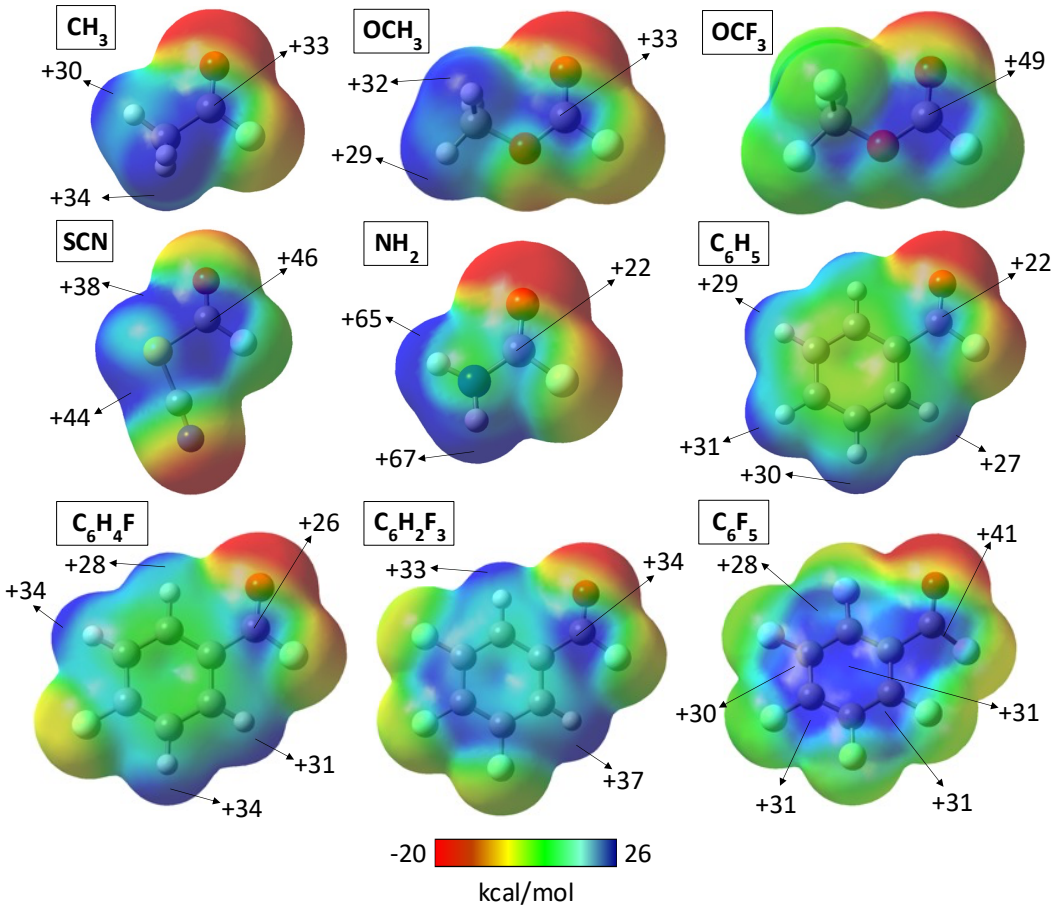

Figure 3.4. MEP maps for fluoroformate derivatives R-COF (R = CH_3, OCH_3, OCF_3, SCN, NH_2, C_6H_5, C_6H_4F, $C_6H_2F_3$, and C_6F_5) calculated at the M06-2X/def2-TZVP level and plotted on the electron density isosurface (s = 0.002 Å). Energies are given in kcal/mol. Red and blue colours indicate a more negative and a more positive MEP value, respectively.

The most positive MEP values are found in R = CF_3, OCF_3, and SCN (56, 49, and 46 kcal/mol, respectively). For R = SCN, the presence of the S atom allows the formation of two clear σ-holes (38 and 44 kcal/mol). As expected, when R is a phenyl ring, the presence of more F atoms reinforces the π-hole on the carbonyl. It is expected, thus, that molecules in the first group can interact with electron donors via the carbonyl carbon whereas the others might find more suitable regions and, thus, establish other types of attractive interactions such as hydrogen bonds.

3.4 Analysis of the Interaction Energies

3.4.1 Effect of X

I have studied, by means of DFT calculations, the effect of the nature of the halogen X on the capability of the attached carbonyl group to act as an electron density acceptor. To that end, a model based on the dimer found in the crystal structure of trifluoromethyl chloroformate (CF_3-COCl; ISADOV)[29] has been used (Figure 3.5).

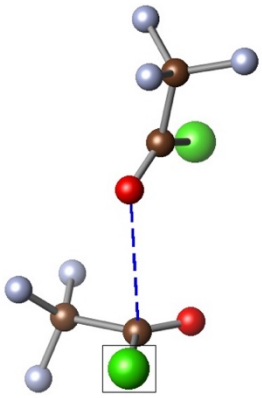

Figure 3.5. Dimer of trifluoromethyl chloroformate (CF_3-COCl; ISADOV)[29] used to analyse the effect of the halide in the acceptor molecule. The framed Cl atom was substituted by F, Br, and I. Colour code: brown, C; red, O; green, Cl; purple, F.

The absence of hydrogen atoms in this structure avoids the formation of H-bonds that could compete with the Y···C=O interaction. The main results are summarized in Table 3.1. Interestingly, the intermolecular O···C distance increases on going from F to I. Such a trend is not followed by the interaction energy, which shows a nice linear correlation with the O···C=O angle α (R^2 = 0.960). Large α angles, closer to the Bürgi-Dunitz trajectory that maximizes the donor-acceptor orbital overlap, are associated with higher interaction energies. It is worth noting that, in all dimers in Table 3.1, there is also a C=O···F-CF_2 contact at a distance shorter than the sum of the van der Waals radii (but

still longer than the main O···C contact). For comparison, I have calculated an interaction energy of -3.39 kcal/mol for the adduct of $(CF_3)_2C=O$ and CF_3-COCl ($d_{O\cdots C}$ = 2.852 Å; $\alpha_{O\cdots C=O}$ = 93.30°).

Table 3.1. Key geometrical parameters and interaction energies for the optimized adducts of trifluoromethyl haloformate (CF_3-COX; X = F, Cl, Br, and I) and CF_3-COCl (ISADOV),[29] calculated at the M06-2X/def2-TZVP level.

X	$d_{O\cdots C}$ (Å)	$\alpha_{O\cdots C=O}$ (°)	ΔE_{INT} (kcal/mol)
F	2.735	95.78	-3.56
Cl	2.801	91.67	-3.13
Br	2.830	90.12	-3.03
I	2.843	90.30	-3.07

3.4.2 Effect of R

The same approach has been applied to analyse the effect of varying the substituent R. I have used the same R groups as in my previous MEP analysis to try to find a relationship between interaction geometries and molecular electron density holes. Remarkably, the cases in which $V_{s,max}$ is on the carbonyl carbon atom (OCH_3, OCF_3, SCN, and C_6F_5) present carbonyl−carbonyl interactions as represented in Figure 3.6. The O···C distances are in the range 2.73−3.14 Å, and the interaction energies are between -2.80 and -5.07 kcal/mol. For R = OCH_3, the stronger interaction is explained by the formation of a reciprocal carbonyl−carbonyl interaction[30] and an additional C=O···H hydrogen bond (2.554 Å). For the other cases (R = CH_3, NH_2, C_6H_5, C_6H_4F, and $C_6H_2F_3$), the interaction is reversed: i.e., the C=O in R-COF acts as the electron density donor while the C=O in CF_3-COCl is the acceptor (Figure 3.6). This can also be explained in terms of MEP distributions by looking at maps in Figure 3.4 since, in such systems, $V_{s,max}$ is no longer located over the carbonyl of R-COF and more favourable H-bonds are established.

The case in which R is an aromatic ring deserves some closer attention. The interaction pattern between Ph-COF and CF_3-COCl can be described by means of three intermolecular distances (Scheme 3.2). While d_1 and d_2 correspond to a reciprocal carbonyl−carbonyl interaction, d_3 is a short contact associated with a σ-hole interaction in which the σ-hole is located on the carbon atom of the CF_3 group. Remarkably, the topology of the supramolecular aggregate is the result of a delicate balance of those three distances. As the number of fluorine atoms in the ring increases, d_1 shortens whereas d_2

and d_3 lengthen. It is worth noting that a nice linear correlation is found between the MEP value at the Ph-COF carbonyl and d_1 ($R^2 = 0.989$). I have not found, however, any clear trend involving the interaction energy and the studied geometrical parameters.

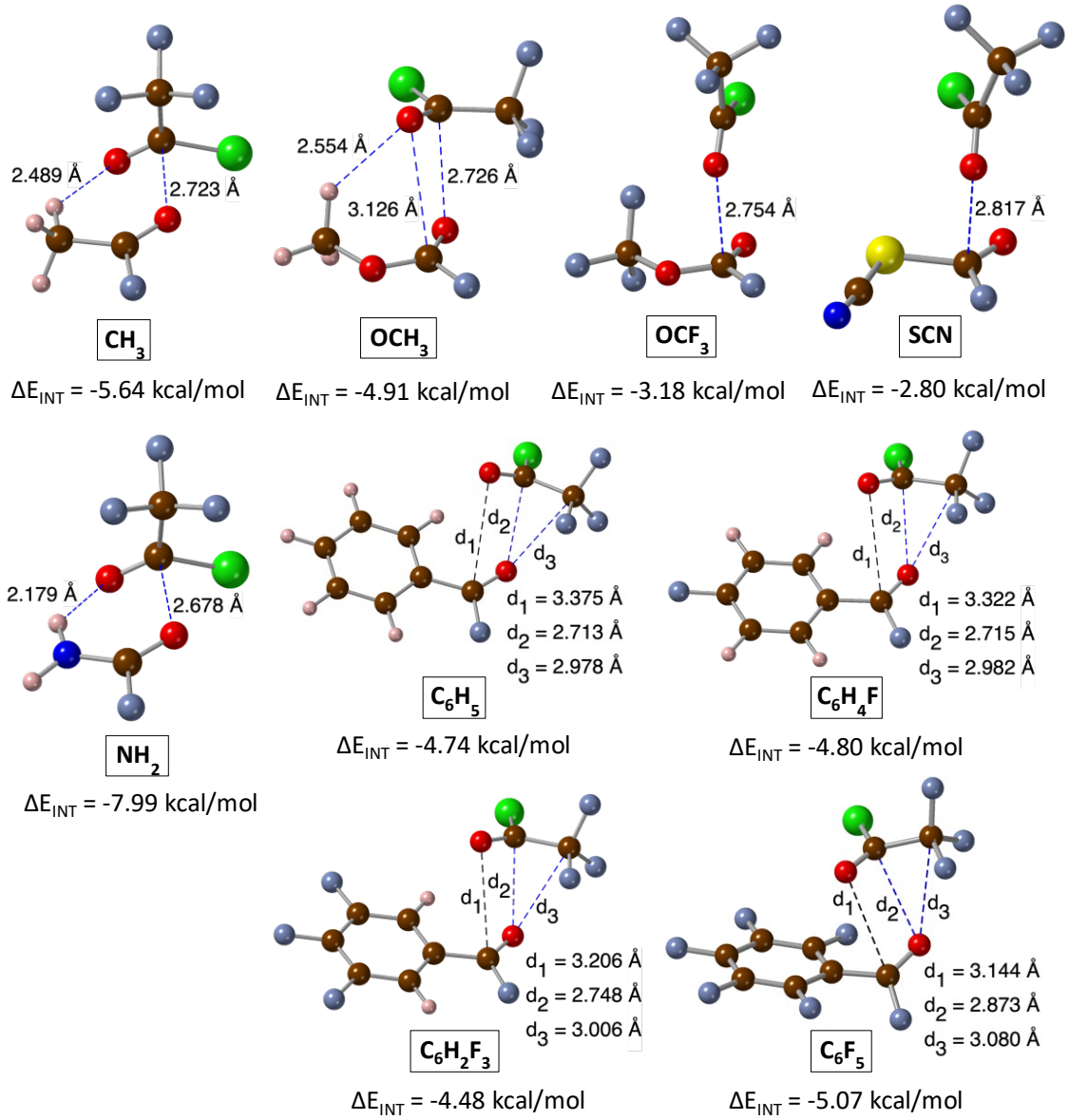

Figure 3.6. Optimized geometries and interaction energies for the adducts formed by CF_3-COCl as the donor and several fluoroformate derivatives (R-COF; R = CH_3, OCH_3, OCF_3, SCN, NH_2, C_6H_5, C_6H_4F, $C_6H_2F_3$, and C_6F_5) as the acceptors calculated at the M06-2X/def2-TZVP level.

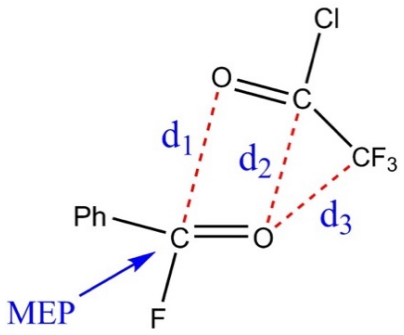

Scheme 3.2. Intermolecular contacts in the adduct formed by CF_3-COCl and Ph-COF.

3.4.3 Effect of Y

I have seen that donor molecules with oxygen atoms are able, in some circumstances, to establish hydrogen bonds that compete with the lone-pair−carbonyl interactions. To avoid this, I have used N_2 as the donor molecule and reoptimized all systems of Figure 3.6. In a recent report, such a molecule was successfully used as a Lewis base to assess the strength of noncovalent interaction in several families of heterocycles.[3] The main geometrical parameters and the corresponding interaction energies are shown in Table 3.2.

Table 3.2. Key geometrical parameters and interaction energies for the optimized $N_2\cdots$R-COF (R = CH_3, OCH_3, OCF_3, SCN, NH_2, C_6H_5, C_6H_4F, $C_6H_2F_3$, and C_6F_5) adducts, calculated at the M06-2X/def2-TZVP level.

R	$d_{N\cdots C}$ (Å)	$\alpha_{N\cdots C=O}$ (°)	ΔE_{INT} (kcal/mol)
CH_3	3.043	92.42	-1.08
OCH_3	2.972	93.14	-1.16
OCF_3	2.943	95.87	-1.46
SCN	3.126	109.75	-1.42
NH_2	3.038	88.42	-0.94
C_6H_5	3.056	95.33	-0.84
C_6H_4F	3.056	93.73	-0.86
$C_6H_2F_3$	3.046	95.65	-0.98
C_6F_5	3.016	97.46	-1.42

For N_2, the N···C=O interaction is the shortest one in all cases with the exception of R = SCN, in which the N···Cl contact (3.036 Å) is slightly shorter than the N···C contact (3.126 Å) due to the interaction of the donor oxygen with the electrophilic region of the chlorine atom. It must be noted that the interaction energies are, in general, smaller than in the previous case, in line with the lower donating capability of N with respect to

O. The $V_{s,min}$ values for CF_3-COCl and N_2 are -18 and -9 kcal/mol, respectively. Also, any possibility of dipole-dipole interaction is eliminated with the use of N_2.

3.5 MEP values as predictors

I wondered about the possibility of making predictions on the strength of an interaction or the associated intermolecular distance on the basis of molecular properties that are known *a priori*. It has been claimed that the value of the MEP at the electrophilic centre ($V_{s,max}$) can be used to predict the strength of halogen bonds.[31,32] Recently, Wheeler and co-workers have developed a model to predict the stacking interaction in biologically active molecules using heterocycle descriptors derived from the electrostatic potential and electric field of the molecules involved.[33]

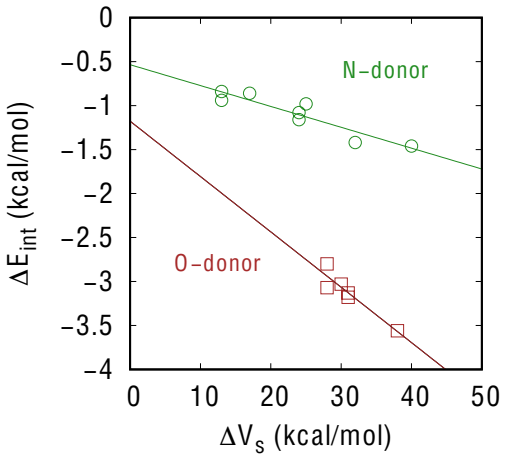

Figure 3.7. Relationship between the donor-acceptor MEP difference (ΔV_s) and the interaction energy (ΔE_{INT}) for the adducts studied in this work, calculated at the M06-2X/def2-TZVP level. Green circles ($R^2 = 0.856$) and red squares ($R^2 = 0.869$) represent donors with nitrogen and oxygen atoms, respectively (see Tables A3.4 − A3.6 and Eqs. A3.1 − A3.2 in the Appendix).

In the present case, the use of MEP values does not allow a general prediction but seems to work well for groups with the same donor species. Fair linear dependences have been found between ΔV_s ($\Delta V_s = V_{s,min(donor)} + V_{s,max(acceptor)}$) and the interaction energy for the same electron-rich donor, containing either N or O (Figure 3.7). This fact indicates that the electrostatic interaction is not the only significant contribution to the intermolecular attraction. Moreover, in the case of an oxygen donor (red squares in Figure 3.7), the more pronounced slope is associated with shorter O···C contacts that should involve enhanced orbital overlap and, thus, a larger charge transfer component. As shown

above, for these short contacts the energy difference is dictated by the O···C=O attack angle, which is characteristic of an orbital interaction.[13]

3.6 Energy Decomposition Analysis

In the light of the above results and to try to understand the nature of lone-pair−carbonyl interactions in acyl halides at different contact distances, I have performed an Energy Decomposition Analysis (EDA) on several different dimers, with oxygen as the lone pair donor, directly retrieved from experimental structures and one computational adduct (F_3C-COCl···CF_3-COF). The results are summarized in Table 3.3.

Table 3.3. Energy Decomposition Analysis for selected systems with O···C=O short contacts calculated at the M06-2X/def2-TZVP level. All energies are given in kcal/mol.

Adduct	Norm. $d_{O\cdots C}$ (Å)	ΔE_{Pauli}	ΔE_{ELEC}	ΔE_{DISP}	ΔE_{POL}	ΔE_{CT}	ΔE_{INT}
F_3C-COCl··· CF_3-COF	-0.516	12.338	-10.481	-3.941	-0.596	-0.504	-3.183
ABAZUY[34]	-0.320	7.085	-5.698	-2.638	-0.335	-0.318	-1.904
AZOYAP[35]	-0.256	5.842	-5.712	-2.304	-0.343	-0.099	-2.617
BAPLUZ[36]	-0.190	7.432	-5.627	-3.219	-0.343	-0.298	-2.054
BEWTIH[37]	-0.293	5.728	-5.545	-2.242	-0.291	-0.188	-2.538
CECBAO[38]	-0.384	6.502	-6.119	-2.606	-0.363	-0.184	-2.771
FAYNOI[25]	-0.680	22.344	-21.436	-5.526	-2.055	-2.121	-8.794
ISADIP[29]	-0.357	7.513	-6.585	-2.888	-0.318	-0.131	-2.410
ISADOV[29]	-0.315	7.623	-6.664	-2.897	-0.391	-0.301	-2.631
LEZZOI[39]	-0.341	7.284	-7.665	-2.664	-0.518	-0.216	-3.780
WEWGIP[40]	-0.179	6.457	-5.109	-3.131	-0.402	-0.301	-2.485
XANLUU[41]	-0.354	9.842	-7.746	-3.856	-0.523	-0.467	-2.750
XANMEF[41]	-0.093	4.502	-2.850	-2.191	-0.403	-0.186	-1.129
YAYHIR[42]	-0.053	7.111	-5.642	-3.643	-0.497	-0.373	-3.046

In general, the interaction energy increases as the O···C distance is shortened. It is worth noting that dispersion contributes to a great extent to the total attractive forces and polarization and charge transfer terms are also present in all cases. I have used the M06-2X functional, and I have checked that adding the D3 dispersion correction (M06-2X-D3) only increases the dispersion component (ΔE_{DISP}) by a 5-6%.

Interestingly, the Pauli repulsion energy (ΔE_{PAULI}) is very large and is greatly compensated by an electrostatic attractive component (ΔE_{ELEC}), both decreasing exponentially in absolute value with the normalized distance, and showing a linear

correlation between them. However, the sum of ΔE_{PAULI} and ΔE_{ELEC} is positive in all cases except in (chlorosulfonyl)carbamic fluoride (LEZZOI).[39] At difference with the other systems, in which only the donor atom is close to the carbonyl carbon atom, in this structure the interaction involves the two acyl groups oriented perpendicularly to each other, which could explain the enhanced electrostatic attraction and a large interaction energy of -3.780 kcal/mol. Although the electrostatic interaction ΔE_{ELEC} is the largest attractive term (negative energies), but since it is in all cases (with the only noted exception) overcome by a larger repulsive Pauli term, it is the dispersion component that reverts the situation and makes the interaction neatly attractive.

The two components associated with orbital interactions, polarization and charge transfer, add only a small amount to the total interaction energy, becoming important only at the shortest distance found in the adduct of 1,4-dioxane and oxalyl fluoride[25] (0.680 Å shorter than the van der Waals radii sum), adding up to -4.18 kcal/mol. Moreover, in this case the contact of the oxygen donor atom from dioxane is not strictly with the carbonyl group but it sits above the centre of the carbon-carbon bond, with O···C distances of 2.59 and 2.61 Å.

3.7 Conclusions

I have carried out a comprehensive analysis, both structural and theoretical, of lone-pair−carbonyl interactions in acyl halides (R-CO-X). A structural analysis of the CSD has shown that these contacts follow precise geometrical arrangements, with attack angles approaching 100° as the lone-pair−carbonyl distance shortens. A MEP analysis has disclosed well-defined π-holes on the carbon atom of the carbonyl groups for all studied acyl halides. I have demonstrated that the value of the electrostatic potential at the π-hole decreases on descending the periodic group for X = F–I, also showing a high sensitivity to the nature of the R substituent.

The strength of the interaction depends on the nature of both the donor and the acceptor. Three main factors affect the interaction energy:

a) The nature of X: I have observed stronger interactions for X = F, which is in good agreement with the MEP analysis; however, the total interaction energy for X = F–I correlates very well with the Y···C=O angle, which reinforces the idea of a non-negligible orbital nature of the interaction.

b) The effect of R: this is crucial because it modulates the electrostatic potential distribution over the molecule and determines whether or not a π-hole interaction may be established.

c) The nature of the lone pair: better donors, such as oxygen, lead to stronger interactions.

I have also seen that the values of the MEP at the π-hole can give a fair approximation of the interaction strength when the same donor atom is used. Furthermore, an EDA analysis has shown that the electrostatic attraction is in all cases overruled by the Pauli repulsion, both being strongly correlated. One is therefore left with the smaller orbital and dispersion attractive forces to make the net interaction attractive, with dispersion being roughly four times stronger than the combination of the polarization and charge transfer terms. Finally, the computed interaction energies, in the range 1 – 3 kcal/mol for a single lone-pair–carbonyl contact, allow the use of these interactions in crystal design and supramolecular chemistry. Notice that I have focused here on carbonyls as donors. If more nucleophilic groups were present, a complete nucleophilic attack can take place due to the fact that halides are very good leaving groups.

3.8 Appendix

Annex 3.1. Normalized Y···C distance (normalized distance = $d_{Y\cdots C} - \sum r_{vdW}$) and $\alpha_{Y\cdots C=O}$ bond angle for molecular adducts of type E-Y···R-CO-X (Scheme 3.1) found in the CSD, represented in Figure 3.1 (Y = O, N, F, and Cl).

Table A3.1. Key geometrical parameters for experimental E-Cl···R-CO-X adducts.

refcode	Norm. $d_{Cl\cdots C}$ (Å)	$\alpha_{Cl\cdots C=O}$ (°)	refcode	Norm. $d_{Cl\cdots C}$ (Å)	$\alpha_{Cl\cdots C=O}$ (°)
ALCOTU	-0.069	85.5	PROPAL	0.039	78.1
BAJSIP	-0.309	66.4	PROPAL	0.030	102.2
DOTNEG	-0.134	83.4	QULWIF	-0.115	93.2
GACDUJ	-0.061	80.7	VAQRAG	-0.102	97.5
GUJZER	0.002	84.6	VOJJUA	-0.141	89.0
IDIQUI	0.084	112.2	WOJXIC	0.062	79.2
ILANEQ	-0.138	83.5	WOJXIC	0.027	80.2
IZICAX	0.034	97.3	XANMAB	-0.070	98.6
JUMXOG	-0.104	90.4	XANMAB	0.084	110.9
OFEFIP	-0.133	88.2	YAYHIR	-0.026	93.7

Table A3.2. Key geometrical parameters for experimental E-O···R-CO-X adducts.

refcode	Norm. $d_{O\cdots C}$ (Å)	$\alpha_{O\cdots C=O}$ (°)	refcode	Norm. $d_{O\cdots C}$ (Å)	$\alpha_{O\cdots C=O}$ (°)
ABAZUY	-0.014	75.7	FOPNUT	-0.133	79.1
ABAZUY	-0.320	98.9	GURCAX	-0.172	91.9
AMORIE	0.056	78.9	HALWUP	-0.467	96.5
AMORIE	0.053	79.5	ILAMUF	0.069	105.4
AMORIE	0.047	112.6	ILANAM	0.053	85.6
AMORIE	0.040	113.3	ISADIP	-0.287	85.2
AXIMEZ	-0.143	77.1	ISADIP	-0.357	92.3
AZOYAP	-0.259	104.7	ISADOV	-0.315	92.0
AZOYAP	-0.256	108.4	IZICAX	-0.231	88.0
BAJSIP	-0.094	63.5	IZICIF	0.056	103.3
BAJSIP	0.012	65.7	LALXEB	0.099	98.2
BAPLUZ	-0.190	100.5	LESYUD	-0.095	75.1
BEWTIH	-0.293	97.0	LESYUD	-0.171	80.4
BEWTIH	-0.153	107.9	LEZZOI	-0.340	100.3
CECBAO	-0.066	87.9	LUNDON	0.081	61.8
CECBAO	-0.383	92.0	MUCONC10	-0.010	83.7
CECBAO	-0.277	93.2	OXALYB	0.047	83.5
CUMVAJ	0.031	90.6	OZOJOE	-0.193	89.4
CUTSAN	-0.248	97.2	PAWNUX	-0.022	100.3
DALJAC	-0.115	77.9	PAXJUU	0.076	100.5
DALJAC	0.002	82.3	PILVIR	-0.010	102.0
DALJAC	-0.054	87.1	RAVSIQ	0.051	71.9
DALJAC	-0.319	89.2	RIJNIH	-0.063	78.3
DALJAC	-0.374	90.6	SAXFOO	-0.146	83.7
DALJAC	-0.304	95.3	TIPMOW	0.017	62.9
DALJAC	-0.455	96.3	TIRNEP	-0.296	96.8
DALJAC	-0.456	97.5	UCIYAJ	-0.214	85.0
DALJAC	-0.081	116.7	VAXTIA	-0.195	86.7
DALNUA	-0.299	99.4	VIHNEF	0.005	92.2
DALNUA	-0.308	100.3	VIHNEF	-0.060	94.0
DALNUA	-0.093	114.3	VIHNEF	-0.415	95.4
DALNUA	-0.041	117.2	WEWGIP	-0.180	104.6
ENPCOY	-0.158	97.8	XANLUU	-0.312	94.6
FAYNOI	-0.680	97.0	XANLUU	-0.354	95.7
FAYNOI	-0.659	100.7	XANMAB	0.081	75.5
FIMWIJ	0.035	83.7	XANMEF	-0.093	108.2
FIMWIJ	-0.165	104.0	YAYHIR	-0.053	100.8

Table A3.3. Key geometrical parameters for experimental E-N···R-CO-X adducts.

refcode	Norm. $d_{N\cdots C}$ (Å)	$\alpha_{N\cdots C=O}$ (°)	refcode	Norm. $d_{N\cdots C}$ (Å)	$\alpha_{N\cdots C=O}$ (°)
AMORIE	-0.093	112.3	XANMAB	0.302	84.4
CECBAO	0.042	85.2	XANMAB	0.282	89.4
PILVIR	0.197	93.2	XANMEF	0.028	101.7
WOJXOI	-0.058	96.5	YELDUR	0.091	99.2

Table A3.4. Key geometrical parameters for experimental E-F···R-CO-X adducts.

refcode	Norm. $d_{F\cdots C}$ (Å)	$\alpha_{F\cdots C=O}$ (°)	refcode	Norm. $d_{F\cdots C}$ (Å)	$\alpha_{F\cdots C=O}$ (°)
AMORIE	-0.089	113.6	ILANIU	-0.054	72.6
CECBAO	-0.089	115.9	ILANIU	-0.088	74.1
HALWUP	-0.101	75.8	PELQIH	0.072	103.0
IBOMUH	-0.170	78.2	VIHNEF	0.042	82.0
IBOMUH	0.033	93.3			

Annex 3.2. Highest value of the electron potential ($V_{s,max}$), donor-acceptor MEP difference ($\Delta V_s = V_{s,max} + V_{s,min}$) and the interaction energy for the adducts studied in this work, calculated at the M06-2X/def2-TZVP level and represented in Figure 3.7. All energies are given in kcal/mol.

Table A3.5. Key parameters for calculated F_3C-CO-Cl and F_3C-CO-X (X = F, Cl, Br, and I) adducts (O-donor; $V_{s,min}$ = -18 kcal/mol).

X	$V_{s,max}$	ΔV_s	ΔE_{INT}
F	56	38	-3.56
Cl	49	31	-3.13
Br	48	30	-3.03
I	46	28	-3.07

Table A3.6. Key parameters for calculated F_3C-CO-Cl and R-CO-F (R = OCF_3 and SCN) adducts (O-donor; $V_{s,min}$ = -18 kcal/mol).

R	$V_{s,max}$	ΔV_s	ΔE_{INT}
OCF_3	49	31	-3.18
SCN	46	28	-2.80

Table A3.7. Key parameters for calculated N_2 and R-CO-F adducts (N-donor; $V_{s,min}$ = -9 kcal/mol).

R	$V_{s,max}$	ΔV_s	ΔE_{INT}
CH_3	33	24	-1.08
OCH_3	33	24	-1.16
OCF_3	49	40	-1.46
NH_2	22	13	-0.94
C_6H_5	22	13	-0.84
C_6H_4F	26	17	-0.86
$C_6H_2F_3$	34	25	-0.98
C_6F_5	41	32	-1.42

Annex 3.2.1. Linear least-squares fitting equations for Figure 3.7.

a) ΔV_s (O-donor) = -1.18 – 0.063·ΔE_{INT} (R^2 = 0.869) [Eq. A3.1]

b) ΔV_s (N-donor) = -0.53 – 0.024·ΔE_{INT} (R^2 = 0.856) [Eq. A3.2]

3.9 References

1. Echeverría, J. Intermolecular Carbonyl···Carbonyl Interactions in Transition-Metal Complexes. *Inorg. Chem.* **2018**, *57*, 5429-5437.
2. Echeverría, J. The n→π* interaction in metal complexes. *Chem. Commun.* **2018,** *54*, 3061-3064.
3. Echeverría, J., Noncovalent Interactions in Succinic and Maleic Anhydride Derivatives. *Cryst. Growth Des.* **2018**, *18*, 506-512.
4. Newberry, R. W.; VanVeller, B.; Guzei, I. A.; Raines, R. T. n→π* Interactions of Amides and Thioamides: Implications for Protein Stability. *J. Am. Chem. Soc.* **2013**, *135*, 7843-7846.
5. Newberry, R. W.; Raines, R. T. A Key n→π* Interaction in N-Acyl Homoserine Lactones. *ACS Chem. Biol.* **2014**, *9*, 880-883.
6. Bretscher, L. E.; Jenkins, C. L.; Taylor, K. M.; DeRider, M. L.; Raines, R. T. Conformational stability of collagen relies on a stereoelectronic effect. *J. Am. Chem. Soc.* **2001**, *123*, 777-778.

7. Singh, S. K.; Das, A. The n→π* interaction: a rapidly emerging non-covalent interaction. *Phys. Chem. Chem. Phys.* **2015**, *17*, 9596-9612.
8. Singh, S. K.; Mishra, K. K.; Sharma, N.; Das, A. Direct Spectroscopic Evidence for an n→π* Interaction. *Angew. Chem. Int. Ed.* **2016**, *55*, 7801-7805.
9. Perras, F. A.; Marion, D.; Boisbouvier, J.; Bryce, D. L.; Plevin, M. J. Observation of CH···π Interactions between Methyl and Carbonyl Groups in Proteins. *Angew. Chem. Int. Ed.* **2017**, *56*, 7564-7567.
10. Doppert, M. T.; van Overeem, H.; Mooibroek, T. J. Intermolecular π-hole/n→π* interactions with carbon monoxide ligands in crystal structures. *Chem. Commun.* **2018**, *54*, 12049-12052.
11. Bauzá, A.; Frontera, A. Theoretical study on σ- and π-hole carbon···carbon bonding interactions: implications in CFC chemistry. *Phys. Chem. Chem. Phys.* **2016**, *18*, 32155-32159.
12. Del Bene, J. E.; Alkorta, I.; Elguero, J. Pnicogen bonds in complexes with CO and CS: differentiating properties. *Mol. Phys.* **2019**, *117*, 1117-1127.
13. Kamer, K. J.; Choudhary, A.; Raines, R. T. Intimate Interactions with Carbonyl Groups: Dipole-Dipole or n→π*? *J. Org. Chem.* **2013**, *78*, 2099-2103.
14. Sahariah, B.; Sarma, B. K. Relative orientation of the carbonyl groups determines the nature of orbital interactions in carbonyl–carbonyl short contacts. *Chem. Sci.* **2019**, *10*, 909-917.
15. Newberry, R. W.; Raines, R. T. The n→π* Interaction. *Acc. Chem. Res.* **2017**, *50*, 1838-1846.
16. Bauzá, A.; Mooibroek, T. J.; Frontera, A. The Bright Future of Unconventional σ/π-Hole Interactions. *ChemPhysChem* **2015**, *16*, 2496-2517.
17. Wang, H.; Wang, W.; Jin, W. J. σ-Hole Bond vs π-Hole Bond: A Comparison Based on Halogen Bond. *Chem. Rev.* **2016**, *116*, 5072-5104.
18. Murray, J. S.; Lane, P.; Clark, T.; Riley, K. E.; Politzer, P. σ-Holes, π-holes and electrostatically-driven interactions. *J. Mol. Model.* **2012**, *18*, 541-548.
19. Horn, P. R.; Mao, Y.; Head-Gordon, M. Probing non-covalent interactions with a second generation energy decomposition analysis using absolutely localized molecular orbitals. *Phys. Chem. Chem. Phys.* **2016**, *18*, 23067-23079.
20. Groom, C. R.; Bruno, I. J.; Lightfoot, M. P.; Ward, S. C. The Cambridge Structural Database. *Acta Crystallogr. Sect. B*. **2016**, *72*, 171-179.

21. Burgi, H. B.; Dunitz, J. D.; Shefter, E. Geometrical reaction coordinates. II. Nucleophilic addition to a carbonyl group. *J. Am. Chem. Soc.* **1973**, *95*, 5065-5067.
22. Burgi, H. B.; Dunitz, J. D.; Lehn, J. M.; Wipff, G. Stereochemistry of reaction paths at carbonyl centres. *Tetrahedron*. **1974**, *30*, 1563-1572.
23. Mayer, F.; Oberhammer, H.; Berkei, M.; Pernice, H.; Willner, H.; Bierbrauer, K.; Paci, M. B.; Argüello, G. A. Structural and Conformational Properties of Fluoroformic Acid Anhydride, FC(O)OC(O)F. *Inorg. Chem.* **2004**, *43*, 8162-8168.
24. Berrueta Martínez, Y.; Reuter, C. G.; Vishnevskiy, Y. V.; Bava, Y. B.; Picone, A. L.; Romano, R. M.; Stammler, H.-G.; Neumann, B.; Mitzel, N. W.; Della Védova, C. O. Structural Analysis of Perfluoropropanoyl Fluoride in the Gas, Liquid, and Solid Phases. *J. Phys. Chem. A*. **2016**, *120*, 2420-2430.
25. Moeller, G.; Olmstead, M. M.; Tinti, D. S. Structure and spectra of the 1:1 addition compound of 1,4-dioxane and oxalyl fluoride. *J. Am. Chem. Soc.* **1987**, *109*, 95-98.
26. Sjoberg, P.; Politzer, P. Use of the electrostatic potential at the molecular surface to interpret and predict nucleophilic processes. *J. Phys. Chem.* **1990**, *94*, 3959-3961.
27. Jabłoński, M. On the Uselessness of Bond Paths Linking Distant Atoms and on the Violation of the Concept of Privileged Exchange Channels. *ChemistryOpen* **2019**, *8*, 497-507.
28. Jabłoński, M. Hydride-Triel Bonds. *J. Comput. Chem.* **2018**, *39*, 1177-1191.
29. Erben, M. F.; Della Védova, C. O.; Boese, R.; Willner, H.; Oberhammer, H. Trifluoromethyl Chloroformate, $ClC(O)OCF_3$: Structure, Conformation, and Vibrational Analysis Studied by Experimental and Theoretical Methods. *J. Phys. Chem. A*. **2004**, *108*, 699-706.
30. Rahim, A.; Saha, P.; Jha, K. K.; Sukumar, N.; Sarma, B. K. Reciprocal carbonyl–carbonyl interactions in small molecules and proteins. *Nature Commun.* **2017**, *8*, 78-90.
31. Perera, M. D.; Desper, J.; Sinha, A. S.; Aakeröy, C. B. Impact and importance of electrostatic potential calculations for predicting structural patterns of hydrogen and halogen bonding. *CrystEngComm* **2016**, *18*, 8631-8636.
32. Corpinot, M. K.; Bučar, D.-K. A Practical Guide to the Design of Molecular Crystals. *Cryst. Growth Des.* **2019**, *19*, 1426-1453.

33. Bootsma, A. N.; Doney, A. C.; Wheeler, S. E. Predicting the Strength of Stacking Interactions between Heterocycles and Aromatic Amino Acid Side Chains. *J. Am. Chem. Soc.* **2019**, *141*, 11027-11035.

34. Romano, R. M.; Della Védova, C. O.; Boese, R. N-sulfinylimine fluorocarbonylsulphane, FC(O)SNSO: solid structure and theoretical calculations. *J. Mol. Struct.* **1999**, *513*, 79-84.

35. Della Védova, C. O.; Downs, A. J.; Novikov, V. P.; Oberhammer, H.; Parsons, S.; Romano, R. M.; Zawadski, A. Fluorocarbonyl Trifluoromethanesulfonate, $FC(O)OSO_2CF_3$: Structure and Conformational Properties in the Gaseous and Condensed Phases. *Inorg. Chem.* **2004**, *43*, 4064-4071.

36. M. Romano, R.; O. Della Védova, C.; Boese, R.; Hildebrandt, P. Structural and spectroscopic characterization of ClC(O)SNSO. A theoretical and experimental study. *Phys. Chem. Chem. Phys.* **1999**, *1*, 2551-2557.

37. Pernice, H.; Berkei, M.; Henkel, G.; Willner, H.; Argüello, G. A.; McKee, M. L.; Webb, T. R. Bis(fluoroformyl)trioxide, FC(O)OOOC(O)F. *Angew. Chem. Int. Ed.* **2004**, *43*, 2843-2846.

38. Boese, R.; Cutin, E. H.; Mews, R.; Robles, N. L.; Della Védova, C. O. ((Fluoroformyl)imido)sulfuryl Difluoride, $FC(O)NS(O)F_2$: Structural, Conformational, and Configurational Properties in the Gaseous and Condensed Phases. *Inorg. Chem.* **2005**, *44*, 9660-9666.

39. Leitz, D.; Stierstorfer, K.; Kornath, A., Crystal Structure and Vibrational Spectra of $ClSO_2NHC(O)F$. *Z. Anorg. Allg. Chem.* **2018,** *644*, 411-414.

40. Erben, M. F.; Della Védova, C. O.; Willner, H.; Boese, R. Synthesis, Structure and Conformational Properties of Fluoroformylchlorodifluoroacetyl Disulfide, $FC(O)SSC(O)CF_2Cl$: Conformational Transferability in –C(O)SSC(O)– Compounds. *Eur. J. Inorg. Chem.* **2006**, *2006*, 4418-4425.

41. Grossel, M. C.; Hursthouse, M. B.; Orton, J. B. Structural investigation of x,y-bis-(chlorocarbonyl) pyridines derivatives: "strength in diversity"—a disparity of supramolecular packing motifs. *CrystEngComm*. **2005**, *7*, 279-283.

42. Fan, X.; Wang, Y.; Jin, C.; Jin, L. Benzene-1,3,5-tricarbonyl trichloride. *Acta Crystallogr. Sect. E*. **2012**, *68*, o1260-o1265.

Chapter 4

Understanding the interplay of dispersion, charge transfer and electrostatics in noncovalent interactions: The case of bromine-carbonyl short contacts

4.1 Introduction

During the last decades, the key role played by noncovalent interactions (NCIs) in many chemical and biological processes has been recognized.[1-3] However, although some advancement has been made, there is yet a lack of understanding of the origin and nature of some types of NCIs. Recently, many NCIs have been revisited, from both experimental and theoretical approaches, in order to gain deeper insight into their physical origin. For instance, halogen bonding has been seen to be the combination of charge transfer and electrostatic attraction in a lesser or greater degree, depending, among other factors, on the nature of the atoms and groups involved in the interaction.[4-8] Similar analyses have been carried out on chalcogen,[9-11] pnicogen,[12,13] tetrel[14,15] or triel bonds. On the other hand, homopolar dihydrogen bonds in alkanes behave differently depending on the substituents attached to the interacting units, going from a pure dispersion-bound system in methane to a considerable charge transfer-stabilized dimer in the case of polyhedranes.[16-18] It has been also demonstrated that the silane-methane dimer, traditionally considered as a dispersion system, has a non-negligible electrostatic contribution.[19] Moreover, the importance of orbital mixing in closed-shell interactions in metals complexes, historically attributed to dispersion forces enhanced by relativistic effects, has been recently well established.[20-22]

It seems thus clear that the complex nature of many NCIs is yet to be investigated. Nevertheless, a deep knowledge of the origin of a given interaction is crucial to control and eventually exploit it at the nanoscale, in crystal engineering or materials design. Especially difficult is to distinguish between the contribution of orbital mixing and electrostatic attraction in σ- and π-hole interactions because the empty orbital and the electron density hole, responsible for the latter and the former respectively, are located at the same region of the molecule.[23-26] This fact has led, for instance, to a long-lasting debate about the dipolar or orbital nature of carbonyl-carbonyl interactions in proteins and organic molecules.[27, 28] Moreover, recent reports have also pointed out the possibility of having attractive interactions between atoms that are electrostatically equivalent, for which the prediction of an attraction based on the molecular electrostatic potentials is no longer useful.[15, 22, 29-37]

I have focused here on short contacts between bromine atoms and carbonyl groups, in particular those involving the C atom of the carbonyl. Such contacts can be

defined by three parameters: the intermolecular distance $d_{Br\cdots C}$ and the C-Br···C and Br···C=O angles, α_c and β_c, respectively (Scheme 4.1). Intuitively, one could expect that, according to the electron density distribution of the halogen atom featuring a σ-hole at the extension of the C-X covalent bond, and assuming that the carbonyl carbon has its characteristic π-hole on the interacting region, the most favourable interaction from an electrostatic point of view will involve α_c angles close to 90°. In Figure 4.1, I represent the abundance of Br···C=O contacts shorter than the sum of the van der Waals radii as a function of the two angles defined in Scheme 4.1. Most of the contacts, as expected, are located around the region in which both angles α_c and β_c have values between 80 and 100° where the interaction should be dominated by attractive electrostatics. There is also a larger region associated with secondary interactions such as hydrogen bonds or short contacts between the bromine and the oxygen atom of the carbonyl, in which the Br···C=O is merely a secondary interaction supported by stronger ones. More interestingly, there is a small set of contacts showing angles α_c = 160° and β_c = 90°, approximately. However, according to the density-holes picture, such contacts should be repulsive, so several questions arise at this point. Is this repulsion compensated by the other components of the interaction? Do charge transfer and/or dispersion play a major role here? Are those contacts really unsupported? In order to try to give answers to those questions, I have undertaken here a combined structural and computational analysis of bromine···carbonyl short contacts with this particular interaction topology.

To shed light on the nature of this particular interaction, I will select the most relevant experimental examples to analyse their geometrical features. Furthermore, I will calculate the interaction energies associated with the contacts under study. Finally, Energy Decomposition Analyses (EDA) will be performed as well as Natural Bond Orbital (NBO) calculations in order to unveil the orbitals involved in a potential charge transfer interaction. My aim here is to understand why short contacts that are, a priori, electrostatically disfavoured are found in crystal structures.

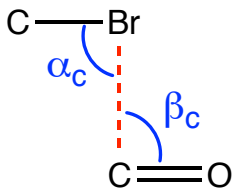

Scheme 4.1. Geometrical parameters involved in bromine···carbonyl interactions.

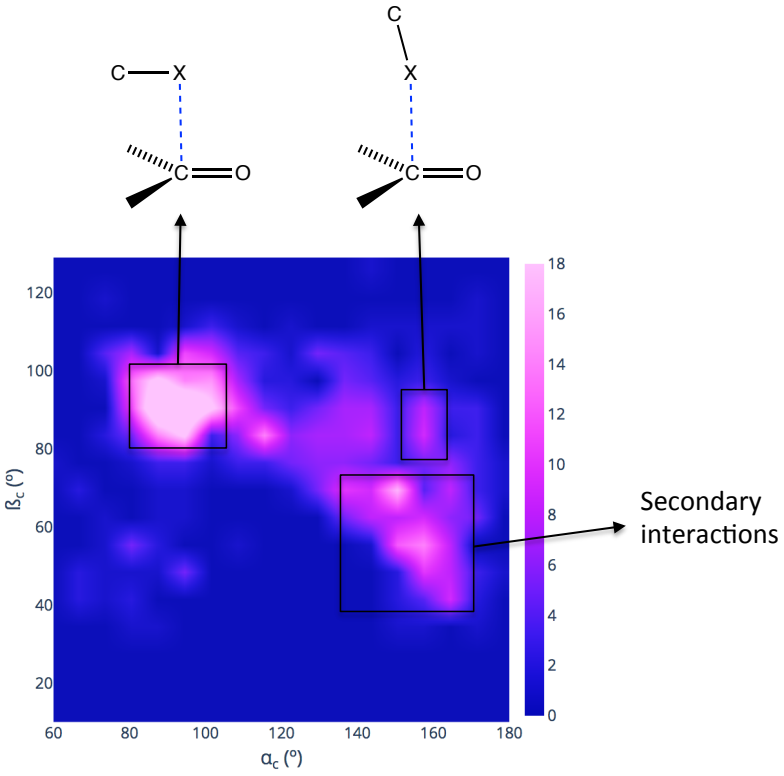

Figure 4.1. 2D histogram for α_c and β_c angles in C-Br···C=O contacts shorter than the sum of the corresponding van der Waals radii. The lateral bar indicates the number of structures.

4.2 Structural Analysis

A search in the Cambridge Structural Database (CSD) for Br···C=O contacts shorter than the sum of the van der Waals radii (3.65 Å) and with angles β_c between 80 and 100° (the region of primary interactions in Figure 4.1) results in 599 crystal structures, 520 with a sp^2 carbon attached to the bromine and 79 with a sp^3 carbon. On the other hand, the carbonyl group belongs to an esther or an amide in 462 crystal structures (77% of the total). The 8.7% of all 599 structures show angles $\alpha_c > 150°$. Figure 4.2 shows two examples of short Br···C contacts with a practically linear C-Br···C moiety. In both cases, the Br···C=O contact is the only one in the dimer at a distance shorter than the van der Waals radii sum.

In Table 4.1, I summarize the main geometrical features of short Br···C=O contacts with $\alpha_c > 165°$. There are four cases in which the Br···C=O contact is the only one with a distance shorter than the sum of the vdW radii that is present in the dimer. In the other six crystal structures, the Br···C=O contact is accompanied by other short contacts involving the bromine or carbon atoms. The shortest contact is found in the crystal structure of 2-(bromomethyl)-2-chloro-4-phenylbutyl-4-bromobenzoate

(LUKQIT)[46] with a Br···C distance 0.4 Å shorter than the vdW radii sum, while the most linear arrangement is that of cis-(1S,2R)-1-(4-Bromobenzoyloxy)-2-methyl-cyclohexanecarbonitrile (FAHREM;[38] Figure 4.2) with an angle α_c = 175.1°. On the other hand, β_c angles are very close to 90° and comprised in the range 86 – 94°.

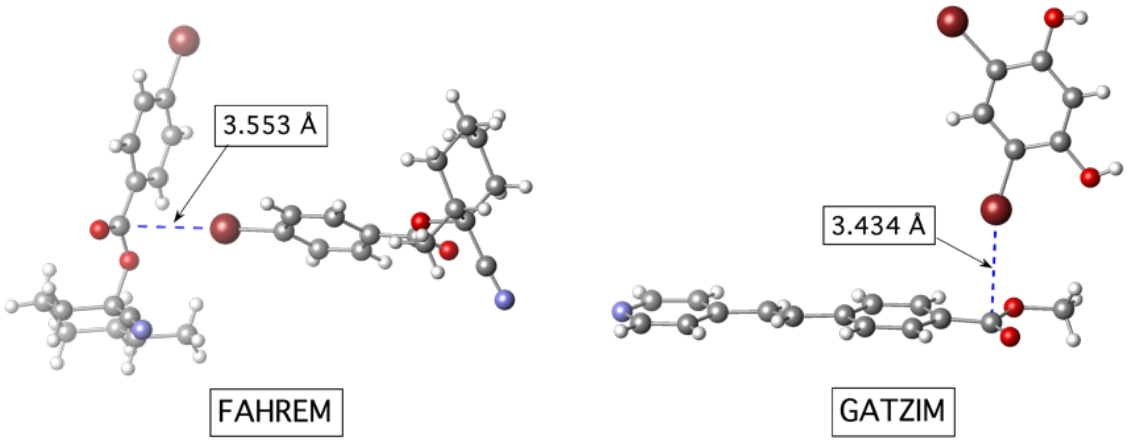

Figure 4.2. Short Br···C=O contacts in the crystal structures of cis-(1S,2R)-1-(4-Bromobenzoyloxy)-2-methyl-cyclohexanecarbonitrile (FAHREM)[38] and bis(Methyl-4-(2-(pyridin-4-yl)vinyl)benzoate)-4,6-dibromobenzene-1,3-diol (GATZIM).[39]

Table 4.1. Summary of experimental short Br···C=O contacts with α_c > 165° including their geometrical features, the substituents at the carbonyl groups, and all other contacts shorter than the van der Waals radii sum.

refcode	$d_{Br\cdots C}$ (Å)	α_c (°)	β_c (°)	CO subst.	Other contacts < $\sum r_{vdW}$
FAHREM[38]	3.553	175.1	91.1	RO-, Ph-	none
MADLEK[40]	3.409	174.2	90.6	R_2N-, Ph-	none
KUTVAX[41]	3.449	172.4	90.6	R_2N-, thiophene	Br···N (-0.08 Å)
DBTCHY[42]	3.345	172.1	90.7	HO-, Cy-	Br···H (-0.03 Å)
QEKMUP[43]	3.636	172.0	86.4	R_2N-, R-	none
LOQQOX[44]	3.540	170.6	86.8	H-, Ph-	Br···H (-0.19 Å)
IYIHEE[45]	3.460	167.2	86.6	RO-, R-	C···H (-0.27 Å)
LUKQIT[46]	3.229	167.1	93.4	RO-, Ph-	Br···C (-0.13 Å) Cl···C (-0.18 Å)
GATZIM[39]	3.434	165.3	93.5	RO-, Ph-	none

4.3 Analysis of the Molecular Electrostatic Potential

The Molecular Electrostatic Potential (MEP) has been extensively used to predict the most favourable geometry in electrostatics-based NCIs.[2,19,47-49] However, as pointed out in the Introduction, this methodology, based on the presence of electron density holes, fails in some cases. For instance, Mo and co-workers recently reported a valence bond computational study of the short contacts between electrophilic caps in which the electrostatic repulsion, which can be predicted using MEP maps, is overcome by a strong charge transfer, leading to an attractive overall interaction.[34] Previously, Alkorta and co-workers reported similar charge transfer stabilization in complexes of PX_3 (X = F, Cl, and Br) and nitrogen bases.[50]

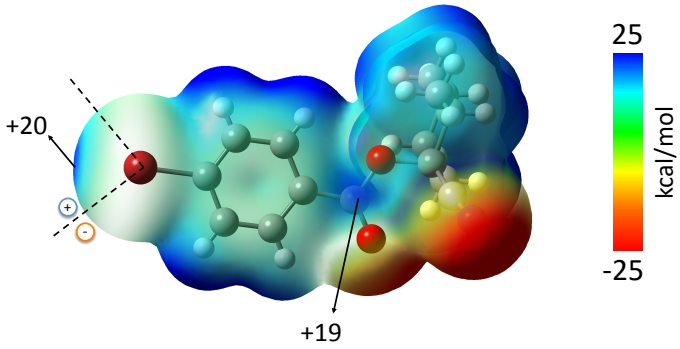

Figure 4.3. MEP map for *cis*-(1*S*,2*R*)-1-(4-bromobenzoyloxy)-2-methyl-cyclohexanecarbonitrile (FAHREM)[38] plotted on the electron density isosurface (s = 0.001 Å). Energies are given in kcal/mol. Red and blue colours indicate a more negative and a more positive MEP value, respectively.

In Figure 4.3, I represent the MEP for the interacting molecule in the crystal structure of FAHREM[38] (Figure 4.2). The carbon atom of the carbonyl group shows a clear region of electron density depletion, the π-hole ($V_{s,max}$ = +19 kcal/mol), whereas the bromine atom exhibits the characteristic σ-hole ($V_{s,max}$ = +20 kcal/mol) in the prolongation of the C-Br covalent bond. Note that the inclusion of polarization in MEP maps[51,52] could modify the picture, but significant changes are mainly detected for sites susceptible to nucleophilic attacks.[53] According to the electron density holes model, one could not expect an attractive Br···C=O interaction for α_c angles greater than 135° because that would involve the approaching of two positively charged regions (see the transition between positive and negative EP values around the Br atom indicated by dashed lines in Figure 4.3). However, the structural analysis has evidenced that such linear arrangements of two electrostatic like-like regions of positive charge do exist in

many crystal structures. It is necessary, therefore, to study the energetics associated with such contacts to unveil whether they are attractive or not as well as their nature.

4.4 Analysis of the Interaction Energies

The interaction energies for the nine supramolecular systems retrieved from the crystal structures presented in Table 4.1 have been calculated. All of them are negative, and thus, the interaction between the corresponding molecules is attractive in all cases (see Table A4.1 in the Appendix). Six adducts have a single Br···C contact with interaction energies ranging from -0.73 to -2.84 kcal/mol, and three of them show interaction energies in the range -1.23 to -1.29 kcal/mol (FAHREM,[38] KUTVAX,[41] and GATZIM[39]). On the other hand, there are three crystal structures in which each dimer establishes, in addition, two short Br···C contacts (MADLEK,[40] QEKMUP,[43] and LUKQIT[46]). Those aggregates present interaction energies between -3.01 and -5.28 kcal/mol, which is approximately twice as large as those associated with single contacts. The single Br···C=O interaction energies (-0.73 to -1.29 kcal/mol) are 40 – 50% smaller than those found for carbonyl-carbonyl contacts in transition metal complexes[25] and organic molecules[26] and similar to π-hole interactions between lone pair-containing atoms and succinic/maleic anhydride derivatives.[54]

4.5 Energy Decomposition Analysis

I have next performed an Energy Decomposition Analysis (EDA) of the four adducts in which Br···C are the only intermolecular contacts shorter than the sum of the vdW radii (including dimers with single and double Br···C contacts) to understand the physical origin of the attraction. The results are summarized in Table 4.2. As expected, the "frozen density" (ΔE_{FRZ}) term, which comprises Coulomb electrostatics (ΔE_{ELEC}) and Pauli exchange-repulsion (ΔE_{PAULI}) is positive in all cases, in good agreement with the predicted electrostatic repulsion based on MEPs. Remarkably, for all systems, dispersion (ΔE_{DISP}) overcomes ΔE_{FRZ} and makes the interaction attractive, while orbital-based interaction terms, polarization (ΔE_{POL}) and charge transfer (ΔE_{CT}), further contribute to the stability of the supramolecular aggregates with a weight of about one fourth that of the dispersion term.

Table 4.2. EDA analyses (M06-2X/def2-TZVP) of NCIs (kcal/mol) in dimers with Br···C=O as the only intermolecular contact shorter than the sum of the corresponding van der Waals radii. The ΔE_{FRZ} term does not include dispersion. All energies are given in kcal/mol.

refcode	ΔE_{FRZ}	ΔE_{PAULI}	ΔE_{ELEC}	ΔE_{DISP}	ΔE_{POL}	ΔE_{CT}	ΔE_{INT}
FAHREM[38]	2.35	5.38	-3.04	-2.98	-0.36	-0.29	-1.29
MADLEK[40]	5.68	12.19	-6.51	-7.00	-0.88	-0.81	-3.01
QEKMUP[43]	5.17	15.32	-10.15	-8.55	-1.05	-0.86	-5.28
GATZIM[39]	1.86	4.83	-2.98	-2.54	-0.22	-0.31	-1.23

To further investigate the effect of the interaction topology, I have performed EDA analyses on the model system bromobenzene···methyl formate at different Br···C distances with a linear C-Br···C moiety (α_c = 180°) and also for different angles at a fixed Br···C distance of 3.5 Å. The results are summarized in Figure 4.4 (see Tables A4.2 – A4.3 in the Appendix). In Figure 4.4a, ΔE_{FRZ} is positive at all studied distances and shows the largest variation with the contact distance, making the total interaction repulsive below 3 Å. For longer distances, the total interaction is attractive, with a minimum at 3.5 Å (-0.73 kcal/mol), in very good agreement with distances found in experimental structures. Dispersion, which was the dominant term in all systems analysed in Table 4.2, does not overcome the frozen energy for short distances and only becomes the largest term at distances longer than 3.5 Å. Interestingly, at 3.2 Å, the total interaction energy of -0.62 kcal/mol is the result of the combination of ΔE_{DISP} (-2.82 kcal/mol), ΔE_{POL} (-0.26 kcal/mol), and ΔE_{CT} (-0.56 kcal/mol) to overcome ΔE_{FRZ} (3.02 kcal/mol).

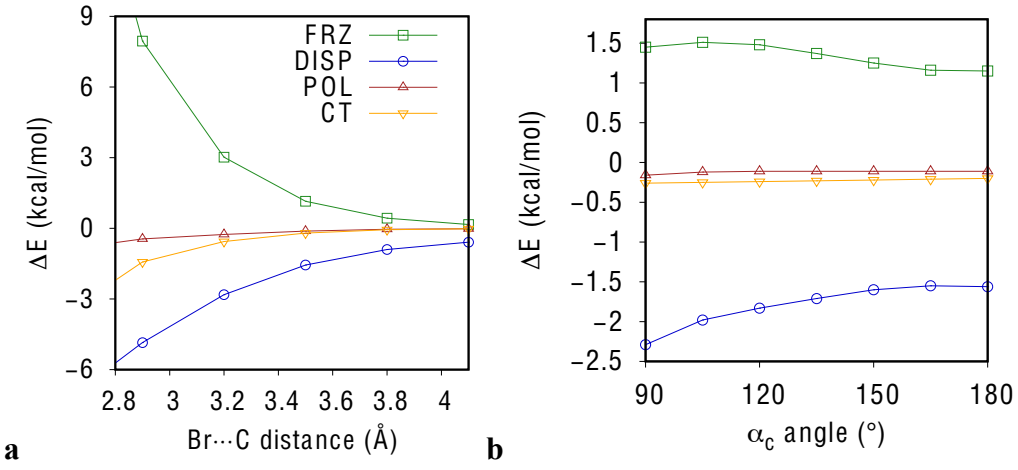

Figure 4.4. Dependence of the different EDA components with (**a**) the Br···C distance (α_c = 180°) and (**b**) the α_c angle ($d_{Br\cdots C}$ = 3.5 Å) in the model supramolecular system bromobenzene-methyl formate. Colours code: green squares = ΔE_{FRZ}; blue circles = ΔE_{DISP}; red triangles = ΔE_{POL}; and yellow inverted triangles = ΔE_{CT}.

In summary, at short distances (≤ 2.9 Å), the interaction is repulsive because of the large Pauli exchange-repulsion. At medium distances (3.2 Å), the interaction becomes attractive due to a smaller ΔE_{FRZ} that is overcome by the sum of dispersion and orbital-based terms. For longer distances (≥ 3.5 Å), dispersion alone is able to stabilize the system, although polarization and charge transfer also contribute to the total stability to a lesser extent.

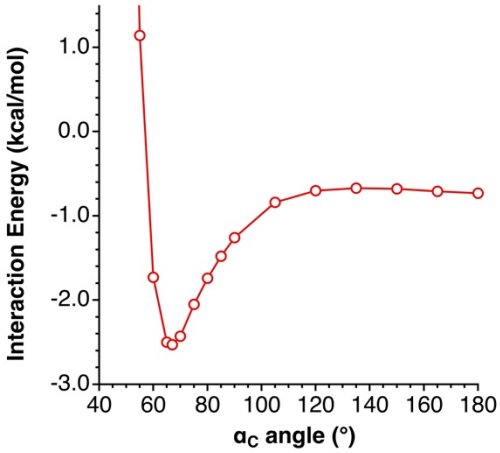

Figure 4.5. Total interaction energy as a function of the α_c angle (55 – 180°) at a Br···C distance of 3.5 Å in the model supramolecular system bromobenzene-methyl formate (See Appendix, Table A4.4).

The scan of the α_c angle was performed at the Br···C distance of 3.5 Å (Figure 4.4b). The first observation is that polarization and charge transfer terms do not vary significantly upon angle modification. On the other hand, dispersion is more variable, reaching a maximum at α_c = 90° and becoming smaller as the angle increases. However, the most interesting energy term is ΔE_{FRZ}, which is larger at 90° and smaller at 180° (1.45 and 1.15 kcal/mol, respectively). This is associated with a decrease in the Pauli exchange-repulsion energy when going from 90 to 180°. Such reduced repulsion for a linear arrangement is responsible for the counterintuitive overall stabilization of systems with α_c angles close to 180°. In fact, if the total interaction energy is represented as a function of the angle α_c (Figure 4.5), it can be clearly observed that α_c = 180° is a local minimum of the energy curve, although α_c = 67° is considerably lower in energy and thus, the global minimum. The steric clash between the phenyl and carbonyl groups produces a drastic increase in the interaction energy for α_c < 67º, being repulsive for α_c = 55º (see Appendix, Table A4.4). Note that, in more congested systems with bulkier substituents at the carbonyl, small angles might involve a considerably larger Pauli exchange-repulsion that displaces the energy minimum to larger angles. Therefore, it seems that the combination

of ΔE_{FRZ} and ΔE_{DISP} determines the subtle energy differences that allows the favourable establishment of interaction topologies with C-Br···C angles different from 80 – 90°. In a recent review, Alkorta and co-workers gave a general definition for weak interactions that exemplifies the situation we have here: *A weak interaction between a Lewis acid and a Lewis base is established if the stabilizing forces overcome the repulsion forces. It is not necessary that the complex should be the lowest minimum, it suffices that there is a barrier between the complex and other minima of lower energy.*[55]

4.6 Analysis of the Natural Bond Orbitals

Since orbital interactions have a considerable weight in the stabilization of bromine···carbonyl dimers (≈ 18% of the attractive terms in EDA), I have undertaken next an NBO analysis of the supramolecular systems in Table 4.1 to unveil the orbitals involved and the corresponding charge transfer processes. Remarkably, in all cases, there is an n→π* charge transfer interaction from a lone pair of Br into an empty antibonding π* orbital of the carbonyl, with associated second-order perturbation energies ranging from 0.08 kcal/mol in QEKMUP[43] to 0.52 kcal/mol in LUKQIT.[46] There is also a reasonable linear correlation between the energy of the $n_{Br}\rightarrow\pi^*_{CO}$ interaction and the intermolecular Br···C distance (Figure 4.6), as expected from the distance dependence of the overlap between the two orbitals involved. Similar relationships between second-order perturbation energies and the interatomic distances have been previously reported in the literature, for instance, in complexes of CO_2 with azoles[56] and in P···B pnicogen bonds.[57]

A charge transfer from the carbonyl to the bromine atom is also found for all systems. In this case, the occupied π bonding orbital of the carbonyl group acts as the donor, whereas a σ* C-Br antibonding orbital behaves as the acceptor. The NBO energies are between 0.14 and 0.43 kcal/mol per interaction. In this way, the overall stabilization of the short Br···C contact is due to these reciprocal charge transfer processes from the carbonyl to the bromine and viceversa. A simplified molecular orbital diagram is shown in Figure 4.7. Note that there is also some mixing between the C=O π* and the C-Br σ* orbitals that confers some extra stabilization to the system. Such interactions are also observed in the NBO analyses as $\pi^*_{C=O}\rightarrow\sigma^*_{C\text{-}Br}$ charge transfers with energies that can be as large as 0.58 kcal/mol in LUKQIT,[46] which features the shortest Br···C distance among all the studied systems. Those attractive interactions are partially counterbalanced

by Pauli exchange-repulsion from the electrons of the C-Br σ and C=O π orbitals, analogous to apparently different NCIs such as intermolecular $d^8\cdots d^8$ metal contacts.[58] The set of orbital interactions found here is similar to that in the Dewar-Chatt-Duncanson model, which has been used to explain the bonding between a π-acid ligand (e.g., an alkene) and a metal centre in some organometallic compounds.

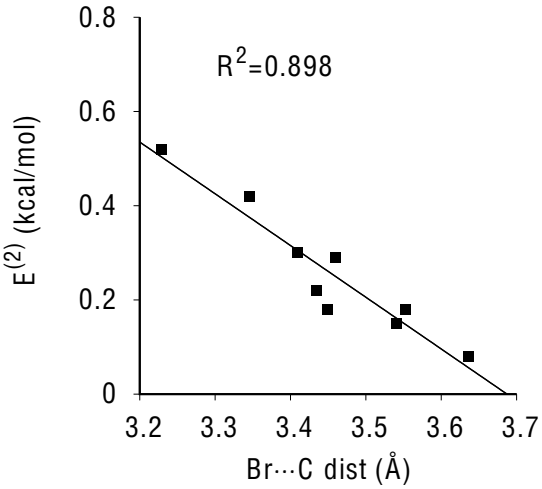

Figure 4.6. Relationship between the second-order perturbation energy of the $n_{Br}\rightarrow\pi^*_{CO}$ interaction (NBO analysis at M06-2X/def2-TZVP level) and the intermolecular Br···C=O distance for all the systems in Table 4.1 (for numerical data see Table A4.5 and Eq. A4.1 in the Appendix).

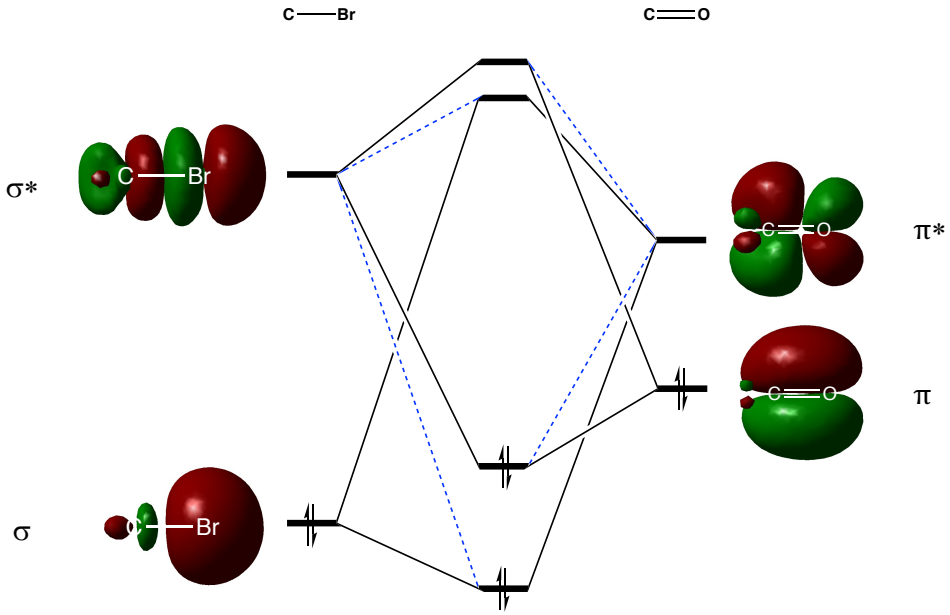

Figure 4.7. Qualitative molecular orbitals diagram for the interaction between C-Br and C=O moieties with perpendicular topology (α_c = 180°; β_c = 90°). Orbitals are depicted from an NBO calculation on FAHREM[38] at the M06-2X/def2-TZVP level of theory.

4.7 Conclusions

I have carried out a combined structural and computational analysis of short contacts between a bromine and the carbon atom of a carbonyl group. The CSD has been inspected first. As expected, the dominant interaction topology is that in which the C-Br···C angle (α_c) is close to 90°, favouring the interaction of the negatively charged region of the halogen atom with the π-hole of the carbonyl group. However, in 8.7% of the cases, a_c is greater than 150°, which should involve an electrostatic repulsion because both electron density depleted regions (the σ- and the π-holes in bromine and carbonyl, respectively) are in close contact. I have observed that such arrangements cannot be predicted by looking at the MEP maps of the molecules involved in the contact. Nevertheless, DFT calculations on several experimental dimers have demonstrated that the interactions are attractive even for α_c values as large as 175°, with interaction energies accounting for 1 kcal/mol per contact.

EDA analyses have allowed me to understand the physical nature of these interactions. In all cases, the frozen term, which comprises Pauli repulsion and electrostatic Coulomb interactions, is repulsive. Such repulsion is compensated by dispersion forces and orbital-based interactions, namely, polarization and charge transfer. As expected, orbital interactions are more relevant at short Br···C distances, whereas Pauli repulsion is diminished as the interatomic distance increases. I have also analysed the α_c angle dependence of the components of the interaction energy in a simplified model. The subtle interplay of dispersion and steric terms makes possible the presence of a local energy minimum at α_c = 180° despite that the global minimum is located at α_c = 65 – 70°, with a small energetic barrier between them (ca. 140°). This allows us to explain the existence of experimental structures with α_c angles greater than 150°.

I have also seen that orbital interactions represent 18% of the total attractive EDA terms in the studied experimental adducts. A comprehensive NBO analysis has shown the beautiful interplay of charge transfer between four orbitals that stabilizes the systems. An n→π* interaction from a Br lone pair into an antibonding π* orbital of the carbonyl is complemented with another charge transfer from a bonding π orbital of the carbonyl into a σ* antibonding orbital at the C-Br covalent bond.

These results show the existence of interactions that remain hidden by looking at MEP maps as the only predictors. Such interactions, both supported and unsupported, do

exist in experimental systems and are strong enough to drive the formation of crystal structures. Thus, not only electrostatics but also the combination of all the forces in play (Pauli repulsion, dispersion, polarization, and charge transfer) must be taken into account when analysing (or predicting) noncovalent interactions. I think these findings contribute to increase our understanding of the interplay of forces that govern the establishment of short contacts between atoms and they will stimulate the use of new approaches in the search for new noncovalent interactions.

4.8 Appendix

Annex 4.1. Analysis of the Interaction Energies.

Table A4.1. Interaction energies for all experimental Br···C=O adducts, represented in Table 4.1.

refcode	ΔE_{INT} (kcal/mol)
FAHREM	-1.29
MADLEK	-3.01
KUTVAX	-1.25
DBTCHY	-2.37
QEKMUP	-5.28
LOQQOX	-0.73
IYIHEE	-2.84
LUKQIT	-4.69
GATZIM	-1.23

Annex 4.2. Energy Decomposition Analysis.

Table A4.2. Energy Decomposition Analysis results calculated at the M06-2X/def2-TZVP level of theory on the model system bromobenzene···methyl formate at different Br···C distances with a linear C-Br···C moiety (α_c = 180°), represented in Figure 4.4a. The ΔE_{FRZ} term does not include dispersion. All energies are given in kcal/mol.

$d_{Br\cdots C}$	ΔE_{FRZ}	ΔE_{PAULI}	ΔE_{ELEC}	ΔE_{DISP}	ΔE_{POL}	ΔE_{CT}	ΔE_{INT}
2.6	20.73	40.20	-19.47	-7.45	-0.92	-3.76	8.60
2.9	7.95	17.66	-9.72	-4.85	-0.45	-1.43	1.22
3.2	3.02	7.51	-4.49	-2.82	-0.26	-0.56	-0.62
3.5	1.15	3.10	-1.95	-1.56	-0.12	-0.20	-0.73
3.8	0.43	1.24	-0.81	-0.90	-0.04	-0.06	-0.57
4.1	0.16	0.48	-0.32	-0.59	-0.02	-0.02	-0.46

Table A4.3. Energy Decomposition Analysis results calculated at the M06-2X/def2-TZVP level of theory on the model system bromobenzene···methyl formate for different angles at a fixed Br···C distance of 3.5 Å, represented in Figure 4.4b. The ΔE_{FRZ} term does not include dispersion. All energies are given in kcal/mol.

α_c	ΔE_{FRZ}	ΔE_{PAULI}	ΔE_{ELEC}	ΔE_{DISP}	ΔE_{POL}	ΔE_{CT}	ΔE_{INT}
90	1.45	4.99	-3.54	-2.29	-0.16	-0.26	-1.26
105	1.51	4.85	-3.34	-1.98	-0.12	-0.25	-0.84
120	1.48	4.53	-3.05	-1.83	-0.11	-0.24	-0.70
135	1.37	4.03	-2.65	-1.71	-0.11	-0.23	-0.68
150	1.25	3.51	-2.26	-1.61	-0.11	-0.22	-0.68
165	1.16	3.16	-2.00	-1.55	-0.11	-0.21	-0.71
180	1.15	3.10	-1.95	-1.56	-0.12	-0.20	-0.73

Table A4.4. Interaction energies at different angles α_c for the model system bromobenzene···methyl formate, represented in Figure 4.5.

α_c	ΔE_{INT} (kcal/mol)	α_c	ΔE_{INT} (kcal/mol)
55	1.14	90	-1.26
60	-1.73	105	-0.84
65	-2.50	120	-0.70
67	-2.53	135	-0.68
70	-2.43	150	-0.68
75	-2.05	165	-0.71
80	-1.74	180	-0.73
85	-1.48		

Annex 4.3. Natural Bond Orbital Analysis.

Table A4.5. Second-order perturbation energy of the $n_{Br} \rightarrow \pi^*_{CO}$ interaction (NBO analysis at M06-2X/def2-TZVP level) and the intermolecular Br···C=O distance for all the systems in Table 4.1, represented in Figure 4.6.

refcode	$d_{Br\cdots C}$ (Å)	$E^{(2)}$ (kcal/mol)	refcode	$d_{Br\cdots C}$ (Å)	$E^{(2)}$ (kcal/mol)
FAHREM	3.553	0.18	LOQQOX	3.540	0.15
MADLEK	3.409	0.30	IYIHEE	3.460	0.29
KUTVAX	3.449	0.18	LUKQIT	3.229	0.52
DBTCHY	3.345	0.42	GATZIM	3.434	0.22
QUEKMUP	3.636	0.08			

Annex 4.3.1. Linear least-squares fitting equation for Figure 4.6.

$$E^{(2)} = 4.05 - 1.10 \cdot d_{Br\cdots C} \qquad (R^2 = 0.90) \qquad \text{[Eq. A4.1]}$$

4.9 References

1. Zhao, Y.; Cotelle, Y.; Sakai, N.; Matile, S. Unorthodox Interactions at Work. *J. Am. Chem. Soc.* **2016**, *138*, 4270-4277.
2. Bauzá, A.; Mooibroek, T. J.; Frontera, A. The Bright Future of Unconventional *σ*/*π*-Hole Interactions. *ChemPhysChem* **2015**, *16*, 2496-2517.
3. Cerny, J.; Hobza, P. Non-covalent interactions in biomacromolecules. *Phys. Chem. Chem. Phys.* **2007**, *9*, 5291-5303.
4. Thirman, J.; Engelage, E.; Huber, S. M.; Head-Gordon, M. Characterizing the interplay of Pauli repulsion, electrostatics, dispersion and charge transfer in halogen bonding with energy decomposition analysis. *Phys. Chem. Chem. Phys.* **2018**, *20*, 905-915.
5. Duarte, D. J. R.; Sosa, G. L.; Peruchena, N. M.; Alkorta, I. Halogen bonding. The role of the polarizability of the electron-pair donor. *Phys. Chem. Chem. Phys.* **2016**, *18*, 7300-7309.
6. Wolters, L. P.; Smits, N. W. G.; Guerra, C. F. Covalency in resonance-assisted halogen bonds demonstrated with cooperativity in N-halo-guanine quartets. *Phys. Chem. Chem. Phys.* **2015**, *17*, 1585-1592.
7. Perera, M. D.; Desper, J.; Sinha, A. S.; Aakeröy, C. B. Impact and importance of electrostatic potential calculations for predicting structural patterns of hydrogen and halogen bonding. *CrystEngComm* **2016**, *18*, 8631-8636.
8. Jabłoński, M.; Palusiak, M. Nature of a hydride-halogen bond. A SAPT-, QTAIM-, and NBO-based study. *J. Phys. Chem. A* **2012**, *116*, 2322-2332.
9. Scheiner, S. Detailed comparison of the pnicogen bond with chalcogen, halogen, and hydrogen bonds. *Int. J. Quantum Chem* **2013**, *113*, 1609-1620.
10. Bortoli, M.; Ahmad, S. M.; Hamlin, T. A.; Bickelhaupt, F. M.; Orian, L. Nature and strength of chalcogen–*π* bonds. *Phys. Chem. Chem. Phys.* **2018**, *20*, 27592-27599.
11. Pascoe, D. J.; Ling, K. B.; Cockroft, S. L. The Origin of Chalcogen-Bonding Interactions. *J. Am. Chem. Soc.* **2017**, *139*, 15160-15167.

12. Alkorta, I.; Elguero, J.; Del Bene, J. E. Pnicogen Bonded Complexes of PO_2X (X = F, Cl) with Nitrogen Bases. *J. Phys. Chem. A.* **2013**, *117*, 10497-10503.
13. Scheiner, S. The Pnicogen Bond: Its Relation to Hydrogen, Halogen, and Other Noncovalent Bonds. *Acc. Chem. Res.* **2013**, *46*, 280-288.
14. Wang, C.; Aman, Y.; Ji, X.; Mo, Y. Tetrel bonding interaction: an analysis with the block-localized wavefunction (BLW) approach. *Phys. Chem. Chem. Phys.* **2019**, *21*, 11776-11784.
15. Franconetti, A.; Frontera, A. "Like–like" tetrel bonding interactions between Sn centres: a combined ab initio and CSD study. *Dalton Trans.* **2019**, *48*, 11208-11216.
16. Danovich, D.; Shaik, S.; Neese, F.; Echeverría, J.; Aullón, G.; Alvarez, S. Understanding the Nature of the CH···HC Interactions in Alkanes. *J. Chem. Theory Comp.* **2013**, *9*, 1977-1991.
17. Echeverría, J.; Aullón, G.; Danovich, D.; Shaik, S.; Alvarez, S. Dihydrogen contacts in alkanes are subtle but not faint. *Nature Chem.* **2011**, *3*, 323-330.
18. Echeverría, J.; Aullón, G.; Alvarez, S. Intermolecular interactions in group 14 hydrides: Beyond C−H···H−C contacts. *Int. J. Quantum Chem.* **2017**, *117*, e25432-e25446.
19. Echeverría, J. The silane-methane dimer revisited: more than a dispersion-bound system? *Phys. Chem. Chem. Phys.* **2017**, *19*, 32663-32669.
20. Mehrotra, P. K.; Hoffmann, R. Copper(I)-copper(I) interactions. Bonding relationships in d^{10}-d^{10} systems. *Inorg. Chem.* **1978**, *17*, 2187-2189.
21. Brands, M. B.; Nitsch, J.; Guerra, C. F. Relevance of Orbital Interactions and Pauli Repulsion in the Metal–Metal Bond of Coinage Metals. *Inorg. Chem.* **2018**, *57*, 2603-2608.
22. Echeverría, J. In(III)···In(III) short contacts: an unnoticed metallophilic interaction? *Chem. Commun.* **2018**, *54*, 6312-6315.
23. Echeverría, J. Frustrated Lewis Trios and Long-Range Hole Interactions: A Combined Structural and Theoretical Study of LB−AX_3···LB and LB···AX_3···LB (A=B, Al, Ga, In) Systems. *ChemPhysChem*. **2017**, *18*, 2864-2872.
24. Echeverría, J. The n→π^* interaction in metal complexes. *Chem. Commun.* **2018**, *54*, 3061-3064.
25. Echeverría, J. Intermolecular Carbonyl···Carbonyl Interactions in Transition-Metal Complexes. *Inorg. Chem.* **2018**, *57*, 5429-5437.

26. Velásquez, J. D.; Echeverría, J.; Alvarez, S. Effect of the Substituents on the Nature and Strength of Lone-Pair–Carbonyl Interactions in Acyl Halides. *Cryst. Growth Des.* **2019**, *19*, 6511-6518.
27. Kamer, K. J.; Choudhary, A.; Raines, R. T. Intimate Interactions with Carbonyl Groups: Dipole-Dipole or n→π*? *J. Org. Chem.* **2013**, *78*, 2099-2103.
28. Fischer, F. R.; Wood, P. A.; Allen, F. H.; Diederich, F. Orthogonal dipolar interactions between amide carbonyl groups. *Proc. Nat. Ac. Sci.* **2008**, *105*, 17290-17294.
29. Eskandari, K.; Lesani, M. Does Fluorine Participate in Halogen Bonding? *Chem. Eur. J.* **2015**, *21*, 4739-4746.
30. Yahia-Ouahmed, M.; Tognetti, V.; Joubert, L. Halogen–halogen interactions in perhalogenated ethanes: An interacting quantum atoms study. *Comput.and Theor. Chem.* **2015**, *1053*, 254-262.
31. Varadwaj, A.; Marques, H. M.; Varadwaj, P. R. Is the Fluorine in Molecules Dispersive? Is Molecular Electrostatic Potential a Valid Property to Explore Fluorine-Centered Non-Covalent Interactions? *Molecules* **2019**, *24*, 379-407.
32. Varadwaj, A.; Varadwaj, P. R.; Yamashita, K. Do surfaces of positive electrostatic potential on different halogen derivatives in molecules attract? like attracting like! *J. Comput. Chem.* **2018**, *39*, 343-350.
33. Varadwaj, A.; Varadwaj, P. R.; Jin, B.-Y. Can an entirely negative fluorine in a molecule, viz. perfluorobenzene, interact attractively with the entirely negative site(s) on another molecule(s)? Like liking like! *RSC Adv.* **2016**, *6*, 19098-19110.
34. Wang, C.; Danovich, D.; Shaik, S.; Wu, W.; Mo, Y. Attraction between electrophilic caps: A counterintuitive case of noncovalent interactions. *J. Comput. Chem.* **2019**, *40*, 1015-1022.
35. Varadwaj, P. R.; Varadwaj, A.; Marques, H. M.; Yamashita, K. Can Combined Electrostatic and Polarization Effects Alone Explain the F···F Negative-Negative Bonding in Simple Fluoro-Substituted Benzene Derivatives? A First-Principles Perspective. *Computation* **2018**, *6*, 51-84.
36. Zhao, T.; Zhou, J.; Wang, Q.; Jena, P. Like Charges Attract? *J. Phys. Chem. Lett.* **2016**, *7*, 2689-2695.
37. Varadwaj, A.; Varadwaj, P. R.; Marques, H. M.; Yamashita, K. Revealing Factors Influencing the Fluorine-Centered Non-Covalent Interactions in Some Fluorine-

Substituted Molecular Complexes: Insights from First-Principles Studies. *ChemPhysChem*. **2018**, *19*, 1486-1499.

38. Kobler, C.; Bohrer, A.; Effenberger, F. Hydroxynitrile lyase-catalyzed addition of HCN to 2- and 3-substituted cyclohexanones. *Tetrahedron* **2004**, *60*, 10397-10410.
39. Elacqua, E.; Kaushik, P.; Groeneman, R. H.; Sumrak, J. C.; Bučar, D.-K.; MacGillivray, L. R. A Supramolecular Protecting Group Strategy Introduced to the Organic Solid State: Enhanced Reactivity through Molecular Pedal Motion. *Angew. Chem. Int. Ed.* **2012**, *51*, 1037-1041.
40. Tang, X.-Y.; Wei, Y.; Shi, M. Ring-Opening Reaction of Methylenecyclopropanes Derived from Methylenecyclopropyl Aldehydes through Cope Rearrangement. *Eur. J. Org. Chem.* **2010**, *2010*, 6038-6042.
41. Jiang, J.-H. N'-(4-Bromobenzylidene)thiophene-2-carbohydrazide. *Acta Crystallogr. Sect. E.* **2010**, *66*, o922-o926.
42. Fleming, I.; Jones, P. G.; Kennard, O.; Michael, J. P. Bromine-initiated, silicon-assisted rearrangement in the norbornene series: crystal and molecular structure of 3-endo,5-endo-dibromotricyclo[2.2.1.0]heptane-7-carboxylic acid. *J. Chem. Soc., Perkin Trans.* 2. **1979**, 808-809.
43. Kalisiak, J.; Skowronek, P.; Gawroński, J.; Jurczak, J. New Macrocycles with Planar Chirality—Synthesis and Determination of Absolute Configurations. *Chem. Eur. J.* **2006**, *12*, 4397-4406.
44. Ohtsu, H.; Iwamoto, M.; Ohishi, H.; Matsunaga, S.; Tanaka, R. Standishinal, a novel carbon skeletal diterpene from the bark of Thuja standishii (Gord.) Carr. *Tetrahedron Lett.* **1999**, *40*, 6419-6422.
45. Sloman, D. L.; Bacon, J. W.; Porco, J. A. Total Synthesis and Absolute Stereochemical Assignment of Kibdelone C. *J. Am. Chem. Soc.* **2011**, *133*, 9952-9955.
46. Hu, D. X.; Seidl, F. J.; Bucher, C.; Burns, N. Z. Catalytic Chemo-, Regio-, and Enantioselective Bromochlorination of Allylic Alcohols. *J. Am. Chem. Soc.* **2015**, *137*, 3795-3798.
47. Sjoberg, P.; Politzer, P. Use of the electrostatic potential at the molecular surface to interpret and predict nucleophilic processes. *J. Phys. Chem.* **1990**, *94*, 3959-3961.
48. Murray, J. S.; Lane, P.; Clark, T.; Riley, K. E.; Politzer, P. σ-Holes, π-holes and electrostatically-driven interactions. *J. Mol. Model.* **2012**, *18*, 541-548.

49. Kozuch, S. Should "anion-π interactions" be called "anion-σ interactions"? A revision of the origin of some hole-bonds and their nomenclature. *Phys. Chem. Chem. Phys.* **2016**, *18*, 30366-30369.

50. Alkorta, I.; Elguero, J.; Del Bene, J. E. Exploring the PX_3:NCH and PX_3:NH_3 potential surfaces, with X=F, Cl, and Br. *Chem. Phys. Lett.* **2015**, *641*, 84-89.

51. Alkorta, I.; Perez, J. J.; Villar, H. O. Molecular polarization maps as a tool for studies of intermolecular interactions and chemical reactivity. *J. Mol. Graph.* **1994**, *12*, 3-13.

52. Alkorta, I.; Villar, H. O.; Perez, J. J. Effect of the basis set on the computation of molecular polarization. *J. Phys. Chem.* **1993**, *97*, 9113-9119.

53. Alkorta, I.; Perez, J. J. Molecular polarization potential maps of the nucleic acid bases. *Int. J. Quant. Chem.* **1996**, *57*, 123-135.

54. Echeverría, J. Noncovalent Interactions in Succinic and Maleic Anhydride Derivatives. *Cryst. Growth Des.* **2018**, *18*, 506-512.

55. Alkorta, I.; Elguero, J.; Frontera, A. Not Only Hydrogen Bonds: Other Noncovalent Interactions. *Crystals* **2020**, *10*, 180-208.

56. Del Bene, J. E.; Elguero, J.; Alkorta, I. Complexes of CO_2 with the Azoles: Tetrel Bonds, Hydrogen Bonds and Other Secondary Interactions. *Molecules* **2018**, *23*, 906-919.

57. Alkorta, I.; Elguero, J.; Del Bene, J. E. Borylene as an electron-pair donor for P···B pnicogen bonds. *Struct. Chem.* **2017**, *28*, 1419-1427.

58. Aullón, G.; Alemany, P.; Alvarez, S. On the existence of a pyramidality effect in $d^8\cdots d^8$ contacts. Theoretical study and structural correlation. *Inorg. Chem.* **1996**, *35*, 5061-5067.

Chapter 5

Experimental and theoretical study of Pb···S and Pb···O σ–hole bonds in the crystal structures of Pb(II) complexes

5.1 Introduction

Lead, despite its toxicity and the environmental problems associated to it,[1] is a very interesting element that can adopt different coordination geometries when forming compounds.[2] Furthermore, the inert pair effect allows the synthesis of many stable Pb(II) complexes. It is known that, in the crystal structures of such compounds, atoms of group 14 can engage in intermolecular *σ*-hole interactions with lone pairs of donor atoms to form what has been termed as tetrel bond.[3,4] *σ*-hole interactions occur between an electron-deficient region and an electron-rich species forming an electrostatic attraction as well as more or less significant electron delocalization from the lone pair into an empty orbital.[5,6] This dual nature strengthens the interaction and *σ*-hole bonding is usually used in supramolecular design and crystal design. For instance, *σ*-hole interactions have been used for the construction of metal Pb(II) organic frameworks (MOFs) by taking advantage of geometrically predictable Pb···O/S/N short contacts.[7-10]

From a topological point of view, the Pb centre must be hemidirectionally coordinated, i.e., the ligands are arranged in such a way that a gap in the coordination sphere is formed, available for the establishment of *σ*-hole interactions. A recent CSD survey showed that hemidirectional Pb(II) has a marked tendency to participate in intermolecular short contacts with donor groups that lie between the sum of the corresponding covalent and van der Waals radii.[11] However, and despite their abundance, these *σ*-hole interactions are not yet fully understood and a better knowledge of them should lead to simpler and accessible ways of exploiting them in solid state chemistry.

In this work, I have studied the *σ*-hole interaction between hemidirectional coordinated Pb(II) and O/S donor atoms. For this reason, I have theoretically studied and categorized the noncovalent interactions found in the crystal structures of two recently synthesized Pb(II) complexes of phenyl-thiosemicarbazone-based ligands with an anionic coligand (**HL^1** y **HL^2**, Scheme 5.1).[12] The ligands coordinate to the Pb(II) metal centre in a tridentate fashion *via* two nitrogen and one sulphur donor atoms in either a mono-deprotonated or a neutral form (Scheme 5.1). Single-crystal X-ray crystallography reveals that the molecular complexes aggregate into larger entities depending on weak interactions. The Pb(II) centre is hemidirectionally coordinated and, consequently, it is sterically suitable for establishing *σ*-hole bonding interactions. Thus, in the crystal structures of both complexes, the Pb atom participates in short contacts with oxygen or

sulphur atoms, that can be defined as noncovalent tetrel bonding interactions. I have analysed the interesting supramolecular assemblies observed in the solid state of both complexes by means of DFT calculations and characterized them using the Bader's Quantum Theory of Atoms in Molecules (QTAIM) and Natural Bond Orbital (NBO) analyses.

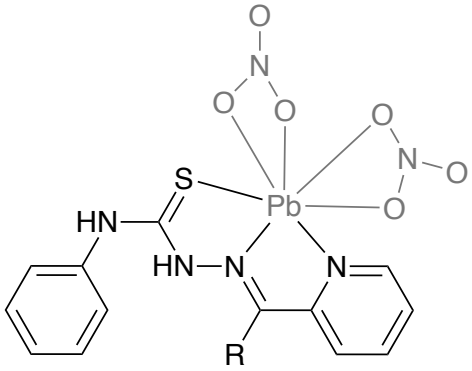

Scheme 5.1. Complexes **1** and **2** studied in this section, R = H (**HL**[1]) or Ph (**HL**[2]). Pb atom and NO_3^- anions are coloured in grey.

5.2 Analysis of the topology of the electron density

I have performed a theoretical analysis of the species **1** and **2** in their crystal structures to gain further insight into the interactions that hold them together. In **1**, the Pb atoms show intermolecular short contacts to the oxygen atoms of the NO_3^- chelating ligands (Pb···O = 2.934 and 3.125 Å; Figure 5.1a). I will focus then on these particular interactions involving the Pb centres. The topology of the electron density has been analysed by means of the QTAIM[13] analyses.

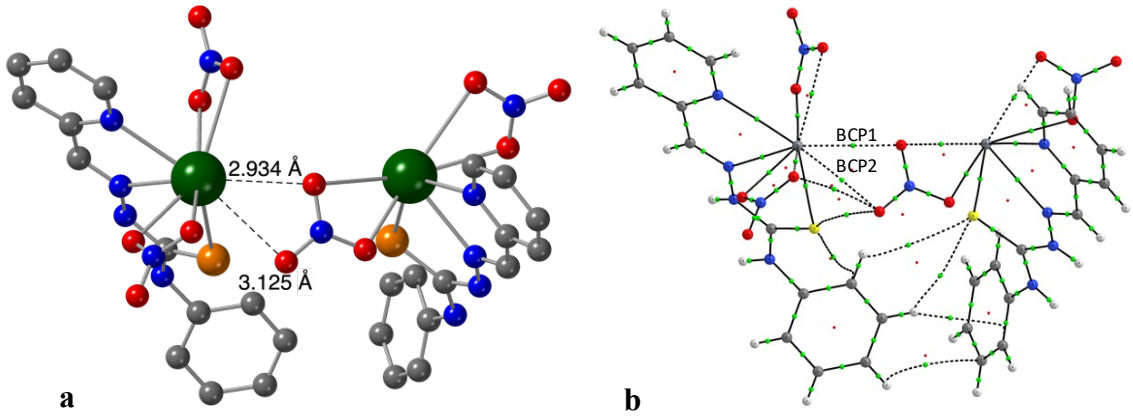

Figure 5.1. (**a**) Short Pb···O contacts in the crystal structure of **1**. (**b**) QTAIM molecular graph of the interactions found in **1** showing the BCPs as green points (BCP1 = 0.0175 and BCP2 = 0.0120 a.u.). Colour code (**a**): grey, C; blue, N; red, O; green, Pb; and orange, S.

I have found bond paths (BPs) between the Pb and the two donor O atoms as shown in Figure 5.1b confirming the tetrel interaction. The values of the electron density at the associated bond critical points (BCPs) are 0.0175 and 0.0120 a.u. for BCP1 and BCP2, respectively, in good agreement with previous reports for similar interactions.[7,9] The QTAIM results also show C–H···π interactions and C–H···S hydrogen bonds between the two molecules as characterized by the corresponding bond paths (Figure 5.1b). The calculated interaction energy associated to the latter dimer is −10.42 kcal/mol.

Next, I have focused on the crystal structure of compound **2**. As shown in Figure 5.2, the molecules are arranged in such a way that they form a 1D chain connected by Pb···S interactions (3.253 and 3.323 Å in crystallographic directions *b* and *a*, respectively). The interaction energy of the dimer displaying two intermolecular Pb···S contacts at 3.323 Å is −15.31 kcal/mol (Figure 5.3a). On the other hand, in the *b* crystallographic direction, I have calculated an interaction energy of −15.47 kcal/mol, for the dimer associated with a Pb···S contact at 3.253 Å and a Pb···O interaction at 3.129 Å (Figure 5.3b). In order to estimate the strength of solely the Pb···S interaction, I have modified the geometry by orientating the interacting NO_3^- group towards the outer part of the molecule, avoiding in this way any Pb···O short contact (the Pb···O distance is now 6.56 Å, see Figure A5.1 in the Appendix). The calculated interaction energy is −10.83 kcal/mol, which also allows me to estimate the strength of the Pb···O short contact (≈ 4.50 kcal/mol).

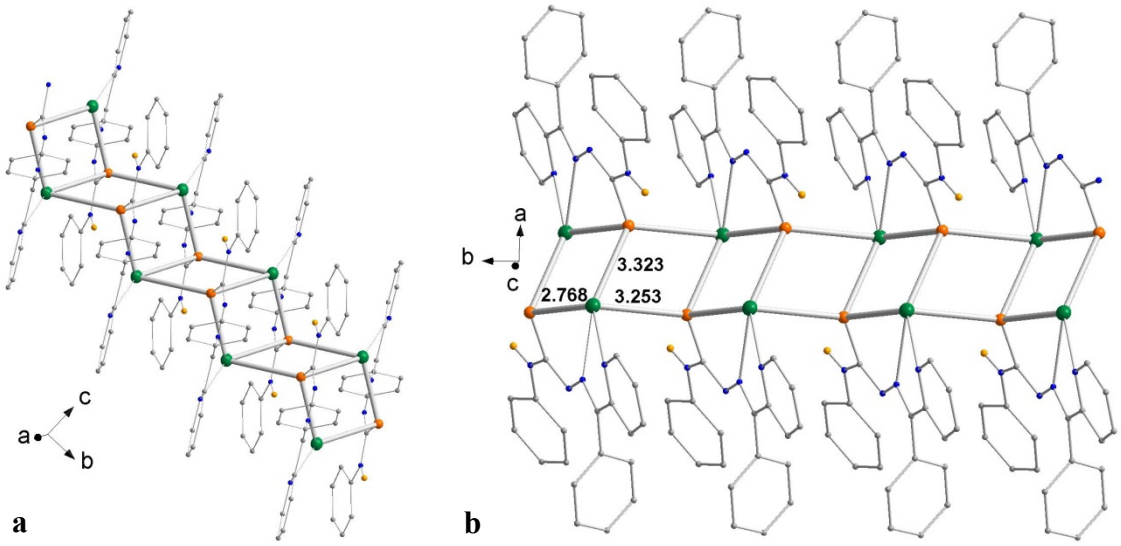

Figure 5.2. Polymeric structure of complex **2** formed by Pb−S bonding interactions in the (**a**) *a* and (**b**) *b* crystallographic directions (distances in Å).

The QTAIM analysis of the dimer of Figure 5.3a clearly shows that Pb···S interactions are the only ones holding the two molecules together (Figure 5.3c). The value of the electron density at the bond critical points BCP3 and BCP4 is 0.0163 a.u. and, more interestingly, the value of the delocalization index DI(Pb,S) at the same BCPs is considerably large (0.1764 a.u.), indicating some degree of charge transfer between the two atoms. The picture of the dimer with a Pb···S contact at 3.253 Å (Figure 5.3b) is more complex since more interactions are present in the QTAIM graph (Figure 5.3d). Besides the Pb···S and Pb···O contacts, a plethora of noncovalent interactions (π/π, C–H···π, and C–H···O) are determined by bond paths and BCPs. BCP6, which corresponds to the shortest Pb···S contact, presents the highest value of the electron density among all those characterized here (0.0177 a.u.). The values of several properties for all the BCPs analysed here can be found in the Appendix (Table A5.1).

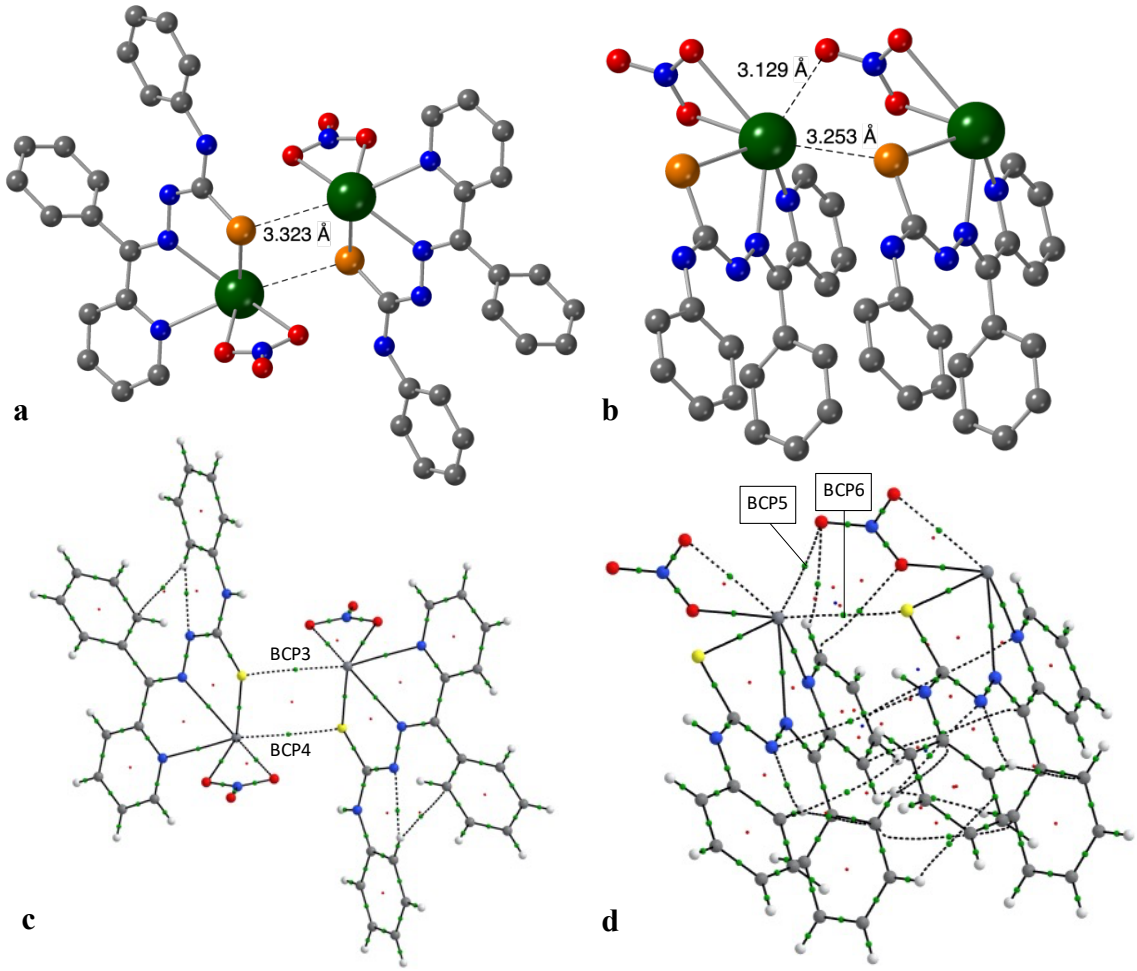

Figure 5.3. The two dimers analysed in the crystal structure of **2** in the (**a**) *a* and (**b**) *b* crystallographic directions, and their corresponding QTAIM molecular graphs (**c** and **d**). BCPs are shown as green points (BCP3/BCP4 = 0.0163, BCP5 = 0.0122, and BCP6 = 0.0177 a.u.). Colour code (**a** and **b**): grey, C; blue, N; red, O; green, Pb; and orange, S.

5.3 Analysis of the Noncovalent Interactions Index

Since many BCPs and BPs are found in the QTAIM analysis depicted in Figure 5.3d, I have performed a Noncovalent Interactions (NCI) Index[14,15] analysis of the dimer to try to clarify the presence of different interactions. The Pb···S and Pb···O interactions are clearly present (Figure 5.4, green surfaces between the corresponding atoms). Moreover, secondary interactions between the aromatic ligands are of the type π/π and C-H···π as already observed in the QTAIM molecular graph of Figure 5.3d.

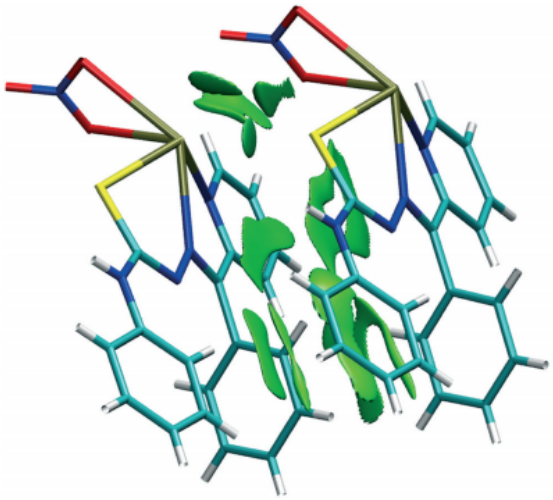

Figure 5.4. NCI isosurfaces (s = 0.3) of the dimer **2** in the *b* crystallographic direction. The isosurfaces are coloured according to a BRG scheme from $-0.035 < \text{sign}(\lambda_2)\rho < 0.030$ a.u. Green areas represent regions of weak noncovalent interactions.

5.4 Analysis of the Molecular Electrostatic Potential

With significant electrostatic contribution to the interaction energy, σ-hole interactions can also be characterized by mapping the Molecular Electrostatic Potential (MEP) of the molecules involved since electron rich regions with negative values of MEP are prone to interact with electron deficient regions of positive MEP.[16-19] In the MEP map of complex **2**, the two areas are clearly differentiated (Figure 5.5): the sulphur and the oxygen atoms of the nitrato ligand with negative MEP and, on the other hand, the exposed region of the Pb atom with positive MEP. This is consistent with the interaction pattern present in the crystal structure of **2**, where these two regions interact with each other to establish Pb···O/S interactions.

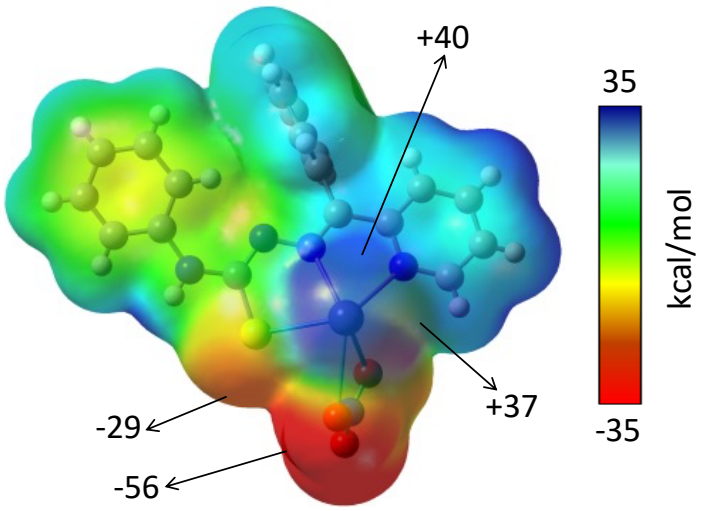

Figure 5.5. MEP map of compound **2**, calculated at the M06-2X/def2-TZVP level and plotted on the electron density isosurface (s = 0.001 Å). Energies are given in kcal/mol. Red and blue colours indicate less and more positive MEP values, respectively.

5.5 Analysis of the Natural Bond Orbitals

Since tetrel interactions also have a non-negligible orbital character, which has also been suggested by the calculated delocalization indexes in my QTAIM study above, I have performed a NBO analysis of the two short Pb···S contacts present in the crystal structure of **2**. In both cases NBO discloses an interaction between the S lone pairs and a Pb empty orbital. For the Pb···S contact at 3.323 Å such interaction accounts for 14.89 kcal/mol whereas in the contact at 3.253 Å the associated NBO energy is 17.59 kcal/mol. This is in good agreement with the observed interatomic distances since a shorter contact should increase the orbital overlap. The electron delocalization is confirmed by looking at the occupancies of the orbitals involved in the interaction. For instance, for the contact at 3.253 Å, the S lone pair orbitals contain 1.949 and 1.818 electrons, respectively, while the occupancy of the acceptor orbital at the Pb is 0.1897.

5.6 Conclusions

In this chapter, I have analysed the tetrel interactions found in the crystal structure of two novel Pb(II) complexes with phenyl-thiosemicarbazone Schiff base ligands. In their crystal structures, these complexes show hemidirected coordination modes that allow them to establish σ-hole interactions with lone pairs from oxygen and sulphur atoms. The Pb···O/S contact distances are longer than the sum of the covalent radii and shorter than the sum of the van der Waals radii.

The strength of the interactions has been calibrated by means of DFT calculations and their nature studied via QTAIM, MEP and NBO analyses. The σ-holes interactions studied here show associated interaction energies between 10 and 15 kcal/mol. Moreover, I have observed that both electrostatic and orbital interactions contribute to the total attraction between Pb and S. On one hand, the electrostatic attraction can be rationalized in terms of the electrostatic potential of the interacting regions and, on the other hand, NBO analyses have revealed a charge transfer from S lone pairs to an empty orbital of Pb. The secondary interactions that present the adducts prevent us from further studying the Pb···O contact. These results are expected to be useful for the development of new Pb-containing MOFs in which the supramolecular assembly is dominated by σ-hole (tetrel) bonding.

5.7 Appendix

Annex 5.1. Analysis of the topology of the electron density.

Table A5.1. Values for selected AIM parameters calculated for BCPs 1-6 (X = O and S).

	ρ	**$\nabla^2\rho$**	**δ(Pb,X)**	**ε**
BCP1	0.0175	0.0605	0.1110	0.0677
BCP2	0.0120	0.0418	0.0599	0.1147
BCP3	0.0163	0.0378	0.1764	0.1283
BCP4	0.0163	0.0378	0.1764	0.1283
BCP5	0.0122	0.0404	0.0779	0.0173
BCP6	0.0177	0.0431	0.1761	0.1013

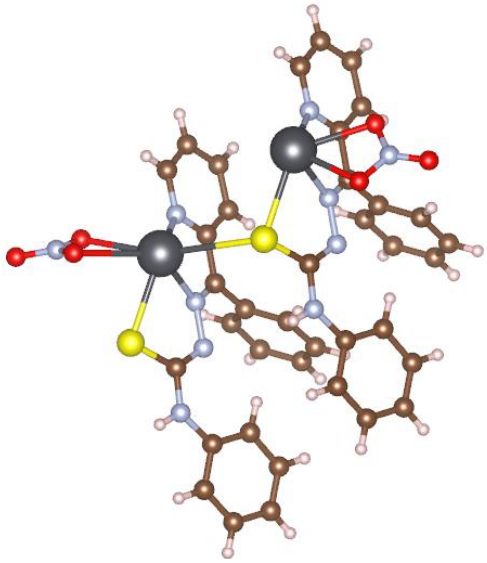

Figure A5.1. Dimer of **1** modified to preclude Pb···O short contact. Colour code: pink, H; brown, C; blue, N; red, O; yellow, S; and black, Pb.

5.8 References

1. Gidlow, D. A. Lead toxicity. *Arch. Environ. Occup. Health*. **2015**, *65*, 348-356.
2. Parr, J. Some recent coordination chemistry of lead(II). *Polyhedron*. **1997**, *16*, 551-566.
3. Bauzá, A.; Seth, S. K.; Frontera, A. Tetrel Bonding Interactions at Work: Impact on Tin and Lead Coordination Compounds. *Coord. Chem. Rev.* **2019**, *384*, 107-125.
4. Bauzá, A.; Mooibroek, T. J.; Frontera, A. Tetrel-Bonding Interaction: Rediscovered Supramolecular Force? *Angew. Chem. Int. Ed.* **2013**, *52*, 12317-12321.
5. Murray, J. S.; Lane, P.; Politzer, P. Expansion of the σ-Hole Concept. *J. Mol. Model.* **2009**, *15*, 723-729.
6. Murray, J. S.; Lane, P.; Clark, T.; Riley, K. E.; Politzer, P. σ-Holes, π-Holes and Electrostatically-Driven Interactions. *J. Mol. Model.* **2012**, *18*, 541-548.
7. Seth, S. K.; Bauzá, A.; Mahmoudi, G.; Stilinović, V.; López-Torres, E.; Zaragoza, G.; Keramidas, A. D.; Frontera, A. On the Importance of Pb···X (X = O, N, S, Br) Tetrel Bonding Interactions in a Series of Tetra- and Hexa-Coordinated Pb(II) Compounds. *CrystEngComm*. **2018**, *20*, 5033-5044.
8. Mahmoudi, G.; Zangrando, E.; Mitoraj, M. P.; Gurbanov, A. V.; Zubkov, F. I.; Moosavifar, M.; Konyaeva, I. A.; Kirillov, A. M.; Safin, D. A. Extended Lead(II) Architectures Engineered via Tetrel Bonding Interactions. *New J. Chem*. **2018**, *42*, 4959-4971.
9. Mahmoudi, G.; Seth, S. K.; Bauzá, A.; Zubkov, F. I.; Gurbanov, A. V.; White, J.; Stilinović, V.; Doert, T.; Frontera, A. Pb···X (X = N, S, I) Tetrel Bonding Interactions in Pb(II) Complexes: X-Ray Characterization, Hirshfeld Surfaces and DFT Calculations. *CrystEngComm*. **2018**, *20*, 2812-2821.
10. Mahmoudi, G.; Bauzá, A.; Frontera, A.; Garczarek, P.; Stilinović, V.; Kirillov, A. M.; Kennedy, A.; Ruiz-Pérez, C. Metal–Organic and Supramolecular Lead(II) Networks Assembled from Isomeric Nicotinoylhydrazone Blocks: The Effects of Ligand Geometry and Counter-Ion on Topology and Supramolecular Assembly. *CrystEngComm*. **2016**, *18*, 5375-5385.
11. Servati Gargari, M.; Stilinović, V.; Bauzá, A.; Frontera, A.; McArdle, P.; Van Derveer, D.; Ng, S. W.; Mahmoudi, G. Design of Lead(II) Metal-Organic

Frameworks Based on Covalent and Tetrel Bonding. *Chem. – Eur. J*. **2015**, *21*, 17951-17958.

12. Velasquez, J. D.; Mahmoudi, G.; Zangrando, E.; Gurbanov, A. V.; Zubkov, F. I.; Zorlu, Y.; Masoudiasl, A.; Echeverría, J. Experimental and Theoretical Study of Pb···S and Pb···O σ-Hole Interactions in the Crystal Structures of Pb(II) Complexes. *CrystEngComm*. **2019**, *21*, 6018-6025.
13. Bader, R. F. W. Atoms in Molecules: A Quantum Theory, Clarendon Press, Oxford, 1990.
14. Johnson, E. R.; Keinan, S.; Mori-Sánchez, P.; Contreras-García, J.; Cohen, A. J.; Yang, W. Revealing Noncovalent Interactions. *J. Am. Chem. Soc.* **2010**, *132*, 6498-6506.
15. Contreras-García, J.; Johnson, E. R.; Keinan, S.; Chaudret, R.; Piquemal, J.-P.; Beratan, D. N.; Yang, W. NCIPLOT: A Program for Plotting Noncovalent Interaction Regions. *J. Chem. Theory Comput*. **2011**, *7*, 625-632.
16. Echeverría, J. The Silane–Methane Dimer Revisited: More than a Dispersion-Bound System? *Phys. Chem. Chem. Phys.* **2017**, *19*, 32663-32669.
17. Echeverría, J. Alkyl Groups as Electron Density Donors in π-Hole Bonding. *CrystEngComm*. **2017**, *19*, 6289-6296.
18. Echeverría, J. Frustrated Lewis Trios and Long-Range Hole Interactions: A Combined Structural and Theoretical Study of LB-AX_3···LB and LB···AX_3···LB (A=B, Al, Ga, in) Systems. *Chemphyschem*. **2017**, *18*, 2864-2872.
19. Echeverría, J. Noncovalent Interactions in Succinic and Maleic Anhydride Derivatives. *Cryst. Growth Des.* **2018**, *18*, 506-512.

Chapter 6

Bonding Analysis in Halonium Compounds

6.1 Introduction

A halogen bond is a highly directional noncovalent interaction between a nucleophilic Lewis base (D) and the electrophilic region of a polarized halogen atom (X).[1] In terms of geometry, bond strength, and origin of the interaction, halogen bonds are similar to hydrogen bonds.[2-7] In some cases, both interactions are found competing[8] or cooperating simultaneously.[9,10] Like tetrel,[11] pnicogen,[12] and chalcogen[13] bonds, the nature of the interaction can be rationalized in terms of a σ-hole interaction[14,15] with non-negligible contributions from charge transfer, dispersion, and polarization.[4-7,16] In contrast to the classical two-centre halogen bond R-X$\cdots$D, in which a covalently-bonded neutral halogen interacts with a Lewis base (D), the electron-deficient halonium ions (X^+) tend to interact simultaneously with two Lewis bases. The resulting linear three-centre bond, $[D\cdots X\cdots D]^+$, is held together by four electrons with the charge distributed over the entire system (Scheme 6.1).[17]

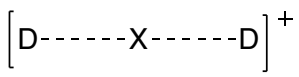

Scheme 6.1. Structure of a halonium cation (X = halogen, D = neutral Lewis base).

The three-centre-four-electron (3c-4e) bonding in halonium ions (X= Cl, Br, and I) is a hypercoordinated system in which the central atom exceeds the octet rule. These strong[18,19] noncovalent complexes with short interatomic distances have attracted interest due to their applicability as synthetic reagents and in the design of complex supramolecular structures.[17,20-24] The nature of such interaction can be described in terms of orbital and electrostatic contributions,[25-30] with smaller contribution of dispersion forces.[26] According to the Pimentel-Rundle[31-33] three-centre model, the halogen cation interacts simultaneously with two Lewis bases by accepting electrons in both lobes of its empty p-orbital. Consequently, three atomic orbitals combine to form three molecular orbitals (Figure 6.1). Two electrons are in the bonding orbital and two in the non-bonding orbital, remaining the antibonding orbital unfilled.[17,19]

Alternatively, one could consider a halonium ion as due to the interaction between two closed-shell groups, D-X^+ and D, to which the σ-hole formalism could be applied, since the anisotropic electron distribution of D-X^+ forms a σ-hole that can establish a Coulombic interaction with the electron density of the lone pair of the incoming donor. Since the σ-hole originates from the lobe of the empty p-orbital of the cationic halogen

atom, X^+, Hakkert has proposed that the two partially positively charged regions of X^+ may best be termed as p-holes.[25]

Notice that a trihalide anion, X_3^-, can be considered as a central halogen cation bonded to two terminal halides, $X^-\cdots X^+\cdots X^-$, the main difference with halonium cations being that the whole assembly is in this case negatively charged. Unsurprisingly, the MO diagram for the trihalides[45] is identical to that of the halonium cations (Figure 6.1). In a similar way, X_3^- can also be described as X_2 and X^- interacting units that could be rationalized by the σ-hole model.

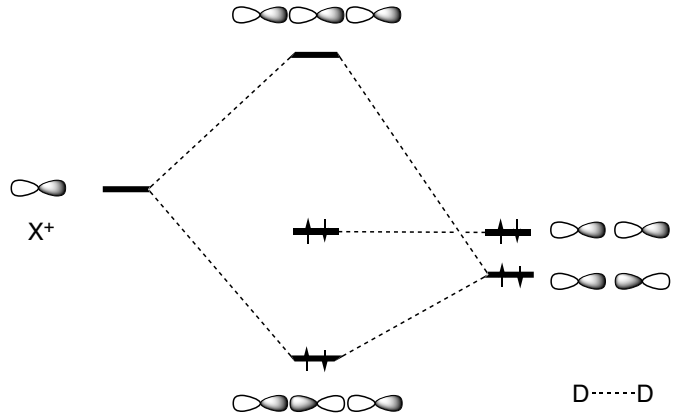

Figure 6.1. Molecular orbital diagram for the 3c-4e halonium bond, $[D\cdots X\cdots D]^+$, for X = Cl, Br, and I.

In the case of the fluoronium complexes, $[D\cdots F\cdots D]^+$, computational studies for D = pyridine suggest that it is best described as $[D\text{-}F]^+\cdots D$ ion-molecule complexes[27] since they prefer an asymmetric geometry with one classical covalent bond (1.360 Å) and a second, weaker and longer halogen bond (3.499 Å).[26] Indeed, it is necessary a highly electron-withdrawing group directly attached to the F centre, thereby improving its σ-hole, to form $[D\cdots F\cdots D]^+$ complexes.[17]

When D is a N-donor base, $[N\cdots I\cdots N]^+$ complexes are static and symmetric in both the solid state and in solution,[19,26,28] regardless of the solvent polarity[35] and the size, charge distribution or coordination strength of the counterion.[36] The effect of the substituents on the electron density of the $[N\cdots I\cdots N]^+$ halonium bond was assessed upon symmetric modulation of the para-position of [bis(4-R-pyridine)iodine]$^+$ model[17,37] and the geometrically restrained [1,2-bis((4-R-pyridine-2-ylethynyl)benzene)iodine]$^+$ complex.[37] To the best of my knowledge, no attempts at analysing the impact of the

electron density alteration on the strength and nature of the bond have been reported when the R groups are located at orto, double orto, meta and double meta-positions relative to the pyridine nitrogen.

Herein, I present a combined structural and computational study of the $[N\cdots I\cdots N]^+$ halonium bond. By means of DFT calculations, the geometry and strength of the 3c-4e halonium bond were studied from various aspects in the present work: (1) the effect of various halogen atoms (X) on the $[py\cdots X\cdots py]^+$ framework, (2) the effect of different nitrogen-donor groups (D) attached to the iodonium cation and (3) the influence of the electron density alteration on the $[N\cdots I\cdots N]^+$ halonium bond by variation of the R substituents at the N-donor. The MN12-SX method was selected after an extensive benchmark study carried out with 10 common DFT functionals along with the second-order Møller-Plesset perturbation theory (MP2) for the prediction of the geometry and interaction energy of bis(Acetonitrile)-iodonium cation (BUKNAX;[40] Figure 6.2). The results were compared with the experimental and calculated data at the coupled cluster singles and doubles (CCSD) and Perturbative Triple excitations (CCSD(T)) level (see Table A6.1 in the Appendix). The covalent vs dative character of the X···N bond in the bis-pyridine halonium cations was discussed by Georgiou and co-workers using both theorical and synthetic techniques. They concluded that the removal of the "first" pyridine is clearly heterolytic, both in gas phase an in the presence of solvent force fields.[27] In the light of these results, I have focussed the analysis on the heterolytic dissociation of the halonium ions (Scheme 6.2). To further investigate the nature of the interaction and the factors that affect its strength I have performed Molecular Electrostatic Potential (MEP) and Energy Decomposition Analyses (EDA) of the same compounds in Scheme 6.2. Since the interaction strength of the halonium bond is related to the positive value of the electrostatic potential ($V_{s,max}$) at the σ-hole and the anisotropic distribution of charge around the halogen atom,[38] I have paid special attention to search for possible correlations between the value of $V_{s,max}$ and computed geometrical and/or energetic descriptors.

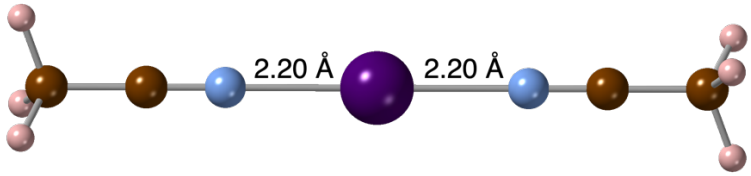

Figure 6.2. Short I···N contacts in the crystal structure of BUKNAX[40] cation. Colour code: pink, H; brown, C; blue, N.; and purple, I.

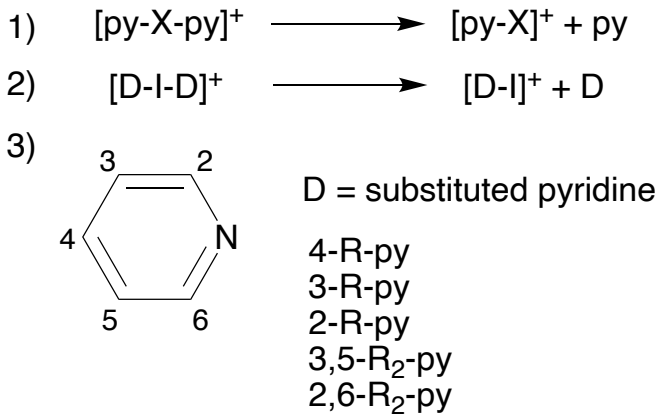

Scheme 6.2. Heterolytic cleavage reactions considered in this study.

6.2 Structural Analysis

I have searched the Cambridge Structural Database (CSD)[39] for dicoordinated compounds containing a [N···X···N] central framework with X···N contacts shorter than the sum of the van der Waals radii. In my searches, the central atom X was set to be I^+, known to form linear and highly symmetric three-centre-four-electron bonds.[40-43]

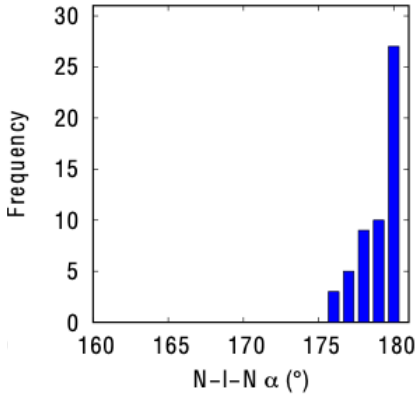

Figure 6.3. N-I-N angle distribution for dicoordinated compounds containing a [N···I···N] central framework.

Only linear $[N\cdots I\cdots N]^+$ halonium systems with neutral donors (Figure 6.3) have been reported in the CSD database, all having angles between 175º and 180º. This result is consistent with the proposal that the central atom employs an empty atomic p-orbital to interact with the N lone pairs of the two donors and thereby give raise to practically linear [N···I···N] frameworks (Figure 6.1). Altogether, 37 crystal structures were found, one with sp nitrogen attached to the iodonium cation (BUKNAX),[40] 35 with sp^2 nitrogen and one with sp^3 nitrogen (HMTITI).[41] Among the sp^2 nitrogen compounds, three are non-aromatic in a $R_3P{=}N{-}I$ phosphazene moiety (HINXIL[42], HINXOR,[42] and

KABRUB[43]). The average I···N distance in these structures is 2.26 Å and the average N···I···N angle is 179º. The difference of less than 3 % between both I···N bond lengths can be attributed to crystal packing forces. Thus, the complexes show an overall symmetric $[N\cdots I\cdots N]^+$ geometry in the solid state. The shortest contact is found for BUKNAX[40] (Figure 6.2), with two identical I···N distances of 2.20 Å, i.e., 1.5 Å shorter than the sum of the van der Waals radii (3.70 Å).[44]

6.3 Analysis of the Molecular Electrostatic Potential

6.3.1 Effect of the central atom X

Figure 6.4 shows the MEP maps of $[X\cdots NC_5H_5]^+$ complexes (X = F, Cl, Br, and I). These systems were selected to evaluate the effect of various central atoms on the magnitude of the σ-hole.

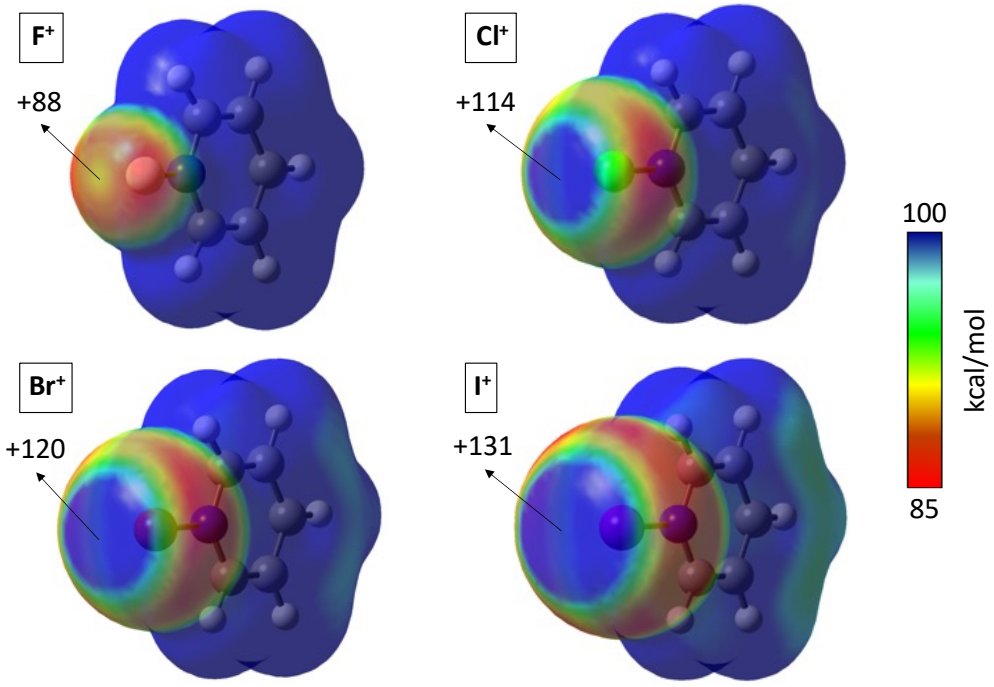

Figure 6.4. MEP maps for pyridine derivative $[X\cdots NC_5H_5]^+$ complexes (X = F, Cl, Br, and I) calculated at the MN12-SX/def2-TZVP level and plotted on the electron density isosurface (s = 0.001 Å). Energies are given in kcal/mol. Red and blue colours indicate less and more positive MEP values, respectively.

Upon initial inspection, all compounds exhibit a σ-hole close to the central atom and opposite to the bonded donor atom. Accordingly to the polarizability of the atom, the maximum MEP value ($V_{s,max}$) of the σ-hole increases when descending down the halogen group, with that of the fluorine teetering on the edge of existence. All in all, the MEP

maps allow me to explain the structural preferences found in the previous section. Halogen(I) compounds (X = Cl, Br, and I) would form highly linear [N···X···N] frameworks since the interaction with the Lewis base along the X···N axis is favoured by Coulombic attraction. Regarding to fluor(I) compounds, its tiny σ-hole might be the cause that the optimized fluoronium compound, [py-F···py]$^+$ would form an asymmetric arrangement ($d_{N\cdots F}$ = 1.337 and 2.790 Å; $\alpha_{N\text{-}F\cdots N}$ = 179.0º), similar to a classical halogen bond. From now on, I will not consider the F centre on the following discussion.

6.3.2 Effect of the donor

Figure 6.5 shows the MEP maps of [I···D]$^+$ complexes, where D is imidazole ($C_3H_4N_2$), pyridine (C_5H_5N), pyrimidine ($C_4H_4N_2$), acetonitrile (NCMe) and ammonia (NH_3).

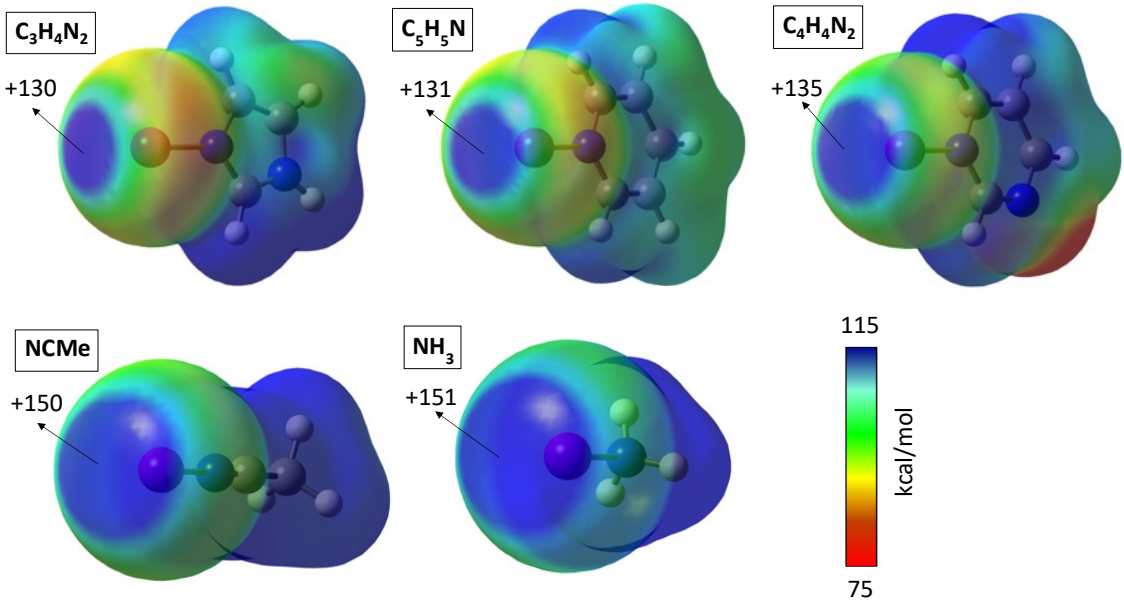

Figure 6.5. MEP map for iodine derivatives [I···D]$^+$ complexes (D = $C_3H_4N_2$, C_5H_5N, $C_4H_4N_2$, NCMe, and NH_3) calculated at the MN12-SX/def2-TZVP level and plotted on the electron density isosurface (s = 0.001 Å). Energies are given in kcal/mol. Red and blue colours indicate less and more positive MEP values, respectively.

Different nitrogen-containing donors (D) have been selected to study their effect on the magnitude of the σ-hole associated to the I···N bond axis (I kept the iodonium cation as the reference central atom X because it showed the most marked σ-hole among the halonium ions). Upon changing from pyridine (C_5H_5N) to other aromatic donors such imidazole ($C_3H_4N_2$) and pyrimidine ($C_4H_4N_2$), the $V_{s,max}$ value of the σ-hole changes

slightly. In contrast, it increases with non-aromatic donors such ammonia (NH_3) and acetonitrile (NCMe).

6.3.3 Effect of the R group

The $[py\cdots I]^+$ complex has been used as reference to analyse the influence of the electron density alteration on the I···N *σ*-hole induced by variation of the R substituents attached in *ortho* (2-R-py and 2,6-R_2-py), *meta* (3-R-py and 3,5-R_2-py) and *para*-positions (4-R-py) relative to the pyridine nitrogen. Several substituents have been studied (R = NMe_2, NH_2, OH, OMe, CH_3, CH_2F, CHF_2, CF_3, F, Cl, Br, I, CN, SO_3H, and NO_2). The $V_{s,max}$ values of *σ*-holes for these compounds are shown in Table 6.1. For comparison, the magnitude of the *σ*-hole of the unsubstituted model (R = H) is +131 kcal/mol (Figures 6.4 and 6.5).

Table 6.1. Highest positive value of the electrostatic potential ($V_{s,max}$) of *σ*-holes related to the iodine atom in the substituted $[(pyridine)iodine]^+$ complexes, and Hammett parameters of the substituents. Energies are given in kcal/mol.

	$V_{s,max}$						
R	2-R-py	2,6-R_2-py	3-R-py	3,5-R_2-py	4-R-py	σ_p	σ_m
NMe_2	123	114	123	117	118	-0.83	-0.21
NH_2	128	126	125	122	121	-0.66	-0.16
OH	127	122	129	130	128	-0.37	0.12
OMe	125	118	128	125	125	-0.28	0.12
CH_3	128	123	128	125	127	-0.17	-0.07
H	131	131	131	131	131	0	0
F	134	137	134	138	132	0.06	0.34
CH_2F	130	130	130	130	129	0.11	0.12
Cl	131	130	132	133	131	0.23	0.37
Br	130	128	132	133	130	0.23	0.39
I	128	123	130	129	128	0.28	0.35
CHF_2	130	131	132	133	132	0.32	0.29
CF_3	133	134	136	138	135	0.54	0.43
SO_3H	131	137	133	136	134	0.64	0.38
CN	135	138	137	144	136	0.66	0.56
NO_2	136	142	139	144	138	0.78	0.71

The smallest positive MEP value is found for NMe_2 and the highest ones for CN and NO_2. Two examples of MEP maps are depicted in Figure 6.6 (for the MEP maps of

all compounds studied see Figure A6.1 – A6.5 of the Appendix). The $V_{s,max}$ values of σ-holes show fair correlations with the electron releasing power of the R groups measured by their Hammett σ_p (4-R-py) and σ_m (3-R-py and 3,5-R_2-py) parameters, whereas no correlation is found for the *ortho* mono- and disubstituted pyridines (2-R-py and 2,6-R_2-py), clearly indicating the important steric effects in these two cases (Figure 6.7 and Eqs. A6.1 – A6.4 in the Appendix). Those trends are most clearly seen in the $CH_{3-n}F_n$-substituted pyridines, for which the magnitude of the σ-hole increases with the number of F atoms, and in the halogenated pyridines, for which it decreases on descending down the periodic group. The strongest inductive effect among singly-substituted pyridines is found for the *para* derivatives. It must be noted also that the incorporation of two substituents at two equivalent positions of the pyridine ring practically doubles the effect of a single substituent. For 2,6-$(SO_3H)_2$-py, there are two additional σ-holes related to the O-H bond axis (both of 144 kcal/mol) parallel to the I···N σ-hole (Figure 6.8).

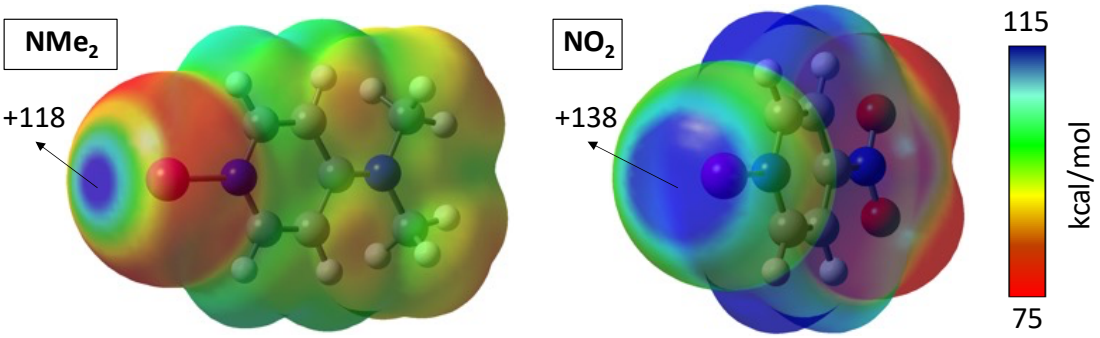

Figure 6.6. MEP maps of $[\{4\text{-}N(CH_3)_2\text{-py}\}I]^+$ and $[\{4\text{-}NO_2\text{-py}\}I]^+$ complexes calculated at the MN12-SX/def2-TZVP level and plotted on the electron density isosurface (s = 0.001 Å). Energies are given in kcal/mol. Red and blue colours indicate less and more positive MEP values, respectively.

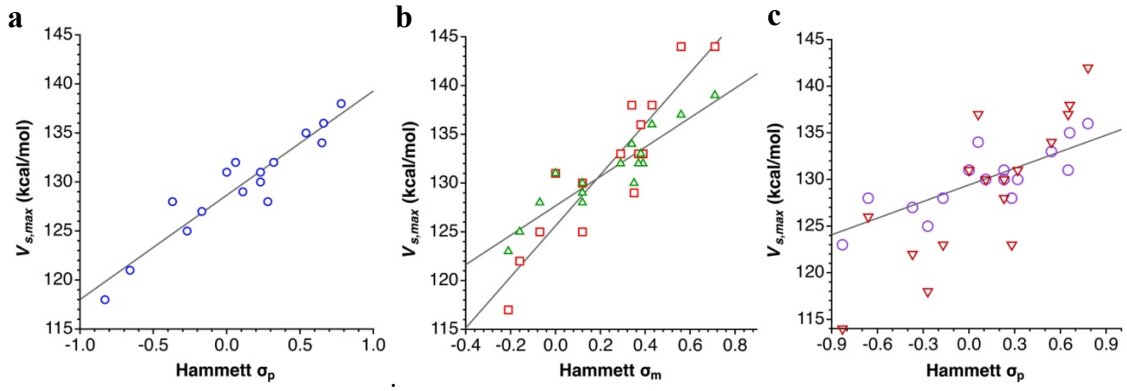

Figure 6.7. Dependence of the electrostatic potential at the σ-hole ($V_{s,max}$) on the Hammett parameters for (**a**) the 4-R-py (R^2 = 0.89), (**b**) the 3-R-py (triangles, R^2 = 0.86) and 3,5-R_2-py (squares, R^2 = 0.84), and (**c**) the 2-R-py (circles, R^2 = 0.67) and 2,6-R_2-py (triangles) compounds.

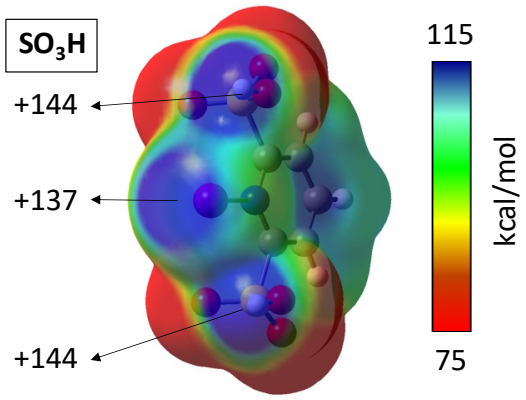

Figure 6.8. MEP map of [{2,6-$(SO_3H)_2$-py}I]$^+$ complex calculated at the MN12-SX/def2-TZVP level and plotted on the electron density isosurface (s = 0.001 Å). Energies are given in kcal/mol. Red and blue colours indicate less and more positive MEP values, respectively.

In summary, it is expected that for a given Lewis base, and considering the electrostatic attraction as the main driving force, an increase of the $V_{s,max}$ value will strengthen the interaction whereas its reduction will weaken it.

6.4 Analysis of the Interaction Energies

6.4.1 Effect of the central atom X

The effect of varying the central atom on the bonding and geometry between the py and [X-py]$^+$ fragments has been studied by means of DFT calculations, (Scheme 6.2.1). I have used the same X atoms of the above MEP analysis (Figure 6.4; X = Cl, Br, and I). The main results are shown in Table 6.2. The optimized geometry of the bis-pyridine halonium(I) cations exhibit D_{2h} symmetry with identical X···N bond distances. The calculated halogen···nitrogen bond lengths are 1.52 Å (N···Cl), 1.43 Å (N···Br) and 1.45 Å (N···I) shorter than the sum of the van der Waals radii of the involved atoms (3.48 Å, 3.52 Å and 3.70 Å, respectively).[44] The interaction energy increases in magnitude from Cl to I, in good agreement with the magnitudes of the σ-hole. A good correlation is observed between $V_{s,max}$ and the bond length of the two X···N bonds (R^2 = 0.995).

Table 6.2. Key geometrical parameters and interaction energies for the optimized [py···X···py]$^+$ model (X = Cl, Br, and I) calculated at the MN12-SX/def2-TZVP level.

X	$d_{N\text{-}X}$ (Å)	$\alpha_{N\text{-}X\text{-}N}$ (°)	$V_{s,max}$ (kcal/mol)	ΔE_{INT} (kcal/mol)
Cl	1.961	180.0	114	-37.37
Br	2.088	180.0	120	-40.01
I	2.255	180.0	131	-41.30

6.4.2 Effect of the donor

The effect of different nitrogen-containing donors (D) on the bond strength and geometry of the D···[I-D]$^+$ interaction (Scheme 6.2.2) has been analysed using the same donors as in the MEP analysis (Figure 6.5), and the results are shown in Table 6.3.

Table 6.3. Key geometrical parameters and interaction energies for the optimized [D···I···D]$^+$ models with different nitrogen-containing Lewis bases (D) calculated at the MN12-SX/def2-TZVP level.

Donor	$d_{N\text{-}I}$ (Å)	$\alpha_{N\text{-}I\text{-}N}$ (°)	$V_{s,max}$ (kcal/mol)	ΔE_{INT} (kcal/mol)
Pyrimidine	2.261	179.8	135	-38.50
Acetonitrile	2.190	180.0	150	-40.09
Pyridine	2.255	180.0	131	-41.30
Ammonia	2.299	180.0	151	-43.48
Imidazole	2.238	180.0	130	-44.87

The optimized [N···I···N]$^+$ frameworks are all linear with the two identical I···N distances. Ammonia, which induces the most marked σ-hole (151 kcal/mol), has an interaction energy of -43.48 kcal/mol. However, even if imidazole has the lowest $V_{s,max}$ value (130 kcal/mol), it gives the most stable adduct. Furthermore, the acetonitrile iodonium is less stable than the pyridine one even though the $V_{s,max}$ value of the former is as high as 150 kcal/mol. In addition, pyrimidine yields the least stable adduct although its $V_{s,max}$ value is the highest among the aromatic donors (135 kcal/mol). It seems thus clear that the strength of the bond cannot be only explained by Coulombic interactions.

6.4.3 Effect of the R group

Upon symmetric modulation of orto (2-R-py), double orto (2,6-R_2-py), meta (3-R-py), double meta (3,5-R_2-py) and para-position (4-R-py) relative to the pyridine nitrogen of the [bis(pyridine)iodine]$^+$ complex with the same substituents groups used in my previous MEP analysis (Table 6.1), I have analysed the impact of the electron density alteration on the stability and geometry of the bonding between pyridine and [I-py]$^+$ (Scheme 6.2.3). Previous works using the same compound have only focused on symmetric alteration of the pyridine *para*-hydrogen using a few substituents.[17,37] The main results are summarized in Tables 6.4 – 6.8.

Table 6.4. Key geometrical parameters, $V_{s,max}$ of σ-holes, and interaction energies for the optimized $[(2\text{-R-py})_2\text{I}]^+$ complexes (2-R-py), calculated at the MN12-SX/def2-TZVP level.

R	$d_{N\text{-}I}$ (Å)	$\alpha_{N\text{-}I\text{-}N}$ (°)	$V_{s,max}$ (kcal/mol)	ΔE_{INT} (kcal/mol)
OH	2.269	176.3	127	-42.10
OMe	2.270	175.7	125	-41.94
NH_2	2.261	176.9	128	-41.33
H	2.255	180.0	131	-41.30
CH_3	2.271	176.0	128	-40.91
NMe_2	2.279	180.0	123	-40.49
CH_2F	2.278	176.6	130	-40.45
CHF_2	2.287	180.0	130	-40.17
F	2.269	179.4	134	-39.44
Cl	2.274	176.5	131	-38.86
SO_3H	2.290	180.0	131	-38.73
CN	2.266	180.0	135	-38.50
CF_3	2.289	180.0	133	-38.36
Br	2.276	176.0	130	-38.28
I	2.277	176.0	128	-37.70
NO_2	2.306	177.8	136	-37.30

Table 6.5. Key geometrical parameters, $V_{s,max}$ of σ-holes, and interaction energies for the optimized $[(2,6\text{-R}_2\text{-py})_2\text{I}]^+$ complexes (2,6-R_2-py), calculated at the MN12-SX/def2-TZVP level.

R	$d_{N\text{-}I}$ (Å)	$\alpha_{N\text{-}I\text{-}N}$ (°)	$V_{s,max}$ (kcal/mol)	ΔE_{INT} (kcal/mol)
SO_3H	2.311	180.0	137	-60.67
OH	2.293	180.0	122	-41.97
OMe	2.296	179.9	118	-41.49
H	2.255	180.0	131	-41.30
NH_2	2.280	180.0	126	-39.81
CH_3	2.292	180.0	123	-39.31
NMe_2	2.305	174.4	114	-38.20
CH_2F	2.296	180.0	130	-37.30
F	2.287	180.0	137	-37.21
Cl	2.302	180.0	130	-35.72
CHF_2	2.306	180.0	131	-35.32
Br	2.304	180.0	128	-34.63
I	2.315	180.0	123	-34.31
CN	2.283	180.0	138	-33.98
CF_3	2.337	179.7	134	-33.16
NO_2	2.358	180.0	142	-30.56

Table 6.6. Key geometrical parameters, $V_{s,max}$ of σ-holes, and interaction energies for the optimized $[(3\text{-R-py})_2\text{I}]^+$ complexes (3-R-py), calculated at the MN12-SX/def2-TZVP level.

R	$d_{N\text{-}I}$ (Å)	$\alpha_{N\text{-}I\text{-}N}$ (°)	$V_{s,max}$ (kcal/mol)	ΔE_{INT} (kcal/mol)
NH_2	2.253	179.8	125	-43.10
NMe_2	2.252	180.0	123	-43.08
OMe	2.255	179.9	128	-42.22
OH	2.255	180.0	129	-42.08
CH_3	2.255	179.9	128	-41.77
CH_2F	2.256	180.0	130	-41.31
H	2.255	180.0	131	-41.30
F	2.257	179.8	134	-39.76
CHF_2	2.257	179.9	132	-39.64
Cl	2.257	179.9	132	-39.06
Br	2.257	179.9	132	-38.75
I	2.257	180.0	130	-38.50
CF_3	2.258	179.7	136	-38.41
SO_3H	2.259	179.6	133	-38.02
CN	2.260	180.0	137	-36.24
NO_2	2.260	180.0	139	-36.15

Table 6.7. Key geometrical parameters, $V_{s,max}$ of σ-holes, and interaction energies for the optimized $[(3,5\text{-R}_2\text{-py})_2\text{I}]^+$ complexes (3,5-R_2-py), calculated at the MN12-SX/def2-TZVP level.

R	$d_{N\text{-}I}$ (Å)	$\alpha_{N\text{-}I\text{-}N}$ (°)	$V_{s,max}$ (kcal/mol)	ΔE_{INT} (kcal/mol)
NMe_2	2.251	179.8	117	-44.46
NH_2	2.252	179.9	122	-44.35
OMe	2.252	179.8	125	-42.31
CH_3	2.254	180.0	125	-41.99
OH	2.255	179.8	130	-41.47
H	2.255	180.0	131	-41.30
CH_2F	2.256	179.9	130	-40.18
F	2.259	180.0	138	-38.06
CHF_2	2.258	179.4	133	-37.76
Cl	2.260	180.0	133	-36.90
Br	2.260	180.0	133	-36.36
I	2.259	180.0	129	-36.12
CF_3	2.260	179.9	138	-35.48
SO_3H	2.263	180.0	136	-35.02
CN	2.264	180.0	144	-31.30
NO_2	2.266	180.0	144	-30.96

Table 6.8. Key geometrical parameters, $V_{s,max}$ of σ-holes, and interaction energies for the optimized $[(4\text{-R-py})_2\text{I}]^+$ complexes (4-R-py), calculated at the MN12-SX/def2-TZVP level.

R	$d_{N\text{-}I}$ (Å)	$\alpha_{N\text{-}I\text{-}N}$ (°)	$V_{s,max}$ (kcal/mol)	ΔE_{INT} (kcal/mol)
NH_2	2.246	180.0	121	-44.65
NMe_2	2.244	180.0	118	-44.32
OMe	2.249	179.9	125	-42.91
OH	2.250	180.0	128	-42.39
CH_3	2.252	180.0	127	-41.96
H	2.255	180.0	131	-41.30
CH_2F	2.253	180.0	129	-40.83
F	2.255	180.0	132	-40.16
Cl	2.254	180.0	131	-39.62
CHF_2	2.255	179.8	132	-39.30
I	2.253	180.0	128	-39.26
Br	2.253	180.0	130	-39.15
CF_3	2.257	179.9	135	-38.04
SO_3H	2.257	179.8	134	-37.41
CN	2.256	180.0	136	-36.00
NO_2	2.259	180.0	138	-35.79

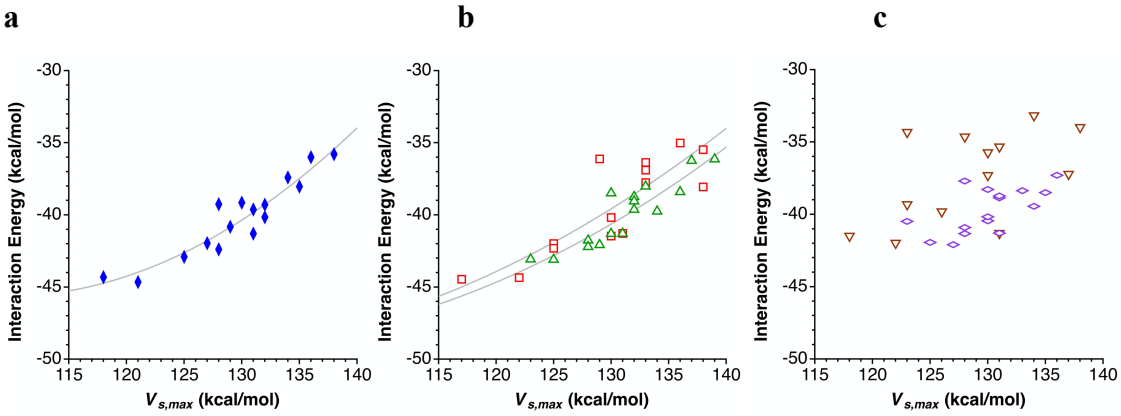

Figure 6.9. Interaction energy between a pyridine donor (D) and the corresponding $[\text{I-D}]^+$ cation, represented as a function of the electrostatic potential at the σ-hole ($V_{s,max}$) for (**a**) the 4-R-py (R^2 = 0.89), (**b**) the 3-R-py (triangles, R^2 = 0.82) and 3,5-R_2-py (squares, R^2 = 0.84), and (**c**) the 2-R-py (rhombuses) and 2,6-R_2-py (triangles) halonium ions.

When comparing the interaction energy between a pyridine donor (D) and the corresponding $[\text{I-D}]^+$ cation and the electrostatic potential at the σ-hole ($V_{s,max}$), good correlations between the two parameters for the 4-R-py, 3-R-py and 3,5-R_2-py families are found (Figure 6.9 and Eqs. A6.5 – A6.7 in the Appendix), whereas no correlation is

found for the *ortho*-substituted families 2-R-py and 2,6-R_2-py. The surprising aspect of that correlation is that it is positive, i.e., the interaction energy is made less attractive as the electrostatic potential increases. This results clearly indicate that the attractive interaction between the two moieties is modulated via substituents by forces other than the electrostatic attraction associated to the σ-hole at the $[I\text{-}D]^+$ cation. Consider, for instance, the 2,6-$(NO_2)_2$-py iodonium cation, that appears in the calculations as the least stable one (ΔE_{INT} = -30.56 kcal/mol), yet its electrostatic potential at the σ-hole is among the highest ones (142 kcal/mol). Another clear example is the 4-NH_2-py adduct, calculated to be the most stable one (ΔE_{INT} = -44.65 kcal/mol) despite its rather low $V_{s,max}$ value (121 kcal/mol).

All optimized compounds show linear $[N\cdots I\cdots N]^+$ frameworks with two equal I···N distances, and a slight bending of a few degrees is obtained only for singly *ortho*-substituted pyridines and $[\{2,6\text{-}(Me_2N)_2\text{-py}\}_2I]^+$ adduct (Tables 6.4 and 6.5, respectively). It must be stressed that, at difference with the wide range of interaction energies affected by the nature and positions of the substituents at the pyridine ring, the I···N distances fall in a narrow range (2.24 – 2.27 Å) for the *meta* and *para*-substituted pyridines, while more variable and longer distances (2.26 – 2.36 Å) result for the *ortho*-substituted ones. For those *ortho*-substituted compounds, the steric hindrance and other secondary interactions such as hydrogen bonds play an important role in the geometry and stability of the system. For instance, despite of the strong electron releasing character of NMe_2, the I···N distance in the 2,6-Me_2N-py compound is longer and the interaction energy smaller than in the unsubstituted compound. In addition, the pyridine donors form a handle-shaped structure around the central $[N\cdots I\cdots N]^+$ framework (Figure 6.10), probably due to the steric hindrance of the methyl groups. Furthermore, in the 2,6-$(HO_3S)_2$-py adduct, four O···H hydrogen bonds of 1.73 Å are formed between the hydrogen sulfonato groups (Figure 6.11a), explaining the unusually high interaction energy between the two fragments (ΔE_{INT} = -60.67 kcal/mol), to be compared with the much smaller value for the monosubstituted *trans*-derivative, 2-HO_3S-py (-38.73 kcal/mol). Comparisons with the interaction energy of the monosubstituted *cis*-derivative 2-HO_3S-py (-49.86 kcal/mol), which shows two O···H hydrogen bonds of 1.76 Å formed between the substituent groups (Figure 6.11b), allow me to estimate the stabilization energy of each hydrogen bond in 5.41 kcal/mol. The interaction energies between *ortho*-substituted pyridines, 2-R-py and 2,6-R_2-py, and the corresponding $[I\text{-}D]^+$ cations are affected by the same effects. As a

result, neither the I···N distances nor the interaction energies in this family correlate with electron withdrawing/releasing power of the substituents, calibrated by the Hammett σ_p parameters. Notice that the same effects have prevented from defining a Hammett parameter for substituents in the *ortho* position.

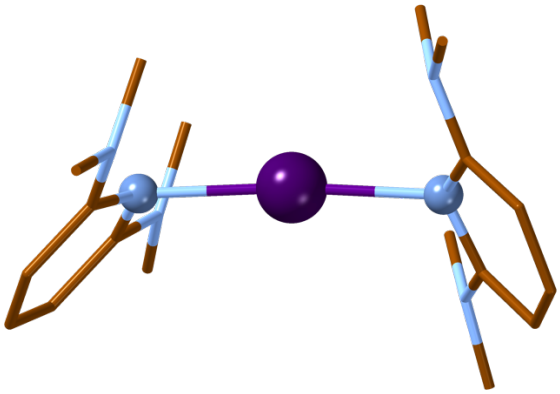

Figure 6.10. Optimized geometry for the $[\{2,6\text{-}(Me_2N)_2\text{-}py\}_2I]^+$ complex. Colour code: brown, C; blue, N; and purple, I. H atoms are omitted for clarity.

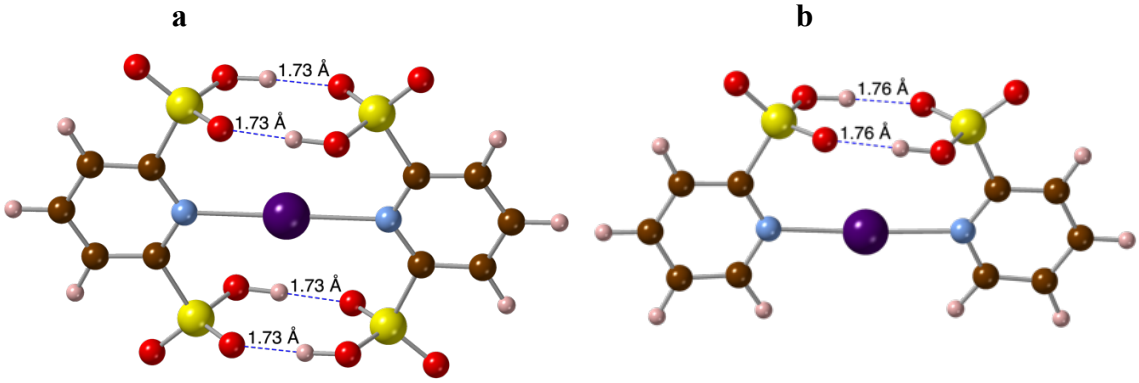

Figure 6.11. Short O···H contacts (dashed lines) in the calculated structure of (**a**) $[\{2,6\text{-}(HO_3S)_2\text{-}py\}_2I]^+$ and (**b**) $[cis\text{-}\{2\text{-}(HO_3S)\text{-}py\}_2I]^+$ adducts.

Both the I···N distances and the interaction energies of 3-R-py, 3,5-R_2-py and 4-R-py compounds are expected to remain unaffected by the steric hindrance and other intramolecular secondary interactions between the R groups and thus are more adequate to analyse the effect of changes in the electron density of the Lewis base. Plots of those two parameters as a function of the Hammett σ_p and σ_m constants of the pyridine substituents (Figures 6.12 and 6.13, respectively) show that they are nicely correlated (see Eqs. A6.8 – A6.9 and Eqs. A6.10 – A6.13, respectively, in the Appendix). Such behaviours bear some similarities with the trends just discussed for the electrostatic potential at the σ-hole. Now the highest interaction energies within each substitution

scheme are found for R = NH_2 and NMe_2 and the lowest ones for CN and NO_2. As for the general trends, the I···N distance increases, and the interaction energy decreases, as the Hammett parameters become more positive, i.e., as the electron releasing power decreases or the electron-withdrawing ability increases. The effect of a *para* substitution at the pyridine ring on the interaction energy is stronger than a single *meta* substitution. However, the incorporation of a second substituent at the *meta* position practically doubles the effect of a single substituent, as can be appreciated by the higher slope of the least-squares lines for the 3,5-R_2-py compounds with respect to the 3-R-py analogues (Figures 6.13a – b).

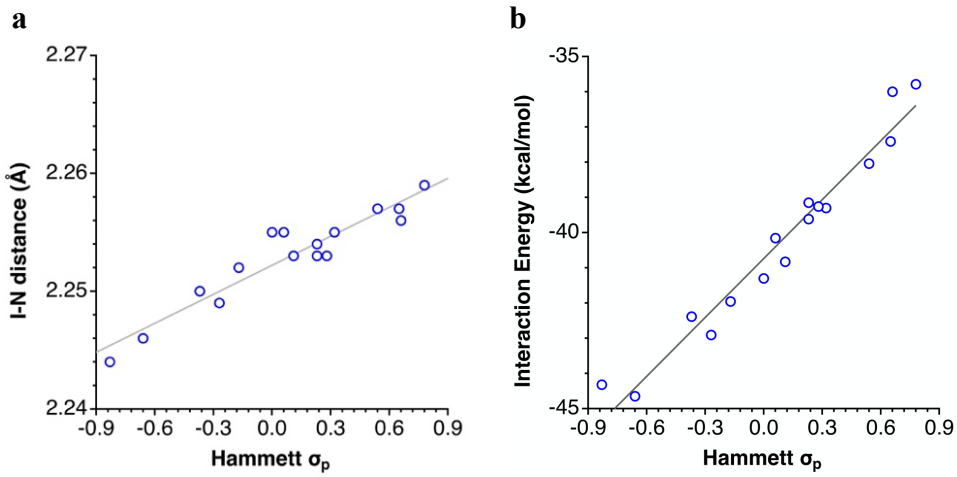

Figure 6.12. Dependence on the Hammett σ_p parameter of (**a**) the I-N bond distances ($R^2 = 0.90$), and (**b**) the interaction energy between the N and $[I\text{-}N]^+$ fragments ($R^2 = 0.96$) in 4-R-py compounds.

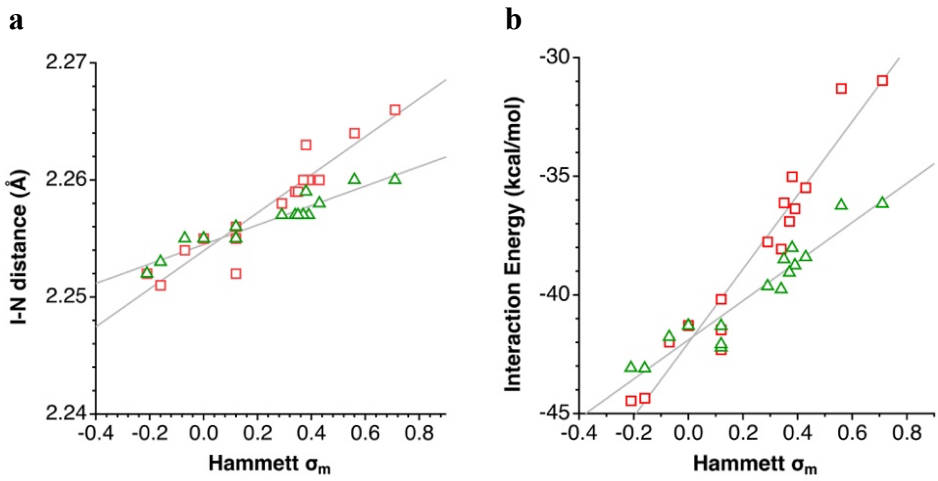

Figure 6.13. Dependence on the Hammett σ_m parameter of (**a**) the I-N bond distances ($R^2 = 0.91$, 0.89), and (**b**) the interaction energy between the N and $[I\text{-}N]^+$ fragments ($R^2 = 0.91$, 0.94) in 3-R-py (triangles) and 3,5-R_2-py (squares) compounds.

Those trends can be clearly seen in the subsets of $CH_{3-n}F_n$ and halogen-substituted pyridines. For the former, the interaction energy is made less stabilising as the number of F atoms increase (Tables 6.4 – 6.8), within every family with a given substitution pattern. While single-substitution with these groups induces changes in the interaction energy of up to 3.4 kcal/mol, double substitution modifies it by 6.5 kcal/mol. Among the halogen-substituted pyridines, the interaction energy decreases on descending down the periodic group, but with smaller changes than those induced by the fluoromethyl groups.

The fact that both the I-N distance and the interaction energy show a dependence on the Hammett parameter of the substituent means that there is also some correlation between the distance and the interaction energy, and comparison of bond distances in halonium ions should give approximate information on relative interaction energies. Moreover, the electrostatic potentials at the σ-hole ($V_{s,max}$) are also correlated with the Hammett parameters, as can be seen in Figures 6.7a – b and, consequently, the interaction energy becomes less attractive as the electrostatic potential at the σ-hole increases, clearly showing that such an interaction is not the main responsible for the strength of the I-N bonds in the studied $[D\cdots I\cdots D]^+$ iodonium cations.

6.5 Energy Decomposition Analysis

In light of the above results, I have performed an Energy Decomposition Analysis (EDA) to investigate the effect of (i) the central atom X, (ii) the N-donor D, and (iii) the substituents R, on the nature of the bond between D and $[X\text{-}D]^+$.

6.5.1 Effect of central atom X

The results for three halogen atoms and D = pyridine (Scheme 6.2.1; X = Cl, Br, and I) are summarized in Table 6.9.

Table 6.9. EDA for the interaction of pyridine and $[X\text{-py}]^+$ in the optimized $[py\cdots X\cdots py]^+$ model (X = Cl, Br, and I), calculated at the MN12-SX/def2-TZVP level. The percentage represents the contribution to the total attractive (negative) interaction energy. Energies are given in kcal/mol.

X	ΔE_{PAULI}	ΔE_{ELEC}	ΔE_{DISP}	ΔE_{POL}	ΔE_{CT}	ΔE_{INT}
Cl	145.88	-81.41 (44.4 %)	-8.83 (4.8 %)	-25.08 (13.7 %)	-67.93 (37.1 %)	-37.37
Br	125.62	-79.71 (48.1 %)	-8.03 (4.8 %)	-26.86 (16.2 %)	-51.14 (30.9 %)	-40.12
I	105.56	-74.44 (50.7 %)	-7.16 (4.9 %)	-25.94 (17.7 %)	-39.32 (26.8 %)	-41.29

The orbital-based interactions, shown as polarization (ΔE_{POL}) and charge transfer (ΔE_{CT}) terms, decrease as we go down the group of the halogens. The less electronegative the central atom is, the higher the energy of its np orbitals, thus enlarging the energy gap between the donor and acceptor orbitals and allowing for a poorer orbital interaction. Simultaneously, the electrostatic (ΔE_{ELEC}) contribution increases, accordingly with the polarizability of the central atom. The sum of ΔE_{POL} and ΔE_{CT} represents the 51 % (Cl), 47 % (Br) and 44 % (I) of the total attractive interaction energy. For the three halogens, the electrostatic term is not enough to overcome the Pauli repulsion but the significant contribution of polarization, charge transfer and dispersion to a lesser extent (< 5 %) makes the net interaction attractive.

6.5.2 Effect of the donor

The results for the nature of the bonding between various nitrogen-containing donors D and the corresponding $[I\text{-}D]^+$ (Scheme 6.2.2) are summarized in Table 6.10.

Table 6.10. EDA for the interaction of different nitrogen-containing Lewis bases (D) and the corresponding $[I\text{-}D]^+$ in the optimized $[D\cdots I\cdots D]^+$ models, calculated at the MN12-SX/def2-TZVP level. The percentage represents the contribution to the total attractive (negative) interaction energy. Energies are given in kcal/mol.

Donor	ΔE_{PAULI}	ΔE_{ELEC}	ΔE_{DISP}	ΔE_{POL}	ΔE_{CT}	ΔE_{INT}
Pyrimidine	101.84	-70.02 (49.9 %)	-6.71 (4.8 %)	-25.44 (18.1 %)	-38.17 (27.2 %)	-38.50
Acetonitrile	91.91	-67.33 (51.0 %)	-5.53 (4.2 %)	-23.28 (17.6 %)	-35.86 (27.2 %)	-40.09
Pyridine	105.56	-74.44 (50.7 %)	-7.16 (4.9 %)	-25.94 (17.7 %)	-39.32 (26.8 %)	-41.29
Ammonia	98.80	-81.42 (57.2 %)	-5.53 (3.9 %)	-18.06 (12.7 %)	-37.27 (26.2 %)	-43.49
Imidazole	107.68	-80.62 (52.9 %)	-6.96 (4.6 %)	-26.30 (17.2 %)	-38.66 (25.3 %)	-44.86

The first observation is that the electrostatic term is the largest attractive contribution, yet it is insufficient to overcome the Pauli repulsion. The dispersion term contributes less than 5 % whereas the polarization and charge transfer terms contribute nearly as much (39 – 45 %) as the electrostatic term to the attractive part of the interaction, making the formation of the adduct energetically favourable in all cases by 38 – 45 kcal/mol. Among the aromatic donors, imidazole has the greatest magnitude of ΔE_{INT} whereas pyrimidine has the smallest one, while the proportion of orbital contribution to the total attractive interactions is smallest for imidazole (43 %) and largest for pyrimidine (45 %). For the non-aromatic donors, ammonia is more stable than acetonitrile. All in all,

these results indicate that, in all cases, the electrostatic term is not enough to overcome the Pauli repulsion and it is the combined effect of the orbital-based terms (polarization and charge transfer) and a smaller contribution of dispersion forces which makes the interaction attractive.

6.5.3 Effect of the R group

Finally, I have applied the same approach to analyse how the energetic contributions change with the electron density modulation of the $[N\cdots I\cdots N]^+$ halonium bond. The modifications of the electron density were achieved by modulation of *ortho* (2-R-py and 2,6-R_2-py), *meta* (3-R-py and 3,5-R_2-py) and *para*-position (4-R-py) relative to the pyridine nitrogen of the $[py\cdots I\cdots py]^+$ complex (R = H; Scheme 6.2.3). I have used the same R groups as in the previous sections. The main results are summarized in Tables 6.11 – 6.15. Energies are given in kcal/mol.

Table 6.11. EDA for the optimized $[(2\text{-R-py})_2I]^+$ complexes, calculated at the MN12-SX/def2-TZVP level. The percentage represents its contribution to the total attractive interaction energy.

R	ΔE_{PAULI}	ΔE_{ELEC}	ΔE_{DISP}	ΔE_{POL}	ΔE_{CT}	ΔE_{INT}
OH	100.68	-72.47 (50.8 %)	-7.84 (5.5 %)	-26.13 (18.3 %)	-36.34 (25.4 %)	-42.10
OMe	101.78	-72.78 (50.6 %)	-7.96 (5.5 %)	-26.56 (18.5 %)	-36.42 (25.3 %)	-41.94
NH_2	114.64	-78.92 (50.6 %)	-8.52 (5.5 %)	-28.61 (18.3 %)	-39.91 (25.6 %)	-41.33
H	105.56	-74.44 (50.7 %)	-7.16 (4.9 %)	-25.94 (17.7 %)	-39.32 (26.8 %)	-41.29
CH_3	108.05	-75.00 (50.3 %)	-8.57 (5.8 %)	-26.62 (17.9 %)	-38.78 (26.0 %)	-40.91
NMe_2	105.22	-71.61 (49.1 %)	-9.72 (6.7 %)	-27.54 (18.9 %)	-36.84 (25.3 %)	-40.50
CH_2F	102.53	-71.60 (50.1 %)	-8.61 (6.0 %)	-26.28 (18.4 %)	-36.49 (25.5 %)	-40.45
CHF_2	96.51	-68.11 (49.8 %)	-8.54 (6.3 %)	-25.41 (18.6 %)	-34.62 (25.3 %)	-40.17
F	96.82	-67.66 (49.7 %)	-7.32 (5.4 %)	-25.63 (18.8 %)	-35.65 (26.2 %)	-39.44
Cl	98.76	-67.59 (49.1 %)	-8.18 (5.9 %)	-26.20 (19.0 %)	-35.65 (25.9 %)	-38.86
SO_3H	94.81	-65.10 (48.8 %)	-9.08 (6.8 %)	-25.58 (19.2 %)	-33.77 (25.3 %)	-38.73
CN	99.52	-67.88 (49.2 %)	-7.89 (5.7 %)	-25.48 (18.5 %)	-36.76 (26.6 %)	-38.50
CF_3	95.44	-65.43 (48.9 %)	-8.48 (6.3 %)	-25.22 (18.9 %)	-34.66 (25.9 %)	-38.36
Br	99.04	-67.01 (48.8 %)	-8.31 (6.1 %)	-26.26 (19.1 %)	-35.73 (26.0 %)	-38.28
I	101.18	-67.56 (48.6 %)	-8.51 (6.1 %)	-26.53 (19.1 %)	-36.28 (26.1 %)	-37.69
NO_2	87.63	-59.60 (47.7 %)	-8.15 (6.5 %)	-24.85 (19.9 %)	-32.33 (25.9 %)	-37.30

Table 6.12. EDA for the optimized $[(2,6\text{-}R_2\text{-}py)_2I]^+$ complexes, calculated at the MN12-SX/def2-TZVP level. The percentage represents the contribution to the total attractive interaction energy.

R	ΔE_{PAULI}	ΔE_{ELEC}	ΔE_{DISP}	ΔE_{POL}	ΔE_{CT}	ΔE_{INT}
SO_3H	150.66	-102.65 (48.6 %)	-19.52 (9.2 %)	-43.23 (20.5 %)	-45.95 (21.7 %)	-60.67
OH	94.38	-69.09 (50.7 %)	-8.54 (6.3 %)	-25.26 (18.5 %)	-33.46 (24.5 %)	-41.97
OMe	96.52	-69.56 (50.4 %)	-8.78 (6.4 %)	-26.04 (18.9 %)	-33.63 (24.4 %)	-41.49
H	105.56	-74.44 (50.7 %)	-7.16 (4.9 %)	-25.94 (17.7 %)	-39.32 (26.8 %)	-41.29
NH_2	122.27	-81.88 (50.5 %)	-9.93 (6.1 %)	-29.76 (18.4 %)	-40.50 (25.0 %)	-39.81
CH_3	112.15	-75.47 (49.8 %)	-10.75 (7.1 %)	-26.48 (17.5 %)	-38.75 (25.6 %)	-39.30
NMe_2	103.88	-66.13 (46.5 %)	-13.32 (9.4 %)	-27.42 (19.3 %)	-35.21 (24.8 %)	-38.20
CH_2F	108.55	-71.21 (48.8 %)	-10.83 (7.4 %)	-26.67 (18.3 %)	-37.13 (25.5 %)	-37.30
F	88.25	-60.82 (48.5 %)	-7.49 (6.0 %)	-24.42 (19.5 %)	-32.73 (26.1 %)	-37.21
Cl	94.53	-62.29 (47.8 %)	-9.86 (7.6 %)	-24.50 (18.8 %)	-33.59 (25.8 %)	-35.72
CHF_2	103.45	-66.46 (47.9 %)	-10.84 (7.8 %)	-26.10 (18.8 %)	-35.38 (25.5 %)	-35.32
Br	97.51	-62.64 (47.4 %)	-10.88 (8.2 %)	-24.73 (18.7 %)	-33.90 (25.7 %)	-34.64
I	102.25	-64.11 (46.9 %)	-12.65 (9.3 %)	-24.40 (17.9 %)	-35.39 (25.9 %)	-34.30
CN	93.76	-59.61 (46.7 %)	-8.65 (6.8 %)	-24.48 (19.2 %)	-35.00 (27.4 %)	-33.99
CF_3	90.08	-58.27 (47.3 %)	-11.09 (9.0 %)	-23.23 (18.8 %)	-30.67 (24.9 %)	-33.19
NO_2	75.59	-45.93 (43.3 %)	-9.33 (8.8 %)	-22.45 (21.1 %)	-28.45 (26.8 %)	-30.56

Table 6.13. EDA for the optimized $[(3\text{-R-py})_2I]^+$ complexes, calculated at the MN12-SX/def2-TZVP level. The percentage represents the contribution to the total attractive interaction energy.

R	ΔE_{PAULI}	ΔE_{ELEC}	ΔE_{DISP}	ΔE_{POL}	ΔE_{CT}	ΔE_{INT}
NH_2	107.51	-77.16 (51.2 %)	-7.35 (4.9 %)	-26.54 (17.6 %)	-39.56 (26.3 %)	-43.10
NMe_2	108.89	-77.79 (51.2%)	-7.44 (4.9 %)	-27.15 (17.9 %)	-39.60 (26.1 %)	-43.08
OMe	105.72	-75.37 (50.9 %)	-7.20 (4.9 %)	-26.26 (17.7 %)	-39.11 (26.4 %)	-42.22
OH	105.09	-74.91 (50.9 %)	-7.18 (4.9 %)	-26.06 (17.7 %)	-39.02 (26.5 %)	-42.08
CH_3	106.51	-75.40 (50.8 %)	-7.23 (4.9 %)	-26.57 (17.9 %)	-39.09 (26.4 %)	-41.77
CH_2F	105.10	-74.19 (50.7 %)	-7.15 (4.9 %)	-26.45 (18.1 %)	-38.62 (26.4 %)	-41.31
H	105.56	-74.44 (50.7 %)	-7.16 (4.9 %)	-25.94 (17.7 %)	-39.32 (26.8 %)	-41.29
F	102.81	-71.24 (50.0 %)	-7.03 (4.9 %)	-25.90 (18.2 %)	-38.40 (26.9 %)	-39.76
CHF_2	103.68	-71.59 (50.0 %)	-7.06 (4.9 %)	-26.77 (18.7 %)	-37.89 (26.4 %)	-39.64
Cl	102.87	-70.32 (49.5 %)	-7.08 (5.0 %)	-26.94 (19.0 %)	-37.60 (26.5 %)	-39.06
Br	102.92	-69.89 (49.3 %)	-7.10 (5.0 %)	-27.33 (19.3 %)	-37.36 (26.4 %)	-38.75
I	103.48	-69.77 (49.1 %)	-7.13 (5.0 %)	-27.49 (19.4 %)	-37.59 (26.5 %)	-38.49
CF_3	102.33	-69.50 (49.4 %)	-7.01 (5.0 %)	-26.50 (18.8 %)	-37.73 (26.8 %)	-38.41
SO_3H	101.48	-68.52 (49.1 %)	-6.94 (5.0 %)	-27.03 (19.4 %)	-37.02 (26.5 %)	-38.03
CN	100.41	-65.81 (48.2 %)	-6.93 (5.1 %)	-25.83 (18.9 %)	-38.08 (27.9 %)	-36.24
NO_2	99.83	-65.57 (48.2 %)	-6.83 (5.0 %)	-25.99 (19.1 %)	-37.59 (27.6 %)	-36.15

Table 6.14. EDA for the optimized $[(3,5\text{-}R_2\text{-}py)_2I]^+$ complexes, calculated at the MN12-SX/def2-TZVP level. The percentage represents the contribution to the total attractive interaction energy.

R	ΔE_{PAULI}	ΔE_{ELEC}	ΔE_{DISP}	ΔE_{POL}	ΔE_{CT}	ΔE_{INT}
NMe_2	111.24	-80.30 (51.6 %)	-7.69 (4.9 %)	-28.16 (18.1 %)	-39.54 (25.4 %)	-44.46
NH_2	108.81	-78.98 (51.6 %)	-7.51 (4.9 %)	-26.90 (17.6 %)	-39.76 (26.0 %)	-44.35
OMe	106.84	-75.82 (50.8 %)	-7.35 (4.9 %)	-26.80 (18.0 %)	-39.18 (26.3 %)	-42.31
CH_3	107.43	-76.02 (50.9 %)	-7.29 (4.9 %)	-26.71 (17.9 %)	-39.40 (26.4 %)	-41.99
OH	104.77	-74.06 (50.6 %)	-7.25 (5.0 %)	-26.00 (17.8 %)	-38.92 (26.6 %)	-41.47
H	105.56	-74.44 (50.7 %)	-7.16 (4.9 %)	-25.94 (17.7 %)	-39.32 (26.8 %)	-41.29
CH_2F	105.07	-72.82 (50.1 %)	-7.14 (4.9 %)	-26.89 (18.5 %)	-38.39 (26.4 %)	-40.18
F	100.18	-67.86 (49.1 %)	-6.94 (5.0 %)	-25.22 (18.2 %)	-38.23 (27.7 %)	-38.06
CHF_2	102.04	-68.56 (49.0 %)	-6.97 (5.0 %)	-26.93 (19.3 %)	-37.35 (26.7 %)	-37.76
Cl	100.46	-66.33 (48.3 %)	-7.02 (5.1 %)	-27.12 (19.7 %)	-36.88 (26.9 %)	-36.90
Br	100.58	-65.63 (47.9 %)	-7.05 (5.2 %)	-27.60 (20.2 %)	-36.65 (26.8 %)	-36.36
I	101.60	-65.75 (47.7 %)	-7.12 (5.2 %)	-27.78 (20.2 %)	-37.07 (26.9 %)	-36.12
CF_3	99.42	-64.58 (47.9 %)	-6.88 (5.1 %)	-26.44 (19.6 %)	-37.00 (27.4 %)	-35.48
SO_3H	97.91	-63.15 (47.5 %)	-6.77 (5.1 %)	-27.06 (20.4 %)	-35.95 (27.0 %)	-35.02
CN	95.88	-57.60 (45.3 %)	-6.74 (5.3 %)	-25.86 (20.3 %)	-36.98 (29.1 %)	-31.30
NO_2	94.65	-56.91 (45.3 %)	-6.53 (5.2 %)	-26.04 (20.7 %)	-36.13 (28.8 %)	-30.96

Table 6.15. EDA for the optimized $[(4\text{-R-py})_2I]^+$ complexes, calculated at the MN12-SX/def2-TZVP level. The percentage represents its contribution to the total attractive interaction energy.

R	ΔE_{PAULI}	ΔE_{ELEC}	ΔE_{DISP}	ΔE_{POL}	ΔE_{CT}	ΔE_{INT}
NH_2	111.21	-81.10 (52.0 %)	-7.52 (4.8 %)	-27.37 (17.6 %)	-39.88 (25.6 %)	-44.65
NMe_2	112.53	-81.35 (51.9 %)	-7.55 (4.8 %)	-28.41 (18.1 %)	-39.53 (25.2 %)	-44.31
OMe	108.61	-77.81 (51.4 %)	-7.36 (4.9 %)	-27.22 (18.0 %)	-39.13 (25.8 %)	-42.91
OH	107.70	-76.75 (51.1 %)	-7.32 (4.9 %)	-26.82 (17.9 %)	-39.19 (26.1 %)	-42.38
CH_3	107.28	-75.99 (50.9 %)	-7.25 (4.9 %)	-26.66 (17.9 %)	-39.34 (26.4 %)	-41.95
H	105.56	-74.44 (50.7 %)	-7.16 (4.9 %)	-25.94 (17.7 %)	-39.32 (26.8 %)	-41.29
CH_2F	106.04	-74.09 (50.4 %)	-7.19 (4.9 %)	-26.60 (18.1 %)	-38.98 (26.5 %)	-40.83
F	104.53	-72.66 (50.2 %)	-7.16 (4.9 %)	-26.22 (18.1 %)	-38.64 (26.7 %)	-40.16
Cl	104.78	-72.10 (49.9 %)	-7.14 (4.9 %)	-26.94 (18.7 %)	-38.23 (26.5 %)	-39.63
CHF_2	104.21	-71.40 (49.8 %)	-7.10 (4.9 %)	-26.60 (18.5 %)	-38.42 (26.8 %)	-39.30
I	105.36	-71.89 (49.7 %)	-7.15 (4.9 %)	-27.48 (19.0 %)	-38.09 (26.3 %)	-39.26
Br	104.94	-71.58 (49.7 %)	-7.14 (5.0 %)	-27.66 (19.2 %)	-37.71 (26.2 %)	-39.15
CF_3	102.85	-69.25 (49.2 %)	-7.04 (5.0 %)	-26.56 (18.9 %)	-38.03 (27.0 %)	-38.03
SO_3H	102.53	-68.31 (48.8 %)	-7.02 (5.0 %)	-26.94 (19.3 %)	-37.66 (26.9 %)	-37.41
CN	102.10	-66.44 (48.1 %)	-6.98 (5.1 %)	-26.24 (19.0 %)	-38.44 (27.8 %)	-36.00
NO_2	100.91	-65.65 (48.0 %)	-6.94 (5.1 %)	-25.98 (19.0 %)	-38.13 (27.9 %)	-35.79

As in the interaction energies, the electrostatic, dispersion, and orbital terms remain unaffected by the steric hindrance and other intramolecular secondary interactions between the R groups for 3-R-py**,** 3,5-R_2-py and 4-R-py compounds and they can therefore be used to study the nature of the $[N\cdots I\cdots N]^+$ halonium bonding. Extreme caution must be taken when interpreting the results obtained for 2-R-py and 2,6-R_2-py compounds. Although these complexes somewhat follow the same trend previously found, the EDA analysis not only decomposes the energetic contributions between the I···N bond, but it is sensible to all the interactions among the fragments, including secondary interactions between the R groups.

For those substitution patterns for which it is sensible to employ Hammett parameters, the interaction energy, as well as the four contributions obtained from the EDA analysis present a clear dependence on the electron releasing power of the substituents. This correlation can be seen for the 4-R-py compounds in Figure 6.14, and the linear least-squares fittings are described by equations 6.1 – 6.5 (all energies in kcal/mol). Although for highly electron withdrawing substituents (positive σ_p values) the weight of the electrostatic and orbital terms is similar, the former presents a stronger dependence on the Hammett parameter and becomes predominant for highly electron releasing groups (negative σ_p values). In all cases, however, the orbital interactions are significant and necessary to overcome the Pauli repulsion.

Notice that although the Pauli repulsion increases with decreasing σ_p, the slope of the electrostatic term is larger and the interaction energy is consequently more attractive for negative Hammett parameters (Figure 6.14a).

$$E_{ORB} = -65.72 + 2.04\cdot\sigma_p \qquad (R^2 = 0.89) \qquad \text{[Eq. 6.1]}$$

$$E_{COUL} = -74.12 + 9.83\cdot\sigma_p \qquad (R^2 = 0.98) \qquad \text{[Eq. 6.2]}$$

$$E_{DISP} = -7.22 + 0.37\cdot\sigma_p \qquad (R^2 = 0.97) \qquad \text{[Eq. 6.3]}$$

$$E_{PAULI} = 106.3 - 6.67\cdot\sigma_p \qquad (R^2 = 0.96) \qquad \text{[Eq. 6.4]}$$

$$\Delta E_{INT} = -40.74 + 5.57\cdot\sigma_p \qquad (R^2 = 0.96) \qquad \text{[Eq. 6.5]}$$

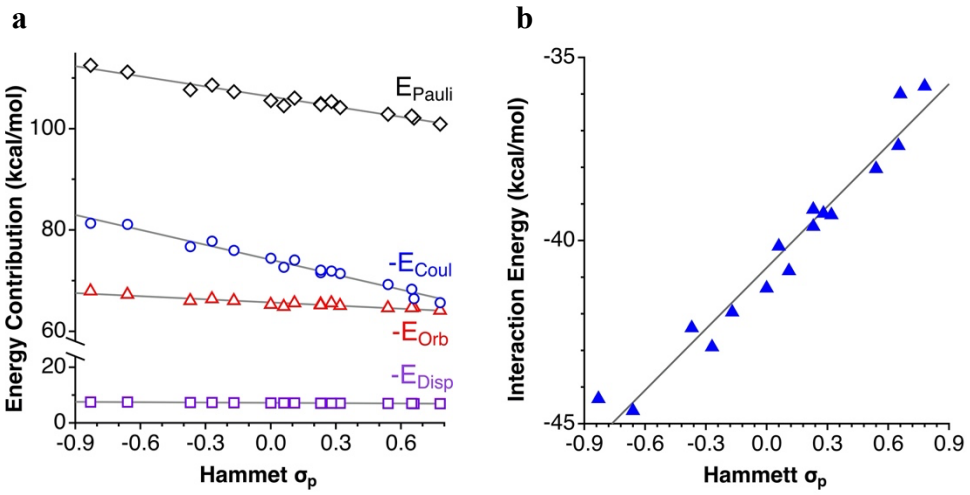

Figure 6.14. Dependence on the Hammett σ_p parameter of (**a**) the EDA contributions to the interaction energy and (**b**) the net interaction energy between the 4-R-py donors and the [(4-R-py)-I]$^+$ cations.

Similar considerations can be made for 3-R-py adducts (Figure 6.15a and equations 6.6 – 6.10),

$$E_{ORB} = -65.60 + 3.04 \cdot \sigma_m \quad (R^2 = 0.89) \quad \text{[Eq. 6.6]}$$

$$E_{COUL} = -75.27 + 14.14 \cdot \sigma_m \quad (R^2 = 0.94) \quad \text{[Eq. 6.7]}$$

$$E_{DISP} = -7.24 + 0.56 \cdot \sigma_m \quad (R^2 = 0.88) \quad \text{[Eq. 6.8]}$$

$$E_{PAULI} = 106.2 - 9.49 \cdot \sigma_m \quad (R^2 = 0.96) \quad \text{[Eq. 6.9]}$$

$$\Delta E_{INT} = -41.89 + 8.26 \cdot \sigma_m \quad (R^2 = 0.91) \quad \text{[Eq. 6.10]}$$

as well as for 3,5-R_2-py adducts (Figure 6.15b and equations 6.11 – 6.15). The main difference with the 4-R derivatives appears for the disubstituted adducts, that induce much wider variations of the interaction energies with the σ_m value (14 kcal/mol) than the monosubstituted ones (7 kcal/mol).

$$E_{ORB} = -65.92 + 5.50 \cdot \sigma_m \quad (R^2 = 0.90) \quad \text{[Eq. 6.11]}$$

$$E_{COUL} = -75.54 + 26.70 \cdot \sigma_m \quad (R^2 = 0.95) \quad \text{[Eq. 6.12]}$$

$$E_{DISP} = -7.34 + 1.07 \cdot \sigma_m \quad (R^2 = 0.87) \quad \text{[Eq. 6.13]}$$

$$E_{PAULI} = 106.8 - 17.72 \cdot \sigma_m \quad (R^2 = 0.95) \quad \text{[Eq. 6.14]}$$

$$\Delta E_{INT} = -42.01 + 15.55 \cdot \sigma_m \quad (R^2 = 0.94) \quad \text{[Eq. 6.15]}$$

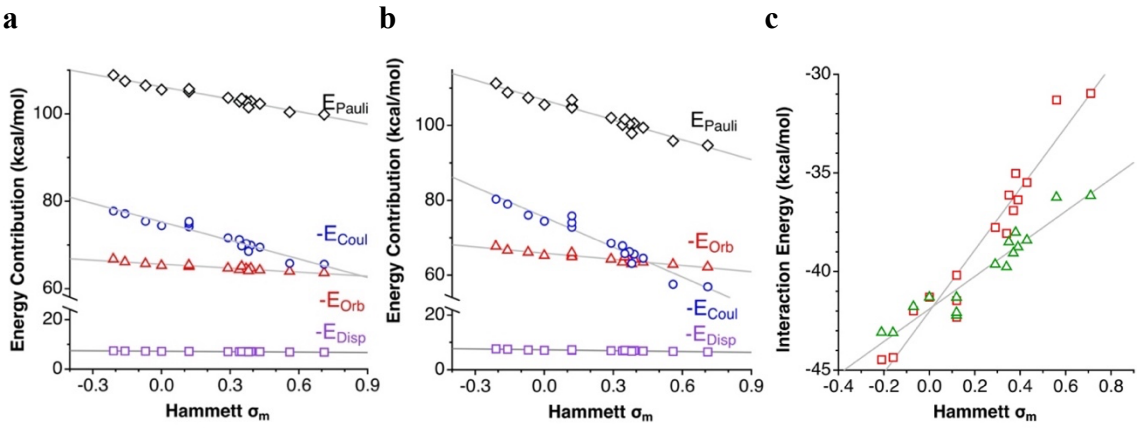

Figure 6.15. Dependence on the Hammett σ_m parameters of (**a**) the EDA contributions to the interaction energy between the 3-R-py donors and the $[(3\text{-R-py})\text{-I}]^+$ cations, (**b**) similarly for (3,5-R_2-py) analogues, and (**c**) the net interaction energy for the two families of compounds (triangles for monosubstituted, squares for disubstituted pyridine).

In the above substitution patterns the contribution of dispersion forces to the total attractive interaction is small, in good agreement with previous works,[26] and show a little dependence on the Hammett parameters. The electrostatic and Pauli contributions are strongly dependent on the nature of the substituent, and highly electron-withdrawing groups result in a predominant orbital term. It is important to stress that for each of the sets of systems studied (Tables 6.11 – 6.15) there is a good linear correlation between the Pauli and electrostatic contributions.

6.6 Halonium bonding in anions

As I mentioned in the Introduction, trihalide anions behave very similar to halonium cations. For example, the bonding in I_3^- could be described as the interaction between two closed-shell groups, I_2 and I^-, and rationalized by the σ-hole model. The anisotropic distribution of the electron density of I_2 form two opposite σ-holes (both of 32 kcal/mol, Figure 6.16) at each side of the I-I bond axis capable of accepting an electron pair of I^- at either side of the iodine molecule.

The optimized geometry of I_3^- is linear (179.9°) and exhibits a $D_{\infty h}$ symmetry with two identical I-I bond distances (2.959 Å), 1.12 Å shorter than the sum of the van der Waals radii of the involved atoms (4.08 Å). Despite the low $V_{s,max}$ value of its σ-holes, the interaction energy of the complex is as high as -39.18 kcal/mol, being comparable in strength to those halonium cations studied here. In addition, EDA analysis shows that both electrostatic and orbital contributions (especially charge transfer) have similar

weight and, with a small contribution of dispersion term (< 5 %), both are necessary to overcome the Pauli repulsion and thus make the net interaction energy attractive (Table 6.16). To sum up, the nature of the interactions that governs the bonding in halonium ions can also explain the geometric parameters and the bonding in trihalides anions.

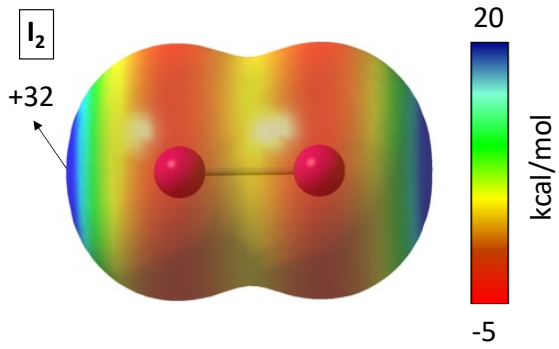

Figure 6.16. MEP map of I_2 molecule calculated at the MN12-SX/def2-TZVP level and plotted on the electron density isosurface (s = 0.001 Å). Energies are given in kcal/mol. Red and blue indicate a more negative and a more positive MEP value, respectively.

Table 6.16. EDA for the optimized I_3^- anion, calculated at the MN12-SX/def2-TZVP level. The percentage represents the contribution to the total attractive (negative) interaction energy. Energies are given in kcal/mol.

X_3^-	ΔE_{PAULI}	ΔE_{ELEC}	ΔE_{DISP}	ΔE_{POL}	ΔE_{CT}	ΔE_{INT}
I_3^-	81.85	-53.79 (44.4 %)	-5.96 (4.9 %)	-15.14 (12.5 %)	-46.13 (38.1 %)	-39.18

6.7 Conclusions

I have carried out a combined structural and computational analysis of the bonding in 3c-4e $[N\cdots I\cdots N]^+$ halonium groups. Only linear $[N\cdots I\cdots N]$ frameworks with neutral donors have been found in the CSD, with nearly equal I···N distances and angles in the range 175 – 178 º. A MEP analysis has disclosed a well-defined σ-hole at the outer of the halogen atom for all compounds studied. Such electron depletion is consistent with the geometric preferences of the interaction since the bond with the Lewis base along the X···N axis (X = Cl, Br, and I) is favoured by Coulombic attraction. The value of the electrostatic potential at the σ-hole increases on going down the halogen group, in good agreement with the polarizability of the central atom. Its value can be modulated by the donor group (D) and the nature of its substituent (R).

The strength of the interaction depends on the nature of both the donor and the acceptor. The stability of the adduct increases whit the size of the halogen, in good

agreement with the MEP analysis. However, aromatic donors show high interaction energies even though the magnitude of their σ-hole is low compared to ammonia and acetonitrile donors. Electron density changes have a strong influence on the stability of the $[N\cdots I\cdots N]^+$ halonium bond in 3-R-py, 3,5-R_2-py and 4-R-py complexes, whereas the I···N bond length remains virtually unaltered. The correlation of the Hammett σ_m and σ_p constants, respectively, with the I···N distances, the interaction energy and the $V_{s,max}$ indicates that the $[N\cdots I\cdots N]^+$ halonium bond is made less stable as the electrostatic potential at the σ-hole and the I···N distances increase. The steric hindrance and other secondary interactions between the R groups in 2-R-py and 2,6-R_2-py complexes plays an important role in the stability of the complex. Consequently, the lack of correlation between the Hammett σ_p parameters and the three parameters mentioned above prevent us from discussing further along this line.

EDA results have shed light on the physical nature of the interaction. As descending down the halogen group, the orbital to dispersion ratio decreases (Cl = 10.53:1, Br = 9.71:1, and I = 9.11:1), in good agreement with the atomic volume of the central atom X. Regarding the effect of the donors (D), the aromatic groups possess the lowest orbital to dispersion ratio (pyrimidine = 9.48:1, pyridine = 9.11:1, and imidazole = 9.33:1). Among the non-aromatic ones, acetonitrile (10.69:1) is a better donor than ammonia (10.01:1). As in the interaction energy, the four energetic contributions obtained from the EDA results of 3-R-py, 3,5-R_2-py and 4-R-py adducts correlate very well with the Hammett σ_m and σ_p parameters, respectively. The Coulombic and Pauli repulsion terms are linearly correlated within each family and overall repulsive. As in the systems studied in Chapters 3 and 4, the orbital and dispersion contributions are required to overcome the net repulsion of the electrostatic and Pauli terms, but in this case the orbital terms are much stronger than dispersion. In the compounds with distal substituents (3, 4 and 5 positions) the orbital/dispersion ratio is nearly invariably 9:1, whereas orto mono- and disubstitutions reduce that proportion to 7.3:1 and 5.7:1, respectively. To sum up, it seems clear that a pure electrostatic model of the σ-hole or "halogen bond" is inadequate to explain the stability of the halonium ions and the Pimentel-Rundle delocalized molecular orbital picture of 3-center-4-electrons bonding is more suitable. Since trihalide anions, X_3^-, behave very similar to halonium cations, the same conclusions found for the halonium ions can be applied to explain the geometric parameters and the nature of the bonding of those anions, as substantiated by present calculations on the triiodide anion.

All in all, I expect that these findings would allow a better understanding of the nature and factors that govern the bonding and the geometry of three-centre-four-electron halonium compounds, enable novel future applications as halonium transfer agents, asymmetric halofunctionalization, or as building blocks in supramolecular chemistry, and, ultimately, contribute to our understanding of chemical bonding.

6.8 Appendix

Annex 6.1. Analysis of the Molecular Electrostatic Potential.

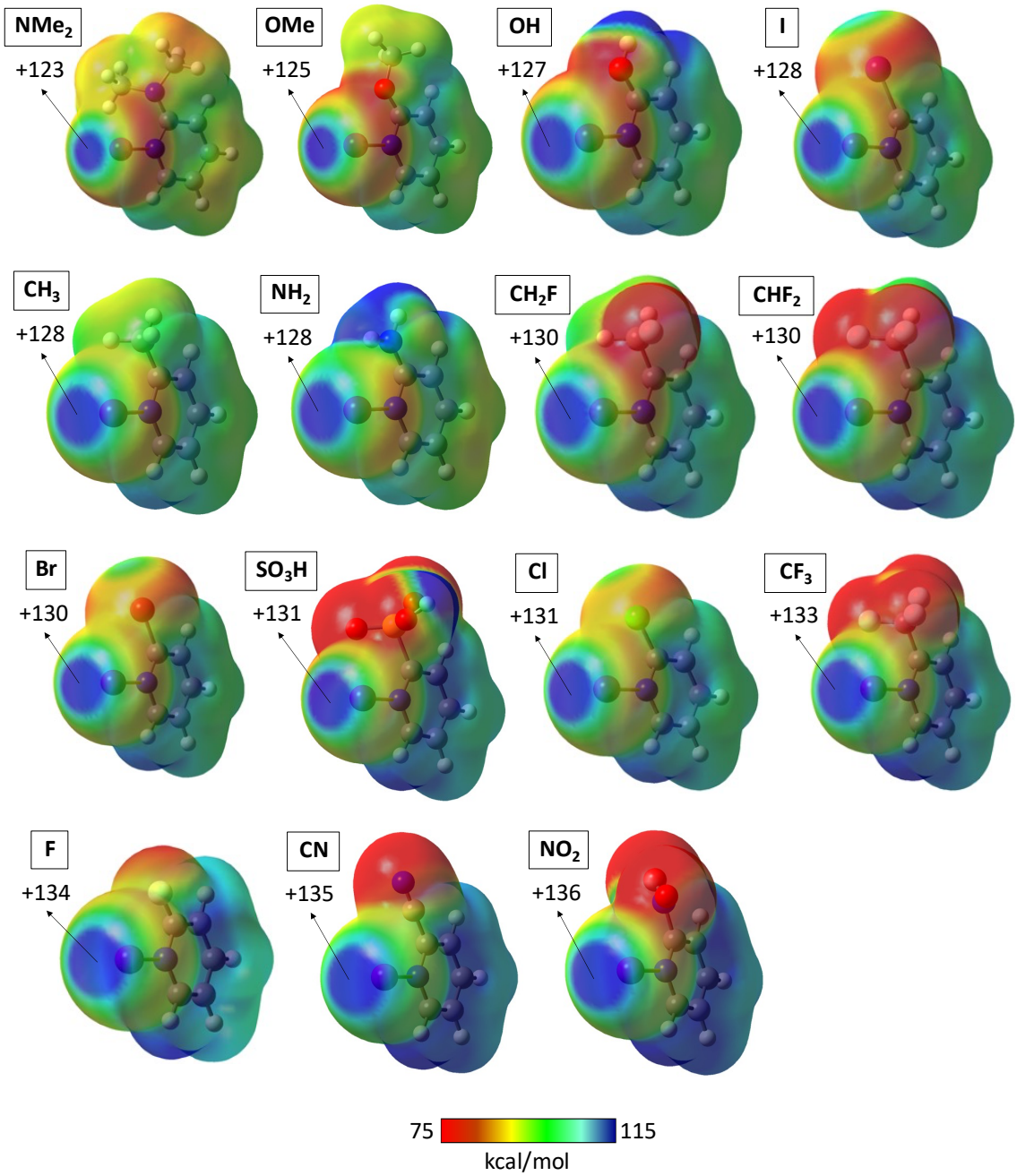

Figure A6.1. MEP maps for $[(2\text{-R-py})I]^+$ complexes (R = NMe_2, NH_2, OH, OMe, CH_3, CH_2F, CHF_2, CF_3, F, Cl, Br, I, CN, SO_3H, and NO_2) calculated at the MN12-SX/def2-TZVP level and plotted on the electron density isosurface (s = 0.001 Å). Energies are given in kcal/mol. Red and blue colours indicate less and more positive MEP values, respectively.

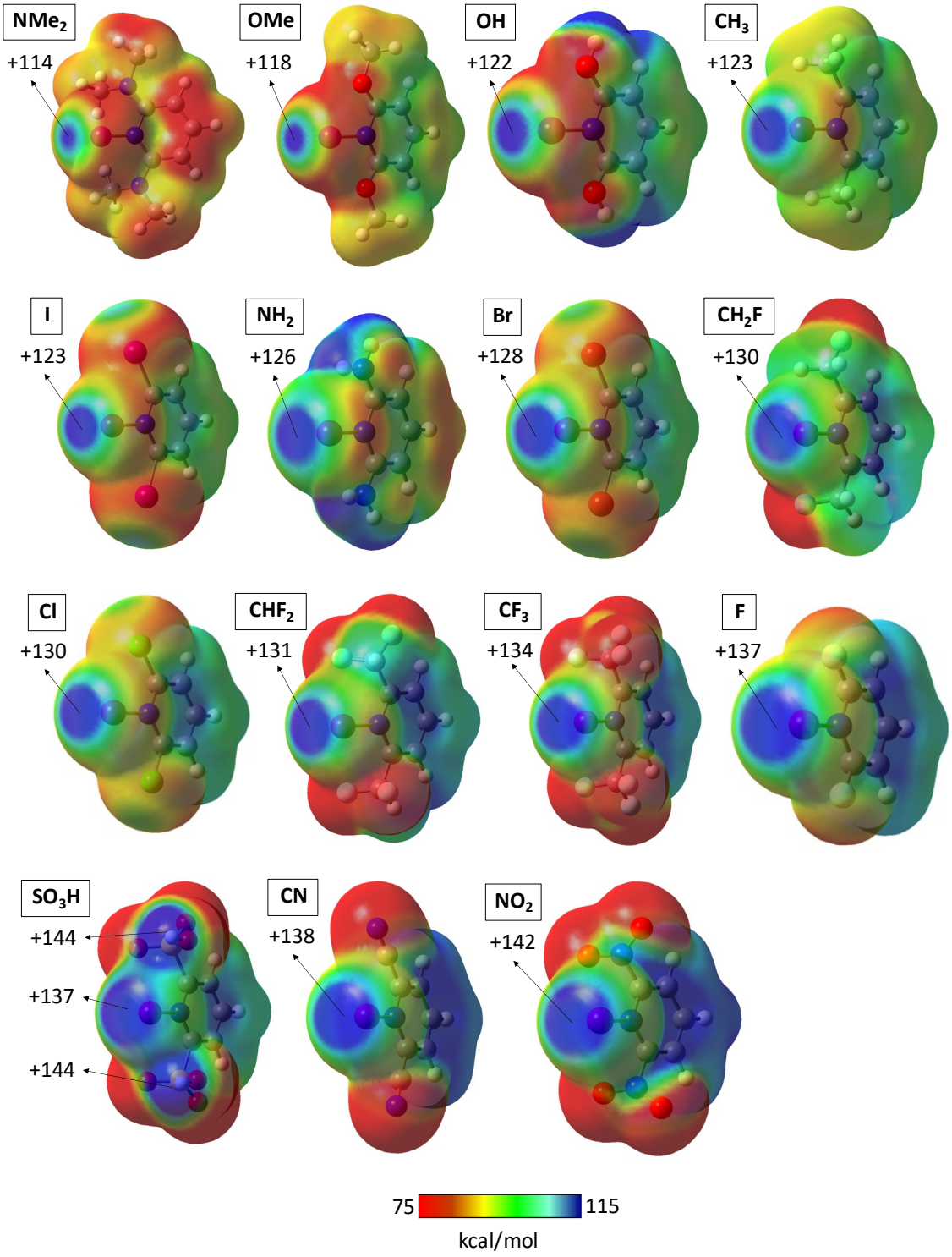

Figure A6.2. MEP maps for $[(2,6\text{-}R_2\text{-py})I]^+$ complexes (R = NMe_2, NH_2, OH, OMe, CH_3, CH_2F, CHF_2, CF_3, F, Cl, Br, I, CN, SO_3H, and NO_2) calculated at the MN12-SX/def2-TZVP level and plotted on the electron density isosurface (s = 0.001 Å). Energies are given in kcal/mol. Red and blue colours indicate less and more positive MEP values, respectively.

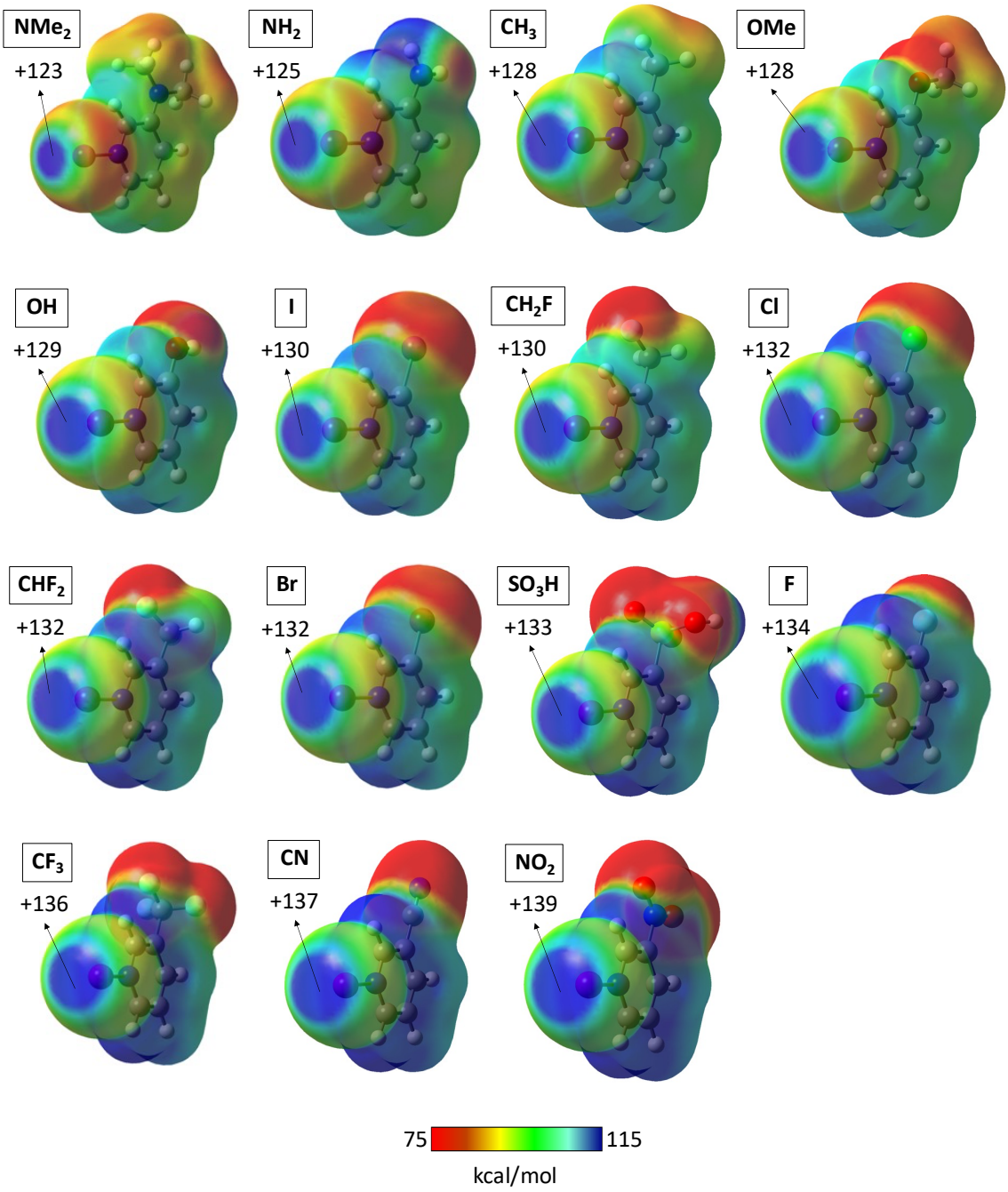

Figure A6.3. MEP maps for $[(3\text{-R-py})I]^+$ complexes (R = NMe_2, NH_2, OH, OMe, CH_3, CH_2F, CHF_2, CF_3, F, Cl, Br, I, CN, SO_3H, and NO_2) calculated at the MN12-SX/def2-TZVP level and plotted on the electron density isosurface (s = 0.001 Å). Energies are given in kcal/mol. Red and blue colours indicate less and more positive MEP values, respectively.

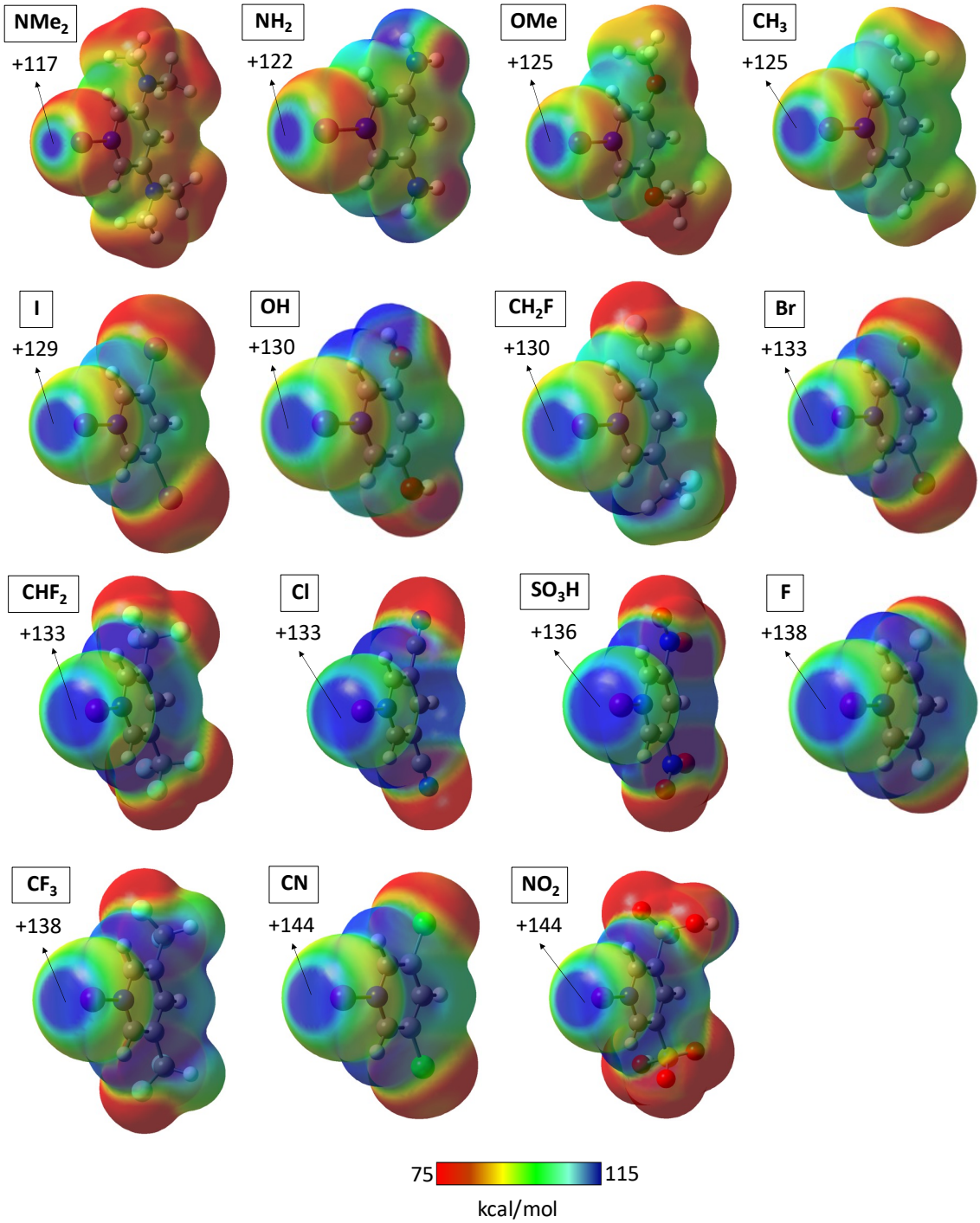

Figure A6.4. MEP maps for $[(3,5\text{-}R_2\text{-py})I]^+$ complexes (R = NMe_2, NH_2, OH, OMe, CH_3, CH_2F, CHF_2, CF_3, F, Cl, Br, I, CN, SO_3H, and NO_2) calculated at the MN12-SX/def2-TZVP level and plotted on the electron density isosurface (s = 0.001 Å). Energies are given in kcal/mol. Red and blue colours indicate less and more positive MEP values, respectively.

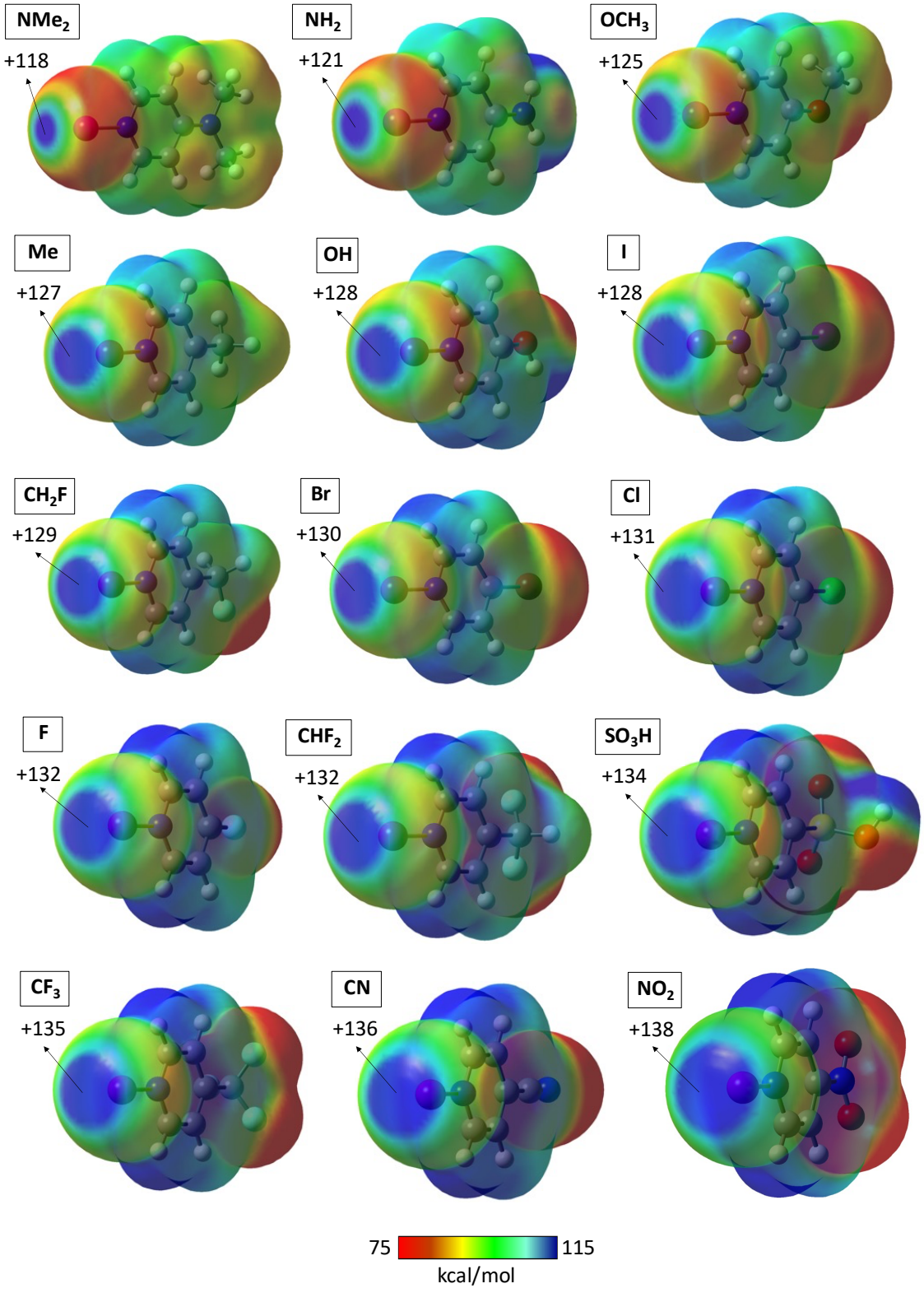

Figure A6.5. MEP maps for $[(4\text{-R-py})I]^+$ complexes (R = NMe_2, NH_2, OH, OMe, CH_3, CH_2F, CHF_2, CF_3, F, Cl, Br, I, CN, SO_3H, and NO_2) calculated at the MN12-SX/def2-TZVP level and plotted on the electron density isosurface (s = 0.001 Å). Energies are given in kcal/mol. Red and blue colours indicate less and more positive MEP values, respectively.

Annex 6.2. Benchmarking studies for the $[N\cdots I\cdots N]^+$ halonium bonding. The bis(Acetonitrile)-iodonium cation (BUKNAX)[40] was used as model to surveying the accuracy of a wide set of DFT functionals (with or without Grimme's D3[46] and D3BJ[47] dispersion correction) and the MP2 method. The results were compared with the experimental and calculated data at the CCSD and CCSD(T) level.

Table A6.1. Key geometrical parameters and interaction energies for the bis(Acetonitrile)-iodonium cation (BUKNAX)[40] model. Otherwise specified, all models were optimized at the corresponding functional and def2-TZVP basis set.

Method	Dispersion	$d_{N\text{-}I}$ (Å)	$\alpha_{N\text{-}I\text{-}N}$ (º)	ΔE_{INT} (kcal/mol)
Experimental		2.198	180	
CCSD[a]		2.198	180	-36.98
CCSD(T)[a]		2.198	180	-37.82
MP2		2.191	180	-41.30
B3LYP		2.218	180	-41.50
	D3	2.220	180	-42.55
	D3BJ	2.214	180	-43.60
CAM-B3LYP		2.213	180	-42.05
	D3	2.214	180	-42.82
	D3BJ	2.211	180	-43.23
Lc-wPBE		2.203	180	-41.61
	D3	2.204	180	-42.42
	D3BJ	2.201	180	-42.92
M06-HF		2.194	180	-40.94
	D3	2.194	180	-41.06
M06-L		2.209	180	-43.35
	D3	2.209	180	-43.44
M06-2X		2.213	180	-41.39
	D3	2.213	180	-41.48
MN12-SX[b]		2.190	180	-40.09
PBEPBE		2.200	180	-44.39
	D3	2.200	180	-44.95
	D3BJ	2.198	180	-45.51
TPSSh		2.197	180	-43.80
TPSSTPSS		2.200	180	-44.16
	D3	2.201	180	-44.94
	D3BJ	2.197	180	-45.69
wB97XD		2.215	180	-41.90

[a] The data was obtained from single point (SP) calculations using the crystal structure of BUKNAX.[40] Optimization at those levels of theory implies a high computational cost. [b] Method selected for the study of the $[N\cdots X\cdots N]^+$ halonium bond (X= Cl, Br, and I).

Annex 6.3. Linear least-squares fitting equations for Figure 6.7.

a) $V_{s,max}$ (4-R-py) = 128.7 + 10.64·σ_p (R^2 = 0.89) [Eq. A6.1]

b) $V_{s,max}$ (3-R-py) = 127.7 + 15.07·σ_m (R^2 = 0.86) [Eq. A6.2]

$V_{s,max}$ (3,5-R_2-py) = 125.6 + 26.19·σ_m (R^2 = 0.84) [Eq. A6.3]

c) $V_{s,max}$ (2-R-py) = 129.4 + 6.16·σ_p (R^2 = 0.67) [Eq. A6.4]

Annex 6.4. 2nd order polynomial least-squares fitting equations for Figure 6.9.

a) E_{INT} (4-R-py) = 104.1 – 2.74·$V_{s,max}$ + 0.013·($V_{s,max}$)^2 (R^2 = 0.89) [Eq. A6.5]

b) E_{INT} (3-R-py) = 8.55 – 1.22·$V_{s,max}$ + 0.007·($V_{s,max}$)^2 (R^2 = 0.82) [Eq. A6.6]

E_{INT} (3,5-R_2-py) = -0.94 – 1.09·$V_{s,max}$ + 0.006·($V_{s,max}$)^2 (R^2 = 0.84) [Eq. A6.7]

Annex 6.5. Linear least-squares fitting equations for Figure 6.12.

a) $d_{I\text{-}N}$ (4-R-py) = 2.25 + 0.008·σ_p (R^2 = 0.90) [Eq. A6.8]

b) E_{INT} (4-R-py) = – 40.73 + 5.58·σ_p (R^2 = 0.96) [Eq. A6.9]

Annex 6.6. Linear least-squares fitting equations for Figure 6.13.

a) $d_{I\text{-}N}$ (3-R-py) = 2.25 + 0.008·σ_m (R^2 = 0.91) [Eq. A6.10]

$d_{I\text{-}N}$ (3,5-R_2-py) = 2.25 + 0.016·σ_m (R^2 = 0.89) [Eq. A6.11]

b) E_{INT} (3-R-py) = -41.89 + 8.26·σ_m (R^2 = 0.91) [Eq. A6.12]

E_{INT} (3,5-R_2-py) = -42.01 + 15.56·σ_m (R^2 = 0.94) [Eq. A6.13]

6.9 References

1. Desiraju, G. R.; Ho, P. S.; Kloo, L.; Legon, A. C.; Marquardt, R.; Metrangolo, P.; Politzer, P.; Resnati, G.; Rissanen, K. Definition of the Halogen Bond (IUPAC Recommendations 2013). *Pure Appl. Chem.* **2013**, *85*, 1711-1713.
2. Metrangolo, P.; Neukirch, H.; Pilati, T.; Resnati, G. Halogen Bonding Based Recognition Processes: A World Parallel to Hydrogen Bonding. *Acc. Chem. Res*. **2005**, *38*, 386-395.
3. Metrangolo, P.; Resnati, G. Halogen vs Hydrogen. *Science*. **2008**, *321*, 918-919.

4. Umeyama, H.; Morokuma, K. The origin of hydrogen bonding. An energy decomposition study**.** *J. Am. Chem. Soc*. **1977**, *99*, 1316-1332.
5. Grabowski, S. J. Hydrogen and halogen bonds are ruled by the same mechanisms**.** *Phys. Chem. Chem. Phys*. **2013**, *15*, 7249-7259.
6. Syzgantseva, O. A.; Tognetti, V.; Joubert, L. On the Physical Nature of Halogen Bonds: A QTAIM Study**.** *J. Phys. Chem. A* **2013**, *117*, 8969-8980.
7. Wolters, L. P.; Bickelhaupt, F. M. Halogen Bonding versus Hydrogen Bonding: A Molecular Orbital Perspective. *Chem. Open.* **2012**, *1*, 96-105.
8. Corradi, E.; Meille, S. V.; Messina, M. T.; Metrangolo, P.; Resnati, G. Halogen Bonding versus Hydrogen Bonding in Driving Self-Assembly Processes. *Angew. Chem. Int. Ed*. **2000**, *39*, 1782-1786.
9. Aakeröy, C. B.; Desper, J.; Helfrich, B. A.; Metrangolo, P.; Pilati, T.; Resnati, G.; Stevenazzi, A. Combining halogen bonds and hydrogen bonds in the modular assembly of heteromeric infinite 1-D chains. *Chem. Commun*. **2007**, 4236-4238.
10. Saha, B. K.; Nangia, A.; Jaskólski, M. Crystal engineering with hydrogen bonds and halogen bonds**.** *CrystEngComm.* **2005**, *7*, 355-358.
11. Velasquez, J. D.; Mahmoudi, G.; Zangrando, E.; Gurbanov, A. V.; Zubkov, F. I.; Zorlu, Y.; Masoudiasl, A.; Echeverría, J. Experimental and theoretical study of Pb···S and Pb···O σ-hole interactions in the crystal structures of Pb(II) complexes. *CrystEngComm* **2019**, *21*, 6018-6025.
12. Scheiner, S. Coordination of a Central Atom by Multiple Intramolecular Pnicogen Bonds**.** *Inorg Chem.* **2020**, *59*, 9315-9324.
13. Zierkiewicz, W.; Wysokinski, R.; Michalczyk, M.; Scheiner, S. Chalcogen bonding of two ligands to hypervalent YF_4 (Y = S, Se, Te, Po). *Phys. Chem. Chem. Phys*. **2019**, *21*, 20829-20839.
14. Politzer, P.; Murray, J. S.; Clark, T. Halogen bonding: an electrostatically-driven highly directional noncovalent interaction. *Phys. Chem. Chem. Phys*. **2010**, *12*, 7748-7757.
15. Politzer, P.; Murray, J. S.; Clark, T. Halogen bonding and other σ-hole interactions: a perspective. *Phys. Chem. Chem. Phys.* **2013**, *15*, 11178-11189.
16. Lommerse, J. P. M.; Stone, A. J.; Taylor, R.; Allen, F. H. The Nature and Geometry of Intermolecular Interactions between Halogens and Oxygen or Nitrogen. *J. Am. Chem. Soc.* **1996**, *118*, 3108-3116.

17. Turunen, T.; Erdélyi, M. Halogen bonds of halonium ions. *Chem. Soc. Rev.* **2020**, *49*, 2688-2700.

18. Koskinen, L.; Hirva, P.; Kalenius, E.; Jääskeläinen, S.; Rissanen, K.; Haukka, M. Halogen bonds with coordinative nature: halogen bonding in a S–I^+–S iodonium complex. *CrystEngComm* **2015**, *17*, 1231-1236.

19. Reiersoelmoen, A. C.; Battaglia, S.; Oeien-Oedegaard, S.; Gupta, A. K.; Fiksdahl, A.; Lindh, R.; Erdelyi, M. Symmetry of three-center, four-electron bonds. *Chem. Sci.* **2020**, *11*, 7979-7990.

20. Warzok, U.; Marianski, M.; Hoffmann, W.; Turunen, L.; Rissanen, K.; Pagel, K.; Schalley, C. A. Surprising solvent-induced structural rearrangements in large [N···I^+···N] halogen-bonded supramolecular capsules: an ion mobility-mass spectrometry study, *Chem. Sci.* **2018**, *9*, 8343-8351.

21. Turunen, L.; Peuronen, A.; Forsblom, S.; Kalenius, E.; Lahtinen, M.; Rissanen, K. Tetrameric and Dimeric [N···I^+···N] Halogen-Bonded Supramolecular Cages**.** *Chem. Eur. J.* **2017**, *23*, 11714-11718.

22. Turunen, L.; Warzok, U.; Puttreddy, R.; Beyeh, N. K.; Schalley, C. A.; Rissanen, K. [N···I^+···N] Halogen-Bonded Dimeric Capsules from Tetrakis(3-pyridyl)ethylene Cavitands**.** *Angew. Chem. Int. Ed.* **2016**, *55*, 14033-14036.

23. Vanderkooy, A.; Gupta, A. K.; Földes, T.; Lindblad, S.; Orthaber, A.; Pápai, I.; Erdélyi, M. Halogen Bonding Helicates Encompassing Iodonium Cations. *Angew. Chem. Int. Ed.* **2019**, *58*, 9012-9016.

24. Turunen, L.; Warzok, U.; Schalley, C. A.; Rissanen, K. Nano-sized $I_{12}L_6$ Molecular Capsules Based on the [N···I^+···N] Halogen Bond. *Chem* **2017**, *3*, 861-869.

25. Hakkert, S. B.; Erdélyi, M. Halogen bond symmetry: the N–X–N bond. *J. Phys. Org. Chem.* **2014**, *28*, 226-233**.**

26. Karim, A.; Reitti, M.; Carlsson, A.-C. C.; Gräfenstein, J.; Erdélyi, M. The nature of [N–Cl–N]$^+$ and [N–F–N]$^+$ halogen bonds in solution. *Chem. Sci.* **2014**, *5*, 3226-3233.

27. Georgiou, D. C.; Butler, P.; Browne, E. C.; Wilson, D. J. D.; Dutton, J. L. On the Bonding in Bis-pyridine Iodonium Cations**.** *Aust. J. Chem*. **2013**, *66*, 1179-1188.

28. Carlsson, A.-C. C.; Gräfenstein, J.; Budnjo, A.; Laurila, J. L.; Bergquist, J.; Karim, A.; Kleinmaier, R.; Brath, U.; Erdélyi, M. Symmetric Halogen Bonding Is Preferred in Solution. *J. Am. Chem. Soc.* **2012**, *134*, 5706-5715.

29. Razmazma, H.; Ebrahimi, A. The effects of cation-π and anion-π interactions on halogen bonds in the $[N\cdots X\cdots N]^+$ complexes: A comprehensive theoretical study. *J. Mol. Graphics Modell.* **2018**, *84*, 134-144.

30. Oliveira, V.; Kraka, E.; Cremer, D. The intrinsic strength of the halogen bond: electrostatic and covalent contributions described by coupled cluster theory. *Phys. Chem. Chem. Phys*. **2016**, *18*, 33031-33046.

31. Pimentel, G. C. The Bonding of Trihalide and Bifluoride Ions by the Molecular Orbital Method. *J. Chem. Phys.* **1951**, *19*, 446-448.

32. Rundle, R. E. Electron Deficient Compounds[1]. *J. Am. Chem. Soc.* **1947***, 69,* 1327-1331.

33. Rundle, R. E. Electron Deficient Compounds. II. Relative Energies of "Half-Bonds". J. Chem. Phys. **1949**, *17*, 671-675.

34. Landis, C. R.; Weinhold, F. 3c/4e *σ*-type long-bonding: a novel transitional motif toward the metallic delocalization limit. *Inorg Chem*. **2013**, *52*, 5154-5166.

35. Carlsson, A.-C. C.; Uhrbom, M.; Karim, A.; Brath, U.; Graefenstein, J.; Erdelyi, M. Solvent effects on halogen bond symmetry. *CrystEngComm*. **2013**, *15*, 3087-3092.

36. Bedin, M.; Karim, A.; Reitti, M.; Carlsson, A.-C. C.; Topic, F.; Cetina, M.; Pan, F.; Havel, V.; Al-Ameri, F.; Sindelar, V.; Rissanen, K.; Graefenstein, J.; Erdelyi, M. Counterion influence on the N-I-N halogen bond. *Chem. Sci*. **2015**, *6*, 3746-3756.

37. By Carlsson, A.-C. C.; Mehmeti, K.; Uhrbom, M.; Karim, A.; Bedin, M.; Puttreddy, R.; Kleinmaier, R.; Neverov, A. A.; Nekoueishahraki, B.; Graefenstein, J.; Rissanen, K.; Erdélyi, M. Substituent Effects on the $[N–I–N]^+$ Halogen Bond. *J. Am. Chem. Soc.* **2016**, *138*, 9853-9863.

38. Ebrahimi, A.; Razmazma, H.; Delarami, H. The Nature of Halogen Bonds in $[N\cdots X\cdots N]^+$ Complexes: A Theoretical Study. *Phys. Chem. Res.* **2016**, *4*, 1-15.

39. Groom, C. R.; Bruno, I. J.; Lightfoot, M. P.; Ward, S. C. The Cambridge Structural Database. *Acta Cryst.* **2016**, *B72*, 171-179.

40. Crawford, M.-J.; Göbel, M.; Karaghiosoff, K.; Klapötke, T. M.; Welch, J. M. Does $[I_3]^+$ Act as an "$[I]^+$" Donor to CH_3CN and N_2O? Structure of $[H_3CCN\text{-}I\text{-}NCCH_3]^+[AsF_6]^-$. *Inorg. Chem.* **2009**, *48*, 9983-9985.

41. Pritzkow, H. Bis(hexamethylenetetramine)iodonium triiodide. *Acta Cryst.* **1975**, *B31*, 1505-1506.

42. Grebe, J.; Geiseler, G.; Harms, K.; Neumuller, B.; Dehnicke, K. Domino Effect in the Buildup of N-I-N-I Chains of the *N*-Iodine(triphenylphosphane)imine. *Angew. Chem. Int. Ed*. **1999**, *38*, 222-225.

43. Grebe-Metz, J.; Weller, F.; Dehnicke, K. $[Et_3PNI)_2I]Cl$ – a Donor-Acceptor Complex of N-Iodo(triethylphosphane)imine with Iodine Monochloride. *Z. Anorg. Allg. Chem.* **2003**, *629*, 1110-1112.

44. Alvarez, S. A Cartography of the Van der Waals Territory. *Dalton Trans.* **2013**, *42*, 8617-8636.

45. Novoa, J. J.; Mota, F.; Alvarez, S. Structure and Stability of the X_3^- Systems (X = F, Cl, Br, I). *J. Phys. Chem.* **1988**, *92*, 6561-6566.

46. Grimme, S.; Antony, J.; Ehrlich, S.; Krieg, H. A consistent and accurate ab initio parametrization of density functional dispersion correction (DFT-D) for the 94 elements H-Pu. *J. Chem. Phys*. **2010**, *132*, 154104-154122.

47. Grimme, S.; Ehrlich, S.; Goerigk, L. Effect of the damping function in dispersion corrected density functional theory. *J. Chem. Phys*. **2011**, *32*, 1456-1465.

Chapter 7

Azido···azido interactions in transition metal complexes

7.1 Introduction

Azides are a versatile class of chemical compounds containing the anion N_3^- or the functional group $-N_3$ attached to an element or radical through one of the terminal nitrogen atoms. Most inorganic[1-4] and organic[5,6] azide compounds are highly explosive and toxic and thus must be handled with extreme caution. Despite the hazards associated with their use (or perhaps even because of them), these molecules have many applications in the fields of synthetic chemistry, biology, and biomedicine. For instance, the ionic sodium azide (NaN_3) salt is used as a propellant in airbags[7] and as a precursor to other inorganic[8] and organic[9] azide compounds, to name just a few examples. Heavy metal azides, such as lead(II) azide ($Pb(N_3)_2$), are used as shock-sensitive detonators.[10] Organic azides are essential components in azide-alkyne "click" reactions[11-13] and bioorthogonal chemistry.[14,15] They are also important precursors to amine[16] and nitrene[17] compounds. Furthermore, most azide-containing drugs have an important pharmaceutical application as enzyme inhibitors.[18,19]

Transition metal (N_3-M) azide complexes are relatively stable compounds containing one or more azide ligands coordinated to transition metals.[1] They are of increasing importance for their use in catalysis,[1,20-25] luminescence,[26,27] magnetism,[1,28-30] inorganic "click" reactions,[31,32] bioorthogonal chemistry,[33] and pharmaceutics.[34-35] Compared to ionic azides (N_3^-, $D_{\infty h}$),[36] all covalent azides of both main group and transition metals display a $-N_3$ moiety with a slightly bent *trans* C_s configuration with a N_α-N_β-N_γ bond angle of approximately 172 ± 3º and two different N-N bond lengths (Scheme 7.1a).[1-3] One of these bonds (N_α-N_β) is shorter than a typical N-N single bond (1.44 Å) while the other (N_β-N_γ) is slightly longer than a N≡N triple bond in the N_2 molecule (1.10 Å).[37] The observed values are in agreement with resonance among structures **b** and **c** (Scheme 7.1) contributing equally. Formal charges indicate the presence of an electron-poor atom (N_β) as well as two electron-rich atoms (N_α and N_γ).

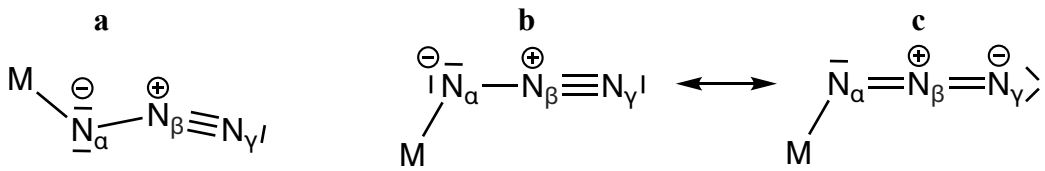

Scheme 7.1. (**a**) Lewis structure and resonance formulas (**b** and **c**) of transition metal (N_3-M) azide complexes.

Recent studies have evaluated the ability of azide compounds, specifically the central nitrogen atom (N_β), to act as electron density acceptors in pnictogen bonds. Regarding organic azides (N_3-R), Bursch and co-workers have studied 44 intermolecular model systems containing an azide moiety in close contact with pnictogen, chalcogen, and halogen atoms, respectively. The nature of such interaction was found to arise from dispersion forces, with an important electrostatic contribution and small or no orbital terms.[38] The O···N_β interaction is strong enough to dictate the conformation of molecules in solid-state, which may be used to freeze the otherwise free-rotating azide group in a conformation suitable for its reaction with an alkyne via topochemical cycloaddition.[39] Scheiner has investigated, among others, the bonding between a Lewis base and two covalent inorganic (N_3-X) azides, with X = F, CN. The Molecular Electrostatic Potential (MEP) maps of the N_3-X molecules show a π-hole equatorial belt enveloping the N_β atom which can electrostatically interact with the lone pairs of an incoming nucleophile.[40] The azido unit can also act as an electron density donor via the lone pair of the N_γ atom with an H-N moiety to form an intermolecular hydrogen bond.[41]

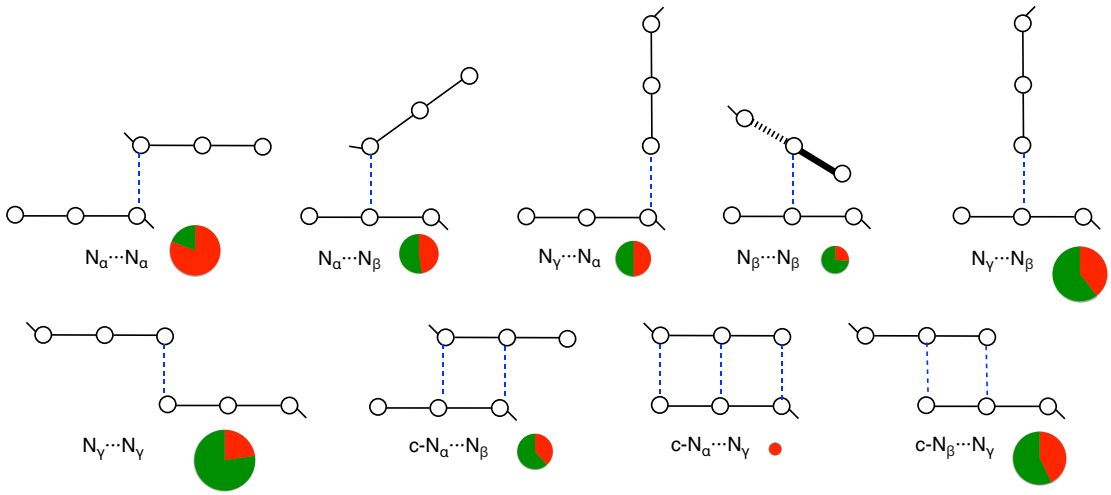

Scheme 7.2. Interaction topologies for azido···azido short contacts (dashed lines) in transition metal azide complexes. For the pie charts, the size of the circle is adjusted to the number of contacts found for each topology, whereas the red and green areas represent supported and unsupported contacts, respectively. The empty circles represent N atoms. The subscripts (α, β, and γ) indicates the position of each N relative to the metal. The prefix "c-" (cyclo-) indicates that a pseudocycle is formed by the N···N contacts.

A search in the Cambridge Structural Database (CSD)[42] of experimental structures containing azides covalently bound to transition metals has identified unnoticed

intermolecular short contacts between the azido moieties with N···N distances shorter than twice the nitrogen van der Waals (vdW) radius (3.32 Å).[43] Scheme 7.2 represents schematically the different azido···azido (dashed lines) interaction topologies that I have found, their abundance (pie charts) and the fraction of supported (red) and unsupported (green) contacts, respectively. The subscripts indicate, in alphabetical order, the position of each nitrogen (empty circles) relative to the metal, with alpha (α) being the nearest and gamma (γ) being the farthest. The prefix "c-" (cyclo-) indicates that the corresponding two N···N contacts form a pseudocycle. Note that c-$N_\alpha\cdots N_\gamma$ also exhibits a $N_\beta\cdots N_\beta$ interaction.

Plotting the experimental structures with N···N contacts shorter than twice the nitrogen vdW radius as a function of the M-N_α-$N_\beta\cdots N_\gamma$ dihedral angle ϕ (see Figure 7.1 for definition) for $N_\gamma\cdots N_\alpha$ and $N_\gamma\cdots N_\beta$ contacts, two wide distributions appear, with a peak at 160º and 90º, respectively. Note that there are no structures with ϕ = 90º in the former contact whereas for the latter there are 10 structures.

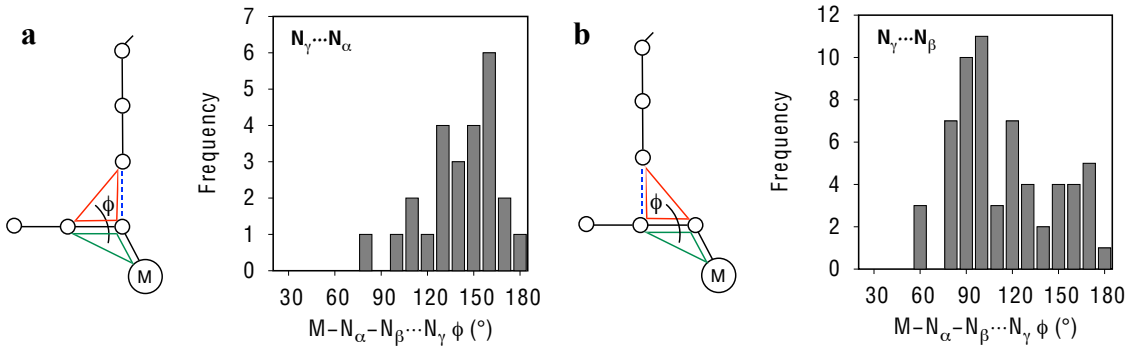

Figure 7.1. Distribution of the dihedral angle ϕ (as defined in the structures) for contacts with (**a**) $N_\gamma\cdots N_\alpha$ and (**b**) $N_\gamma\cdots N_\beta$ interaction topologies. The empty circles represent N atoms. The dashed lines represent the azido···azido contacts.

Upon initial inspection, and assuming that the MEP maps of N_3-M are similar to those found for NNN-F and NNN-CN,[40] it is expected that $N_\alpha\cdots N_\beta$, $N_\gamma\cdots N_\beta$, c-$N_\alpha\cdots N_\beta$, and c-$N_\beta\cdots N_\gamma$ contacts might be attractive from the electrostatic point of view since regions of electron potential of opposite sign would be close to each other. The electrophilic region surrounding the central N_β atom would act as a binding site for the lone pairs of the incoming nucleophiles (N_α or N_γ), thus forming a π-hole bond. Nevertheless, all interaction topologies, except c-$N_\alpha\cdots N_\gamma$, exhibit several systems that are only bound by intermolecular azido···azido contacts, without any other secondary

interaction supporting them. At this point, two hypotheses can be made to explain the stabilization of the electrostatically repulsive $N_\alpha\cdots N_\alpha$, $N_\gamma\cdots N_\alpha$, $N_\beta\cdots N_\beta$, $N_\gamma\cdots N_\gamma$, and c-$N_\alpha\cdots N_\gamma$ contacts. The first one is that the dispersion term and/or other attractive contributions can counterbalance the electrostatic repulsion and make all these adducts stable. The second one is that these contacts are only an artefact due to solid state packing effects. To verify these hypotheses, I undertake a combined structural and computational analysis of azido···azido short contacts with all the interaction topologies found for this particular NCIs.

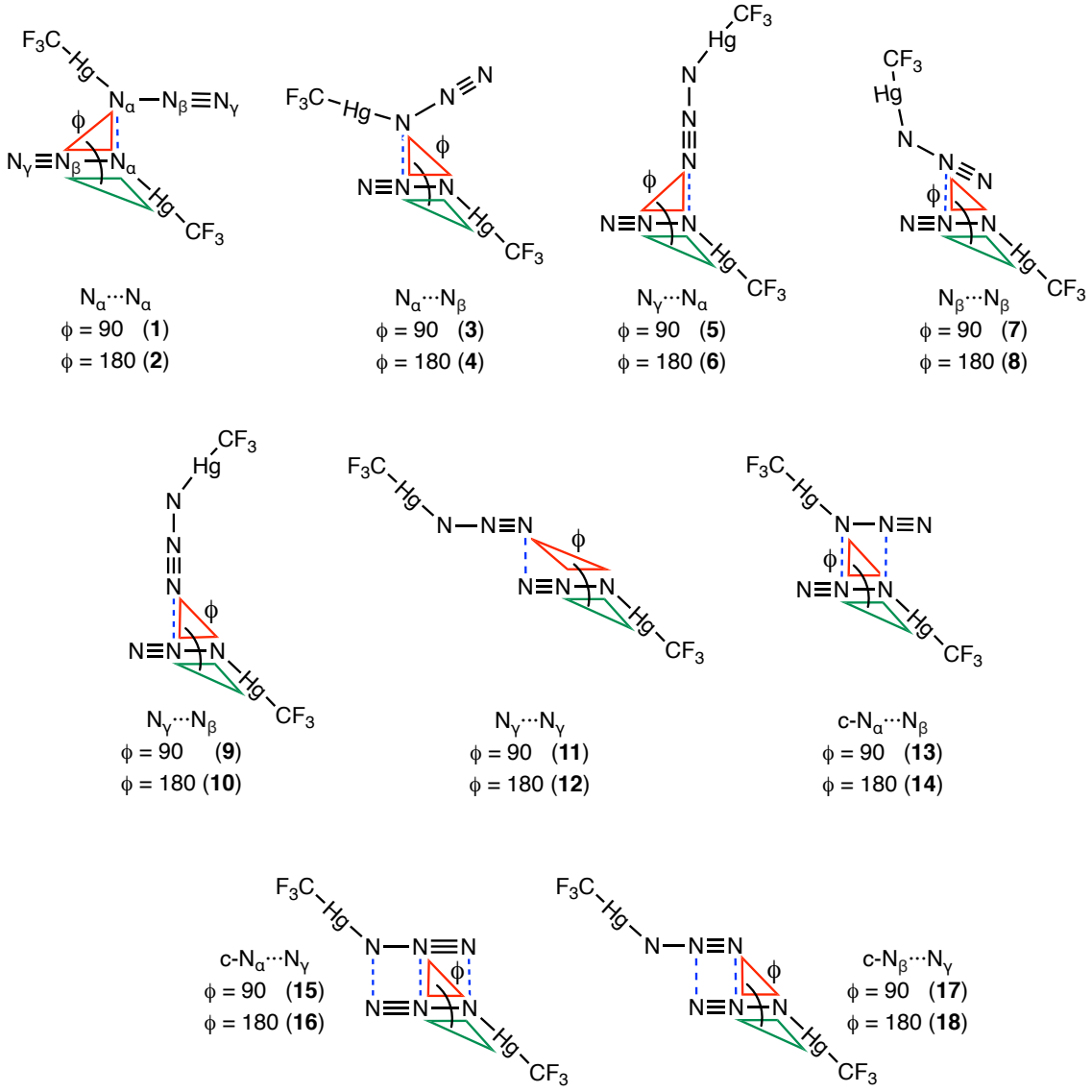

Scheme 7.3. Interaction topologies for the azido···azido short contacts (dashed lines) in the [N_3-$Hg(CF_3)$]$_2$ model. The dihedral angle ϕ is 90º for the first model and 180º for the second one.

Starting from the optimized structure of trifluoromethyl-azido-mercury(II) (FMHGAZ),[44] I have designed two sets of models based on this dimer with the different

interaction topologies shown in Scheme 7.2. Taking into account the distribution found for $N_\gamma\cdots N_\alpha$ and $N_\gamma\cdots N_\beta$ contacts, I will study each interaction topology at a dihedral angle ϕ of 90º and 180º, respectively. In both $N_\alpha\cdots N_\beta$ compounds (**3** and **4**), the $N_\beta\cdots N_\alpha$-N_β bond angle was set to be 130º. All dimers were partially optimized because of the free rotation around the Hg-N bond. In each of these calculations, only the intermolecular N···N distance was optimized while the rest of the structure was fixed at a given bonding pattern. In the case of systems with two or more N···N contacts, only one of them was partially optimized. To further investigate the nature and the strength of the interaction I have performed Molecular Electrostatic Potential (MEP), Energy Decomposition Analyses (EDA), Quantum Theory of Atoms in Molecules (QTAIM) and Noncovalent Interactions (NCI) Indices of the compounds in Scheme 7.3. Cooperative or secondary intermolecular N···Hg bonds were also observed in several cases, that may further enhance the stability of the cluster.

7.2 Analysis of the Molecular Electrostatic Potential

To try to rationalise the azido···azido short contacts from the electrostatic point of view, I have computed the MEP map of the optimized structure of trifluoromethyl-azido-mercury(II) (Figure 7.2).

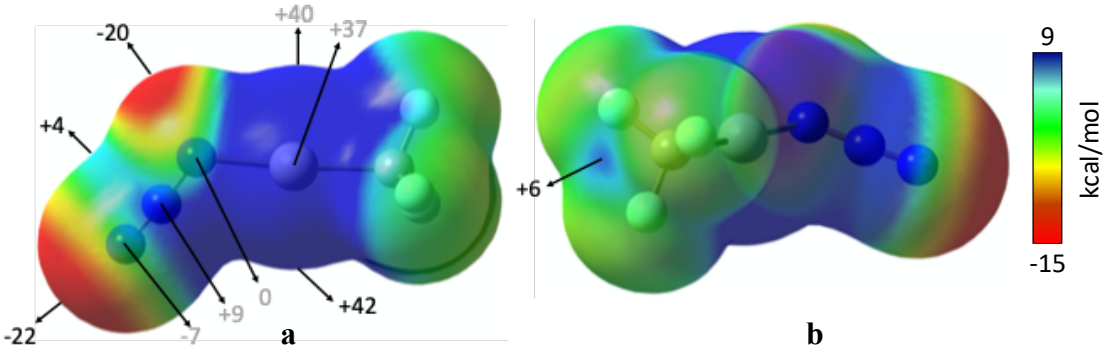

Figure 7.2. MEP maps for trifluoromethyl-azido-mercury(II) ([N_3-Hg(CF_3)]; FMHGAZ)[44] calculated at M06-2X/def2-TZVP level and plotted on the electron density isosurface (s = 0.001 Å). Energies are given in kcal/mol. Red and blue colours indicate a more negative and a more positive MEP value, respectively. Values in grey do not represent either local minima or maxima.

As expected, the MEP map of the monomer is similar to those reported earlier for NNN-F and NNN-CN.[40] The electron-poor region of the azide unit is found near the central N_β atom, and its shape resembles the π-hole equatorial belt that those covalent inorganic azides exhibit. This small and slightly positive electron-deficient region is

surrounded by two highly electron-rich regions of the N_α and N_γ atoms. In particular, the most negative region of the isosurface is located at the terminal N_γ atom, with a minimum MEP value ($V_{s,min}$) of -22 kcal/mol. On the other hand, the most positive region envelops the Hg atom, with a maximum MEP value ($V_{s,max}$) of 42 kcal/mol. Seen from above the molecular plane, there is an electron charge concentration at N_γ (V = -7 kcal/mol), an electron charge depletion at N_β (V = 9 kcal/mol), and neutral potentials at N_α ($V \approx 0$ kcal/mol). The MEP map also shows the existence of a σ-hole located at the extension of the Hg-C bond (Figure 7.2b). If the electrostatic contribution is the main driving force for the interaction, only those dimers in which the electron-rich areas of one monomer are directed to the electron-poor areas of the other are expected to be stable. It is worth mentioning that, given the tendency of the negative electrostatic potential regions to interact with the most positive one, a total optimization of the dimers would promote the intermolecular N···Hg interaction over the N···N interaction, since the $V_{s,max}$ is located near the metal atom.

7.3 Analysis of the Interaction Energies

By means of DFT calculations, I have examined the impact of the interaction topology on its strength. The main results are shown in Table 7.1. There are no local minima for compounds **6**, **16** and **18**. As can be inferred from Figure 7.2, these dimers are unstable due to electrostatic repulsion since the electrostatic potential regions of the same sign in the two monomers are facing each other. The shortest calculated N···N distances vary from 2.823 to 3.730 Å. Except for structures **5** and **15**, all N···N distances are found to be less than twice the nitrogen van der Waals radius (3.32 Å). Interestingly, structures **1**, **3**, **4**, **5**, **7** and **13** exhibit short N···Hg contacts whereas structure **15** displays a slightly longer N···Hg (+0.13 Å) contact compared to the sum of the vdW radii (4.11 Å).

It is worth noting that the strongest interactions, with interaction energies between -2.2 and -3.7 kcal/mol, correspond all to topologies that allow for N···Hg contacts shorter than 3.9 Å, i.e., models **1**, **3**, **4**, **7** and **13**. Topologies with no N···Hg contact have interaction energies between -0.1 and -1.1 kcal/mol (**2**, **8** – **12**, **14** and **17**). The two models with longer N···Hg distances (**5** and **15**, $d_{N\cdots Hg} > 4.0$ Å) show also weak attractions (-0.63 and -0.75 kcal/mol, respectively), even if the N···N distances are the longest ones (3.46 and 3.73 Å, respectively) and clearly longer than the vdW sum (3.32 Å). This secondary contact play therefore an important role in the stability of these compounds.

Table 7.1. Key geometrical parameters and interaction energies for all studied interaction topologies of the [N_3-Hg(CF_3)] dimers, calculated at the M06-2X/def2-TZVP level.[a]

Compound	ϕ (°)	N contact	N···N (Å)	N-Hg contact	N···Hg (Å)	ΔE_{INT}
1	90	$N_\alpha \cdots N_\alpha$	3.082	$N_\beta \cdots Hg$	3.540	-2.20
2	180	$N_\alpha \cdots N_\alpha$	3.062			-1.12
3	90	$N_\alpha \cdots N_\beta$	2.823	$N_\gamma \cdots Hg$	3.561	-3.71
4	180	$N_\alpha \cdots N_\beta$	2.846	$N_\gamma \cdots Hg$	3.533	-2.74
5	90	$N_\gamma \cdots N_\alpha$	3.463	$N_\gamma \cdots Hg$	4.019	-0.63
7	90	$N_\beta \cdots N_\beta$	2.936	$N_\gamma \cdots Hg$	3.764	-2.52
8	180	$N_\beta \cdots N_\beta$	3.045			-0.91
9	90	$N_\gamma \cdots N_\beta$	3.064			-0.59
10	180	$N_\gamma \cdots N_\beta$	3.072			-0.10
11	90	$N_\gamma \cdots N_\gamma$	3.133			-0.75
12	180	$N_\gamma \cdots N_\gamma$	3.138			-0.21
13	90	$N_\alpha \cdots N_\beta$	3.067	$N_\gamma \cdots Hg$	3.440	-2.71
		$N_\beta \cdots N_\alpha$	3.067			
14	180	$N_\alpha \cdots N_\beta$	3.161			-1.08
		$N_\beta \cdots N_\alpha$	3.161			
15	90	$N_\alpha \cdots N_\gamma$	3.730	$N_\gamma \cdots Hg$	4.242	-0.75
		$N_\beta \cdots N_\beta$	3.782			
		$N_\gamma \cdots N_\alpha$	3.730			
17	90	$N_\beta \cdots N_\gamma$	3.153			-0.89
		$N_\gamma \cdots N_\beta$	3.153			

[a] No local minima were found for dimers **6**, **16** and **18**.

7.4 Energy Decomposition Analysis

In light of the above results, I have performed an Energy Decomposition Analysis (EDA) of the 8 dimers in which N···N are the only intermolecular contacts shorter than the sum of the vdW radii (including dimers with single and double N···N contacts) to investigate the physical origin of the attraction. The results are summarized in Table 7.2.

The first observation is that the Pauli repulsion is large and is partially counterbalanced by the electrostatic attractive component. The dispersion force is the largest attractive term, accounting for 56 to 80 % of the attractive part of the interaction, thus making the formation of the adducts energetically favourable by 0.10 – 1.10 kcal/mol. However, in compound **10**, the dispersion term is not enough to overcome the

repulsive frozen term. Orbital-based terms (i.e., the sum of the polarization and charge transfer contributions) are also necessary in this case for the net interaction to be attractive. Notice that, in the same case, the orbital-based contribution overweighs the electrostatic component. This can be qualitatively explained by the fact that (1) the electron depletion region located at the N_β atom is small and is surrounded by two regions of large negative potential, and (2) the lone pair of the incoming nucleophile can delocalize to the π^* antibonding orbital also located at the N_β atom.[39,40]

Table 7.2. Energy Decomposition Analysis of NCIs in [N_3-Hg(CF_3)] dimers with N···N as the only intermolecular contact shorter than the sum of the corresponding van der Waals radii, calculated at the M06-2X/def2-TZVP level. The percentage represents the contribution to the total attractive (negative) interaction energy. Energies are given in kcal/mol.

Cpd.	ϕ (°)	ΔE_{PAULI}	ΔE_{ELEC}	ΔE_{DISP}	ΔE_{POL}	ΔE_{CT}	ΔE_{INT}
2	180	2.82	-1.41 (36.1 %)	-2.19 (56.0 %)	-0.15 (3.9 %)	-0.15 (4.0 %)	-1.10
8	180	2.73	-0.50 (14.0 %)	-2.84 (78.9 %)	-0.16 (4.6 %)	-0.09 (2.6 %)	-0.87
9	90	1.81	-0.45 (18.8 %)	-1.57 (65.7 %)	-0.20 (8.5 %)	-0.17 (7.0 %)	-0.59
10	180	1.70	-0.14 (7.9 %)	-1.42 (79.3 %)	-0.14 (7.8 %)	-0.09 (5.0 %)	-0.10
11	90	1.64	-0.77 (32.1 %)	-1.43 (60.1 %)	-0.11 (4.4 %)	-0.08 (3.4 %)	-0.75
12	180	1.49	-0.20 (11.5 %)	-1.37 (80.4 %)	-0.07 (4.2 %)	-0.07 (3.9 %)	-0.22
14	180	3.42	-1.64 (36.4 %)	-2.65 (59.1 %)	-0.17 (3.7 %)	-0.03 (0.8 %)	-1.08
17	90	2.56	-0.67 (19.4 %)	-2.33 (67.7 %)	-0.23 (6.6 %)	-0.22 (6.4 %)	-0.88

7.5 Analysis of the topology of the electron density

Finally, I have analysed the topology of the electron density of all dimers by means of QTAIM analysis to gain further insight into the interactions that hold them together. Topological properties at the bond critical point (BCP) for N···N contacts in [N_3-Hg(CF_3)] dimers are collected in Table 7.3.

For all intermolecular N···N contacts, I observed that (1) the computed electron density (ρ_{BCP}) is low, ranging from 0.002 to 0.012 a.u., typical of weak bonds, (2) the sign of the Laplacian of the electron density ($\nabla^2\rho_{BCP}$) is positive, indicating an electron charge depletion in the bonding region,[45] (3) the local electron kinetic energy (G_{BCP}) dominates the local electron potential energy in absolute value ($|V_{BCP}|$), leading to an overall positive (although small) total energy density (H_{BCP}), and (4) the $|V_{BCP}|/G_{BCP}$ ratio is lower than 1, which is characteristic of dispersion-bound systems.[46,47] These topological parameters support the classification of the azido···azido contacts as

noncovalent "closed-shell" interactions, whose dispersion-dominated nature has been shown in the previous section. Exponential relationships between the intermolecular N···N distance and the ρ_{BCP}, $\nabla^2\rho_{BCP}$, $|V_{BCP}|$ and G_{BCP}, respectively, are found in agreement with previous reports for other weak interactions[47-50] (Figure 7.3 and Eqs. A7.1 – A7.4 in the Appendix).

Table 7.3. Topological data at the BCP for all N···N intermolecular interactions in [N_3-Hg(CF_3)] dimers, calculated at M06-2X/def2-TZVP level of theory. All topological parameters are given in atomic units (a.u.).

Cpd.	ϕ (°)	N···N (Å)	ρ_{BCP}	$\nabla^2\rho_{BCP}$	V_{BCP}	G_{BCP}	H_{BCP}	$\lvert V_{BCP}\rvert/G_{BCP}$
1	90	3.082	0.009	0.031	-0.006	0.007	0.001	0.828
2	180	3.062	0.009	0.030	-0.005	0.006	0.001	0.817
3	90	2.823	0.012	0.051	-0.009	0.011	0.002	0.825
4	180	2.846	0.011	0.049	-0.008	0.010	0.002	0.810
5	90	3.463	0.004	0.014	-0.002	0.003	0.001	0.662
7	90	2.936	0.008	0.041	-0.006	0.008	0.002	0.744
8	180	3.045	0.006	0.033	-0.004	0.006	0.002	0.695
9	90	3.064	0.006	0.030	-0.004	0.006	0.002	0.702
10	180	3.072	0.006	0.030	-0.004	0.006	0.002	0.684
11	90	3.133	0.007	0.026	-0.004	0.005	0.001	0.730
12	180	3.138	0.006	0.025	-0.003	0.005	0.001	0.718
13	90	3.067	0.007	0.031	-0.005	0.006	0.001	0.764
		3.067	0.008	0.034	-0.005	0.007	0.002	0.775
14	180	3.161	0.006	0.026	-0.004	0.005	0.001	0.727
		3.161	0.006	0.026	-0.004	0.005	0.001	0.727
15	90	3.730	0.002	0.008	-0.001	0.001	0.000	0.668
		3.730	0.002	0.008	-0.001	0.002	0.001	0.660
17	90	3.153	0.006	0.027	-0.003	0.005	0.002	0.669
		3.153	0.006	0.027	-0.003	0.005	0.002	0.669

All these four topological parameters increase as the distances shorten. There is a positive correlation between the ρ_{BCP}, $|V_{BCP}|$ and G_{BCP}. A higher ρ_{BCP} is related to a higher accumulation of electrons at that point ($|V_{BCP}|$), which in turn implies higher repulsion between them (G_{BCP}).[48] The lack of BCPs for N···Hg contacts in all dimers prevents applying a similar analysis to that used for N···N contacts.

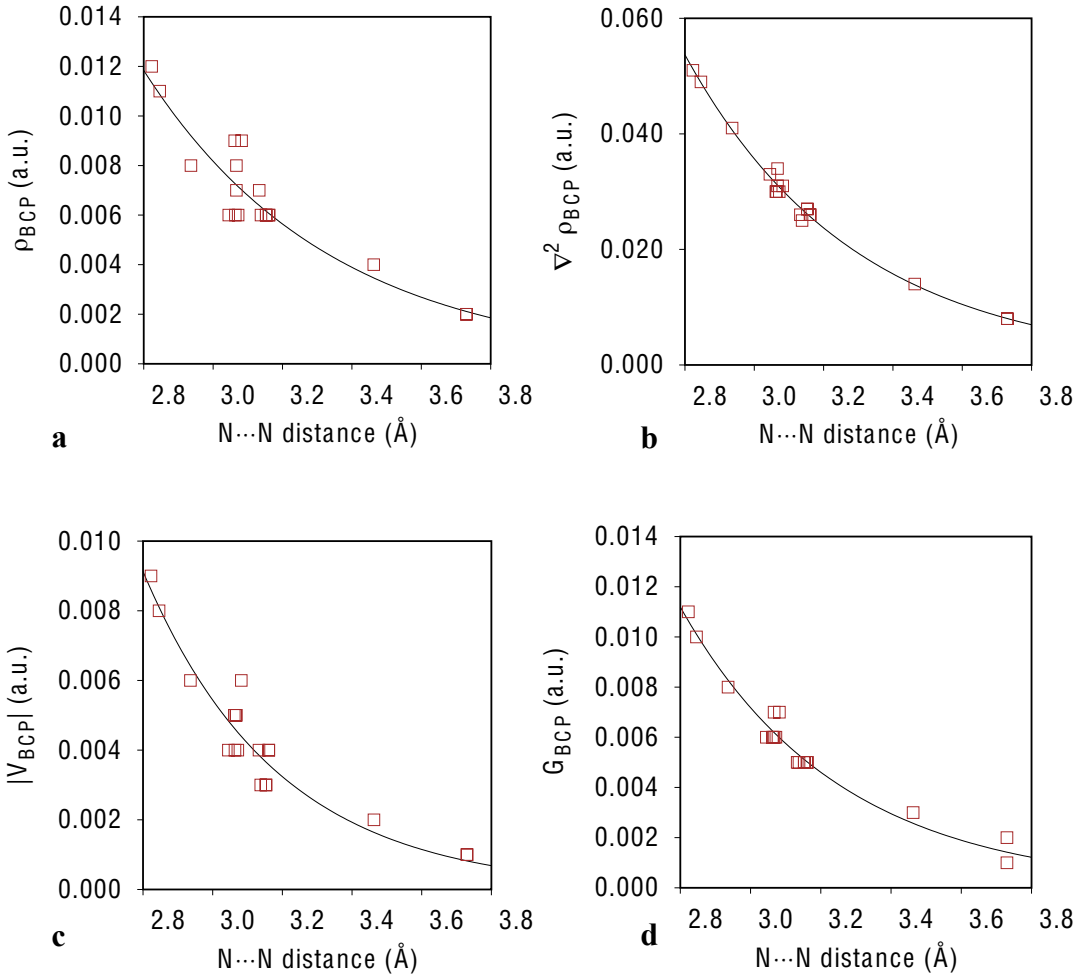

Figure 7.3. Dependence on the N···N distances of (**a**) ρ_{BCP} ($R^2 = 0.85$), (**b**) $\nabla^2\rho_{BCP}$ ($R^2 = 0.99$), (**c**) $|V_{BCP}|$ ($R^2 = 0.90$) and (**d**) G_{BCP} ($R^2 = 0.96$).

The presence of a bond path (BP) and a BCP is associated with the presence of an interaction. Conversely, the opposite is not true.[52,53] For this reason, the molecular graph of the dimers is complemented with NCI isosurfaces, to find other NCIs that remain undetected due to the stringent BCP criterion of QTAIM theory. Six examples of molecular graphs are depicted in Figure 7.4 (for the molecular graphs of all compounds see Figure A7.1 in the Appendix). A total of eleven systems involving a single interaction have been found (compounds **1** – **5** and **7** – **12**). The topological analysis of the electron density of these structures reveals a single BP and the corresponding BCP connecting the shortest N···N contacts. The interaction appears in the NCI plot as green pill-shaped isosurface (compounds **2**, **8** and **9** – **12**) or as flat almond-shaped bicoloured green-yellow isosurfaces (compounds **1**, **3**, **4** and **5**). In both cases, the green portion is surrounding the BCP and is aligned with the N···N contacts indicating weak stabilizing interactions, as expected due to the low ρ_{BCP} values (0.004 – 0.012 a.u.). In the latter group, there is a

second green portion assigned to weak stabilizing interactions between the N atom of one monomer and the Hg(II) atom of the other. No topological descriptors are found between these N···Hg contacts (Figure 7.4b, dashed lines) and, thus, this interaction remains undetected by the QTAIM topology. The same isosurface exhibits a yellow part, which indicates steric strain induced by the formation of the intermolecular four-membered pseudoring. No RCP is associated with the destabilizing region. QTAIM topology is also blind to this steric hindrance. Especially noteworthy is that structures **3** and **4** (see Figure A7.1c – d in the Appendix), which possess the shortest N···N distances and the highest ρ_{BCP} values (0.011 – 0.012 a.u.), show a dark-green isosurface between the azido···azido contacts, indicating a stronger interaction.

Regarding compounds **13** and **14**, two BPs and two BCPs that interconnect $N_\alpha\cdots N_\beta$ and $N_\beta\cdots N_\alpha$, respectively, were identified (Figures 7.4c and d). A ring critical point (RCP) is found at the centre of the four-membered pseudoring formed by the BPs. Both structures exhibit similar NCI green-yellow isosurfaces. The green areas appear around each BCP(N···N), whereas the yellow ones are enveloping the RCP. In compound **13**, the isosurface is extended to account for the $N_\gamma\cdots$Hg interaction forming a second four-membered pseudoring linking the dimers. The green colour indicates vdW-type interaction (ρ_{BCP} = 0.006 – 0.008 a.u.), namely N···N and N···Hg, whereas the yellow ones indicate steric strain within the pseudorings.

The analysis of the molecular graph of the last two structures (Figures 7.4e and f) was quite challenging because of certain abnormal trends. For instance, I observed that compound **15** shows one BP and one BCP for the $N_\alpha\cdots N_\gamma$ and $N_\gamma\cdots N_\alpha$ contacts, respectively (Figure 7.4e). An RCP is found between the $N_\beta\cdots N_\beta$ contacts, at the centre of the intermolecular six-membered pseudoring formed by the BPs, indicating some steric repulsion within the ring. According to the QTAIM analysis, there is no interaction between the central atoms. The NCI Index analysis, however, shows that all N···N (and N···Hg) contacts are of vdW type, separated by two barely discernible yellow regions. The lack of BCP between $N_\beta\cdots N_\beta$ interaction might be explained by the flatness of the electron density inside the ring (ρ_{BCP} = 0.001 – 0.002 a.u.). The yellow regions would indicate steric strain within both four-membered pseudorings, instead of the six-membered one formed by the BPs.

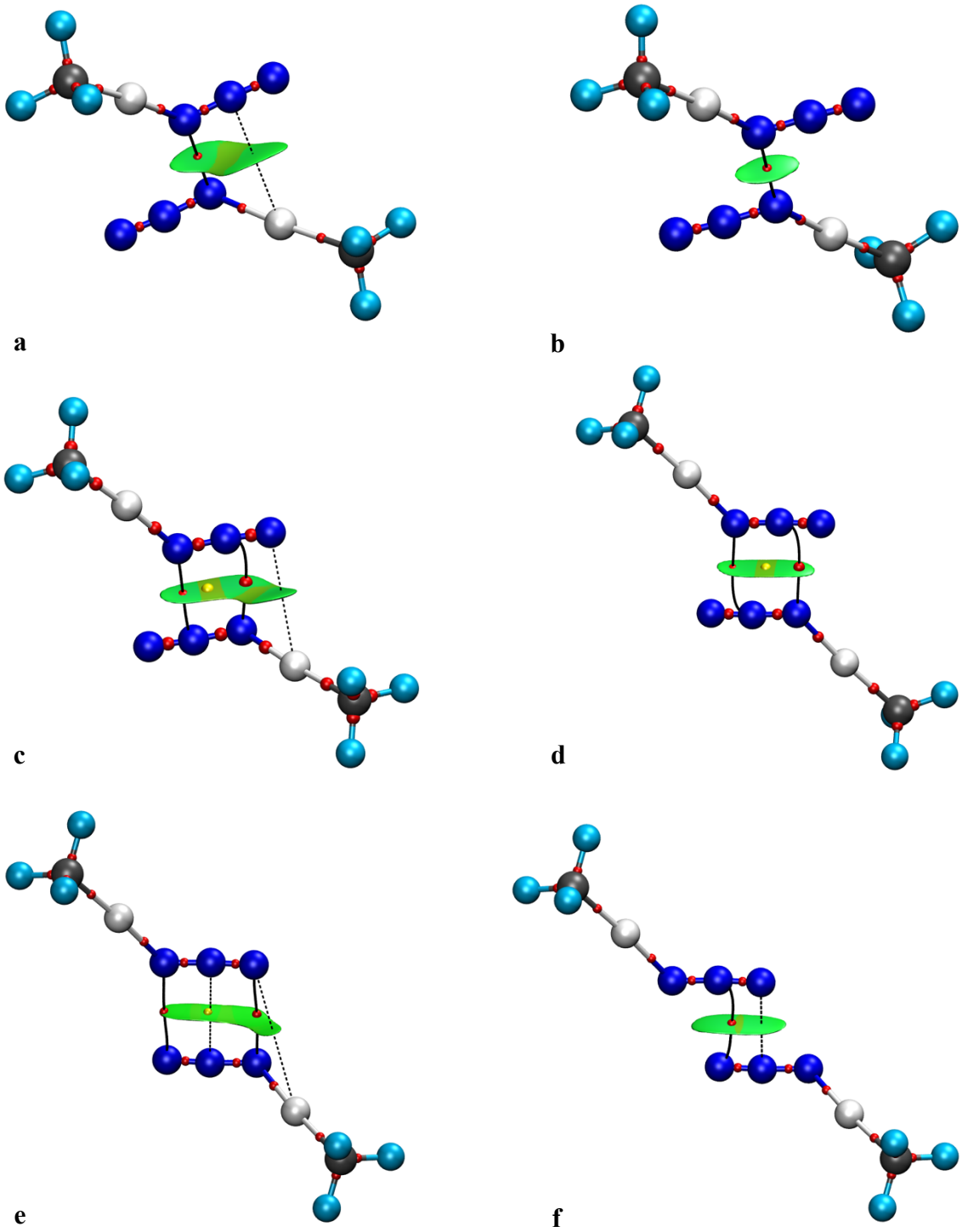

Figure 7.4. Molecular graphs and NCI isosurfaces (s = 0.4) for structures (**a**) **1**, (**b**) **2**, (**c**) **13**, (**d**) **14**, (**e**) **15** and (**f**) **17**. The isosurfaces are coloured according to a BRG scheme from -0.035 < sign(λ_2)ρ < 0.030 a.u. Small spheres represent BCP (red) and RCP (yellow). The solid lines represent the azido···azido BP and the dashed lines indicate the secondary N···Hg contact.

In compound **17**, the bond length of $N_\beta \cdots N_\gamma$ and $N_\gamma \cdots N_\beta$ contacts are the same (Figure 7.4f). Hence, it is expected that both show a BP and the corresponding BCP in the molecular graph. Nevertheless, only the former contact exhibits these topological

descriptors. Significantly, the BCP is displaced towards the centre of the bonding region. The NCI Index method indicates that both contacts are weakly attractive interactions, as expected due to the low ρ_{BCP} value (0.006 a.u.). There is a yellow region in the middle of the isosurface, indicating destabilizing crowding effect within the four-membered pseudoring.

7.6 Conclusions

In this chapter, I have investigated the intermolecular N···N interaction between the azido ligands in a transition metal azide complex. A MEP analysis has disclosed an electron-poor region near the central N_β atom, surrounded by two electron-rich regions near the N_α and N_γ atoms. The MEP map is a useful tool for predicting which interaction topology would be unstable from the electrostatic point of view. Upon closer inspection of the electron density distribution of the azido ligand, it can be predicted that all N···N contacts in dimers **6**, **16** and **18** would be electrostatically repulsive and thus the system would dissociate. Indeed, no local minima are found for these systems. All other dimers are found to be stable, with interaction energy ranging from -0.10 to -3.71 kcal/mol. The secondary N···Hg interaction plays an important role in stabilizing systems with electrostatically disfavourable azido···azido contacts such as dimers **5** and **15**, and in making dimers **1**, **3**, **4**, **7**, and **13** the most stable ones.

EDA results have shed light on the physical nature of the interaction. As in other cases, the electrostatic contribution partially counterbalances the Pauli exchange-repulsion, and dispersion is the main attractive force in all cases, with small contributions of orbital-based terms, namely polarization and charge transfer contributions.

The combined QTAIM and NCI Index analyses have confirmed the closed-shell, dispersion-dominated nature of the azido···azido contacts. Almost all the N···N short contacts exhibit a BP and the corresponding BCP, which are associated with the existence of an attractive interaction. No topological parameters are found between the intermolecular N···Hg contact in the molecular graph. Regardless of the presence or absence of BCP, a green isosurface is found between both interactions, indicating weak stabilizing van der Waals interactions. However, the yellow isosurfaces denote steric strain induced by the formation of intermolecular pseudorings in the azido bonding region.

These results show the existence of azido···azido interactions, while only interactions between azido groups and pnictogen, chalcogen, and halogen atoms or N-H hydrogen bonds have been reported in the literature.[38-41] These interactions may be useful for dictating the conformation of the molecules and therefore might have various applications in the field of catalysis, reactivity and crystal engineering, to name just a few examples.

7.7 Appendix

Annex 7.1. Exponential least-squares fittings equations for Figure 7.3.

a) $\rho_{BCP} = 2.12 \cdot e^{(-1.85 \cdot N \cdots N)}$ ($R^2 = 0.85$) [Eq. A7.1]

b) $\nabla^2 \rho_{BCP} = 16.33 \cdot e^{(-2.04 \cdot N \cdots N)}$ ($R^2 = 0.99$) [Eq. A7.2]

c) $|V_{BCP}| = 12.91 \cdot e^{(-2.59 \cdot N \cdots N)}$ ($R^2 = 0.90$) [Eq. A7.3]

d) $G_{BCP} = 5.60 \cdot e^{(-2.22 \cdot N \cdots N)}$ ($R^2 = 0.96$) [Eq. A7.4]

Annex 7.2. Combined molecular graphs and NCI plot for all azido···azido interaction topologies.

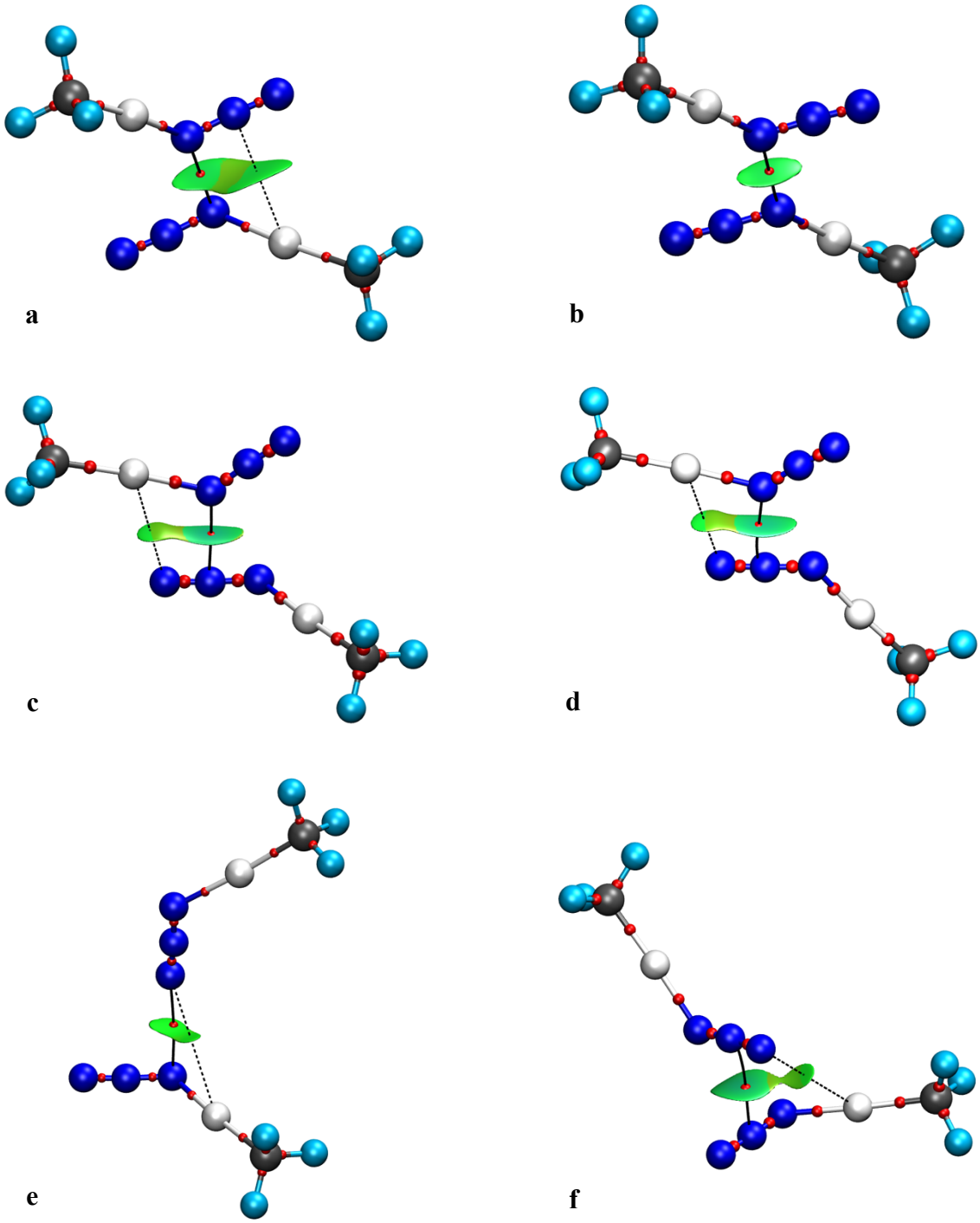

Figure A7.1. Molecular graphs and NCI isosurfaces (s = 0.4) for structures (**a**) **1**, (**b**) **2**, (**c**) **3**, (**d**) **4**, (**e**) **5,** (**f**) 7, (**g**) **8**, (**h**) **9**, (**i**) **10**, (**j**) **11**, (**k**) **12**, (**l**) **13**, (**m**) **14**, (**n**) **15**, and (**o**) **17**. The isosurfaces are coloured according to a BRG scheme from -0.035 < sign(λ_2)ρ < 0.030 a.u. Small spheres represent BCP (red) and RCP (yellow). The solid lines represent the azido···azido BP and the dashed lines indicate the secondary N···Hg contact.

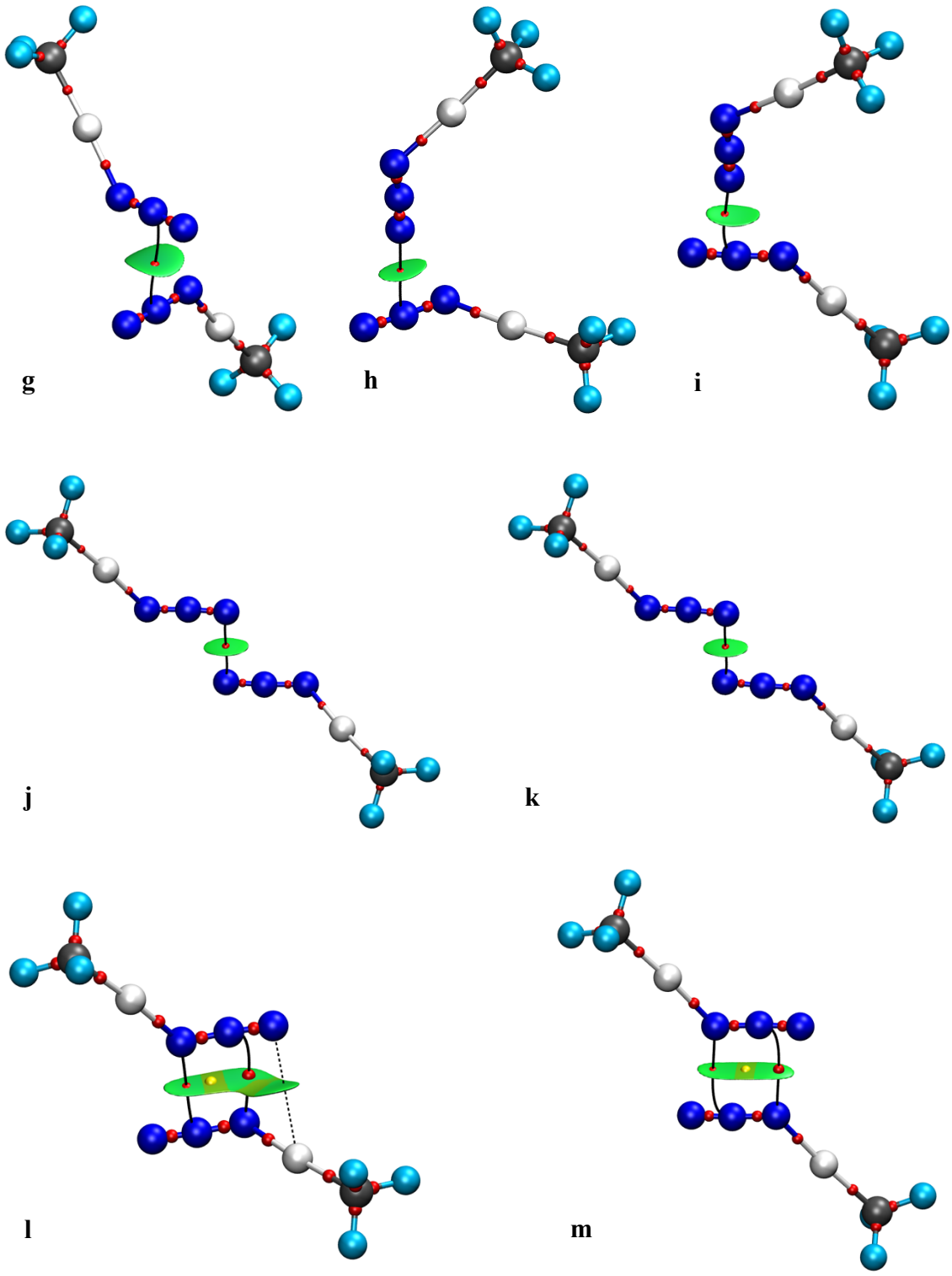

Figure A7.1. Molecular graphs and NCI isosurfaces (s = 0.4) for structures (**a**) **1**, (**b**) **2**, (**c**) **3**, (**d**) **4**, (**e**) **5,** (**f**) 7, (**g**) **8**, (**h**) **9**, (**i**) **10**, (**j**) **11**, (**k**) **12**, (**l**) **13**, (**m**) **14**, (**n**) **15**, and (**o**) **17**. The isosurfaces are coloured according to a BRG scheme from -0.035 < sign(λ_2)ρ < 0.030 a.u. Small spheres represent BCP (red) and RCP (yellow). The solid lines represent the azido···azido BP and the dashed lines indicate the secondary N···Hg contact. (continuation)

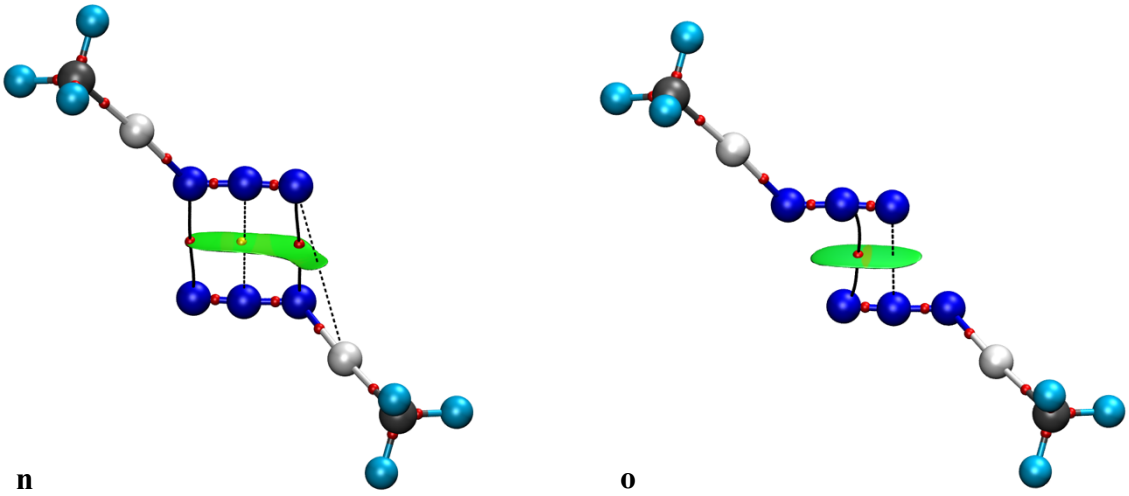

Figure A7.1. Molecular graphs and NCI isosurfaces (s = 0.4) for structures (**a**) **1**, (**b**) **2**, (**c**) **3**, (**d**) **4**, (**e**) **5,** (**f**) 7, (**g**) **8**, (**h**) **9**, (**i**) **10**, (**j**) **11**, (**k**) **12**, (**l**) **13**, (**m**) **14**, (**n**) **15**, and (**o**) **17**. The isosurfaces are coloured according to a BRG scheme from -0.035 < sign(λ_2)ρ < 0.030 a.u. Small spheres represent BCP (red) and RCP (yellow). The solid lines represent the azido···azido BP and the dashed lines indicate the secondary N···Hg contact. (continuation)

7.8 References

1. Fehlhammer, W. P.; Beck, W. Azide Chemistry - an Inorganic Perspective, Part I Metal Azides: Overview, General Trends and Recent Developments. *Z. Anorg. Allg. Chem.* **2013**, *639*, 1053-1082.
2. Seok, W.-K.; Klapötke, T. M. Inorganic and Transition Metal Azides. *Bull. Korean Chem. Soc.* **2010**, *31*, 781-788.
3. Tornieporth-Oetting, I. C.; Klapötke, T. M. Covalent Inorganic Azides. *Angew. Chem. Int. Ed.* **1995**, *34*, 511-520.
4. Tornieporth-Oetting, I. C.; Klapötke, T. M. Covalent Inorganic Nonmetal Azides. In *Combustion Efficiency and Air Quality*; Springer US: Boston, MA, 1995; pp 51-62.
5. Bräse, S.; Gil, C.; Knepper, K.; Zimmermann, V. Organic Azides: An Exploding Diversity of a Unique Class of Compounds. *Angew. Chem. Int. Ed*. **2005**, *44*, 5188-5240.
6. *Organic Azides: Syntheses and Applications*; Bräse, S., Banert, K., Eds.; John Wiley & Sons: Nashville, TN, 2011.

7. Betterton, E. A. Environmental Fate of Sodium Azide Derived from Automobile Airbags. *Crit. Rev. Environ. Sci. Technol.* **2003**, *33*, 423-458.
8. Biegańska, J. The Effect of the Reaction pH on Properties of Lead(II) Azide. *Materials*. **2021**, *14*, 2818-2829.
9. Li, J.-J. Sodium Azide (NaN_3): A Versatile Reagent in Organic Synthesis. *Synlett*. **2007**, *2007*, 0505-0506.
10. Bock, H.; Dammel, R. The Pyrolysis of Azides in the Gas Phase. *Angew. Chem. Int. Ed.* **1987**, *26*, 504-526.
11. Wang, C.; Ikhlef, D.; Kahlal, S.; Saillard, J.-Y.; Astruc, D. Metal-Catalyzed Azide-Alkyne "Click" Reactions: Mechanistic Overview and Recent Trends. *Coord. Chem. Rev.* **2016**, *316*, 1-20.
12. Singh, M. S.; Chowdhury, S.; Koley, S. Advances of Azide-Alkyne Cycloaddition-Click Chemistry over the Recent Decade. *Tetrahedron* **2016**, *72*, 5257-5283.
13. Li, H.-K.; Sun, J.-Z.; Qin, A.-J.; Tang, B. Z. Azide-Alkyne Click Polymerization: An Update. *Chin. J. Polym. Sci.* **2012**, *30*, 1-15.
14. Agard, N. J.; Baskin, J. M.; Prescher, J. A.; Lo, A.; Bertozzi, C. R. A Comparative Study of Bioorthogonal Reactions with Azides. *ACS Chem. Biol.* **2006**, *1*, 644-648.
15. Gutmann, M.; Memmel, E.; Braun, A. C.; Seibel, J.; Meinel, L.; Lühmann, T. Biocompatible Azide-Alkyne "Click" Reactions for Surface Decoration of Glyco-Engineered Cells. *Chembiochem*. **2016**, *17*, 866-875.
16. Nyffeler, P. T.; Liang, C.-H.; Koeller, K. M.; Wong, C.-H. The Chemistry of Amine-Azide Interconversion: Catalytic Diazotransfer and Regioselective Azide Reduction. *J. Am. Chem. Soc.* **2002**, *124*, 10773-10778.
17. Wang, Y.-C.; Lai, X.-J.; Huang, K.; Yadav, S.; Qiu, G.; Zhang, L.; Zhou, H. Unravelling Nitrene Chemistry from Acyclic Precursors: Recent Advances and Challenges. *Org. Chem. Front.* **2021**, *8*, 1677-1693.
18. Jönsson, B.M.; Håkansson, K.; Liljas, A. The structure of human carbonic anhydrase II in complex with bromide and azide. *FEBS Lett.* **1993**, *322*, 186-190.
19. Zidovudine. https://www.drugs.com/monograph/zidovudine.html (accessed Feb 15, 2022).

20. Blandy, C.; Gervais, D.; Cardenas, M. S. The Role of Early Transition Metal Azides as Catalysts of the Ring-Opening Reaction of Epoxides with Trimethylsilylazide. *J. Mol. Catal.* **1986**, *34*, 39-46.

21. Blandy, C.; Choukroun, R.; Gervais, D. Synthesis of O-Protected Azidohydrins Catalyzed by Titanium and Vanadium Complexes. *Tetrahedron Lett.* **1983**, *24*, 4189-4192.

22. Lopez-Sanchez, J. A.; Morisse, C.; Winfield, J. M.; Krumm, B.; Klapötke, T. M.; Lennon, D. The Preparation of a Residue-Free, Alumina-Supported Gold Catalyst by Decomposition of an Azido-Gold(III) Complex and an Evaluation of the Effectiveness of the Catalyst for the Hydrogenation of Propyne: Preparation of a Residue-Free, Alumina-Supported Gold Catalyst. *Z. Anorg. Allg. Chem.* **2015**, *641*, 694-698.

23. Hennig, H.; Ritter, K.; Billing, R. Photokatalytische Bildung von Wasserstoff aus Thiolen in Gegenwart von Vitamin B12-Modellverbindungen mit Azid als photochemischem Opferliganden. *J. Prakt. Chem.* **1996**, *338*, 604-613.

24. Hennig, H. Homogeneous Photo Catalysis by Transition Metal Complexes. *Coord. Chem. Rev.* **1999**, *182*, 101-123.

25. Kurz, D.; Hennig, H.; Reinhold, J. The molecular and electronic structure of nickelatetrazole - A theoretical study. *Z. Anorg. Allg. Chem.* **2001**, *627*, 1895-1900.

26. Ohata, J.; Vohidov, F.; Aliyan, A.; Huang, K.; Martí, A. A.; Ball, Z. T. Luminogenic Iridium Azide Complexes. *Chem. Commun*. **2015**, *51*, 15192-15195.

27. Lin, J.-D.; Li, Y.-H.; Xu, J.-G.; Zheng, F.-K.; Guo, G.-C.; Lv, R.-X.; He, W.-C.; Huang, Z.-N.; Liu, J.-F. Stabilizing Volatile Azido in a 3D Nitrogen-Rich Energetic Metal-Organic Framework with Excellent Energetic Performance. *J. Solid State Chem.* **2018**, *265*, 42-49.

28. Ma, Y.; Wen, Y.-Q.; Zhang, J.-Y.; Gao, E.-Q.; Liu, C.-M. Structures and Magnetism of Azide- and Carboxylate-Bridged Metal(II) Systems Derived from 1,2-Bis(N-Carboxymethyl-4-Pyridinio)Ethane. *Dalton Trans.* **2010**, *39*, 1846-1854.

29. Ghosh, M.; Chakrabarty, P. P.; Jana, A. D.; Schollmeyer, D.; Sakiyama, H.; Mikuriya, M.; Debnath, R.; Brandão, P.; Mal, D.; Saha, S. Ligand Mediated

Structural Diversity of Copper(II)-Azido Moiety: Synthesis, Structure and Magnetic Study. *Inorg. Chim. Acta*. **2022**, *531*, 120713-120719.

30. Escuer, A.; Aromí, G. Azide as a Bridging Ligand and Magnetic Coupler in Transition Metal Clusters. *Eur. J. Inorg. Chem.* **2006**, *2006*, 4721-4736.
31. Evangelio, E.; Rath, N. P.; Mirica, L. M. Cycloaddition Reactivity Studies of First-Row Transition Metal-Azide Complexes and Alkynes: An Inorganic Click Reaction for Metalloenzyme Inhibitor Synthesis. *Dalton Trans.* **2012**, *41*, 8010-8021.
31. Beto, C. C.; Zeman, C. J., IV; Yang, Y.; Bullock, J. D.; Holt, E. D.; Kane, A. Q.; Makal, T. A.; Yang, X.; Ghiviriga, I.; Schanze, K. S.; Veige, A. S. An Application Exploiting Aurophilic Bonding and iClick to Produce White Light Emitting Materials. *Inorg. Chem.* **2020**, *59*, 1893-1904.
32. Shen, Y.-H.; Esper, A. M.; Ghiviriga, I.; Abboud, K. A.; Schanze, K. S.; Ehm, C.; Veige, A. S. SPAAC iClick: Progress towards a Bioorthogonal Reaction in-Corporating Metal Ions. *Dalton Trans.* **2021**, *50*, 12681-12691.
33. He, M.; Chen, F.; Shao, D.; Weis, P.; Wei, Z.; Sun, W. Photoresponsive Metallopolymer Nanoparticles for Cancer Theranostics. *Biomaterials* **2021**, *275*, 120915-120938.
34. Toscani, A.; Hind, C.; Clifford, M.; Kim, S.-H.; Gucic, A.; Woolley, C.; Saeed, N.; Rahman, K. M.; Sutton, J. M.; Castagnolo, D. Development of Photoactivable Phenanthroline-Based Manganese(I) CO-Releasing Molecules (PhotoCORMs) Active against ESKAPE Bacteria and Bacterial Biofilms. *Eur. J. Med. Chem.* **2021**, *213*, 113172-113184.
35. Müller, U. Strukturchemie Der Azide. *Struct. Bonding.* **2005**, *14*, 141-172.
36. Campana, C. F.; Lo, F. Y.-K.; Dahl, L. F. Stereochemical Analysis of $Fe_2(CO)_6(\mu$-$Se_2)$: A Diselenium Analog of $Fe_2(CO)_6(\mu$-$S_2)$. *Inorg. Chem.* **1979**, *18*, 3060-3064.
37. Bursch, M.; Kunze, L.; Vibhute, A. M.; Hansen, A.; Sureshan, K. M.; Jones, P. G.; Grimme, S.; Werz, D. B. Quantification of Noncovalent Interactions in Azide-Pnictogen, -Chalcogen, and -Halogen Contacts. *Chem. Eur. J.* **2021**, *27*, 4627-4639.
38. Madhusudhanan, M. C.; Balan, H.; Werz, D. B.; Sureshan, K. M. Azide···Oxygen Interaction: A Crystal Engineering Tool for Conformational Locking. *Angew. Chem. Int. Ed*. **2021**, *60*, 22797-22803.

39. Scheiner, S. On the Ability of Nitrogen to Serve as an Electron Acceptor in a Pnicogen Bond. *J. Phys. Chem. A*. **2021**, *125*, 10419-10427.

40. Setifi, Z.; Setifi, F.; Glidewell, C.; Gil, D. M.; Kletskov, A. V.; Echeverria, J.; Mirzaei, M. An Iron(II) Complex of Trans, Trans, Trans-Bis(Azido)Bis(4-Amino-3,5-Bis(2-Pyridyl)-1,2,4-Triazole): Insight into Molecular and Supramolecular Structures Using Hirshfeld Surface Analysis and DFT Studies. *J. Mol. Struct.* **2021**, *1235*, 130155-130163.

41. Groom, C. R.; Bruno, I. J.; Lightfoot, M. P.; Ward, S. C. The Cambridge Structural Database. *Acta Crystallogr., Sect. B: Struct. Sci., Cryst. Eng. Mater*. **2016**, *72*, 171-179.

42. Alvarez, S. A cartography of the van der Waals territories. *Dalton Trans*. **2013**, *42*, 8617-8636.

43. Brauer, D. J.; Bürger, H.; Pawelke, G.; Flegler, K. H.; Haas, A. Schwingungsspektren und normalkoordinatenanalyse von CF_3,-verbindungen: XXVI. Molekülstrukturen und schwingungsspektren von α-CF_3HgN_3 und CF_3HgNCO. *J. Organomet. Chem.* **1978**, *160*, 389-401.

44. Matta, C. F.; Boyd, R. J. An Introduction to the Quantum Theory of Atoms in Molecules. In *The Quantum Theory of Atoms in Molecules: From Solid State to DNA and Drug Design*; Matta, C. F., Boyd, R. J., Eds.; Wiley-VCH: Weinheim, 2007, pp 1-34.

45. Cremer, D; Kraka, E. A Description of the Chemical Bond in Terms of Local Properties of Electron Density and Energy**.** *Croat. Chem. Acta*. **1984**, *57*, 1259-1281.

46. Grabowski, S. J.; Sokalski W. A.; Leszczynski, J. Wide spectrum of H···H interactions: van der Waals contacts, dihydrogen bonds and covalency. *Chem. Phys*. **2007**, *337*, 68-76.

48. Espinosa, E.; Molins, E.; Lecomte, C. Hydrogen Bond Strengths Revealed by Topological Analyses of Experimentally Observed Electron Densities. *Chem. Phys. Lett.* **1998**, *285*, 170-173.

49. Sánchez-Sanz, G.; Alkorta, I.; Elguero, J. Theoretical Study of Intramolecular Interactions in Peri-Substituted Naphthalenes: Chalcogen and Hydrogen Bonds. *Molecules* **2017**, *22*, 227-242.

50. Trujillo, C.; Alkorta, I.; Elguero, J.; Sánchez-Sanz, G. Cooperative Effects in Weak Interactions: Enhancement of Tetrel Bonds by Intramolecular Hydrogen Bonds. *Molecules* **2019**, *24*, 308-320.

51. Munshi, P.; Row, T. N. G. Evaluation of Weak Intermolecular Interactions in Molecular Crystals via Experimental and Theoretical Charge Densities. *Crystallography Reviews*. **2005**, *11*, 199-241.

52. Lane, J. R.; Contreras-García, J.; Piquemal, J.-P.; Miller, B. J.; Kjaergaard, H. G. Are Bond Critical Points Really Critical for Hydrogen Bonding? *J. Chem. Theory Comput*. **2013**, *9*, 3263-3266.

54. Contreras-García, J.; Yang, W.; Johnson, E. R. Analysis of Hydrogen-Bond Interaction Potentials from the Electron Density: Integration of Noncovalent Interaction Regions. *J. Phys. Chem. A*. **2011**, *115*, 12983-12990.

General Conclusions

In this doctoral thesis, a combined structural and computational analysis of various types of intra and intermolecular noncovalent interactions (NCIs) is presented. Special attention was paid to the description of the energetics and the physical origin of the studied interactions as well as the geometric parameters that maximize their strength. To that end, searches for experimental structures in the Cambridge Structural Database (CSD), accurate Density Functional Theory (DFT) calculations and other computational tools currently available have been used to analyse, characterize, quantify, and visualize the NCIs.

One of the most widely used computational tools, the Molecular Electrostatic Potential (MEP), has allowed us to rationalise these interactions from the electrostatic point of view in some cases. However, it has some limitations. Prediction of NCIs based only on the sign of the electrostatic potential of the regions in contact fails in other cases (Chapters **4** and **7**).[1,2] For those reasons, it has to be complemented with methods that also explore the interactions from the orbital point of view, such as Natural Bond Orbital (NBO) and Natural Population Analyses (NPA). Methods based on the analysis of the topology of the electron density are also useful to determine molecular structure and the nature of chemical bonds. The Quantum Theory of Atoms in Molecules (QTAIM) is the most popular among them. However, the stringent bond critical point (BCP) criterion causes some NCIs to remain undetected. To overcome this problem, the NCI Index method, based on the inspection of the reduced density gradient, can be used since it provides with a graphical representation of the attractive and repulsive forces between the molecules, allowing for an intuitive chemical interpretation (Chapter **1**).

The noncovalently-bonded systems studied in this work are different. The chemical properties of the atoms or fragments in contact, the orbitals involved, the geometric features (e.g., bond angles), and the interaction strength vary from one system to another. However, the forces that govern the establishment of such weak interactions are the same, one contribution eventually predominating over the others. According to the ALMO-EDA-II method, these forces can be classified as dispersion, charge transfer and polarization (orbital-based or “covalent” contributions), electrostatic, and Pauli exchange-repulsion terms. A weak interaction is established if and only if the stabilizing forces overcome the repulsion of the electron clouds. The noncovalently-bonded system does not need to be the lowest energy minimum, as long as there is a barrier separating it from other minima of lower energy (Chapter **4**).[1,3]

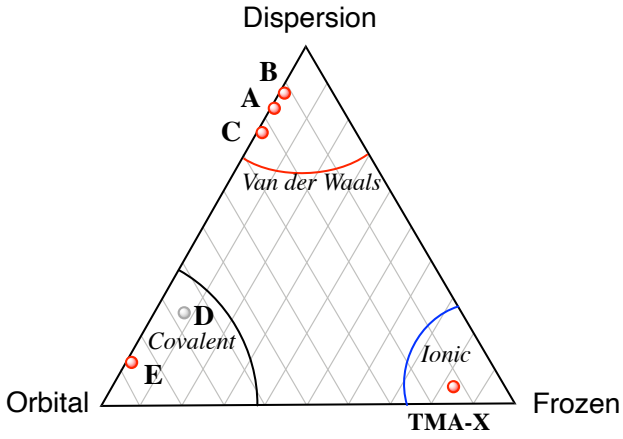

Figure 1. Ternary diagram of main stabilizing contributions acting upon the formation of noncovalently-bonded systems, on which each intermolecular noncovalent interaction studied in this work is represented by a capital letter, except for the intramolecular through-ring bonding in Li_2X_2 rings. The vertices represent pure dispersion, orbital or frozen contributions, respectively, and the semicircles represent regions of predominance of one of the terms. The NCIs are located in the diagram according to the relative contribution of the two main attractive terms. They are sorted alphabetically according to the increasing magnitude of the interaction strength. (**A**) Electrostatic repulsive Br···C=O contacts, (**B**) azido···azido interactions, (**C**) lone-pair-carbonyl in acyl halides, (**D**) sigma-hole interactions between lead(II) and sulphur, and (**E**) $[N\cdots I\cdots N]^+$ halonium bonding. System **D** is represented as a grey circle because the data was obtained from NBO analyses.

The nomenclature and classification of all NCIs known so far have been based on the atom that acts as a Lewis acid (i.e., pnictogen, chalcogen or halogen), base (i.e., hydride) or the origin of the electron depletion of the acceptor molecule (sigma or pi-hole) which had led to confusion.[4] Here, I propose to classify them according to the relative contribution of the attractive (negative) forces to the total interaction energy, and to visualize them in a ternary diagram (Figure 1), at whose vertices would appear the noncovalent interactions dominated by ionic, covalent or dispersion forces. Since it has been shown in several chapters of this thesis that the Pauli and electrostatic terms are correlated and in all the cases studied their sum (frozen term) is always destabilizing, I propose to disregard that term in those cases and consider only the orbital and dispersion contributions as the attractive energy that overcomes the repulsive "steric" (or frozen) interaction and stabilize the supramolecular entity. In those cases, the bonding interactions will be found at the line connecting the pure dispersion and orbital interactions. There are other cases, in which a strong Coulombic force can overcome the

Pauli repulsion, notably cation-anion interactions or strongly dipolar interactions. Then the attractive terms must include orbital, dispersion and frozen contributions, and we can start to obtain a wider perspective of the types of intermolecular bonding. As an example, I include in Figure 1 the case of the tetramethylammonium-halide ion pairs, (TMA)X, studied recently in our group, which are found to be predominantly electrostatic with non-negligible orbital contributions and a lesser dispersion supplement.[5]

Dispersion-dominated systems (**A** – **C**) possess the lowest interaction energy among all those studied in this work (~ 1 kcal/mol per contact, that can reach up to 3 kcal/mol in some of the acyl halide systems **C**).[1,2,6] Systems **B** that incorporates an additional N···Hg contact are further stabilized by 1 – 2 kcal/mol.[2] Orbital-based dominated system **E** possess the strongest interactions, with energies in the range 35 – 45 kcal/mol.[7] The Pb···S systems **D**, have interaction energies of around 15 kcal/mol, which can be mostly attributed to a donor-acceptor interaction according to the NBO results.[8] Although no EDA analysis was carried out for these interactions, the NBO results allow us to tentatively place them closer to the covalent vertex of the ternary diagram. The intramolecular Li···Li and X···X through-bonding in Li_2X_2 rings are not included in this classification. The cyclic nature of the Li_2X_2 groups is not amenable to a partition in two fragments as required by the above methods. However, NPA results indicate that the Li-X bonding has an ionic (electrostatic) nature with a non-negligible covalent contribution. The two Li ions are in closer contact than those in the Li_2 molecule, thanks to a through-bond interaction that overcomes the through-space Coulombic repulsion (Chapter 2).[9]

To sum up, the work done so far in this thesis has explained some of the properties of noncovalent interactions and classified them according to the physical origin of the attraction. Overall, the results obtained here are expected to provide a useful guide in chemistry, especially in crystal and supramolecular design, stimulate the use of novel approaches in the search for novel noncovalent interactions and, ultimately, contribute to a better understanding of chemical bonding in general and noncovalent interactions in particular.

1. References

1. Echeverria, J.; Velasquez, J. D.; Alvarez, S. Understanding the Interplay of Dispersion, Charge Transfer, and Electrostatics in Noncovalent Interactions: The Case of Bromine–Carbonyl Short Contacts. *Cryst. Growth Des.* **2020**, *20*, 7180-7187.
2. Velasquez, J. D.; Echeverría, J.; Alvarez, S., Azido···Azido interactions in transition metal complexes. **2022**, in press.
3. Alkorta, I.; Elguero, J.; Frontera, A. Not Only Hydrogen Bonds: Other Noncovalent Interactions. *Crystals* **2020**, *10*, 180-208.
4. Grabowski, S. J. Classification of So-Called Non-Covalent Interactions Based on VSEPR Model. *Molecules* **2021**, *26*, 4939-4961.
5. Gil, M. D.; Echeverria, J.; Alvarez, S. The Tetramethylammonium Cation: Directionality and Covalency in its Interactions with Halide Ions. *Inorg. Chem.*, in press, doi: 10.1021/acs.inorgchem.2c00600.
6. Velasquez, J. D.; Echeverria**,** J.; Alvarez, S., Effect of the Substituents on the Nature and Strength of Lone-Pair–Carbonyl Interactions in Acyl Halides. *Cryst. Growth Des.* **2019**, *19*, 6511-6518.
7. Velasquez, J. D.; Echeverría, J.; Alvarez, S. Bonding Analysis in Halonium Compounds. **2022**, in press.
8. Velasquez, J. D.; Mahmoudi, G.; Zangrando, E.; Gurbanov, A. V.; Zubkov, F. I.; Zorlu, Y.; Masoudiasl, A.; Echeverría, J., Experimental and Theoretical Study of Pb···S and Pb···O σ-Hole Interactions in the Crystal Structures of Pb(II) Complexes. *CrystEngComm*. **2019**, *21*, 6018-6025.
9. Velasquez, J. D.; Echeverría, J.; Alvarez, S. Delocalized Bonding in Li_2X_2 Rings: Probing the Limits of the Covalent and Ionic Bonding Models. *Inorg. Chem.* **2021**, *60*, 345–356.